Influence of climate change and extreme weather events on intermittent renewable power generation and electricity demand

Zur Erlangung des akademischen Grades eines
Doktors der Ingenieurwissenschaften (Dr.-Ing.)
von der KIT-Fakultät für Wirtschaftswissenschaften des
Karlsruher Instituts für Technologie (KIT)

genehmigte

DISSERTATION

von

M.Sc. Wenxuan Hu
aus Hubei, China

Tag der mündlichen Prüfung:	24.07.2025
Referent:	Prof. Dr. Patrick Jochem
Korreferent:	Prof. Dr. Oliver Grothe
Karlsruhe	(2025)

Abstract

Renewable energy plays a crucial role in mitigating climate change by significantly reducing carbon emissions in the energy sector. Over the past decades, many regions have transitioned toward renewable energy, increasing the share of renewables in global power generation and driving electrification in modern energy systems. To understand, analyze, and optimize these evolving energy systems, energy systems modeling is essential, as it can provide insights and guidelines for policy decisions. However, the reliability of energy systems modeling is often challenged by the uncertainties, particularly concerning weather variability, future electricity demand, and extreme weather events. These uncertainties in input data pose significant challenges for energy systems modeling and can greatly impact the robustness of system designs. Therefore, this dissertation aims to improve the accuracy and reliability of energy systems modeling by addressing these uncertainties.

One of these uncertainties is the spatial resolution of meteorological input data. This is particularly critical for wind speed, which is highly sensitive to spatial resolution due to its strong local variability influenced by topography. Therefore, this dissertation focuses first on improving the spatial resolution of wind speed data, which is a core input data in energy systems modeling. By applying a machine learning–based statistical downscaling technique, coarse-resolution reanalysis data are downscaled into high-resolution, hourly wind speed time series. The improved data increases the accuracy of renewable energy generation modeling, enables local-scale energy system analysis, improves the assessment of extreme weather events at regional scales, and builds the foundation for more accurate and detailed energy system models.

The main climate change induced uncertainty on the demand side is considered next. Electricity demand is highly sensitive to temperature variations and is influenced by socio-economic factors such as the electrification of demand sectors and energy efficiency improvements in buildings. The evolving patterns of these factors introduce significant uncertainty in accurate demand projections. To better capture the dynamic nature of electricity demand under different climate scenarios and policy implementations, this dissertation investigates future demand trends using Temperature Response Functions (TRFs), which characterize the nonlinear relationship between temperature and electricity demand. Therewith, the role of the building sector is accounted for through a novel piecewise regression model that considers the influence of space cooling, passive cooling, electrification, and thermal insulation. This improved approach enables a more realistic and robust projection of future electricity demand under varying climate and policy conditions.

The third uncertainty addressed in this dissertation concerns extreme weather events. As the frequency and intensity of such events increase, it becomes increasingly important to integrate them into energy systems modeling. By exploring how extreme weather events impact energy system reliability, this dissertation aims to identify the key factors contributing to robust energy system design. To achieve this, methods for generating synthetic extreme weather years that capture critical extreme weather conditions are proposed. These synthetic extreme weather years are then used as input data for a sector-coupled energy system optimization model to investigate their impact on energy systems. This comprehensive approach significantly improves the current literature. The findings reveal that dispatchable generation technologies play a crucial role in ensuring system robustness and that short-term extreme events significantly influence the required dispatchable generation capacities.

The novelty of this dissertation lies in its methodological contributions to addressing these three major uncertainties in energy systems modeling. For high-resolution wind speed data, this dissertation presents a novel machine learning–based statistical downscaling approach. In contrast to commonly used methods such as computationally intensive dynamic downscaling or distribution-based methods, the proposed method enables efficient, high-resolution wind speed downscaling over large geographical areas while requiring minimal computational resources. For electricity demand projection, this dissertation expands the application of TRFs, which are commonly used in the literature but rarely explored at large geographical scales. More importantly, while most studies assume that TRFs remain static over time, this work is the first to investigate the dynamic characteristics of TRFs under various socioeconomic factors. Finally, for robust energy system design, this study focuses on generating a comprehensive volume of synthetic weather years specifically tailored for extreme residual load events, a topic rarely discussed in the literature. By examining the close relationship between dispatchable generation, short-term extreme events, and system robustness, this dissertation provides guidance for energy modelers on selecting or synthesizing weather years for optimization and simulation models.

Together, these three contributions enhance the reliability of energy systems modeling by reducing uncertainties in meteorological input data, improving demand projection, and evaluating system robustness against extreme weather events. This work provides valuable insights into how climate variability and extreme weather shape future energy systems, offering a foundation for more robust energy planning and policy development.

Zusammenfassung

Erneuerbare Energien spielen eine wesentliche Rolle bei der Bekämpfung des Klimawandels, da sie das Potenzial haben, die Kohlendioxid Emissionen im Energiesektor deutlich zu reduzieren. Mit dem steigenden Anteil erneuerbarer Energien und der zunehmenden Elektrifizierung werden Energieangebot und nachfrage jedoch stärker von Wetterbedingungen abhängig. Wetterabhängige erneuerbare Energiequellen wie Wind und Solar unterliegen natürlichen Schwankungen, was Unsicherheiten im Energiesystem mit sich bringt. Gleichzeitig wird auch die Energienachfrage vom Klima beeinflusst, da Temperaturveränderungen den Bedarf an Heizung und Kühlung verändern. Da extreme Wetterereignisse infolge des Klimawandels häufiger werden, ist das Verständnis des Einflusses klimatischer Variabilität auf sowohl die erneuerbare Stromerzeugung als auch die Stromnachfrage entscheidend für die Analyse von Energiesystemen.

Um diese Einschränkungen zu überwinden und die Lücke zwischen Wetterdaten und Energiesystemanalyse zu schließen, konzentriert sich diese Dissertation auf zwei wesentliche Eingangsdaten für Energiesystemmodelle: Windgeschwindigkeit und Stromnachfrage, und untersucht deren Einfluss auf die Systemresilienz. Die Dissertation bringt methodische Beiträge zur Bewältigung großer Unsicherheiten in der Energiesystemmodellierung. Sie führt einen neuen maschinellen Lernansatz für hochauflösendes Windgeschwindigkeits-Downscaling ein und erweitert die Anwendung von TRFs zur Projektion der Stromnachfrage auf große geografische Skalen. Zudem werden erstmals die dynamischen Eigenschaften von TRFs unter sozioökonomischen Faktoren untersucht. Schließlich konzentriert sich die Studie auf die Erstellung synthetischer Wetterjahre für extreme Residual-Last-Ereignisse und bietet Energiemodellierern eine Orientierung zur Auswahl oder Synthese von Wetterjahren für die Optimierung und Simulation robuster Systeme.

Gemeinsam verbessern diese drei Beiträge die Zuverlässigkeit der Energiesystemmodellierung, indem sie Unsicherheiten in den Eingangsdaten verringern, die Nachfrageprojektion verbessern und die Robustheit des Systems gegenüber extremen Wetterereignissen bewerten. Diese Arbeit bietet wertvolle Einblicke, wie klimatische Variabilität und extreme Wetterereignisse zukünftige Energiesysteme gestalten und bietet eine Grundlage für eine robustere Energieplanung und -politik.

Preface

This dissertation presents a collection of publications that contribute to addressing three key uncertainties in energy systems modeling: weather variability, future electricity demand, and extreme weather events. The publications included are as follows:

- Hu, Wenxuan, Yvonne Scholz, Madhura Yeligeti, Lueder von Bremen, and Ying Deng. **"Downscaling ERA5 wind speed data: A machine learning approach considering topographic influences."**. *Environmental Research Letters* (impact factor: 5.8) 18, no. 9 (2023): 094007.

  This publication addresses the uncertainty associated with the spatial resolution of wind speed data. As of June 10, 2025, it has been cited 18 times according to Google Scholar. The publication is open access, and the corresponding topographic data, preprocessing maps, and downscaled wind speed time series for the year 2018 are publicly available on Zenodo (DOI: 10.5281/zenodo.8100208). The main contributions of each author are detailed below:

  - Wenxuan Hu: Collection and preprocessing of reanalysis and station observation data, development of the machine learning methodology, results analysis and visualization, and writing of the original manuscript draft.
  - Yvonne Scholz: Supervision, funding acquisition, manuscript review and editing, and active involvement in methodology development.
  - Madhura Yeligeti: Manuscript review and editing, as well as contributions to methodological discussions and development.
  - Lueder von Bremen: Manuscript review and editing, and participation in methodological discussions.
  - Ying Deng: Manuscript review and editing, and involvement in methodological discussions.

- Hu, Wenxuan, Yvonne Scholz, Madhura Yeligeti, Ying Deng, and Patrick Jochem. **"Future electricity demand for Europe: Unraveling the dynamics of the Temperature Response Function."** *Applied Energy* (impact factor: 11.0), 368 (2024): 123387.

  This publication addresses the uncertainty in the dynamic characteristics of electricity demand under evolving climate conditions and policy intervention scenarios. As of June 10, 2025, it has been cited 4 times according to Google Scholar. The projected electricity demand time series for

European countries from 2023 to 2100 are available on Zenodo (DOI: 10.5281/zenodo.10678016). Four supplementary materials are available on the publication page of *Applied Energy*. The main contributions of each author are outlined below:

  - Wenxuan Hu: Collecting electricity demand, temperature, and policy interventions data, developing the methodology for projecting future electricity demand, presenting and visualizing the results, and writing the manuscript.
  - Yvonne Scholz: Supervision, funding acquisition, manuscript review and editing, providing climate scenario data, active participation in methodology development.
  - Madhura Yeligeti: Manuscript review and editing, active participation in methodology development and discussion.
  - Ying Deng: Manuscript review and editing, methodological discussion.
  - Patrick Jochem: Manuscript review and editing, methodological discussion.

- Hu, Wenxuan, Yvonne Scholz, Madhura Yeligeti, Eugenio Salvador Arellano Ruiz, and Patrick Jochem. **"Robustness of cost-optimal energy system designs: The role of short-term extreme weather events and dispatchable generation."** 2025. Submitted to *Solar Energy* (impact factor: 6.6).

  This paper addresses the uncertainty of extreme weather events in energy systems modeling. The paper has been submitted to *Solar Energy* and is currently under review. The raw data and the generated synthetic weather years are available on Zenodo (DOI: 10.5281/zenodo.14983895). The main contributions of each author are as follows:

  - Wenxuan Hu: Collecting residual load time series data, developing the methodology for generating synthetic weather years, implementing the data into an energy system optimization model, analyzing and presenting the results, and writing the manuscript.
  - Yvonne Scholz: Supervision, funding acquisition, manuscript review and editing, providing renewable generation data, active participation in methodology development.
  - Madhura Yeligeti: Manuscript review and editing, active participation in methodology development and discussion, supporting application of the Energy System Optimization Model.
  - Eugenio Salvador Arellano Ruiz: Manuscript review and editing, supporting application of the Energy System Optimization Model.
  - Patrick Jochem: Manuscript review and editing, active participation in methodology development and discussion.

In addition to the three main publications, I have also contributed as a co-author to the following papers during my PhD:

- Yeligeti, Madhura, Wenxuan Hu, Yvonne Scholz, Ronald Stegen, and Kai von Krbek. **"Cropland and rooftops: the global undertapped potential for solar photovoltaics."** *Environmental Research Letters* (impact factor: 5.8). 18, no. 5 (2023): 054027.

  This publication estimates the geographic potential of agrivoltaic and rooftop photovoltaic systems. As of June 10, 2025, it has been cited 16 times according to Google Scholar. My contributions include calculating and estimating the rooftop photovoltaic potential, actively engaging in the analysis of agrivoltaic potential, drafting the original rooftop photovoltaic sections, and reviewing and editing the manuscript.

- Deng Ying, Karl-Kiên Cao, Wenxuan Hu, Ronald Stegen, Kai von Krbek, Rafael Soria, Pedro Rua Rodriguez Rochedo, and Patrick Jochem. **"Harmonized and open energy dataset for modeling a highly renewable Brazilian power system."** *Scientific Data* (impact factor: 5.8) 10, no. 1 (2023): 103.

  This publication provides an open energy dataset for the Brazilian power system. As of June 10, 2025, it has been cited 9 times according to Google Scholar. My contributions include active engagement in data collecting and preprocessing discussions, manuscript review and editing.

- Deng, Ying, Karl-Kiên Cao, Manuel Wetzel, Wenxuan Hu, and Patrick Jochem. **"Carbon-neutral power system enabled e-kerosene production in Brazil in 2050."** *Scientific Reports* (impact factor: 3.8) 13, no. 1 (2023): 21348.

  This publication provides an open-source energy system model framework to analyze and optimize the integration of e-kerosene production into Brazil's energy system. As of June 10, 2025, it has been cited 7 times according to Google Scholar. My contributions include active engagement in methodological discussions and development, manuscript review, and editing.

- Arellano Ruiz, Eugenio Salvador, Niklas Wulff, Benjamin Fuchs, and Wenxuan Hu. **"autumn: A Python library for dynamic modelling of captured CO_2 cost potential curves."** *Journal of Open Source Software* 6, no. 64 (2021): 3203.

  This publication provides a Python library for modeling CO_2 cost potential curves. As of June 10, 2025, it has been cited once according to Google Scholar. My contributions included providing a test dataset for the Python library, as well as manuscript review and editing.

- Heinrichs, Heidi, Russell McKenna, Jann M. Weinand, Sebastian Kebrich, Juan Camilo Gómez Trillos, Maxmilian Hoffmann, Tsamara Tsani, Ruihong Chen, Shuying Chen, Wenxuan Hu, Johannes Schmidt, Carolin Ulbrich, Vladyslav Mikhnych, and Jochen Linßen. **"High-resolution large-scale resource assessments for solar photovoltaics: A review of potential definitions, methodologies and future research needs."** 2025. Submitted in *Renewable Energy* (impact factor: 9.0).

This paper provides a systematic literature review on estimating solar photovoltaic potential. My contributions included conducting and writing the original draft of the literature review focusing on the geographic potential of rooftop photovoltaics, as well as manuscript review and editing.

Contents

Acknowledgments

As the famous Chinese poem goes, '*The mountains rise steep and the waters stretch endless, leaving no path in sight; yet, through the shadowed willows and blooming flowers, a new village suddenly unfolds*'. This poem perfectly conveys the story of my 5-year PhD journey. After countless failures, sleepless nights, endless revisions, and worsening eyesight, I have finally learned one of the most valuable lessons in life: When life gives you lemons, make lemonade.

Looking back on my PhD journey, I feel a mix of both challenges and gratitude. Although I faced the difficulty of having no financial support at a certain stage during my PhD journey, I feel extremely lucky and deeply grateful for the opportunity to work with two amazing teams and surround myself with such talented people. Their support, guidance, and wisdom have been indispensable. My sincere gratitude goes to my supervisors, Prof. Dr. Patrick Jochem and Dr. Yvonne Scholz, without whom this dissertation would not exist. Thank you, Patrick, for your invaluable insights, constructive feedback, and for your prompt and consistent support during the time I needed it the most. Thank you, Yvonne, for your countless suggestions, invaluable guidance, and for the many enriching weekly meetings throughout my PhD journey. More importantly, thank you for always believing in me. Your support and comforting words have truly made a difference. I can't express how fortunate and thankful I am to have received supervision from both of you and to have worked alongside you.

I also wish to extend my heartfelt thanks to my talented colleagues in both DLR and KIT, who have provided not only valuable academic support and insights but also true friendships in life. Thank you, Madhura, for your innovative ideas and the engaging and occasionally mind-blowing discussions we had. I am especially grateful for your collaboration in co-authoring all of my published papers. Our weekly meetings with Yvonne will always remain a highlight of my PhD journey. Thank you, Hans Christian, for your valuable advice and feedback on my work. Your ability to consistently deliver high-quality work while managing time so effectively is truly something I can learn from. Thank you, Ying, for your input and discussions, and for your wonderful personality and positive attitude, which have been a huge source of support throughout my academic journey.

Many thanks to Eugenio, Ben, and Sonja for your contributions at various stages of my PhD. A special thanks to all my PhD colleagues at DLR, especially Jens and Carina, for organizing the regular PhD meet-ups. I am truly grateful for the chance to meet such amazing, talented people and to bond over games, concerts, and food. You have definitely made surviving this PhD a lot more enjoyable! Ad-

ditionally, I want to express my gratitude to my second supervisor, Prof. Dr. Oliver Grothe, for your invaluable insights into my dissertation. I also want to thank Prof. Dr. Wolf Fichtner and Viktor for your constructive input and the guidance you provided during my time at KIT. I am deeply thankful for your belief in me and for providing me with the opportunity to work with such an exceptional team at KIT.

Thank you to my family and friends for being my rock and a safe place where I could always find comfort, encouragement, and support throughout this journey. Thank you, my parents, Lingli and Zhigang, and my grandmother, Dongying, for your unconditional love, which has been my remedy and greatest motivation throughout my life. You have taught me how to be a better person, how to grow, and how to appreciate the small moments in life. Thank you, my dear friend Raffahel, for your constant support throughout my journey, for being a steady source of delicious food, and for believing in me even when I doubted myself. A huge thank you to all my other friends, Fangwen, Decai, Weiwen, Tianqi, Chris, Chao, Gergő, and many others, for your great support during different stages of my life. A special thank you to my dearest cats, Jianbing and Naicha, for your paw-some love, comfort, and joy you bring into my life. Your purrs and playful shenanigans have been my sweetest escape during the toughest moments of my journey.

I would also like to express my sincere gratitude to the VERMEER project (03EI1010A), funded by the Federal Ministry for Economic Affairs and Climate Action (BMWK) of Germany. This funding has played a pivotal role in establishing the foundation for my PhD research, and I truly appreciate the opportunity it has provided.

Lastly, I want to acknowledge how much this PhD journey and the world of science have meant to me. This rollercoaster of a journey has taught me how to embrace obstacles, keep a positive attitude, find optimal solutions, adapt to different environments, and never give up. As Laozi wisely said, '*A journey of a thousand miles begins with a single step*'. Though that first step was often filled with uncertainty, it has led me to where I am today. I am deeply thankful for this wonderful journey and the person it has allowed me to be. With that, I am excited to embrace the next chapter of my life with the lessons I have learned and the challenges that lie ahead.

Acronyms

ANN	Artificial Neural Network
AC	Air Conditioning
AR	Autoregressive
ARIMA	Autoregressive Integrated Moving Average
BPT	Balance Point Temperature
CC	Correlation Coefficient
CDD	Cooling Degree Days
CDF	Cumulative Distribution Function
CF	Capacity Factor
CFM	Change Factor Method
CH4	Methane
CHP	Combined Heat and Power
CV	Coefficient of Variation
DEM	Digital Elevation Model
DSY	Design Summer Year
EHY	Extreme High Residual Load Year
ELY	Extreme Low Residual Load Year
ESOM	Energy System Optimization Model
ExCCGT	Backpressure Combined Cycle Gas Turbine with Heat Extraction
EPBD	Energy Performance of Buildings Directive

ESM	Energy System Model
ESOM	Energy System Optimization Model
EU	European Union
EV	European Vehicle
FS	Finkelstein–Schafer
GAN	Generative Adversarial Network
GCM	Global Climate Model
GDP	Gross Domestic Product
GT	Gas Turbine
GWD	Gravity Wave Dissipation
$\mathbf{H_2}$	Hydrogen
HDD	Heating Degree Days
IRE	Intermittent Renewable Energy
KSD	Kolmogorov-Smirnov D statistic
MAE	Mean Absolute Error
ML	Machine Learning
MSE	Mean Squared Error
PCC	Pearson Correlation Coefficient
PV	Photovoltaics
RCM	Regional Climate Model
RCP	Representative Concentration Pathway
RE	Renewable Energy
RWY	Representative Weather Year
RMSE	Root Mean Square Error

SEE	Sum of Squared Errors
SWY	Synthetic Weather Year
SVM	Support Vector Machine
TDP	Temperature Dependence Patterns
TRF	Temperature Response Function
TDI	Terrain Diversity Index
TMM	Typical Meteorological Month
TMY	Typical Meteorological Year
TPI	Topographic Position Index
WAsP	Wind Atlas Analysis and Application Program
WTM	Weather Typing Method
WRF	Weather Research and Forecasting
XGBoost	eXtreme Gradient Boosting

1. Introduction

The transition to renewable energy sources is a key aspect of global efforts to mitigate climate change and reduce dependency on fossil fuels. Over the past decades, the share of renewable energy in electricity generation has increased significantly, driven by technological advancements, policy incentives, and the urgent need to decarbonize the energy sector (Gielen et al., 2019; Thellufsen and Lund, 2016). However, the increasing integration of intermittent renewable energy (IRE) sources, such as wind and solar energy, introduces significant challenges to the stability and reliability of energy systems. Unlike conventional power plants, IRE sources are inherently dependent on weather conditions, leading to fluctuations in power generation that must be balanced through storage, flexible demand, and dispatchable capacity. To investigate the impacts of renewable energy variability and the strategies required to ensure system robustness, Energy System Models (ESMs), especially Energy System Optimization Models (ESOMs) are widely used to understand, analyze, and optimize modern energy systems.

ESOMs are mathematical models developed to represent the complex interactions between energy demand, energy supply, conversion technologies, transmission networks, and other relevant factors (Brown et al., 2017; Sinha and Chandel, 2015). Through the application of mathematical algorithms, optimization techniques, and simulation methods, ESOMs can capture the factors influencing energy supply and demand dynamics. These models play an important role for policymakers, energy planners, and stakeholders, providing a range of insights and analyses of energy systems. A fundamental component of ESOMs is the input data, which includes meteorological data and energy demand profiles. Accurately capturing the variability and minimizing the uncertainties of these input data is essential for producing realistic and robust simulations. Furthermore, understanding the collaborative impact of input data on energy systems, such as extreme conditions characterized by fluctuations in meteorological data input and demand, is crucial for addressing the challenges of climate change.

Meteorological data is one of the most essential inputs for ESOMs, as it determines renewable generation availability, which is especially critical for planning and operation in modern energy systems with high penetration of renewable energy (Liao et al., 2017; van der Most et al., 2022; Hassan et al., 2021). It includes wind speed for wind power generation modeling, solar irradiation, such as Global Horizontal Irradiance (GHI) and Direct Normal Irradiance (DNI) for solar PV modeling, as well as inflow data for run-of-river and reservoir hydro power modeling. These data are crucial for deriving important parameters, including installable capacities and generation potentials for ESOMs (Scholz, 2012; Stetter, 2014). The most frequently used meteorological dataset is reanalysis data (Staffell and Pfenninger, 2016;

Ritter et al., 2015). Reanalysis datasets, such as ERA5, MERRA2, and COSMO REA6, are frequently used in ESOMs due to their spatial and temporal consistency (Staffell and Pfenninger, 2016; Ritter et al., 2015; Hersbach et al., 2020). However, the coarse spatial resolution of these datasets limits their ability to capture small-scale meteorological effects (Jourdier, 2020) and brings significant uncertainties in energy systems modeling. Over the years, in-depth studies of local effects and the development of local storage models have drawn more and more attention in the energy systems modeling community, which cannot be achieved through the use of coarse-resolution reanalysis data. To overcome this limitation, high-resolution meteorological datasets are required to better capture local effects and improve the accuracy of renewable energy simulations.

In addition to the meteorological data, electricity demand data is another critical input for ESOMs, particularly as electrification continues to expand globally. Electricity demand has a significant impact on climate change, primarily due to the substantial greenhouse gas emissions from electricity generated to meet the demand (Qin et al., 2020). However, the relationship between electricity demand and climate change is reciprocal, as shifts in climate also impact the need for heating and cooling. Many countries have implemented policies to adapt and mitigate this impact. For instance, Europe introduced the Energy Performance of Buildings Directive (EPBD) in 2002, which was later revised as Directive 2010/31/EU (Parliament and the Council of the European Union, 2010), aimed at enhancing energy efficiency within the European Union's building sector. Such regulations and actions play a critical role in influencing electricity demand, offering a promising pathway to avoid a vicious cycle and protect the population from discomforting conditions. Given the increasing challenges posed by climate change, a comprehensive analysis of how policy interventions shape future electricity demand is necessary. A better understanding of these interactions can enhance long-term energy system planning, improve electricity system management, optimize grid infrastructure, assess the impacts of extreme weather events, and inform the design of effective climate adaptation strategies.

The influence of weather conditions on energy system resilience is also an area of active research. Climate variability introduces uncertainties in energy supply and demand, making the design of robust energy systems increasingly important (Brown et al., 2017). To capture these uncertainties and understand their impacts on ESOMs, multiple years of meteorological data are often used to represent average system performance. However, this approach significantly increases model complexity and computational demands (Janjai and Deeyai, 2009; Yilmaz et al., 2019; Knight et al., 1991). Although representative weather years are sometimes used to simplify the process, they may fail to account for extreme weather conditions that are essential for understanding the resilience of energy systems. As such, representative weather years must include extreme events to ensure that energy systems can operate reliably under future climate scenarios. The development of such synthetic extreme weather years is a key strategy for integrating extreme weather conditions into energy system planning, ensuring the resilience of infrastructure investments and operational strategies under challenging climate conditions.

To overcome these limitations and bridge the gap between weather data and energy system analysis, this dissertation focuses on two essential input datasets for ESOMs, wind speed and electricity demand, and examines the impact of weather conditions on energy system robustness. Figure 1.1 provides an overview of the three main research directions discussed in this dissertation.

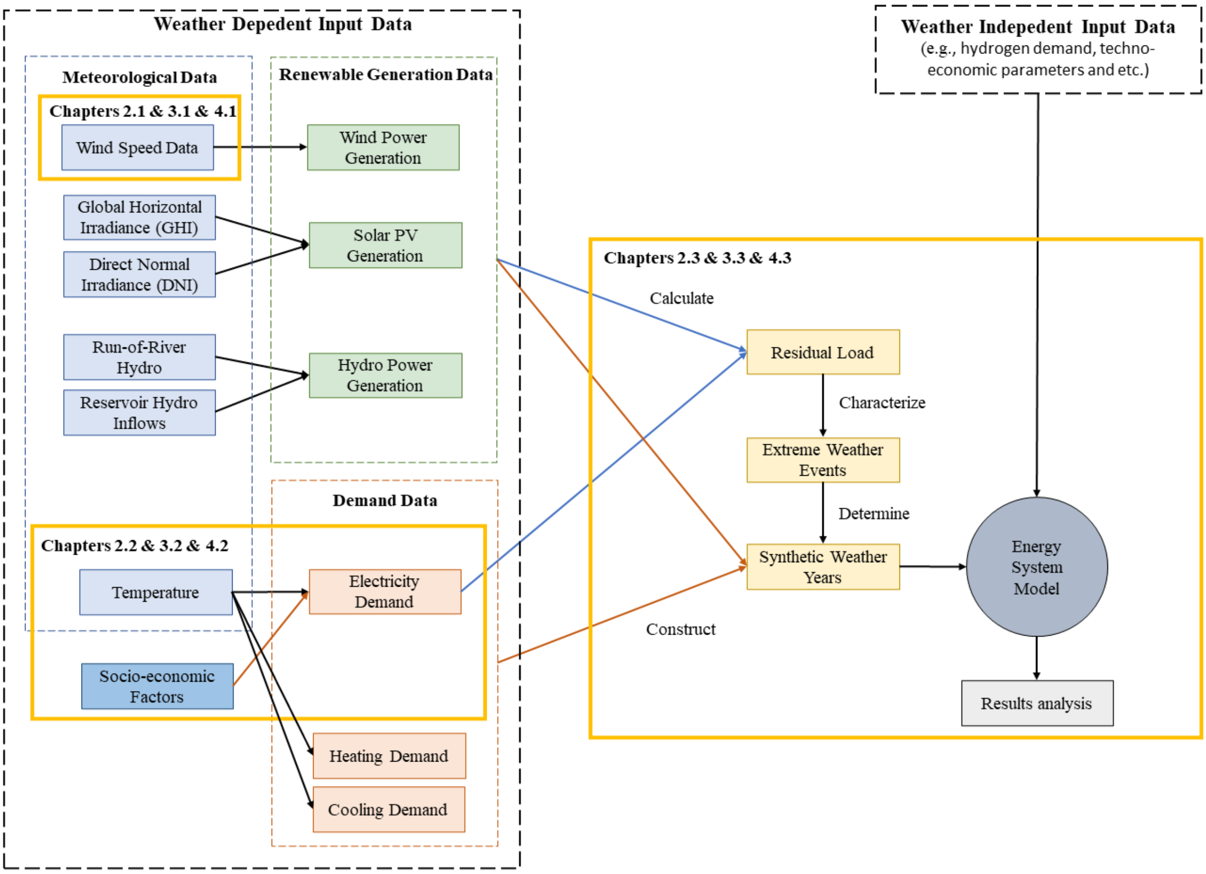

Figure 1.1.: Overview of main input data and the influence of weather on these data in energy systems modeling, along with the three key research focuses of this dissertation [1].

The dissertation is structured as follows. In Chapter 2, a comprehensive literature review is conducted. The chapter begins by discussing reanalysis data and various downscaling techniques for meteorological data, presenting state-of-the-art methods used to improve the spatial resolution of weather data for energy systems modeling. It then explores electricity demand, including the definition and construction of the TRF, and examines the key factors that influence its shape, providing a broad overview of electricity demand modeling approaches in energy system analysis. Furthermore, the chapter introduces state-of-the-art methods for generating synthetic weather data and investigates extreme weather events, with a focus on residual load. This offers insight into the current application of synthetic weather years in

---

[1] The overview only focuses on weather influences on renewable generation and demand time series. Other weather-related effects, such as impacts on geothermal power plant efficiency, grid performance, battery storage efficiency, and so on, are not presented in this overview.

energy system studies. Finally, this chapter concludes by identifying research gaps and summarizing the limitations of existing studies, thereby addressing the contribution of this dissertation.

Chapter 3 presents the data and methodology to address the three key uncertainties discussed in this dissertation. To improve the spatial resolution of reanalysis wind speed data, a statistical downscaling method is proposed. This approach improves the spatial resolution of wind speed time series data from approximately 31 km × 31 km to 1 km × 1 km. By incorporating topographic features, the method provides robust and computationally efficient results with minimal input requirements. Meanwhile, this chapter investigates the dynamic nature of TRF by identifying and analyzing four key factors influencing residential electricity demand: thermal insulation, heating electrification, space cooling, and passive cooling. A piecewise regression model is employed to evaluate their collaborative impact on the future shape of TRFs, offering a more realistic projection of electricity demand. Finally, this chapter explores the role of extreme weather events in energy system analysis. Several methods for generating synthetic extreme weather years are developed to capture critical residual load conditions. These synthetic years enable the identification of a representative weather year that ensures system robustness across all historical weather conditions.

Chapter 4 presents the results and discussion of the proposed methodology. This chapter begins by presenting and comparing the downscaled wind speed data with both measurement data and other reanalysis datasets, demonstrating a significant improvement in spatial resolution, particularly in regions with complex terrain. A cross-dataset validation further supports the effectiveness of the proposed downscaling method. This chapter then presents projections of future TRFs and electricity demand, revealing substantial changes in electricity demand under different climate and policy intervention scenarios. The findings present the importance of accounting for uncertainties introduced by assuming static TRFs in electricity demand modeling. Finally, the influence of various synthetic weather year inputs on energy systems modeling is examined under two system configuration scenarios. The analysis shows a strong correlation between system robustness and both dispatchable generation capacity and short-term extreme residual load events, emphasizing the need to consider these extreme conditions in system design and planning.

Chapter 5 outlines the limitations of this dissertation, while Chapter 6 concludes with a summary of the key findings and insights derived from this dissertation. Overall, by addressing these critical uncertainties, this dissertation contributes novel perspectives to the field of energy systems modeling. It introduces improved methodologies for generating high-resolution renewable energy data, modeling future electricity demand, and designing robust energy systems under extreme weather conditions. The findings of this dissertation can support policymakers, energy planners, and researchers in optimizing future energy systems for reliability and sustainability.

This dissertation is based on the author's published and submitted journal articles:

- **Chapters 2.1, 3.1, 4.1, and 5.1** are based on the author's publication 'Downscaling ERA5 wind speed data: A machine learning approach considering topographic influences' published in the journal *Environmental Research Letters* in 2023.
- **Chapters 2.2, 3.2, 4.2, and 5.2** are based on the author's publication 'Future electricity demand for Europe: Unraveling the dynamics of the Temperature Response Function' published in the journal *Applied Energy* in 2024.
- **Chapters 2.3, 3.3, 4.3, and 5.3** are based on the author's submitted manuscript 'Robustness of cost-optimal energy system designs: The role of short-term extreme weather events and dispatchable generation' currently under review at the journal *Solar Energy*.

2. Literature Review

2.1. Reanalysis Data and Downscaling Techniques

2.1.1. Reanalysis Dataset

Reanalysis data is one of the most widely used meteorological datasets in energy system models (Staffell and Pfenninger, 2016; Mathews et al., 2023), particularly for assessing renewable energy resources such as wind and solar power. Reanalysis data integrates historical weather observations, such as those from satellite measurements and weather station records, with numerical weather models to produce a continuous and spatially consistent representation of past atmospheric conditions (Hersbach et al., 2020). Unlike raw observational data, which may be sparse, inconsistent, or subject to gaps in time due to limitations in measurement coverage or instruments, reanalysis data offers meteorological data in a spatially and temporally consistent way (Hersbach et al., 2020).

Several global reanalysis datasets are widely used for climate and energy applications. Table 2.1 compares the attributes of the commonly used reanalysis dataset. This table reveals that COSMO-REA2 and COSMO-REA6 offer significantly higher spatial resolutions compared to other reanalysis datasets. However, these datasets are no longer being updated, and their spatial coverage is restricted to Central Europe and Europe. In contrast, up-to-date global reanalysis datasets such as ERA5, MERRA-2, and NCEP/NCAR provide comprehensive global coverage, but they have relatively coarse spatial resolutions. Among them, ERA5 offers the highest spatial resolution at approximately 31 km x 31 km. Despite this, the low spatial resolution of these reanalysis datasets limits their ability to capture small-scale details, such as local wind patterns. As a result, the spatial resolution of these datasets imposes limitations on their ability to resolve fine-scale variability, introducing uncertainty into ESMs, especially for local-scale energy systems (Jourdier, 2020).

Table 2.1.: Comparison of commonly used reanalysis datasets

Dataset	Institution	Spatial Resolution	Temporal Resolution	Spatial Coverage	Temporal Coverage
ERA5	ECMWF[1]	∼31 km (0.25°)	Hourly	Global	1940–present
MERRA-2	NASA[2]	∼50 km (0.5° × 0.625°)	Hourly	Global	1980–present
COSMO-REA2	DWD[3]	∼2 km (0.018°)	Hourly	Central Europe	2007–2019
COSMO-REA6	DWD	∼6 km (0.055°)	Hourly	Europe	1995–2019
NCEP/NCAR	NOAA[4]	∼210 km (2.5°)	6-hourly	Global	1948–present

To address this uncertainty and improve the spatial resolution of reanalysis data, numerous efforts have focused on downscaling, the most commonly used technique. Downscaling derives high-resolution climate and climate change information from global climate models (Pielke Sr and Wilby, 2012), enhancing the accuracy of renewable energy assessments by providing more detailed meteorological data. It is generally classified into two main approaches: dynamic downscaling and statistical downscaling.

2.1.2. Dynamic Donwscaling

Dynamic downscaling is a technique used to derive high-resolution climate or weather data from coarser Global Climate Models (GCMs) or reanalysis datasets. It employs physics-based models, typically Regional Climate Models (RCMs), to simulate the effects of large-scale climate processes at a regional or local scale (Castro et al., 2005), as illustrated in Figure 2.1. This approach ensures that individual variables remain physically consistent in both time and space while maintaining internal consistency across different variables (Giorgi and Gutowski Jr, 2015).

---

[1] European Centre for Medium-Range Weather Forecasts (ECMWF)

[2] National Aeronautics and Space Administration (NASA)

[3] Deutscher Wetterdienst (DWD), German Weather Service

[4] National Oceanic and Atmospheric Administration (NOAA)

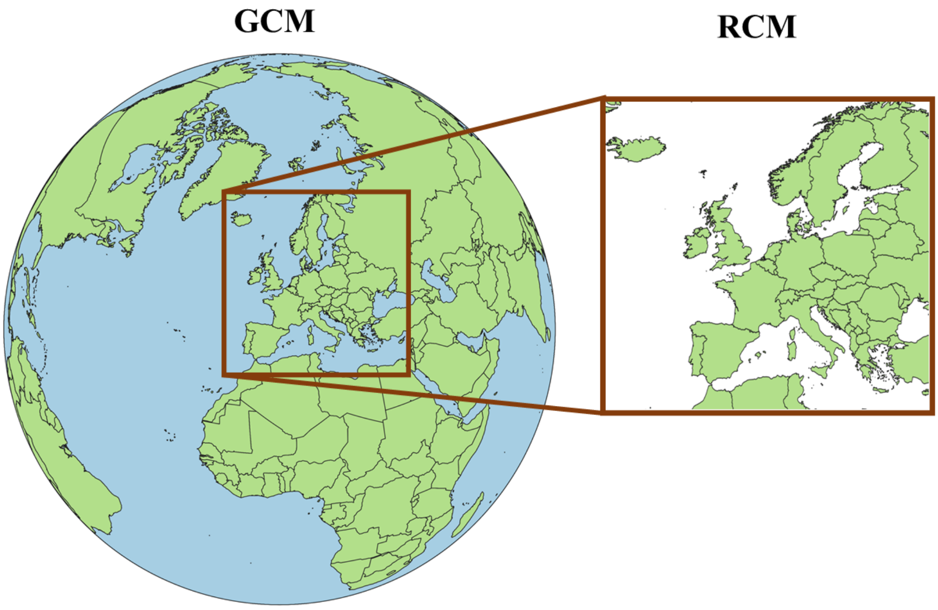

Figure 2.1.: Schematic representation of the relationship between Global Climate Models (GCMs) and Regional Climate Models (RCMs) in dynamic downscaling.

RCMs are high-resolution climate models developed to better capture regional climate dynamics and local phenomena compared to GCMs. Although RCMs solve the same fundamental physical equations as GCMs, they operate at a much finer spatial resolution. This allows them to more accurately represent critical regional features such as topography, mesoscale weather systems, and localized circulation patterns (Giorgi and Mearns, 1991). The increased resolution makes RCMs particularly effective for analyzing climate variability and climate change at the regional scale, where GCMs often lack sufficient granularity. Table 2.2 provides an overview of commonly used RCMs.

Table 2.2.: Overview of Commonly Used RCMs across studies

RCMs	**Developer**	**Characteristics**
WRF [1]	NCAR [2]	Widely used for both weather forecasting and climate modeling worldwide
CanRCM4	CCCma [3]	Primiarly used for north America, especially Canada
ECPC/ECP2	ECPC [4]	Primarily used in North America, including applications in the NARCCAP [5]
HadRM3	Hadley Centre	Used in the NARCCAP
MM5I	Iowa State University	Primarily used in North America, including applications in the NARCCAP
RegCM	ICTP [6]	Can be applied to any region of the World, with grid spacing of up to about 3 km
ALADIN	International ALADIN Consortium	Widely used in various climate studies across Europe, Middle East and North Africa
ALARO-0	RMIB [7] and Ghent University	Resolution up to 12.5 km to 50 km, based on the numerical weather prediction model ALADIN
COSMO-CLM	Deutscher Wetterdienst (DWD)	Mainly used for Europe
REMO-RCM	Climate Service Center Germany (GERICS)	Mainly used for Europe
CRCM5	UQAM [8] and ECCC [9]	Provide detailed climate projections over North America
Eta	NCEP [10]	Widely used over South America
HIRHAM5	Danish Meteorological Institute (DMI)	Particularly used high-latitude regions such as Greenland and the Arctic
RCA4	SMHI [11]	Mainly used for Europe

---

[1] Weather Research and Forecasting Model (WRF)
[2] National Center for Atmospheric Research (NCAR)
[3] Canadian Centre for Climate Modelling and Analysis (CCCma)
[4] Experimental Climate Prediction Center (ECPC)
[5] North American Regional Climate Change Assessment Program (NARCCAP)
[6] International Centre for Theoretical Physics (ICTP)
[7] Royal Meteorological Institute of Belgium (RMIB)
[8] Université du Québec à Montréal (UQAM)
[9] Environment and Climate Change Canada (ECCC)
[10] National Centers for Environmental Prediction (NCEP)
[11] Swedish Meteorological and Hydrological Institute (SMHI)

However, RCMs typically require initial and boundary conditions derived from GCMs (Giorgi and Bates, 1989; Dickinson et al., 1989). The most conventional dynamic downscaling method involves directly using the simulation results obtained from a GCM as the boundary conditions for an RCM, a technique known as the direct dynamic downscaling method (Giorgi and Bates, 1989; Dickinson et al., 1989). However, boundary conditions derived from GCMs often contain inherent systematic errors (Hawkins and Sutton, 2009, 2011). As a result, RCMs running direct dynamic downscaling simulations inherit these systematic errors (Caldwell et al., 2009; Rojas and Seth, 2003; Wu et al., 2005). Numerous efforts in dynamic downscaling research have aimed to not only eliminate model biases associated with the boundary conditions provided by global datasets, but also to offer further insights into the mechanisms of regional climate response to climate change in specific regions (Adachi and Tomita, 2020). To address these issues, several methods have been proposed, including Surrogate Climate Change (Schär et al., 1996), Pseudo Global Warming (Kimura and Kitoh, 2007; Sato et al., 2007), Mean Bias Correction (Misra and Kanamitsu, 2004; Holland et al., 2010), Mean and Variance Bias Control (Xu and Yang, 2012), Quantile-Quantile Correction (Colette et al., 2012), and Nesting Bias Correction (Rocheta et al., 2017), among others, to handle dynamic downscaling with modified boundary conditions.

One of the key advantages of dynamic downscaling is that the physical interpretation of the results is straightforward, as the method is based on fundamental physical principles. These physical principles, such as the laws of thermodynamics, fluid dynamics, and radiative transfer, form the foundation of the model's behavior, making the downscaled results easier to interpret in terms of the underlying climatic mechanisms (Adachi and Tomita, 2020). However, this process requires solving a vast number of equations that describe complex physical and chemical interactions, including atmospheric dynamics, cloud formation, radiation processes, and surface-atmosphere exchanges (Adachi and Tomita, 2020). Due to the high spatial resolution at which these interactions are simulated, this approach demands significant computational resources. Additionally, dynamic downscaling relies on high-resolution boundary conditions from GCMs, and the need to effectively adjust and modify these boundary inputs introduces further complexity to the process.

2.1.3. Statistical Donwscaling

Statistical downscaling derives a statistical or empirical relationship between the variables simulated by the GCMs or reanalysis data, called predictors, and station-scale hydrologic variables, called predictands (Bhuvandas et al., 2014). Statistical downscaling includes a variety of methods. Broadly, it can be categorized into four main approaches in the literature: the Change Factor Method (CFM), Weather Typing Methods (WTM), Weather Generators, and Regression-Based Methods (Ekström et al., 2015b; Wilks, 2010; Vrac et al., 2007).

Change Factors Method

The Change Factor Method (CFM), also known as the Simple Scaling Method, Delta Method, or Perturbation Method, is the simplest statistical downscaling approach. It estimates future or localized climate conditions by applying change factors, derived from GCMs, to historical observations in the form of time series or gridded datasets (New et al., 2007). Several techniques exist for deriving these scaling factors. The most basic approach involves calculating the absolute or relative differences between a coarse-resolution dataset (e.g., a GCM or reanalysis dataset) and higher-resolution historical observations. These scaling factors can be applied uniformly across the dataset or refined using distributional scaling methods, such as Quantile–Quantile Mapping or Quantile-Based Mapping, which adjust the distribution of values to better match observed variability across quantiles (Vidal and Wade, 2008). CFM is both computationally efficient and straightforward to implement. However, it often requires careful consideration of spatial and temporal variability, as well as adjustments to account for complex climatic and topographic influences. Relying on a single change factor may be insufficient to accurately represent these variations, particularly in highly variable regions (Wilks, 2010).

Weather Typing Method

The Weather Typing Method (WTM), also known as the Weather Classification Method, categorizes atmospheric conditions into distinct weather types and establishes statistical relationships between large-scale atmospheric variables and local-scale meteorological parameters. WTM is based on the assumption that similar large-scale weather patterns lead to comparable local-scale effects. The process typically involves three steps: first, large-scale atmospheric circulation patterns are classified into different weather types using variables such as geopotential height and sea-level pressure. Next, statistical relationships are established between these weather types and local meteorological conditions (e.g., wind speed at a specific location). Finally, these relationships are applied to estimate local-scale conditions by associating projected large-scale circulation patterns with their corresponding weather types (Bermúdez et al., 2020).

Several methods exist for classifying weather types. One of the most well-known methods is the Lamb Weather Type (LWT) classification for the British Isles (Lamb, 1950), a manual selection method that categorizes atmospheric circulation into predefined types. In addition to manual classification, modern techniques such as hierarchical descending clustering (Zorita et al., 1995; Schnur and Lettenmaier, 1998), K-means clustering (Zhao et al., 2024b,a; Zhong et al., 2025), Self-Organizing Maps (SOMs) (Diday and Vrac, 2005; Huang and Chang, 2021; Wang and Sun, 2022), and Hidden Markov Models (HMMs) (Vrac et al., 2007; Jiang et al., 2023) are widely used for automated weather classification. One of the key advantages of WTM is its ability to capture the physical consistency between large-scale atmospheric circulation and local-scale meteorological conditions. However, accurately classifying weather types and establishing their statistical relationships requires careful selection of classification techniques and predictor variables (Van Uytven et al., 2020). Misclassification or oversimplification of atmospheric patterns can lead to errors in the downscaled results.

Weather Generators

Weather generators are parametric stochastic models that explicitly incorporate randomness to simulate synthetic weather time series. These models are designed to replicate the statistical properties of historical weather observations (Wilks and Wilby, 1999). The selection of an appropriate weather generator depends on the target variable and the intended application. For instance, Markov Chain-based models are commonly used for simulating precipitation occurrence (Chen et al., 2012, 2014; Kemsley et al., 2024), while probability distribution models (e.g., Gamma, Weibull) are frequently applied to simulate wind speed (Wais, 2017) and temperature variability (Chen et al., 2012, 2014). The statistical parameters of the selected model are derived from historical data, ensuring that the generated synthetic series maintain key statistical characteristics, including mean, variance, persistence, and seasonal patterns. These estimated parameters are then used to generate synthetic weather sequences for the specified location or time period.

Weather generators offer the advantage of producing high-resolution synthetic weather time series that retain the statistical properties of observed data. This capability makes them valuable tools for extending short observational records, filling in missing data, and generating localized weather sequences from large-scale datasets. Additionally, the stochastic nature of weather generators enables the creation of multiple realizations of potential weather scenarios, which is particularly useful for assessing uncertainty in local-scale conditions (Jones et al., 2010; Semenov, 2008; Wilks, 2002). However, it is important to note that while these models preserve statistical characteristics, they do not simulate the physical processes of the atmosphere. Consequently, the generated time series remains synthetic and may deviate significantly from actual weather patterns (Wilks, 2010).

Regression-Based Methods

Regression-Based Methods rely on statistical relationships between large-scale predictors and local-scale predictands. By analyzing historical observations, regression models learn these relationships and apply them to downscale coarse-resolution datasets, enabling more detailed site-specific climate assessments and improving the spatial resolution of meteorological data (Wilks, 2010). Various Machine Learning (ML) techniques have been widely employed to establish these empirical relationships. These methods include Multiple Linear Regression (MLR) (Schoof and Pryor, 2001), Support Vector Machines (SVM) (Chen et al., 2010; Pour et al., 2018; Sulaiman et al., 2022), Random Forests (Davy et al., 2010; Legasa et al., 2022; Tang et al., 2021), Artificial Neural Networks (ANN) (Laddimath and Patil, 2019; Hosseini Baghanam et al., 2022, 2024), and Deep Learning models (Dujardin and Lehning, 2022; Höhlein et al., 2020; Yang et al., 2022). These data-driven techniques enhance the accuracy and flexibility of regression-based downscaling by capturing complex, nonlinear relationships between large-scale and local-scale variables.

One key advantage of regression-based methods, particularly for wind speed downscaling, is their flexibility in incorporating terrain-related variables as additional predictors. Unlike methods such as WTM or Weather Generators, which may oversimplify or fail to account for local terrain impacts, regression models can be tailored to reflect the influence of terrain on wind dynamics more accurately. This adaptability leads to a more precise representation of local wind conditions, ensuring that terrain effects are appropriately captured.

For example, Curry et al. (2012) investigated the statistical correlations between climate forecast variables and reanalysis data to derive monthly Weibull distribution parameters. These Weibull distributions are often used to describe wind speed data and can offer a simplified but effective approach to understanding wind patterns on a regional scale. Similarly, Kirchmeier et al. (2014) and Gonzalez-Aparicio et al. (2017) used a vector generalized linear model to predict a daily-varying probability density function of local wind speeds conditioned on large-scale daily wind speed predictors. Other significant contributions in this area include works by Davy et al. (2010), Oh et al. (2022), and Alizadeh et al. (2019). By focusing on downscaling probability distribution parameters of wind speed using regression-based methods, these studies are valuable in quantifying local wind speed ranges and estimating energy output, but they are limited in generating high-resolution time series data, which are essential for accurate energy systems modeling and optimization. In energy systems modeling, continuous, temporally resolved data are often required, and such time series cannot be derived solely from probability distribution functions.

Meanwhile, several studies have aimed to use regression-based methods to generate high-resolution time series data, rather than focusing on probability distribution parameters. For instance, Monahan (2012) used multiple linear regression to downscale monthly wind speed time series at buoy locations. Jung et al. (2022) employed a least squares boosting approach to downscale the monthly extreme wind speed values for North America and Europe. Winstral et al. (2017) developed an optimization scheme for downscaling wind speed time series in Switzerland, incorporating local terrain structure. These studies, along with others such as Tang and Bassill (2018), Goubanova et al. (2011), and van der Kamp et al. (2012), explicitly focus on generating high spatial resolution time series data, rather than just probability distribution parameters. However, many of these approaches have been limited to site-specific corrections or aimed at generating daily or monthly wind speed time series, which restricts their spatial and temporal applicability when used in energy system models.

To summarize, Figure 2.2 provides an overview of the various dynamic and statistical downscaling methods introduced in this dissertation.

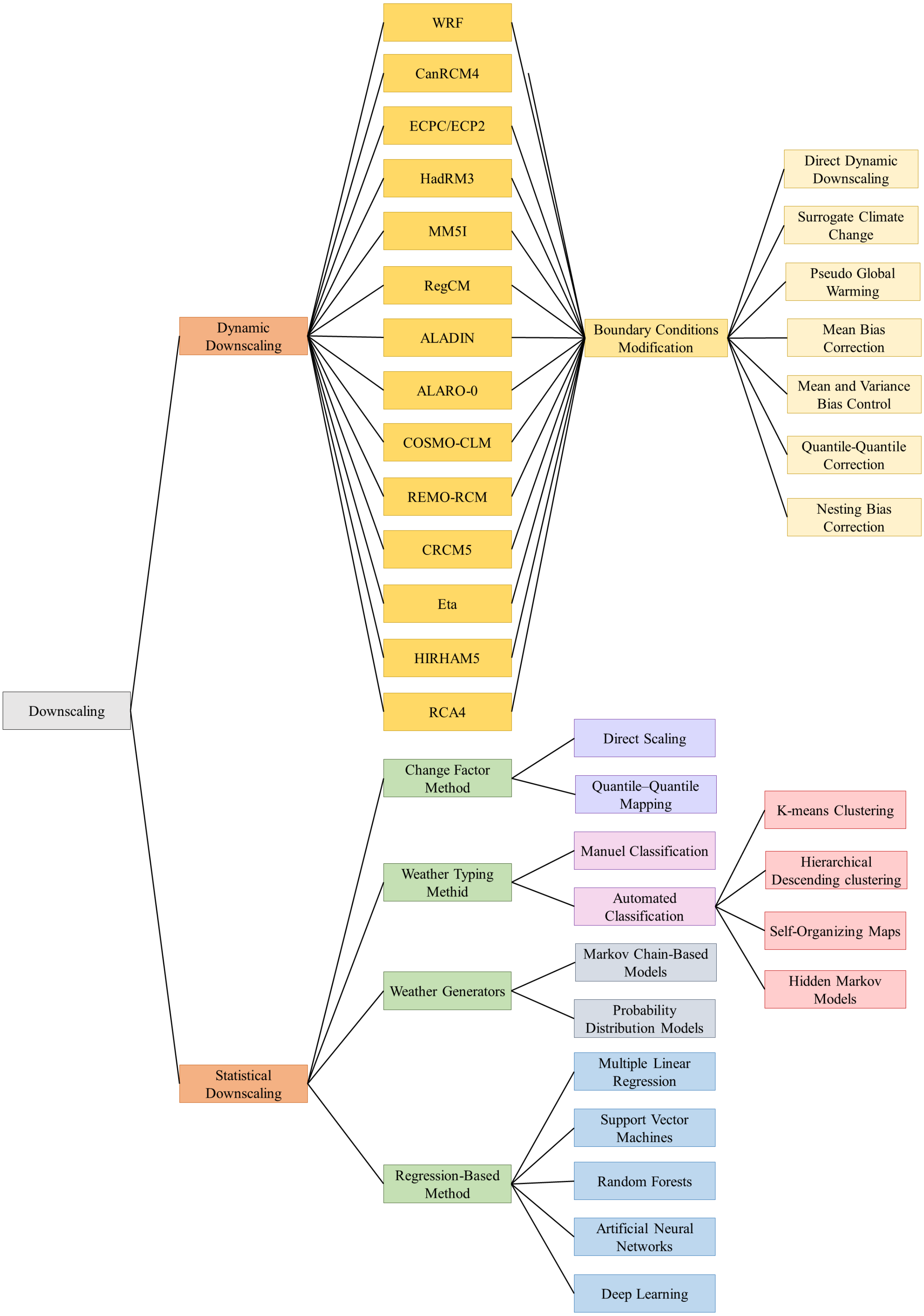

Figure 2.2.: Overview of the various dynamic and statistical downscaling methods.

2.1.4. Wind Atlas Platforms

In recent years, the emergence of wind atlas platforms has significantly enhanced the acquisition of high spatial resolution wind speed data. Alongside various national and regional wind atlases in Europe (Badger et al., 2019), two prominent and widely recognized atlases, namely Global Wind Atlas (Technical University of Denmark , 2023) and the New European Wind Atlas (Dörenkämper et al., 2020), have gained recognition for their ability to provide high spatial resolution and open-access estimations of wind characteristics at specific locations.

These wind atlases are based on numerical mesoscale model simulations, a method commonly referred to as the numerical wind atlas approach. This two-step process involves both mesoscale and microscale modeling, as shown in Figure 2.3, which requires considerable computational power at each stage. Both the Global Wind Atlas and the New European Wind Atlas employ this approach. For instance, the latest version of the Global Wind Atlas uses the ERA5 reanalysis dataset as input. The first step involves applying the WRF model to capture additional flow phenomena, typically at the kilometer to tens-of-kilometer scale, that are not included in the reanalysis data. The second step involves microscale downscaling using the Wind Atlas Analysis and Application Program (WAsP) model, which focuses on local topographic effects to further refine wind resource estimations at higher spatial resolutions (Davis et al., 2023).

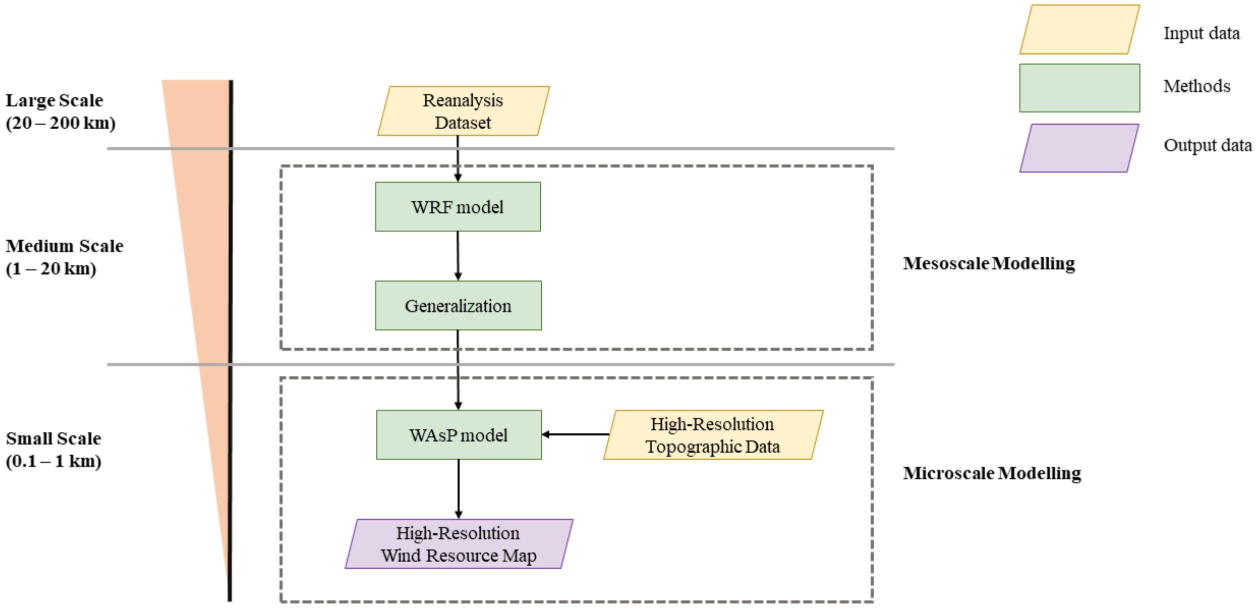

Figure 2.3.: Schematic of the workflow used in the Numerical Wind Atlas Method.

However, it is worth noting that while these wind atlases offer high-resolution maps of the wind climate, such as long-term averaged wind speed and variability, they do not provide wind speed time series data as shown in Figure 2.4. To address this limitation, researchers have explored the use of wind atlases to bias-adjust reanalysis data. One common approach involves scaling the reanalysis time series data to align with the long-term averaged wind speed provided by the wind atlas (Murcia et al., 2022; Gruber and Schmidt, 2019; Gruber et al., 2019). However, this method has a notable drawback: the resulting time series tends to be excessively smooth when compared to point measurements. As a consequence, it fails to accurately capture the significant fluctuations in wind speed commonly observed in measurements.

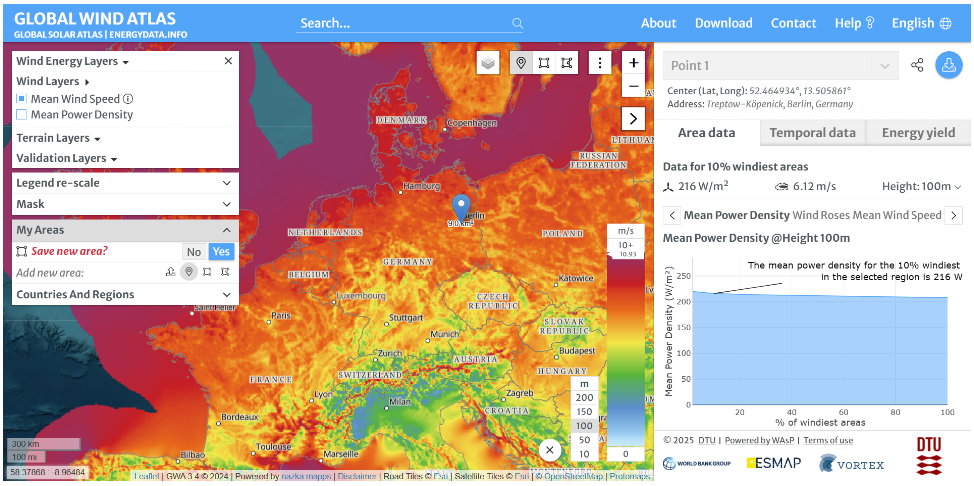

☑ Mean Wind Speed
☐ Mean Power Density

Point 1
Center (Lat, Long): 52.464934°, 13.505861°
Address: Treptow-Köpenick, Berlin, Germany

Data for 10% windiest areas
216 W/m² 6.12 m/s Height: 100m

Figure 2.4.: Interface of the Global Wind Atlas platform, which provides only long-term average wind speeds rather than time series data.

2.2. Electricity Demand and Temperature Response Function (TRF)

Accurate electricity demand modeling is crucial in energy system analysis, as it enables reliable capacity planning, grid stability assessments, and the integration of renewable energy sources by assessing demand patterns under various scenarios. Overall, electricity demand can be influenced by various factors. These factors can be broadly categorized into climatic, socio-economic, and calendrical variables.

- **Climatic variables**: climatic variables have been found to impact electricity demand through their effects on heating and cooling needs. These include variables such as temperature (Hor et al., 2005), sunshine duration (Hor et al., 2005; Fan et al., 2019), humidity (Apadula et al., 2012), precipitation (Hou et al., 2021), and wind speed (Apadula et al., 2012).

- **Socio-economic factors**: socio-economic factors are known to affect electricity demand by influencing consumption patterns. These factors include Gross Domestic Product (GDP) (Fotis et al., 2017; Szustak et al., 2022), population (Hirsh and Koomey, 2015; Günay, 2016), personal income (Jamil and Ahmad, 2011), electricity prices (Dai and Zhao, 2020), tourism (Toktarova et al., 2019), electrification on heating (Connolly, 2017), space cooling (International Energy Agency, 2018; UNEP DTU Partnership, 2021), electric vehicles (Jochem et al., 2021; Crozier et al., 2020;

Brouwer et al., 2013), the increasing demand for green hydrogen production (Zainal et al., 2024; Bouckaert et al., 2021) and so on.

- **Calendrical data**: calendrical data can also influence electricity demand patterns. These include variables such as weekdays (Palacios-Garcia et al., 2018; Mattsson et al., 2021), weekends (Palacios-Garcia et al., 2018; Mattsson et al., 2021), and holidays (Trull et al., 2021)

However, the interactions between demand and these various interrelated factors are complex and ambiguous (Hekkenberg et al., 2009a), making it challenging to investigate their impacts in a comprehensive way. As a result, researchers often focus their studies on specific factors or a limited number of factors to gain a more general understanding of their effects on electricity demand.

2.2.1. Temperature Response Function (TRF)

Among the various factors, temperature is one of the most important factors (Apadula et al., 2012; Yildiz et al., 2017; Henley and Peirson, 1997; Li and Sailor, 1995). To assess the impact of temperature on electricity demand, a commonly used method is the employment of Temperature Response Functions (TRFs). TRFs, also known as Temperature Dependence Patterns (TDPs), characterize the nonlinear relationship between temperature and electricity demand. TRFs are often portrayed in three forms across various studies. As illustrated in Figure 2.5, these curves commonly appear in a V-shaped (Sailor and Muñoz, 1997; Amato et al., 2005), or a U-shaped (Ruth and Lin, 2006; Hiruta et al., 2022) pattern, or in a V-shaped pattern with an intermediate comfort zone.

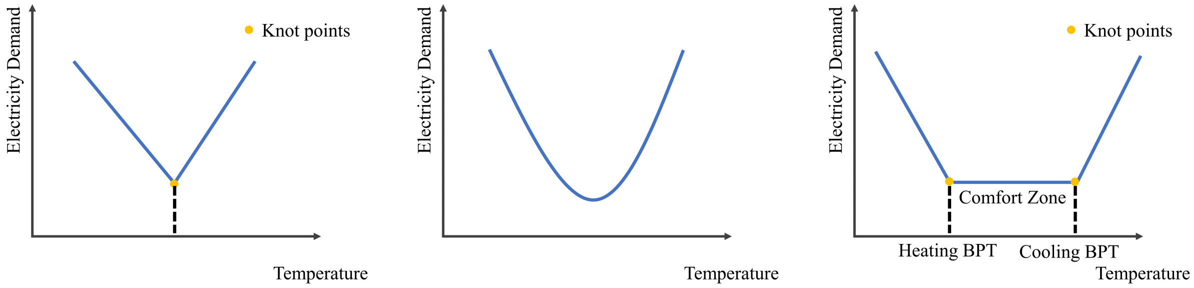

(a) V-shape (b) U-shape (c) V-shape with comfort zone

Figure 2.5.: Typical pattern of Temperature Response Function (TRF).

All these curves exhibit a consistent trend. In a V-shaped curve, high electricity demand for heating purposes during the cold winter time is shown, followed by a decrease in demand as temperatures rise. Eventually, at a certain temperature, the demand begins to rise again, due to the increased use of cooling appliances during the hot summer months. This inflection temperature is commonly referred to as the Balance Point Temperature (BPT), which is widely used in determining Heating Degree Days (HDD) and Cooling Degree Days (CDD) (Woods and Fuller, 2014; Krese et al., 2018). In comparison, the

V-shaped pattern with an intermediate comfort zone represents a temperature range where electricity demand exhibits no sensitivity to temperature fluctuations.

The use of TRFs stands out in exploring the long-term effects of temperature on electricity demand (Fazeli et al., 2016; Miller et al., 2008; Auffhammer and Aroonruengsawat, 2011), particularly when compared to "grey-box" models like Machine Learning and ANN, which are usually inadequate for capturing the underlying correlation between different variables and electricity demand. Moreover, unlike TRFs, "grey-box" models are largely limited when applied to future scenarios, due to their difficulty in accurately extrapolating when faced with scenarios that differ significantly from the training data. This constraint makes them more suitable for short-term demand forecasting (Hou et al., 2021; Günay, 2016; Mukherjee and Nateghi, 2017) rather than exploring the long-term implications of temperature on demand.

2.2.2. Methods for Generating TRFs

Previous studies have proposed various methods to determine TRFs. Typically, this involves the application of non-linear regression analysis. For example, Li et al. (2019) applied a spline function to represent the daily temperature and electricity consumption TRFs in Shanghai, China. Ihara et al. (2008) employed multiple regression to analyze the temperature and electric power consumption relationships in business districts of Tokyo, Japan. Wang and Bielicki (2018) used a segmented regression technique to determine the hourly temperature and electricity load TRFs for two transmission zones in the United States. Meanwhile, Moral-Carcedo and Vicéns-Otero (2005) used a logistic smooth transition regression to determine the daily temperature and electricity demand TRFs for Spain. Wang and Bielicki (2018) compared the use of multiple linear regression, adaptive linear filter algorithms, and Gaussian mixture model regression for temperature and hourly electricity consumption TRFs for two specific buildings in Chicago and Des Moines, United States. Hiruta et al. (2022) employed multivariate adaptive regression splines to determine the temperature and electricity demand TRFs at different temporal scales for 10 regions in Japan. Other related studies include Hor et al. (2005), Hashimoto et al. (2019), Moral-Carcedo and Pérez-García (2015), Brown et al. (2016), and Alberini et al. (2019).

These studies, which focused on particular geographical regions, and in some cases, individual buildings, can provide valuable insights into the correlation between temperature and electricity demand within specific climate zones. However, such regional foci may limit the generalizability of their findings to broader regions. This limitation arises due to the potential variation in the temperature-electricity demand relationship across various climate zones, given the substantial differences in TRFs across different countries (Bessec and Fouquau, 2008).

Due to the limitations of regional studies, some researchers have conducted more comprehensive investigations in a broader geospatial extent. For example, Bessec and Fouquau (2008) employed a panel threshold regression model to investigate the nonlinear relationship between temperature and electricity demand for 15 European Union member states. By disaggregating southern and northern countries, they discovered that this nonlinear pattern varies substantially across different countries. This study implies the need for a more expansive investigation to better understand the influence of temperature on electricity demand. However, it did not develop a sophisticated model for long-term electricity demand projections. More recent studies, such as Castillo et al. (2022), applied integrated assessment models incorporating empirical data on typical daily and hourly demand patterns across different sectors to calculate future demand projections. Although they took different sectors, socio-economic and technological development into consideration, this study lacks an in-depth analysis of temperature influences. More importantly, the use of 18 °C as the BPT for HDD and CDD calculation for all countries until the year 2100 is biased due to varying TRFs across different countries (Bessec and Fouquau, 2008), which can potentially lead to inaccurate estimations (Hiruta et al., 2022).

Given these aspects, it becomes evident that the lack of a comprehensive investigation of TRFs on a wider geographical scale stands as a notable limitation in current research. Furthermore, a critical drawback lies in the underlying assumption that the TRFs are static. Studies employing current temperature influence models or TRFs to project electricity demand often assume stationary models and fixed TRFs across different time horizons and climate zones. This oversight disregards substantial disparities between countries and the impact of evolving policy interventions. The assumption of static TRFs may increase the risk of inaccurate estimations, posing a considerable challenge for policymakers to adapt future electricity planning. While studies such as those conducted by Hekkenberg et al. (2009a,b) have aimed to tackle this static nature, their efforts were restricted to a singular case study. They fell short of providing a quantitative analysis of how various socio-economic factors influence the TRFs. Consequently, these studies fail to capture the intricate complexities inherent in real-world scenarios.

2.2.3. Key Drivers of TRF in Residential Buildings

To comprehend the dynamics of TRFs, it is essential to examine the various factors shaping their form. TRFs depict the correlation between temperature and demand, reflecting a direct influence of temperature on demand levels. It is important to note that while temperature directly influences demand, it does not change the fundamental shape of the TRFs. Instead, the shape of the TRFs is primarily shaped by socio-economic variables (Hekkenberg et al., 2009b). However, the specific socio-economic factors shaping the TRFs and their influences are rarely discussed in existing literature. This section aims to address this gap by conducting an in-depth investigation into the factors influencing electricity demand in residential buildings with a focus on heating and cooling. By analyzing these factors, this section aims to enhance the understanding of the dynamic nature of TRFs and, therefore, construct future demand time series.

According to the European Commission, buildings within the EU account for 40% of the total energy consumption, representing the highest share of final energy consumption in the EU (European Commision, 2018). This indicates the essential role of the building sector in understanding country-specific electricity demand. In residential buildings, electricity consumption serves multiple purposes, including the operation of heating and cooling systems, as well as appliances like refrigerators, freezers, lighting, electric vehicles, and so on (Nishimwe and Reiter, 2021; Economidou et al., 2011; Jochem et al., 2021). While certain electric devices may exhibit sensitivity to weather conditions (Hart and De Dear, 2004), it is noteworthy that the most weather-dependent usages are typically associated with heating and cooling systems.

This section primarily focuses on residential buildings due to the complexity of the non-residential sector, which constitutes a relatively small percentage of the overall buildings, and its less temperature-sensitive characteristics. In Europe, residential buildings constitute a significant 75% of the overall building stock, with the remaining 25% comprising non-residential buildings. Compared to residential buildings, non-residential buildings are more complex and heterogeneous. This sector's complexity arises from variations in usage patterns, their energy consumption levels, and the construction methods employed. The impact of residential buildings on electricity demand can be observed in the following key aspects.

Space Cooling

Space cooling is the fastest-growing end use of energy in buildings (International Energy Agency, 2018). In Europe, the adoption of cooling appliances, particularly air conditioning (AC), has steadily increased in recent years, driven by rising summer temperatures and more frequent heatwaves (Pezzutto et al., 2016; Füssel et al., 2012). According to the estimation of the International Energy Agency (IEA), the usage of AC is anticipated to increase in the next three decades, emerging as a key driver of global electricity demand (International Energy Agency, 2018). This growing dependence on cooling appliances is expected to significantly increase electricity consumption in buildings, potentially leading to higher peak loads and increasing the risk of power outages (International Energy Agency, 2018; UNEP DTU Partnership, 2021; European Environment Agency, 2021). Given this trend, it is crucial to integrate the rising demand for space cooling into future electricity demand projections.

Passive Cooling

Passive cooling is another important factor influencing cooling demand. The European Environment Agency (EEA) stresses the significance of passive cooling as a key solution for sustainable cooling (European Environment Agency, 2022). Passive cooling is a building design approach that works either by removing heat from the building to a natural heat sink or by preventing heat from entering the living space from external heat sources to improve indoor thermal comfort with low or no energy consumption (Song et al., 2021; Samuel et al., 2013). In general, passive cooling can be classified into three categories:

solar and heat control, heat exchange reduction, and heat removal (Song et al., 2021). An overview of various passive cooling technologies is provided in the Appendix A.1.

The integration of passive cooling offers multiple benefits, including reducing and shifting peak loads, stabilizing indoor temperatures, and maintaining thermal comfort, ultimately lowering the overall cooling demand (Song et al., 2021). A practical example is observed in low-cost housing in southern Spain, where the appropriate use of natural ventilation at night resulted in an average indoor temperature reduction of 5°C (Escandón et al., 2019). According to Song et al. (2021), the application of passive cooling techniques is estimated to reduce energy consumption by a range of 8% to 70%, depending on the specific technique employed. Therefore, integrating passive cooling measures is essential for future buildings to mitigate the impact of heatwaves and decrease the potential peak load associated with space cooling.

Meanwhile, it is also worth mentioning that the impact of passive cooling on heating demand is scarcely addressed in the existing literature. In a specific case study (Alhuwayil et al., 2023), buildings with passive solar shading were found to slightly increase heating demand. However, it is important to note that the passive cooling measure assessed in the study specifically involved an overhang adjustment. Specifically, the overhang angle can be tailored and optimized to ensure sufficient sunshine during the winter months. Additionally, passive cooling includes a variety of other measures, such as night ventilation, which, if not activated during winter, does not impact heating demand. Therefore, this dissertation assumes that, in general, passive cooling measures have no significant impact on heating demand.

Electrification of the Heating Sector

Electrification plays an important role in achieving net-zero goals, offering significant potential for reducing emissions and decarbonizing energy supply chains (International Energy Agency, ndb). Within the heating sector, electrification can be implemented by, for example, heat pumps (Hedegaard et al., 2012; Waite and Modi, 2014). Heat pumps driven by low-emission electricity play a central role in the global shift toward secure and sustainable heating. While heat pumps met around 10% of global space heating needs in 2021, the rate of installation is rapidly accelerating (International Energy Agency, 2022). In the EU, heat pump sales increased by 33.8% in 2021 over the previous year, making the EU the fastest-growing market globally for this technology (International Energy Agency, 2022). However, the rise in the electricity share for heating also implies an increase in electricity demand. It has been shown that if electric heating is employed to electrify the heat demand in EU28 countries, it would more than double the annual electricity demand (Connolly, 2017). Although heat pumps can serve cooling purposes, their use in this context categorizes them as cooling appliances and is already considered in space cooling.

Thermal Insulation

The significance of thermal insulation has long been recognized as crucial in shaping the future energy consumption in buildings and achieving objectives related to greenhouse gas emissions reduction (European Commision, 2018). Thermal insulation systems and materials are designed to curtail the transmission of heat flow. By enhancing the insulation properties of building envelopes through the use of advanced materials, overall energy efficiency and the sustainability of buildings can be significantly elevated (Asdrubali et al., 2015). To evaluate the thermal insulation performance of building materials, thermal transmittance, commonly referred to as U-Value, is frequently used (Asdrubali et al., 2015). The U-value measures the rate at which heat is transferred through a building element, such as walls, windows, or roofs. A lower U-value indicates better insulation properties, meaning less heat loss occurs through the material. A consistent reduction in this value over the year has occurred (Lechtenböhmer and Schüring, 2011), indicating an ongoing improvement in the thermal performance of buildings.

On the European scale, there are regional disparities in the thermal insulation standards of buildings. Northern and Western European countries, with a longstanding tradition of implementing thermal insulation requirements since the 1970s (Economidou et al., 2011), demonstrate relatively high thermal insulation in their building stock (Economidou et al., 2011; Enerdata, nd). In contrast, in southern countries such as Spain and Portugal, where winters are milder, the building inventory is dominated by buildings with little thermal envelope insulation (Economidou et al., 2011; Enerdata, nd). For instance, in Spain, an estimated 90.4% of existing dwellings lack thermal efficiency due to a lack of thermal envelope requirements or a lightweight building code compared to the Technical Building Code in force (Palma et al., 2023). However, recent years have witnessed a positive trend in Portugal, with a 50% reduction in U-values (Economidou et al., 2011), attributed to the implementation of European regulations in the building sector. Key regulations, such as the Energy Performance of Buildings Directive (EPBD) (Directive 2018/844/EU) (Parliament and the Council of the European Union, 2010), require Member States to establish minimum requirements for the energy performance of both newly constructed buildings and existing structures undergoing major renovations. Complemented by other regulations like the Energy Efficiency Directive (EED) (Directive 2018/2002/EU) (Parliament and the Council of the European Union, 2012), these directives explicitly focus on enhancing the thermal insulation of buildings. According to the IEA, the global average space heating intensity has decreased by 10% over the past decades, attributed to more widespread and stringent building regulations and higher retrofit rates (International Energy Agency, nda). Consequently, future analyses of electricity demand should consider the impact of the thermal insulation of the buildings

While improving thermal insulation can reduce the electric heating demand, its effect on cooling demand is intricate. On the one hand, there is a potential for increased cooling demand as improved insulation may lead to a higher probability of overheating due to the greater retention of heat within the building

(Jakubcionis and Carlsson, 2017). On the other hand, proper use of ventilation, particularly during nighttime, could counterbalance the potential negative effects of enhanced insulation (Jakubcionis and Carlsson, 2017). Furthermore, a relevant case study comparing buildings with insulation to those without was conducted, revealing that the cooling demands for highly insulated buildings and the base case are similar (Alhuwayil et al., 2023). Therefore, it can be concluded that thermal insulation is unlikely to significantly impact cooling demand.

In conclusion, based on the comprehensive literature review conducted in this section, the impact of the four key residential building drivers on electricity demand can be summarized as follows:

- **Space Cooling**: Affects only the cooling demand, with no impact on heating demand.
- **Passive Cooling**: Primarily influences the cooling demand, with a negligible impact on heating demand.
- **Electrification of the heating sector**: Affects only the heating demand, without influencing cooling demand.
- **Thermal insulation**: Primarily influences the heating demand. The impact on cooling demand is contradictory and lacks sufficient research in the reviewed literature; therefore, it is assumed to have no influence on cooling demand.

2.3. Synthetic Weather Data Generation and Extreme Weather Events

As stated in the previous chapters, the implementation of ESMs requires weather data as input. For example, hourly meteorological data on regional granularity, covering at least all four seasons of a year, is commonly applied. However, each year presents unique conditions. To accurately calculate the long-term average performance of the system, it is important to have a sufficient dataset covering multiple years and a suitable method for selecting the relevant patterns. Given the interannual variability and high granularity of meteorological data, such as wind and solar data, many studies incorporate data from several years to capture this variability and ensure robust system performance across different conditions. This approach, however, makes the modeling process cumbersome, time-consuming, and significantly increases model complexity (Janjai and Deeyai, 2009; Yilmaz et al., 2019; Knight et al., 1991).

As a result, many researchers have started using an average weather year to simplify the representation of climate conditions. An average weather year is typically constructed by aggregating meteorological data, such as temperature, precipitation, solar radiation, and others, from multiple years, and calculating the mean for each corresponding time period (e.g., monthly or daily values). This approach offers a "typical" representation of weather by smoothing out the extremes and fluctuations that naturally occur in any given year. However, relying solely on an average weather year can be problematic, as weather conditions are inherently variable. By averaging over multiple years, the result may present a "normal" year that fails to capture the full spectrum of variability that could occur in reality.

To address this issue, a Representative Weather Year (RWY) is often used. An RWY is selected as a single historical year that most accurately reflects the long-term statistical distribution of weather variables. While it offers a more realistic representation than an average weather year, a key limitation of the RWY is its reliance on just one year. Even if this year is the most statistically representative, it may still contain anomalies or biases that do not fully capture the broader climate conditions. Another drawback of the RWY is its inability to account for the full range of variability observed across different years. For example, if a particular year experienced an early winter or an unusually prolonged dry season, the RWY would incorporate these patterns, even though they may not reflect typical seasonal trends.

To address these limitations, Synthetic Weather Years (SWYs) have become a widely adopted solution. An SWY is an artificially generated weather dataset designed to capture specific climate characteristics for a given location and application. SWYs serve a range of purposes, such as enabling the generation of weather data for regions with limited or no detailed meteorological or energy-related records. They also enable the simulation of environmentally driven systems in areas where historical data may be lacking. From an energy systems modeling perspective, using a single SWY can yield results comparable to those obtained from long-term datasets, while significantly reducing the computational effort needed to assess long-term system performance (Knight et al., 1991).

Due to their flexibility, synthetic weather years are used not only in energy system analysis but also in various other fields. In addition to large-scale energy systems modeling, SWYs are applied in building energy and performance simulations (Chan et al., 2006; Wu et al., 2023), statistical downscaling using weather generators (Chen et al., 2012, 2014), assessments of building-integrated photovoltaic (PV) systems (Huang and Ou, 2011), and agricultural studies examining crop yields and related processes (Qian et al., 2011; Kuchar, 2004; Alodah and Seidou, 2019). The creation of synthetic weather years typically involves methods for constructing synthetic weather sequences, including both deterministic and stochastic approaches.

2.3.1. Deterministic Approach

The deterministic approach constructs a synthetic weather sequence by directly selecting or modifying historical weather data to create a representative dataset. In the context of weather years, one of the most well-known synthetic weather years produced using this method is the Typical Meteorological Year (TMY). A TMY is a compilation of weather data that, based on specific criteria, is considered representative of typical or average conditions (Clarke, 2007). The first attempt to generate a TMY was carried out by Hall et al. (1978a), resulting in the widely adopted Sandia method, named after Sandia National Laboratories. This method involves selecting 12 Typical Meteorological Months (TMM) from historical data to create a TMY by comparing the long-term cumulative distribution function (CDF) with the individual months using Finkelstein–Schafer (FS) statistics. The month with the smallest CDF differences is chosen as the TMM. This process is repeated for all 12 months, after which the typical months are assembled to form the TMY, as depicted in Figure 2.6.

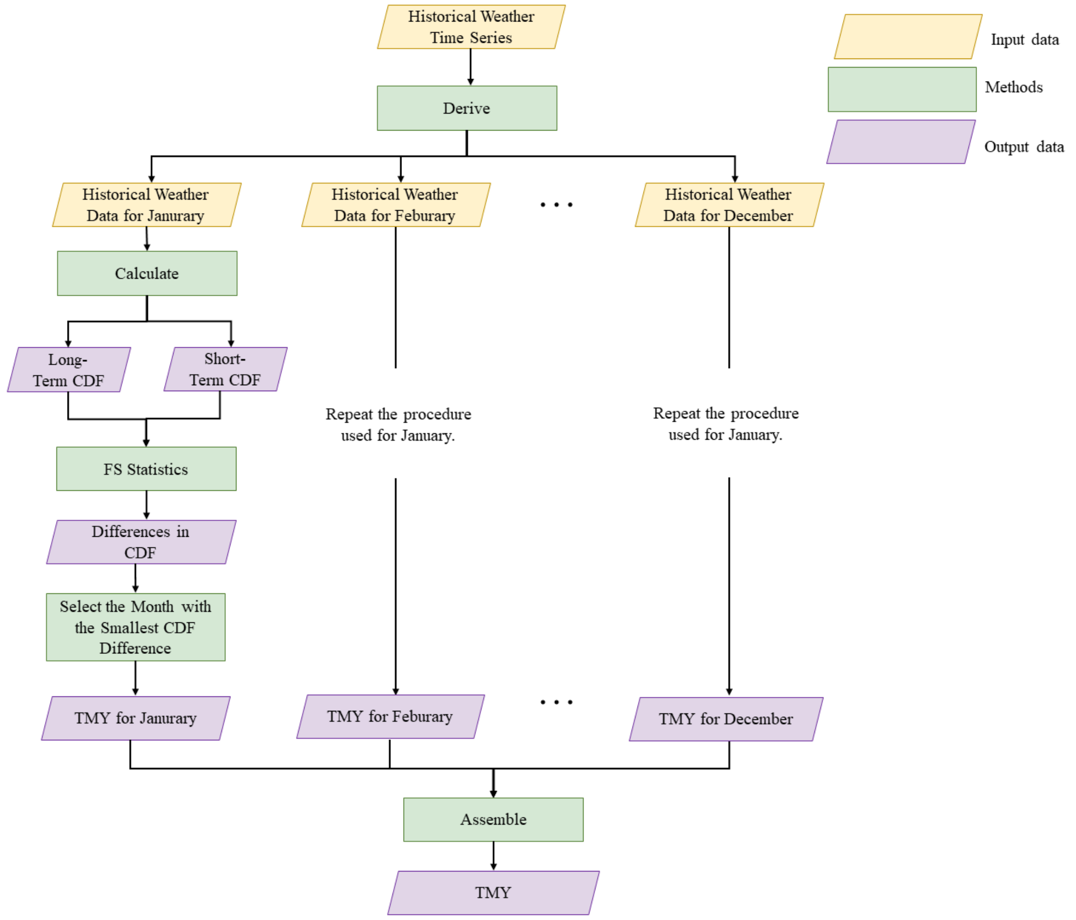

Figure 2.6.: Flowchart illustrating the process of generating a TMY using the Sandia Method.

The Sandia method evaluates nine weather indices, including dry bulb and dew point temperatures, wind speeds, and solar radiation. By assigning weighting factors to each weather index, the TMY computation accounts for the monthly mean, median, and persistence of weather patterns, ensuring that the final dataset accurately represents average climatic conditions. Lund (1991) established three fundamental requirements for TMYs, which have since become widely accepted in the literature. These criteria (Lund, 1991; Hall et al., 1978b) are as follows:

- **True Frequencies**: The mean values of the weather data should closely align with the long-term averages derived from actual measurements, ensuring that the distributions reflect long-term climate conditions.

- **True Sequences**: The duration and sequence of meteorological episodes should accurately reflect the prevailing long-term climate. In other words, the temporal order of weather events should resemble those typically observed over extended periods.
- **True Correlations** The relationships between different meteorological parameters should be precisely represented, with cross-correlations matching those observed in actual meteorological data.

To enhance the TMY method, several refinements have been introduced over the years, particularly regarding adjustments to the weighting factors of weather indices to better suit specific applications. For instance, Huang and Ou (2011) increased the weighting factor for total horizontal solar radiation to develop a Typical Solar Radiation Year for assessing Building Integrated Photovoltaic (BIPV) systems. Other studies have applied the Sandia method to different regions and meteorological parameters, such as Jiang (2010), who generated TMYs for eight cities in China, and Rahman and Dewsbury (2007), who applied it to Subang, Malaysia. In response to the need for more efficient TMY generation, software tools have been developed, such as the one created by Petrakis et al. (1996) using Delphi 6.0.

Beyond the Sandia method, alternative approaches have also been explored. For example, Festa and Ratto (1993) applied more comprehensive statistical indicators to estimate deviations of short-term CDFs from long-term CDFs, using three standardized magnitudes. Gazela and Mathioulakis (2001) introduced a system-oriented method, emphasizing the monthly solar gains over multiple years of operation for a solar hot water system, along with average solar gains. Additionally, Song et al. (2007) proposed a method that uses normalized monthly mean values, calculated by subtracting the mean and dividing by the standard deviation, to select the typical month with the least variability over a specified period.

The deterministic approach for generating SWYs is simple to implement and computationally efficient, as it relies on directly selecting or modifying historical weather data to create a representative SWY. Meanwhile, it is also reliable, as it uses real historical data, ensuring that the SWYs accurately reflect actual conditions. Therefore, it is the most widely used method in energy systems modeling.

2.3.2. Stochastic Approach

In addition to deterministic methods, stochastic approaches are also employed for generating synthetic time series. While deterministic methods offer simplicity and ease of implementation, they often fall short in capturing the high variability inherent in real-world conditions (Goffart et al., 2017). Stochastic approaches, on the other hand, provide a more flexible framework by incorporating randomness and probability, allowing for the generation of multiple plausible weather sequences (Rastogi, 2016). Various stochastic modeling techniques are used to create synthetic weather datasets, which can generally be categorized into four main categories: Traditional Statistical Methods, Sampling-Based Methods, Machine Learning Methods, and Probabilistic Methods.

Traditional Statistical Methods

Traditional statistical methods are among the most commonly used stochastic approaches for generating synthetic weather sequences. These methods rely on predefined assumptions about the distribution and temporal structure of the data, with models designed to capture the statistical properties of the time series. Popular models in this category include Autoregressive (AR) models and Markov Chains. More advanced techniques, such as Autoregressive Integrated Moving Average (ARIMA) and Vector Autoregressive (VAR) models, extend or combine these foundational approaches to improve model accuracy and flexibility.

For instance, an AR model assumes that the current value of a time series depends linearly on its past values, plus a random error term (Knight et al., 1991; Amato et al., 1986). Rastogi (2016) used this approach to generate synthetic time series for variables like dry bulb temperature, global horizontal irradiation, and relative humidity for building energy simulations. This process involved fitting a Fourier series to the original data, modeling residuals with an AR model to generate a synthetic time series. Similarly, Farah et al. (2018) decomposed dry bulb temperature and global horizontal solar radiation into deterministic and stochastic components using the Fourier transformation. The stochastic components were modeled with 1-lag and 2-lag AR models. Other noteworthy studies of using AR models include those by Rastogi and Andersen (2015), Magnano et al. (2008), Ge et al. (2019), and Klöckl and Papaefthymiou (2010).

In comparison, Markov Chains model the probability of transitions between different weather states, offering an effective way to capture the stochastic components of weather data. For example, Pesch et al. (2015) applied Markov Chains to model the stochastic components of wind power time series, providing a more accurate representation of wind variability. Other studies using this method include those by Nfaoui et al. (2004) and Papaefthymiou and Klockl (2008). Advanced models, such as ARIMA, combine AR features with differencing and moving averages to address non-stationary time series data and are widely used in synthetic weather sequence generation (Kennedy and Rogers, 2003; Hill et al., 2011; Ge et al., 2019). Additionally, Vector Autoregressive (VAR) models (Ekström et al., 2015a; Morales et al., 2010; Le et al., 2015) and Wavelet Transform Models (Mohammadi et al., 2023; Gao et al., 2021; Lin et al., 2022) have also been employed for generating synthetic weather sequences.

Sampling-Based Methods

In addition to traditional statistical approaches, sampling-based methods provide robust options for generating synthetic weather data while maintaining the statistical characteristics of historical datasets. For example, Grantham et al. (2018) employed nonparametric bootstrapping techniques to generate synthetic global horizontal irradiation data that accurately reflect the distributions and variability of real-world weather data. Similarly, Saraiva et al. (2021) combined bootstrapping with ANN and SVM to forecast daily streamflow in reservoirs. In addition, Monte Carlo methods, which rely on probability distributions to randomly generate new time series based on historical trends, are also widely used. A typical approach combines Monte Carlo with Markov chains. For instance, Al-Duais and Al-Sharpi (2023) used this combination for both short-term and long-term wind power forecasting. Similarly, Castrogiovanni et al. (2025) applied this approach to estimate atmospheric input and output fluxes of CO_2 from ice core data. The Iman-Conover method, another sampling-based technique, was employed by Goffart et al. (2017) to generate synthetic time series for a single season, including variables such as temperature, humidity, solar irradiation, wind speed, and wind direction.

Machine Learning Methods

Machine Learning method learns the mapping between input and output spaces using training data and is another widely used stochastic method to generate synthetic weather data. For instance, Crone and Kourentzes (2010) used ANN to predict time series based on the ESTSP'08 competition dataset. One of the most widely used neural network models in this regard is Generative Adversarial Networks (GANs), which are particularly effective in synthetic time series generation due to their ability to capture complex temporal dependencies and generate highly realistic sequences through adversarial training (Jeon et al., 2022). Studies such as (Jeon et al., 2022; Li et al., 2022; Gatta et al., 2022) have widely explored the application of GANs for generating synthetic time series. Additionally, Variational Autoencoders (VAEs) have also been widely used in various studies (Desai et al., 2021; Li et al., 2023a; Jin et al., 2022), offering advantages such as structured latent spaces, the ability to model uncertainty, and stable training processes (Desai et al., 2021).

Probabilistic methods

Probabilistic methods are used in synthetic time series generation because they explicitly account for uncertainty and probabilistic relationships within the data. One of the most common probabilistic approaches is Bayesian Networks, which are graphical models that capture the probabilistic dependencies between variables in a time series. Studies such as those by Van der Heijden et al. (2014), Xiao et al. (2017), and Nodelman et al. (2012) have employed Bayesian Networks to predict time series across various applications. Other widely used probabilistic methods include Gaussian Mixture Models (GMM) (Eirola and Lendasse, 2013; Wu et al., 2021; An et al., 2022) and Gaussian Process Regression (GPR) (Aigrain and Foreman-Mackey, 2023; Jin and Xu, 2024; Ghasemi et al., 2021).

While stochastic approaches provide a flexible framework by incorporating randomness and probability, they are primarily applied to short-term synthetic weather data generation, such as forecasting hourly or daily sequences. This is because these methods often assume stationarity in statistical properties, which aligns with the relatively stable characteristics observed over short periods. However, when generating synthetic weather data over longer periods, such as entire years in the application of energy systems modeling, these methods are not typically designed to adequately capture long-term climatic patterns.

To summarize, Figure 2.7 provides an overview of various synthetic weather data generation methods introduced in this chapter.

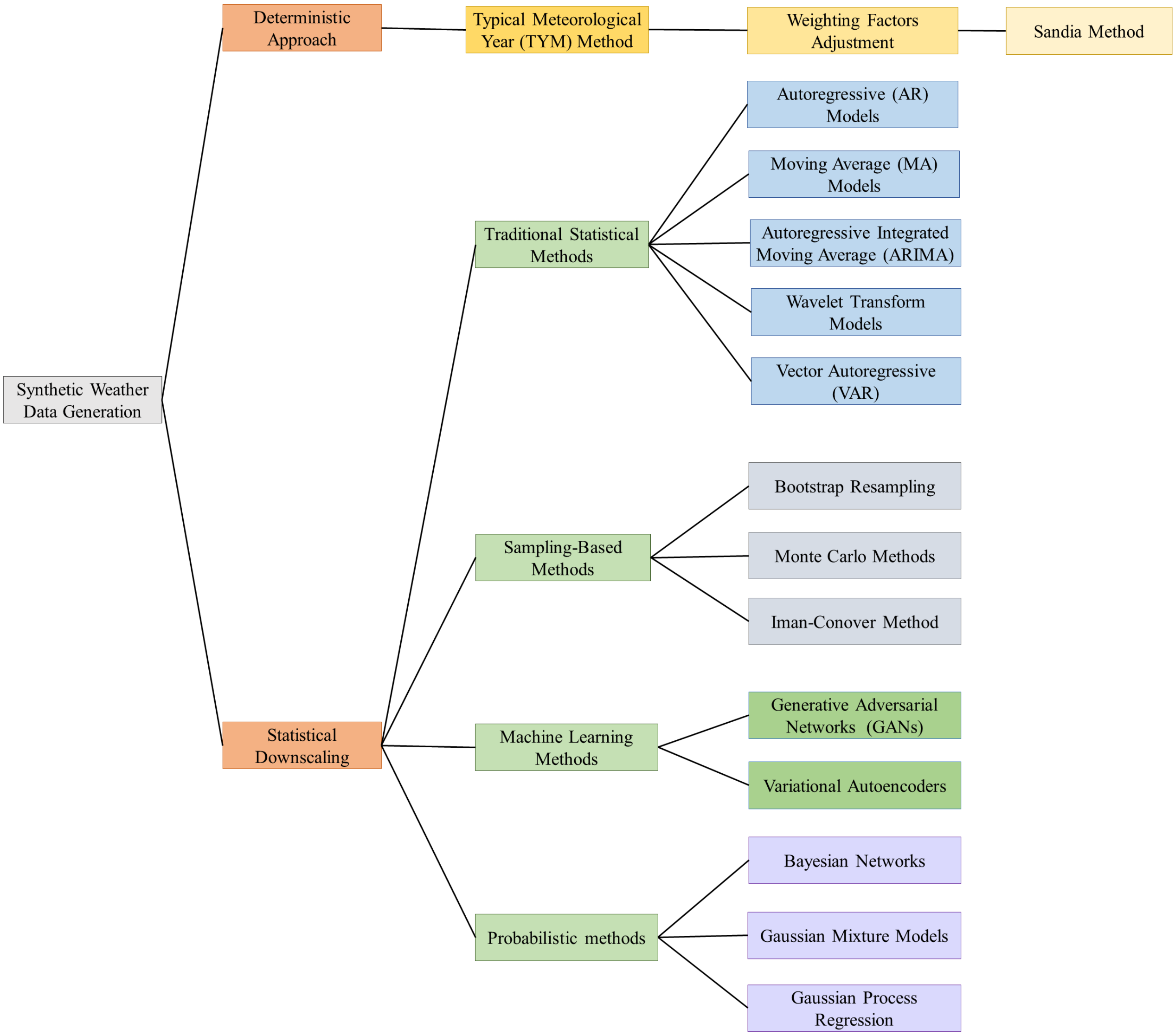

Figure 2.7.: Overview of the various synthetic weather data generation methods.

2.3.3. Extreme Weather Events

Extreme weather events refer to instances when weather and climate conditions significantly deviate from their average state, representing low-probability occurrences that are statistically unlikely (Li et al., 2023b). These events can severely disrupt energy systems, potentially leading to partial or total blackouts due to disruptions in energy supply (Gonçalves et al., 2024). They have profound effects on critical infrastructure and are recognized as one of the primary causes of large-scale electrical disturbances globally (Gonçalves et al., 2024). A range of extreme weather events can impact the energy system. Table 2.3

provides an overview of the main extreme weather events, their effects on energy systems, and relevant global case studies.

Table 2.3.: Extreme Weather Events and Their Impacts on Energy Systems

Event	Definition	Impacts on Energy Systems	Examples
Heatwaves	Prolonged period of excessive heat (Zuo et al., 2015)	Increased cooling demand, reduced transmission line capacity, risks to cooling supplies (e.g., nuclear), damage to substations (Hawker et al., 2024; Añel et al., 2017)	2003 European heatwave (Black et al., 2004), 2006 European heatwave (Fouillet et al., 2008), 2023 North China heatwave (Qian et al., 2024)
Cold Spells (Cold Waves)	Extended periods of extremely low temperatures (Rajeevan et al., 2023)	Increased heating demand and the freezing of critical infrastructure (e.g., pipelines) (Hawker et al., 2024)	2008 Southern China cold spell (Xie et al., 2013), 2012 European cold spell (Planchon et al., 2015), 2022 Northe America cold spell (Yao et al., 2023)
High winds	Extremely high average wind speeds and gusts (e.g., hurricanes and tornadoes) (Zhong et al., 2008)	Damage to transmission and distribution networks, wind turbine shutdowns, and the destruction of infrastructure (Hawker et al., 2024)	2005 Hurricane Katrina across the Gulf of Mexico (Reed et al., 2010) 2017 Hurricane Harvey in the Southern United States (Frame et al., 2020)
Flooding	An overflow of water onto normally dry land. (National Weather Service, nd)	Flooding of critical infrastructure (Hawker et al., 2024)	2021 Western Europe floods (Tradowsky et al., 2023), 2024 United Arab Emirates floods (Hussein et al., 2025)

Table 2.3 – continued from previous page

Event	Definition	Impacts on Energy Systems	Examples
Droughts	Prolonged dry period in the natural climate cycle (World Meteorological Organization, nd).	Reduced hydroelectric generation and the impact on thermal power plants that rely on water supplies for cooling (Hawker et al., 2024)	2019 and 2020 Brazilian drought (Marengo et al., 2021), 2022 European drought (Bevacqua et al., 2024)
Wildfires	Uncontrolled fire that burns in the wildland vegetation, often in rural areas (National Geographic, nd)	Grid outages caused by damaged infrastructure (Hawker et al., 2024) and the impact of wildfire smoke on solar PV performance (Gilletly et al., 2023)	2025 California wildfires (Seydi, 2025) 2019–2020 australia wildfires (Senf et al., 2023)
Dunkelflaute (Energy Droughts, Dark Doldrums)	Prolonged periods with extremely low wind and/or solar availability (Kittel and Schill, 2024)	Reduced renewable energy output and increased reliance on dispatchable backup generation (Kittel and Schill, 2024; Li et al., 2021a).	2018 North Sea Dunkelflaute event (Li et al., 2021b)

However, it is important to note that investigating all these extreme weather events simultaneously in energy system models is challenging, as each event affects the system in complex and often overlapping ways. For example, heatwaves, droughts, and wildfires can occur concurrently or in sequence. Therefore, this dissertation focuses on residual load, which is typically defined as the total electricity demand minus the feed-in from IRE (Schill, 2014; Trieb and Thess, 2020; Ruggles and Caldeira, 2022). Unlike analyzing individual extreme weather events, residual load offers a more systematic way to identify critical periods without manually defining each event. It captures the effect of all weather-driven variations in energy demand and renewable supply in a single metric, providing a more integrated and simplified approach to understanding the system's response to extreme conditions.

Synthetic Extreme Weather Years

To address the importance of extreme weather events, it is crucial for ESMs to consider extreme weather events through the use of SWYs that capture these extreme conditions (i.e., synthetic extreme weather years), rather than focusing solely on identifying a representative weather year that reflects average conditions. Extensive research has been conducted in this field.

For example, the Design Summer Year (DSY) is defined as a year positioned at the median of the upper quartile of historical datasets (Barrett et al., 2002) or as the third hottest summer year (Levermore and Parkinson, 2006). This method ranks historical years based on the average dry-bulb temperature during the summer months. A variant of the DSY, the Probabilistic Design Summer Year, selects years using different metrics instead of average dry-bulb temperature (CIBSE, 2014; Eames, 2016). Another approach involves adjusting the TMY through polynomial regression to adjust parameters such as dry-bulb temperature, global horizontal radiation, wet-bulb temperature, and wind speed, thereby generating a summer reference year (Jentsch et al., 2015; Lau et al., 2017). Other methods include the Extreme Meteorological Year, which combines months with the highest and lowest hourly average values from all historical years to form a year with the hottest summer and coldest winter (Ferrari and Lee, 2008; Crawley et al., 2015). More recent approaches include quantile regression aggregate summer years (Herrera et al., 2018), extremely warm and cold years for building hydrothermal simulations (Nik, 2017), and extremely hot and cold reference years (Pernigotto et al., 2020).

Additionally, some studies focus on selecting representative months or years by characterizing extreme weather events. For instance, Guo et al. (2019) proposed three different years to characterize heat wave events, defining heat waves as temperatures exceeding 31.5 °C indoors and 35 °C outdoors. They introduced Typical Hot Years-Intensity, which identifies the year with the highest annual total heat event intensity based on simulated indoor dry-bulb temperature, emphasizing the intensity of extreme events. They also defined Typical Hot Years-Nights as the year with the greatest number of hot nights and Typical Hot Years-Events as the year with the highest combined event intensity and duration, both determined using simulated indoor dry-bulb temperatures. Similarly, Li et al. (2023b) used thresholds between the 5th to the 95th percentile to consider both the intensity and duration of extreme events, selecting representative extreme months based on this ranking.

However, these advanced studies have largely focused on meteorological aspects, particularly temperature extremes, without addressing the impact of extreme weather on energy systems, where factors such as residual load play more important roles. Research on residual load provides an estimation of the dispatchable power capacity required to meet electricity demand, which is particularly important given the inter-annual variability of solar PV and wind resources in highly renewable energy systems (Ruggles and Caldeira, 2022). For example, Ohba et al. (2023) explored the correlation between high residual load events and weather patterns, such as enhanced cold surge-type weather patterns during winter in Japan.

Scholz et al. (2023) used rolling averages of residual load anomalies, calculated as residual load minus its mean, to identify three types of extreme weather events: Dunkelflaute, seasonal electricity shortages, and long-term electricity shortages. Nitsch et al. (2023) ranked extreme residual load events across historical years by categorizing them into durations of 1 day, 7 days, 14 days, and up to 365 days. Their analysis identified the winter of 1997 as the extreme period for various durations. Similarly, Höltinger et al. (2019) investigated positive residual load events in Sweden lasting less than 4 hours, 5–12 hours, and 13–24 hours, finding that the climatic conditions of 1987, 1996, and 2010 resulted in the highest number of extreme residual load events among the 29 investigated years. These studies have examined the characteristics of residual load, such as its frequency, duration, and intensity, establishing the strong correlation between high residual load events and extreme weather events. However, little effort has been devoted to generating SWYs specifically designed to capture extreme residual load conditions.

2.4. Summary and Research Gap

Meteorological input data, such as wind speed, are crucial components of ESOMs. Among the available datasets, ERA5 reanalysis data is widely used due to its global coverage, timely updates, and relatively high spatial resolution. However, its coarse resolution can introduce substantial uncertainty into energy systems modeling. To overcome this, downscaling techniques are commonly applied. Compared to dynamic downscaling, statistical downscaling offers a more computationally efficient alternative. Within this category, regression-based methods are particularly well-suited for wind speed downscaling, as they can account for the influence of local terrain, which is crucial for accurate local-scale wind speed simulations. However, many studies in this direction focus solely on downscaling wind distributions, which is insufficient for energy systems modeling that typically requires time series data. Other studies that focus on time series data are often site-specific or limited to coarse temporal resolutions, which restricts their spatial and temporal capabilities for energy systems modeling.

To address these limitations and reduce the uncertainty in meteorological data for energy systems modeling, this dissertation proposes a Machine Learning-based statistical downscaling method. The developed model enhances the spatial resolution of ERA5 wind speed time series data to approximately 1 km x 1 km by considering the influence of topographic conditions in local wind speed estimates. This approach offers a robust, computationally efficient solution with simple input requirements, enabling accurate local wind speed estimation. Researchers only need Digital Elevation Model (DEM) and observation station data to downscale the ERA5 wind speed data to a high spatial resolution. Furthermore, this dissertation identifies several key topographic variables and demonstrates their influence on local-scale wind speed. Finally, the downscaling method is applied to provide publicly available wind speed time series data for all of Europe at a 1 km x 1 km spatial resolution for the year 2018.

In addition to meteorological data, electricity demand is another critical component of ESOMs. Among the many drivers of electricity demand, temperature is one of the most influential. To capture this relationship, the TRF is commonly used. However, the scale and dynamic characteristics of the TRF are often overlooked in existing studies. Different countries typically exhibit different TRF shapes, and socio-economic factors also influence these shapes. As a result, projecting electricity demand based solely on the current TRF shape introduces significant uncertainty in energy systems modeling, as it neglects the variability in TRF patterns across countries and the evolving influence of socio-economic factors.

A comprehensive literature review indicates that, while previous studies have explored the impact of various residential building factors on electricity demand, few have specifically addressed their influence on TRFs. To date, no research has presented a method to capture the dynamics of TRFs in the context of future policy changes. To bridge this gap, this dissertation offers a comprehensive analysis of electricity demand time series across Europe. By employing a piecewise regression model and examining four key residential building factors, namely space cooling, passive cooling, electrification, and thermal insulation, the relationship between these factors and TRFs across different countries is explored. By investigating the dynamic nature of TRFs, this analysis aims to capture shifts in demand patterns under varying climate scenarios, ultimately providing more realistic projections of future electricity demand.

Lastly, accurately estimating the long-term performance of an energy system poses a significant challenge due to the complexities of meteorological data input. Inputting multiple weather years into the model can be cumbersome and time-consuming, while selecting an average or representative year from historical data can lead to the loss of variability. To address this challenge, SWYs are often used. Compared to the stochastic approach, which is mainly used for short-term weather data generation, the deterministic approach is generally employed by energy system modelers to generate years such as the TMYs. However, the existing literature lacks in-depth studies on generating SWYs that incorporate extreme weather conditions, particularly with respect to residual load. In modern energy systems with high penetration of IRE sources, neglecting extreme residual load conditions introduces significant uncertainty in capacity planning, system reliability, storage requirements, and the adequacy of backup generation.

To address this issue, this dissertation proposes several methods for generating synthetic extreme weather years that capture critical residual load conditions for energy systems. These synthetic years are then used as inputs for a sector-coupled energy system model to evaluate their impact on system performance. The ultimate goal is to identify a representative weather year that allows an energy system, designed based on this year, to accommodate and withstand all investigated historical weather years. By analyzing two energy system scenarios, exogenous and endogenous renewable capacity expansion, and examining the key factors that contribute to energy system robustness, this dissertation aims to provide valuable insights into coping with possible future extreme weather events for energy system modelers.

3. Data and Methodology

3.1. Statistical Downscaling for High-Resolution Wind Speed Data

3.1.1. Data Description

To develop the Machine Learning Model for the regression-based statistical downscaling method, local-scale observational data is essential for both the training and validation processes. In addition, large-scale reanalysis data and topographic metrics are necessary for training the model. This section provides a comprehensive description of each dataset used in the statistical downscaling method to generate high-resolution wind speed data.

Local-scale Observation Data

In this dissertation, two observation datasets are used, MeteoSwiss observations for Switzerland and German Meteorological Service (DWD) observations for Germany. MeteoSwiss observations are used for training, testing, and cross-dataset validation of the Machine Learning Model, while the DWD observations representing an independent dataset are exclusively used for cross-dataset validation.

The MeteoSwiss observations are collected from the website of the Federal Office of Meteorology and Climatology of Switzerland (MeteoSwiss, 2013). This dataset comprises 10-meter hourly wind speed measurements gathered from weather stations distributed throughout Switzerland. In total, there are more than 150 measurement stations. However, stations with missing values accounting for over 10% of the data are excluded. The final dataset contains measurements from 116 weather stations for the years 2017, 2018, and 2019. Of these years, only observations from 2018 are used to develop the Machine Learning Model, while measurements from 2017 and 2019 are used for cross-dataset validation. The distribution of the MeteoSwiss weather stations used in this study is presented in Figure 3.1.

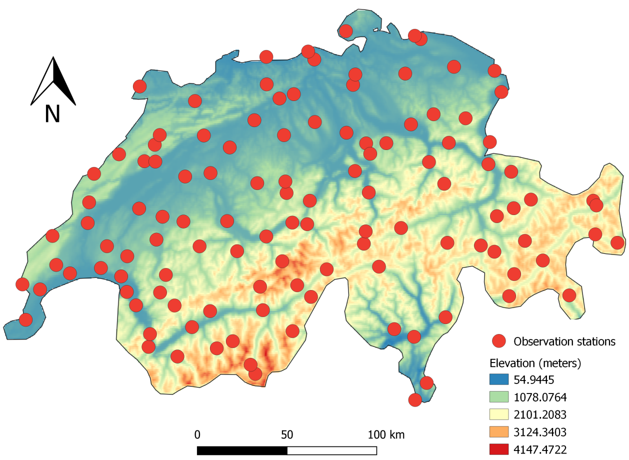

Figure 3.1.: The distribution of 116 MeteoSwiss stations across Switzerland.

The DWD (German Meteorological Service) observations, accessible from the DWD Open Data Server, also provide 10-meter hourly wind speed observations from over 500 weather stations (DWD Climate Data Center, 2013). As the focus of this study is on topographic influence, offshore weather stations are excluded. In addition, stations with missing values exceeding 10% of the data are also excluded. The final dataset contains measurements from 272 stations in 2018. Figure 3.2. shows the distribution of these DWD weather stations.

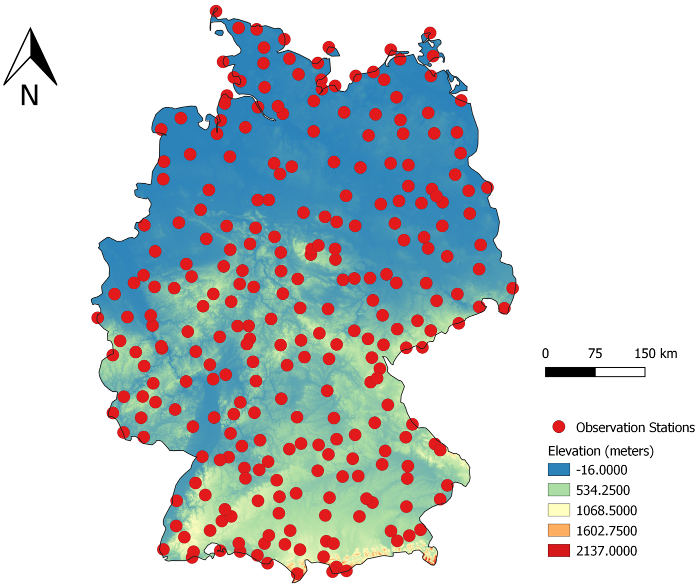

Figure 3.2.: The distribution of 272 DWD stations across Germany.

Large-scale Reanalysis Data

ERA5 is a widely used reanalysis dataset due to its extensive temporal and spatial coverage (Olauson, 2018; Molina et al., 2021; Jourdier, 2020; Doddy Clarke et al., 2021), as also highlighted in Table 2.1. In addition, ERA5 provides more than 200 other variables, including topography-related variables, which have significant impacts on wind speeds. Due to these advantages, ERA5 is chosen as the source dataset for developing the statistical downscaling model.

ERA5 data is publicly available through the European Centre for Medium-Range Weather Forecasts (ECMWF). Wind speed and wind direction time series can be derived from the "10-meter U-component of wind" and "10-meter V-component of wind" available in ERA5. The U-component represents the zonal wind, with positive values indicating eastward winds and negative values indicating westward winds, while the V-component represents the meridional wind, with positive values indicating northward winds and negative values indicating southward winds. Wind speed can be calculated from these two components, as shown in Figure 3.3 and Equation 3.1.

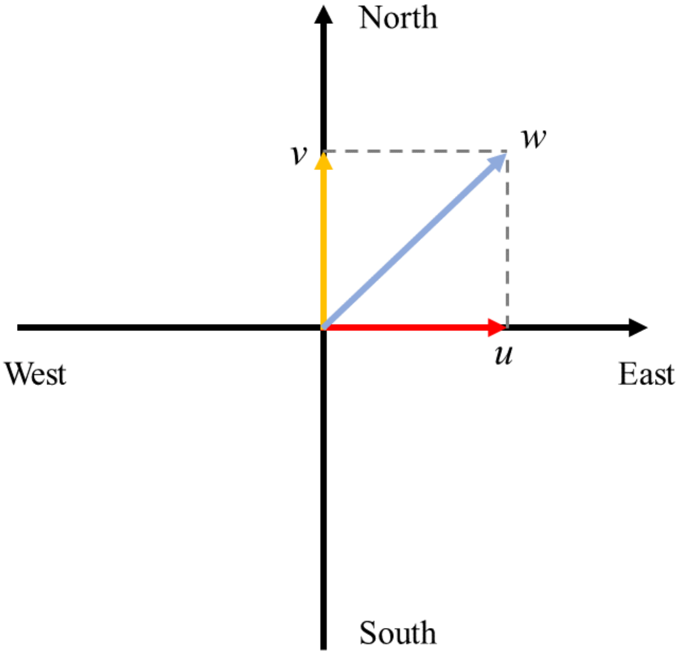

Figure 3.3.: The U- and V- components of wind speed.

$$W = \sqrt{u^2 + v^2} \tag{3.1}$$

where:

- W is the wind speed.
- u is the zonal wind component.
- v is the meridional wind component.

In addition to ERA5, COSMO-REA6 (Bollmeyer et al., 2015) is used as a reference dataset for result comparison. With a higher spatial resolution of approximately 6 km x 6 km, COSMO-REA6 offers greater detail than ERA5, making it especially useful for cross-dataset validation. COSMO-REA6 is also publicly accessible via the DWD website, where the 10-meter wind speed data can be directly downloaded.

As reanalysis data is provided in a gridded format, nearest-neighbor interpolation is applied to obtain the wind speed time series data for a specific weather location. This method first identifies the closest grid point based on the latitude and longitude of each weather station, then assigns the time series data from that grid point to the station. As shown in Figure 3.4, for a given weather station (S), the nearest-neighbor algorithm calculates the distances from station S to four surrounding grid points (P1 to P4). The grid point with the shortest distance is selected—in this case, P1. As a result, the wind speed time series for station S is taken directly from grid point P1.

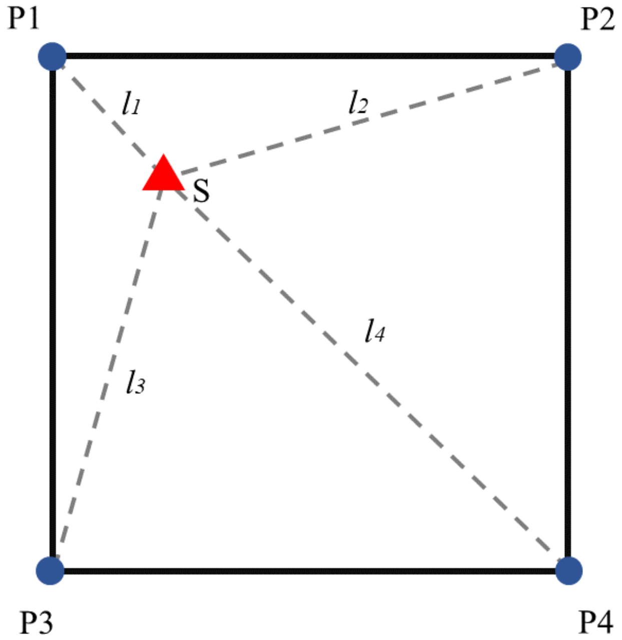

Figure 3.4.: Using nearest-neighbor interpolation to obtain wind speed time series data for a weather location (S).

Topographic Metrics

To thoroughly examine the effect of topography on local-scale wind speed, six crucial topographic metrics are calculated and analyzed: elevation, slope, aspect, small and large-scale Topographic Position Index (TPI), and Terrain Diversity Index (TDI). These topographic metrics can all be derived from a Digital Elevation Model (DEM). DEM is a representation of the Earth's surface topography in a digital format, where elevation data is stored as a grid of evenly spaced points. The DEM used in this study is Global Land One-Kilometer Base Elevation (GLOBE), which has a spatial resolution of 0.0083 degrees (around 1 km x 1 km) (GLOBE Task Team et al., 1999).

Among these topographic metrics, elevation data can be directly retrieved from DEM as presented in Figure 3.5.

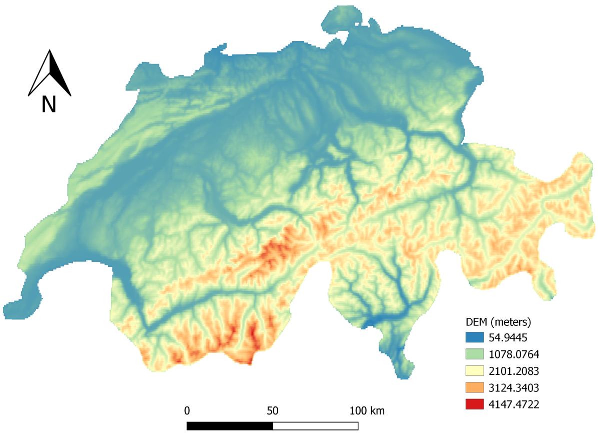

Figure 3.5.: DEM map in Switzerland that represents the elevation of terrains.

Slope represents the degree of steepness at each cell within a raster surface. Lower slope values indicate flatter terrain, while higher slope values signify steeper areas, as illustrated in Figure 3.6. It is calculated by dividing the vertical change in elevation by the horizontal distance (ESRI (Environmental Systems Research Institute), 2023b), and the slope in degrees can be derived using Equation 3.2. The slope map for Switzerland is shown in Figure 3.7.

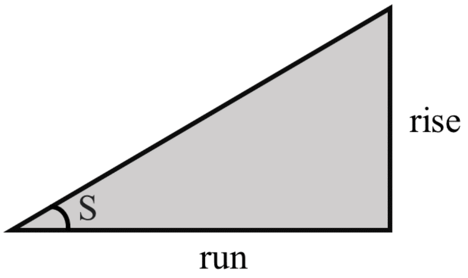

Figure 3.6.: Slope calculation illustration, showing the relationship between vertical change in elevation (rise) and horizontal distance (run).

$$S = \tan^{-1}\left(\frac{\text{rise}}{\text{run}}\right) \times \frac{180}{\pi} \tag{3.2}$$

where:

- S is the slope angle in degrees.
- rise is the vertical change in elevation.
- run $= \sqrt{(\Delta x)^2 + (\Delta y)^2}$ is the horizontal distance over which the elevation change occurs.
- Δx is the change in the east-west direction; Δy is the change in the north-south direction.

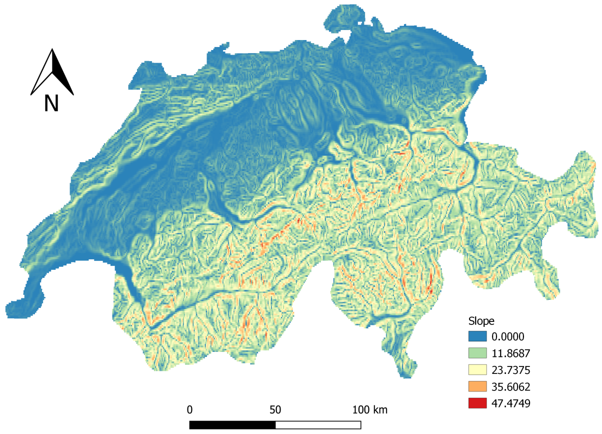

Figure 3.7.: Slope map in Switzerland that represents the degree of steepness.

Aspect refers to the orientation of the steepest slope on a terrain surface, indicating the direction the slope faces. It is measured in degrees clockwise from north, ranging from 0° to 360° (ESRI (Environmental Systems Research Institute), 2023a). Specifically, 0° (or 360°) corresponds to North, 90° to East, 180° to South, and 270° to West, as illustrated in Figure 3.8. The aspect calculation is provided in Equation 3.3, and the aspect map for Switzerland is shown in Figure 3.9.

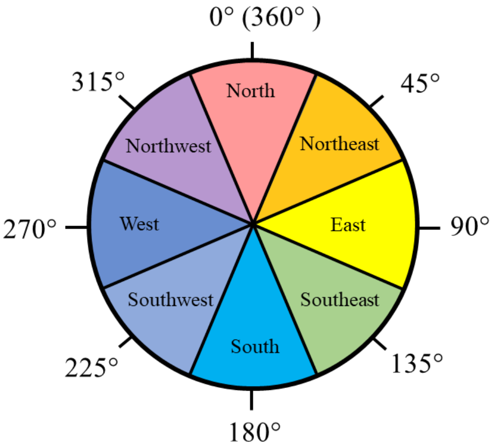

Figure 3.8.: Diagram illustrating the directional orientation of aspect values on a terrain surface.

$$A = 180 + \frac{180}{\pi} \tan^{-1}\left(\frac{\frac{\partial z}{\partial x}}{\frac{\partial z}{\partial y}}\right) \tag{3.3}$$

where:

- A is the aspect, measured in degrees clockwise from north.
- $\frac{\partial z}{\partial x}$ is the rate of elevation change in the east-west direction.
- $\frac{\partial z}{\partial y}$ is the rate of elevation change in the north-south direction.
- $\frac{180}{\pi}$ converts the angle from radians to degrees.

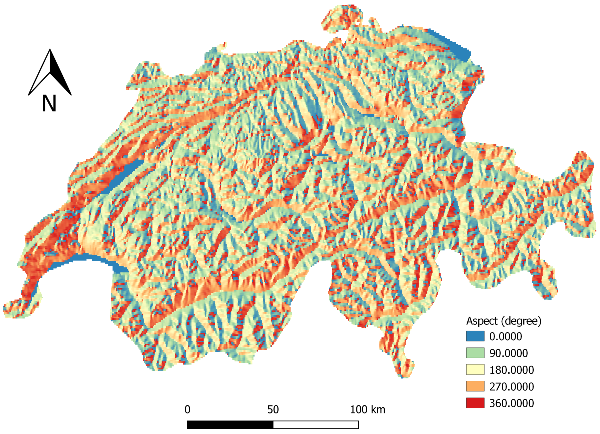

Figure 3.9.: Aspect map showing the terrain orientations across Switzerland, with color gradients representing different directional slopes

Topographic Position Index (TPI), first introduced by Weiss (2001), is a measure used to describe the relative elevation of a specific location in comparison to its surrounding terrain. It helps identify various landform features, including ridges, valleys, and flat areas. TPI provides useful information about the complexities of the terrain and its influence on wind dynamics, making it a useful tool in wind-related studies (Winstral et al., 2017; Solbakken et al., 2021; Molina et al., 2021). TPI is calculated by subtracting the mean elevation of neighboring points within a defined radius from the elevation of the target point. Positive TPI values indicate higher elevations relative to the surroundings (e.g., mountain tops and ridges), negative values indicate lower elevations (e.g., valleys), and values close to zero suggest flat or gently sloping areas. The formula for calculating TPI is presented in Equation 3.4.

$$TPI = z_0 - \frac{1}{n}\sum_{i=1}^{n} z_i \tag{3.4}$$

where:

- TPI is the Topographic Position Index.
- z_0 is the elevation of the central point.
- z_i represents the elevation of surrounding pixels within a specified radius.
- n is the number of neighboring pixels considered.

In this dissertation, two different radii are used for TPI calculation: 5 km and 75 km. This allows for the capture of both large landscape units and smaller local features. A 5 km radius focuses on small-scale terrain variations, such as hills, valleys, and ridges, while a 75 km radius captures broader landscape features like mountain ranges, large valleys, and plateaus. Relying solely on a small radius could overemphasize minor variations, whereas using only a large radius might overlook important local features. By combining both radii, it is possible to better distinguish localized landforms within the broader terrain context, providing a more comprehensive understanding of the landscape. Figure 3.11 shows the TPI maps for both 5 km and 75 km radii for Switzerland.

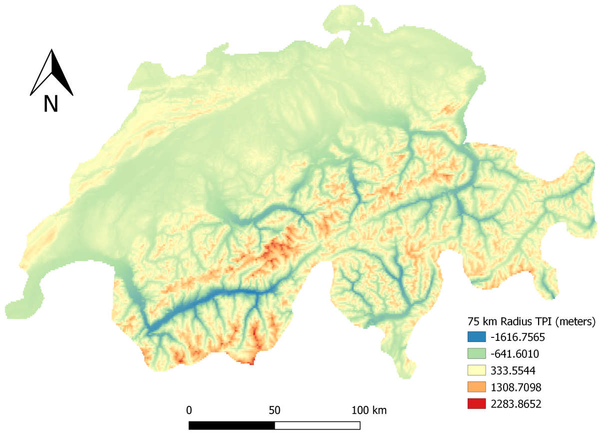

(a) TPI calculated with a 75 km radius in Switzerland, representing major landscape features.

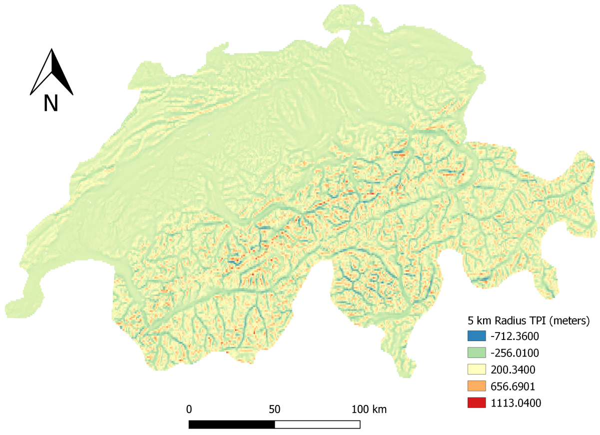

(b) TPI calculated with a 5 km radius in Switzerland, capturing small local features.

Figure 3.10.: TPI maps for Switzerland at two different radii, representing both small-scale and large-scale terrain features.

In addition to these widely recognized and established topographic metrics, this dissertation introduces a novel index: Terrain Diversity Index (TDI). This index quantifies the topographic variety of an area by computing the ratio of the range of elevations to the mean elevation, as indicated in Equation 3.5, thus reflecting the diversity of the terrain. For this study, an 11 km radius window is used for the TDI calculation. The value of TDI serves as an indicator of the degree of topographic diversity in a given region. A higher TDI value signifies a greater range of elevations, thereby implying a more intricate topography. Conversely, a lower TDI implies a more uniform landscape. The maps of TDI for Switzerland are provided in Figure 3.11.

$$TDI = \frac{z_{max} - z_{min}}{z_{mean}} \tag{3.5}$$

where:

- TDI is the Terrain Diversity Index
- z_{max} is the maximum elevation of an area
- z_{min} is the minimum elevation of an area
- z_{mean} represents the average elevation of an area

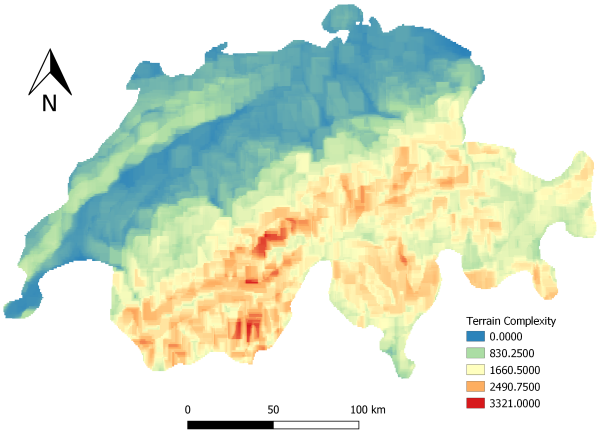

Figure 3.11.: TDI map in Switzerland, illustrating the topographic variety.

3.1.2. Classifying ERA5 Biases Using Topographic Metrics

The proposed statistical downscaling approach involves a regression analysis aimed at establishing the relationship between ERA5, observed data, and topographic metrics. However, before this process, a data preprocessing step that classifies the study region into various categories based on the aforementioned topographic metrics is conducted. This classification step is important as it ensures a thorough consideration of the terrain impact. Topographic features can significantly influence wind speed, and by categorizing the region into distinct topographic groups, the model can capture terrain-specific variations. This allows the regression analysis to be applied more accurately within homogeneous terrain types, enhancing model precision and reducing biases that could arise from applying a single regression process across the whole study area.

When comparing ERA5 with observations, it becomes evident that the biases of ERA5 vary depending on the site location. More specifically, in mountainous areas or valleys, ERA5 tends to exhibit significant biases, while in flat regions, the biases are generally small. This observation aligns with the findings of other studies (Jourdier, 2020; Vanella et al., 2022). To examine the influence of topography on the quality of ERA5, the method proposed by Winstral et al. (2017) is first applied, in which the TPI was used to evaluate the performance of COSMO-REA6. Their study revealed that COSMO-REA6 overestimates wind speeds in areas with low TPI values and underestimates them in areas with high TPI values. However, the results for ERA5 differ, as it is observed that ERA5 frequently underestimates wind speed, even in regions with low TPI values. This discrepancy may be attributed to the coarser spatial resolution of ERA5 compared to COSMO-REA6, as well as the limitations of relying solely on a single topographic metric such as TPI.

To address this issue, further investigation into the influence of various topographic metrics on the accuracy of ERA5 is necessary. Therefore, a preprocessing step is proposed that evaluates the impact of these topographic factors, enabling more accurate predictions of ERA5's quality for any given region based on its specific terrain conditions. This step involves integrating multiple topographic metrics, as outlined in Section 3.1.1, into a Random Forest Classification Model implemented using the scikit-learn Python package (Pedregosa et al., 2011). Random Forest is an ensemble learning method that builds multiple decision trees during training and combines their outputs to improve predictive performance and reduce overfitting. Each tree is trained on a random subset of the data, and the final prediction is made through majority voting for classification or averaging for regression. This approach enhances robustness by minimizing the influence of individual noisy or biased trees, making it well-suited to capture the underlying relationships (Breiman, 2001).

To conduct the Random Forest Classification, the training data, including ERA5 quality and topographic metrics for all available weather stations, is needed. However, due to the limited sample size of MeteoSwiss stations, the classification process is performed for both MeteoSwiss and DWD weather stations. This measurement ensures that the classification is more representative and generalizable, improving the robustness and accuracy of the classification model. The preprocessing step starts by classifying weather stations into three classes based on the root mean square error (RMSE) between observations and ERA5, as detailed in Table 3.1. Class 1 represents stations with good ERA5 quality, characterized by an RMSE of less than 1.5 m/s. Class 2 indicates moderate ERA5 quality, with an RMSE between

1.5 m/s and 3 m/s, while Class 3 corresponds to poor ERA5 quality, with an RMSE greater than 3 m/s. The distribution of stations across these classes is shown in Figure 3.12.

Table 3.1.: The classification scheme employed in the preprocessing step.

Class	Number of stations	RMSE range
Class 1	276	RMSE $\leq$ 1.5 m/s
Class 2	88	1.5 m/s $<$ RMSE $\leq$ 3 m/s
Class 3	24	RMSE $>$ 3 m/s

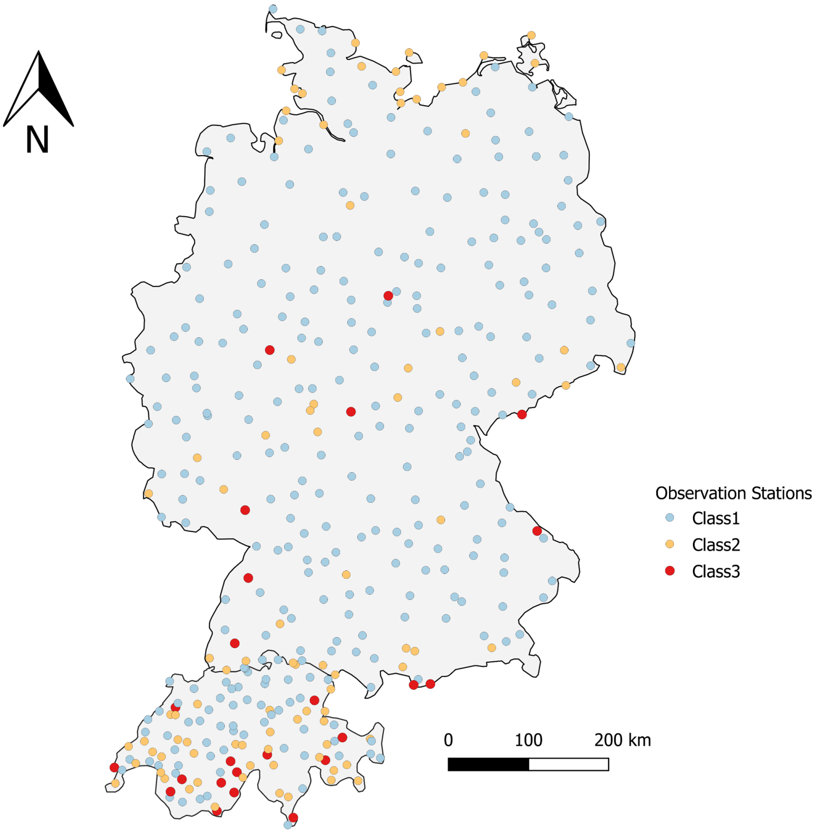

Figure 3.12.: Distribution of measurement stations classified into three classes based on ERA5 quality. Class 1 (276 stations) represents stations with good ERA5 quality, Class 2 (88 stations) indicates moderate ERA5 quality, and Class 3 (24 stations) corresponds to stations with poor ERA5 quality.

In addition, topographic metrics, including elevation, slope, aspect, TPI (with 5 km and 75 km radii), and TDI, are calculated for each station and serve as input features for the classification model. The flow chart of the whole preprocessing step is presented in Figure 3.13. To assess the model performance, a data split of 80% training data (310 stations) and 20% testing data (78 stations) is applied.

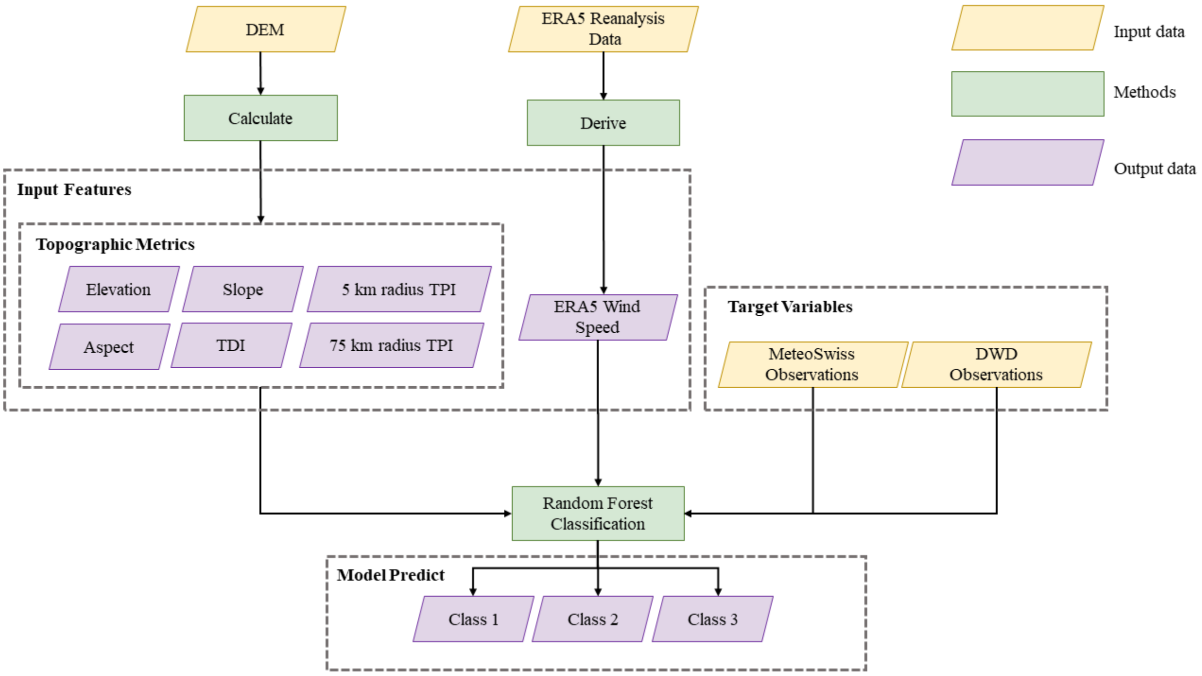

Figure 3.13.: Flow Chart illustrating the preprocessing steps.

3.1.3. Regression Analysis of ERA5 and Topographic Influences

After the preprocessing step, a regression analysis is conducted for each class to examine the correlations between input features and the target variable. In this case, the input features consist of both large-scale ERA5 data and local-scale topographic metrics. The large-scale ERA5 data are time-dependent and provided as time series, including ERA5 wind speed, ERA5 wind direction, and Gravity Wave Dissipation (GWD). On the other hand, the local-scale topographic metrics in this study are time-independent and provided as constants, including TPI values with 5 km and 75 km radii. The target variable, observed wind speed, is time-dependent and is also provided as a time series.

Including GWD as an input feature in the analysis serves a specific purpose. GWD represents the cumulative conversion of kinetic energy into thermal energy in the mean flow over the entire atmospheric column per unit area, resulting from stress effects associated with low-level orographic blocking and orographic gravity waves (Hersbach et al., 2020). The incorporation of GWD enables the model to account for the impact of gravity waves, which are generated by topographic features such as unresolved valleys, hills, and mountains at scales between 5 km and the ERA5 grid (Hersbach et al., 2020). By including GWD, the model gains additional insights from the gravity waves, providing a better understanding of the topographical influences on local-scale wind speed.

Before being introduced to the Machine Learning Model, all predictors are normalized to set the features on a common scale. The regression process is then implemented using the eXtreme Gradient Boosting

(XGBoost) algorithm, a scalable and optimized tree-boosting framework (Chen and Guestrin, 2016). XGBoost is a powerful Machine Learning algorithm widely used for supervised learning tasks. It is an enhanced version of the gradient boosting framework, which builds strong predictive models by combining multiple weaker models, typically decision trees, in a sequential manner. The objective function of XGBoost is displayed in Equation 3.6. The key advantage of XGBoost lies in its combination of high performance and flexibility. It extends traditional gradient boosting by incorporating regularization techniques, specifically L1 and L2, which help mitigate overfitting and enhance the model's generalization capabilities (Chen and Guestrin, 2016). Figure 3.14 presents the flow chart of the regression process.

$$f_{obj} = \sum_{i=1}^{n} \ell(y_i, \hat{y}_i) + \sum_{k=1}^{K} \Omega(f_k) \tag{3.6}$$

Where:

- f_{obj} is the objective function.
- $\ell(y_i, \hat{y}_i)$ represents the loss function, such as the squared error for regression, where y_i is the true label and $\hat{y}_i$ is the predicted value for the i-th sample.
- f_k represents the k-th tree in the ensemble.
- $\Omega(f_k)$ is the regularization term,

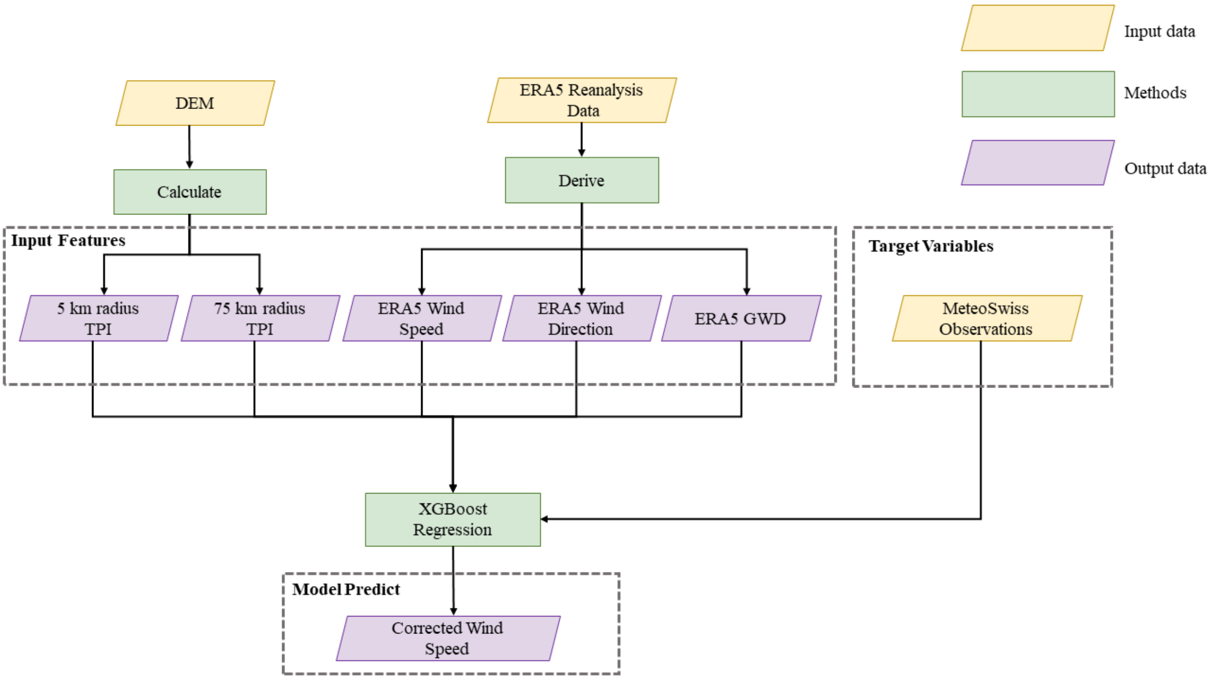

Figure 3.14.: Flow Chart illustrating the regression process. This process is conducted separately for each Class identified in the preprocessing step.

Data for both input features and target variables are collected for all MeteoSwiss stations in 2018. Similar to the preprocessing step, all time series data are split into 70% for training and 30% for testing. To estimate the performance of the regression model, four statistical metrics are used in this dissertation: RMSE, Pearson Correlation Coefficient (PCC), coefficient of determination (R^2 score), and Kolmogorov-Smirnov D statistic (KSD). These metrics provide a comprehensive evaluation of the model's performance by assessing prediction accuracy, correlation, and distribution matching.

- **Root Mean Square Error (RMSE)** measures the average magnitude of the prediction errors as shown in Equation 3.7. A lower RMSE indicates better model accuracy, representing the typical deviation between predicted and actual values.

  $$\mathrm{RMSE} = \sqrt{\frac{1}{n}\sum_{i=1}^{n}(y_i - \hat{y}_i)^2} \tag{3.7}$$

  Where:

  - y_i is the observed value.
  - $\hat{y}_i$ is the predicted value.
  - n is the number of observations.

- **Pearson Correlation Coefficient (PCC)** quantifies the linear relationship between observed and predicted values as indicated in Equation 3.8. A value close to 1 means a strong positive correlation, indicating the model captures the trends of the data well.

  $$\mathrm{PCC} = \frac{\sum_{i=1}^{n}(x_i - \bar{x}(y_i - \bar{y}}{\sqrt{\sum_{i=1}^{n}(x_i - \bar{x}^2 \sum_{i=1}^{n}(y_i - \bar{y}^2}} \tag{3.8}$$

  Where:

  - x_i and y_i are the individual data points of variables X and Y, respectively.
  - $\bar{x}$ is the mean of variable X.
  - $\bar{y}$ is the mean of variable Y.
  - n is the number of data points.

- **Coefficient of Determination (R^2 Score)** assesses the proportion of the variance in the target variable that is explained by the model as displayed in Equation 3.9. A higher R^2 indicates better explanatory power of the model.

  $$R^2 = 1 - \frac{\sum_{i=1}^{n}(y_i - \hat{y}_i)^2}{\sum_{i=1}^{n}(y_i - \bar{y}^2} \tag{3.9}$$

  Where:

- y_i is the observed value.
- $\hat{y}_i$ is the predicted value.
- $\bar{y}$ is the mean of the observed values.

- **Kolmogorov-Smirnov *D* Statistic (KSD)** evaluates the similarity between the distributions of the observed and predicted data as displayed in Equation 3.10. A KSD of 0 indicates a perfect match between the two distributions.

$$\mathrm{KSD} = \sup_{x} |F_n(x) - F(x)| \tag{3.10}$$

Where:

- $F_n(x)$ is the empirical cumulative distribution function (ECDF) of the sample.
- $F(x)$ is the cumulative distribution function (CDF) of the reference distribution.
- $\sup_x$ denotes the supremum (maximum) over all values of x.

3.2. Modeling Electricity Demand Under Future Climate and Policy Scenarios

3.2.1. Data Description

To investigate TRFs and project electricity demand under various scenarios, electricity demand and temperature data are essential. This section provides a detailed overview of the historical electricity demand time series data and country-specific temperature profiles. Additionally, it introduces the space cooling generation rate data and climate scenarios data used to project future electricity demand.

Electricity Demand Time Series

The electricity demand data used in this section is derived from the "Actual Total Load" data collected by the European Network of Transmission System Operators for Electricity (ENTSO-E) transparency platform. The dataset comprises time series for 38 European countries, with data availability ranging from 2015 to the present day. However, it is worth noting that the available years and temporal resolution of the time series may vary across different countries.

To better investigate the correlation between temperature and electricity demand, the time series is aggregated into daily units by summing the load values for each day. This measurement is taken to mitigate the impact of factors such as sunshine duration and working hours, which strongly influence hourly electricity demand. The daily electricity demand time series for every country in each calendar year are regarded as individual datasets for examination and analysis. However, if an individual dataset exhibits missing values exceeding 5% of its entirety, it is excluded from the total dataset. The final dataset contains 36 countries including Austria, Bosnia and Herzegovina, Belgium, Bulgaria, Switzerland, Cyprus, Czechia, Germany, Denmark, Estonia, Spain, Finland, France, Georgia, Croatia, Hungary, Ireland, Italy, Lithuania, Luxembourg, Latvia, Moldova, Montenegro, North Macedonia, Netherlands, Norway, Poland, Portugal, Romania, Serbia, Sweden, Slovenia, Slovakia, Ukraine, the United Kingdom, and Kosovo. After a thorough screening, the final dataset comprises 254 individual datasets. In Figure 3.15, a graphical representation is provided to illustrate the distribution of countries included in the dataset, along with the associated temporal coverage of data availability. This figure shows that the majority of study countries have data available for eight years. However, a lack of data is observed in the Balkan countries, particularly in Albania, where no data is available.

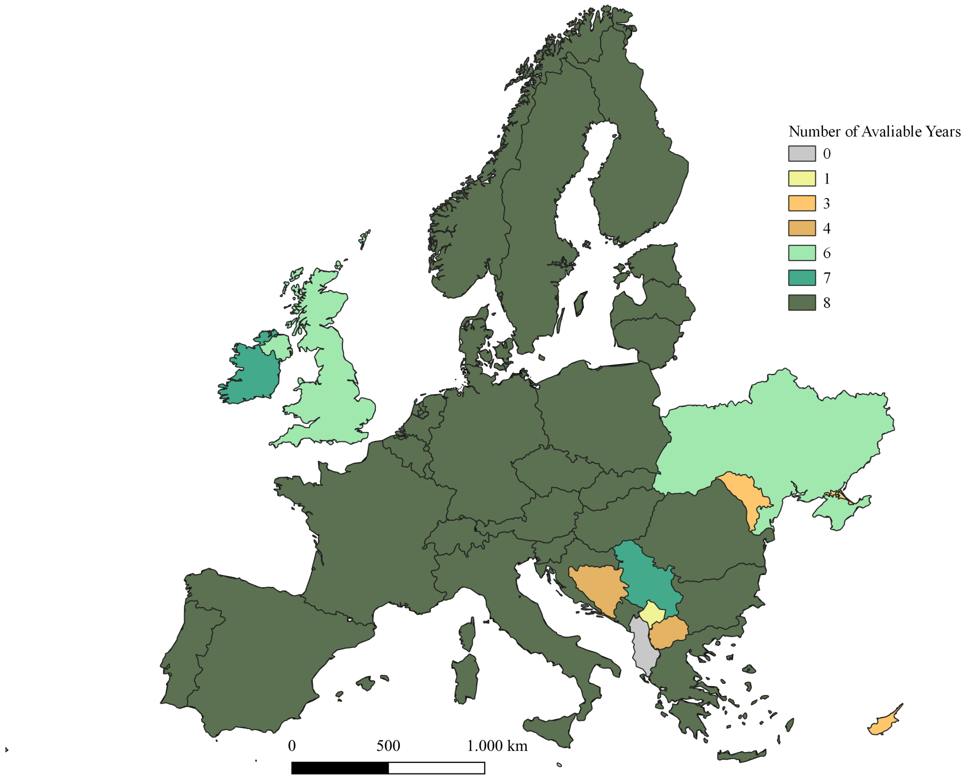

Figure 3.15.: Availability of electricity demand data (in years) for each study country.

Country-specific Temperature Profiles

The temperature data used in this section are also collected from the European Centre for Medium-Range Weather Forecasts (ECMWF) ERA5 dataset (Hersbach et al., 2020), as introduced in Section 2.1.1. However, for this section, the "2m temperature" variable is derived and used.

To obtain country-specific temperature profiles, in contrast to many studies that rely on a general interpolation of temperature data across the country's grid cells, a more rigorous approach that accounts for the influence of population on electricity demand is adopted. Specifically, the 10 most populated cities in each country is first identified and the temperature data is interpolated to the latitude and longitude of the corresponding city to obtain a time series. A population-weighted mean of the temperature is then calculated to generate a country-specific temperature profile. The population data for each city is derived from GeoNames, a publicly available geographical database maintained by the Open Geospatial Consortium (Geonames, 2023). The latitudinal and longitudinal information for each city is obtained through the Bing Maps REST Services Application Programming Interface (API). Finally, similar to the electricity demand data, the hourly temperature time series is resampled into a daily averaged temperature time series by taking the mean value for each day.

Space Cooling Penetration Rate

To determine the space cooling penetration rate, the Integrated Database of the European Energy System from the Joint Research Centre (JRC) Data Catalogue (Mantzos et al., 2018) is used. This database comprehensively records the installation of AC systems in households across 28 European Union countries from 2000 to 2015.

The AC penetration rate is used as a proxy for the space cooling penetration rate, given that AC systems account for approximately 99% of the European market for space cooling technologies (Brown and Domanski, 2014). Data from the most recent available year 2015 is designated as the present space cooling penetration rate, representing the percentage of households equipped with cooling appliances. For the future space cooling penetration rate, the study by Jakubcionis and Carlsson (2017) is referenced. Their research estimates the potential for space cooling in the EU residential sector, establishing a correlation between cooling demand and the number of CDD in the United States. The estimation is based on the assumption that, over the long term, the space cooling demand potential, characterized by specific cooling demand and space cooling penetration, would be comparable in both American and European dwellings under similar climatic conditions. The current and projected space cooling penetration rates are illustrated in Figure 3.16a and Figure 3.16b, respectively.

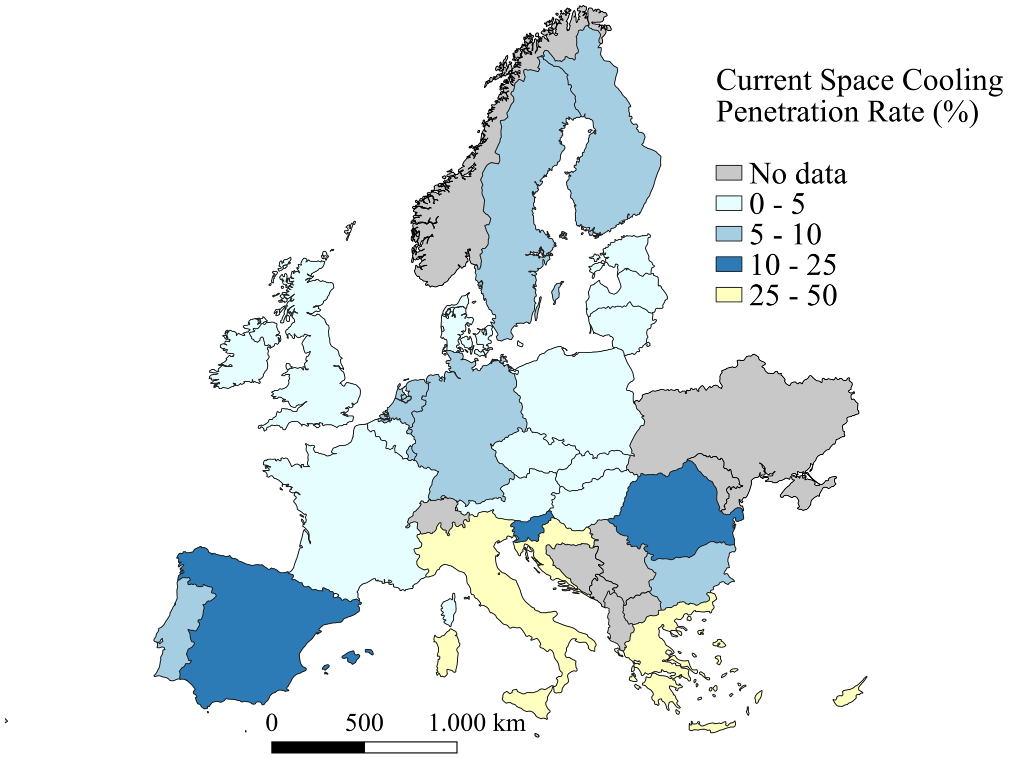

(a) Current space cooling penetration rate

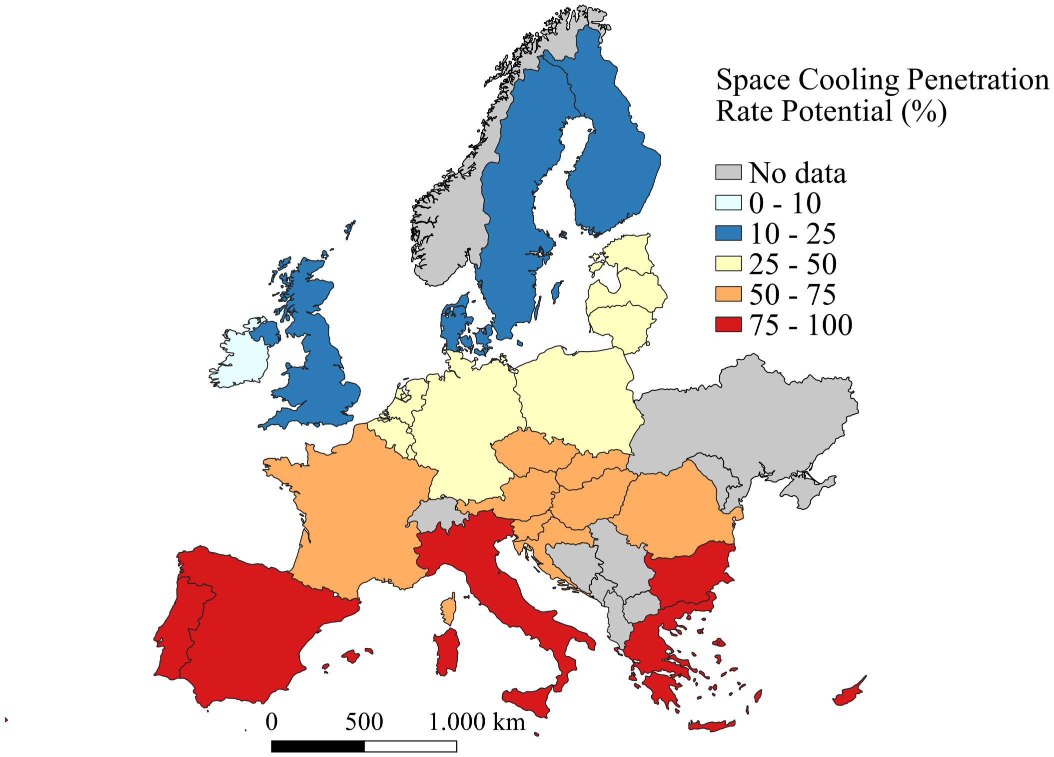

(b) Space cooling penetration rate potential

Figure 3.16.: Current and future space cooling penetration rate

Climate Scenarios

To project electricity demand, climate scenario data is essential. In this dissertation, the climate scenario data is obtained from the Coordinated Downscaling Experiment of the European Domain (EURO-CORDEX), the European branch of the international CORDEX initiative. This initiative aims to establish a globally coordinated framework for producing improved regional climate change projections (EURO-CORDEX, 2023). The specific data used in this section is derived from the datasets of the fifth phase of the Coupled Model Intercomparison Project (CMIP5) (Taylor et al., 2012). The RCM employed is the REMO-RCM, developed by the Climate Service Center Germany (GERICS), and downscaled from the Max Planck Institute Earth System Model at base resolution (MPI-ESM-LR) (Giorgetta et al., 2012) as also introduced in Section 2.1.2. Specifically, realizations r1 and r2 are used as ensemble members. These realizations represent different simulations within the same climate model, initialized with slightly varying initial conditions to account for internal climate variability. By incorporating multiple realizations, the analysis can better capture uncertainties in future climate projections and improve the reliability of projected electricity demand time series.

The analysis incorporates different Representative Concentration Pathways (RCPs), which are a set of greenhouse gas concentration trajectories used to model future climate change (Moss et al., 2010). Different RCP scenarios assume different levels of greenhouse gas emissions over the next century and result in distinct trajectories of radiative forcing and global warming (Moss et al., 2010). Three RCPs are used in this dissertation:

- **RCP2.6**: assumes that global greenhouse gas emissions peak around 2020 and then decline rapidly. This scenario represents a future with very stringent climate policies aimed at limiting global warming to below 2 °C by 2100.
- **RCP4.5**: assumes that greenhouse gas emissions will continue to increase until 2040 and then begin to decline. It is an intermediate scenario that represents a future with moderate climate policies aimed at limiting global warming to 2 °C to 3 °C by 2100.
- **RCP8.5**: assumes that greenhouse gas emissions will continue to increase throughout the 21st century. It is the highest baseline emissions scenario and is sometimes referred to as the worst-case scenario.

Similar to the procedure of obtaining temperature information from ERA5, the country-specific temperature profiles for these three scenarios are derived till the year 2100.

3.2.2. TRF Construction Methods

Decomposition of Electricity Demand Time Series

When examining the correlation between temperature and electricity demand through the scatter plot, two distinct clusters of data points often emerge. For example, Figure 3.17 presents the scatter plot depicting this correlation for the year 2022 in Germany, where these two clusters are clearly observable. This occurrence is primarily attributed to the influence of the day of the week and holidays, both of which can significantly impact electricity demand. To mitigate these influences, a time series decomposition technique is applied to decompose the time series into trend, seasonal, and residual components. The time series decomposition is conducted via the statsmodel Python package. Specifically, an additive model is applied, as indicated in Equation 3.11.

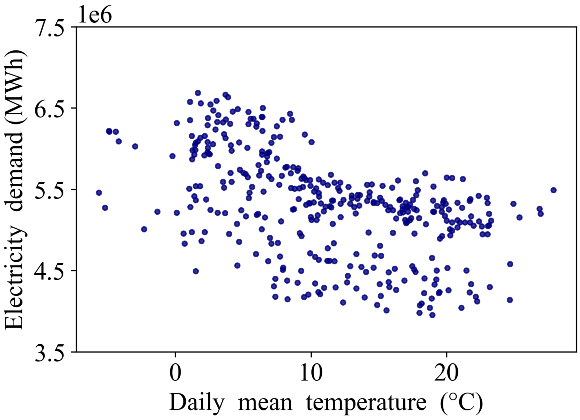

Figure 3.17.: Scatter plots of daily mean temperature and overall electricity demand.

$$Y_t = T_t + S_t + R_t \tag{3.11}$$

Where:

- Y_t is the observed value at time t.
- T_t is the trend component, representing the long-term movement or direction in the data.
- S_t is the seasonal component, which captures the recurring seasonal patterns in the data. In this analysis, it is set to 7 to capture the weekly pattern.
- R_t is the residual component, reflecting random noise or irregular fluctuations in the data.

The trend component represents the long-term direction or movement in the data. For example, if electricity demand is generally increasing over time due to social economic parameters, the trend component captures this gradual change. By isolating the trend, broader patterns without the interference of short-term fluctuations can be analyzed. The trend component is usually calculated by applying a smoothing filter, such as a moving average, to the time series. A moving average helps to smooth out short-term fluctuations and capture longer-term trends. In this analysis, a window size of 7 is used, specifying a 7-day period to smooth the time series and capture weekly recurring patterns. Equation 3.12 illustrates the calculation of the trend component from the time series data.

$$T_t = \frac{1}{n} \sum_{i=t-k}^{t+k} Y_t \tag{3.12}$$

Where:

- T_t is the trend component.
- n is the window size, in this case, $n = 7$ for weekly smooth.
- $t-k$ and $t+k$ indicates the window around time t. In this case $k = 3$.
- Y_t is the original time series value at time t.

The seasonal component reflects regular, periodic fluctuations or cycles that happen at fixed intervals, such as weekly patterns. These fluctuations can capture the fluctuations in the electricity usage, for example, with higher demand on weekdays and lower demand on weekends. To calculate the seasonal component for a weekly pattern, the average deviation from the trend for each of the 7 days across the entire time series is calculated, as shown in Equation 3.13.

$$S_t = \frac{1}{n} \sum_{i=t-k}^{t+k} (Y_t - T_t) \tag{3.13}$$

Where:

- S_t is the seasonal component.
- n is the window size, in this case $n = 7$ for weekly smooth.
- $t-k$ and $t+k$ indicates the window around time t. In this case $k = 3$.
- Y_t is the original time series value at time t.
- T_t is the trend component value at time t.

The residual component, also referred to as the "error" or "irregular" component, captures the random and unpredictable variations in the time series that cannot be explained by the trend or seasonal components. This can include factors such as holidays, extreme weather events, or sudden economic changes. By excluding the residuals, unusual events or irregularities in the data can be identified. It is calculated as the difference between the original time series, the trend, and the seasonal components, as shown in Equation 3.14.

$$R_t = Y_t - T_t - S_t \tag{3.14}$$

Where:

- R_t is the residual component.
- Y_t is the original time series value at time t.
- T_t is the trend component value at time t.
- S_t is the seasonal component value at time t.

Therefore, by excluding seasonal and residual components from the time series, the trend component, which represents the overall direction of the time series, can offer a more generalized depiction of the correlation between temperature and electricity demand. An example of the scatter plot between daily mean temperature and the trend component for the year 2022 in Germany is shown in Figure 3.18. Compared to Figure 3.17, this plot clearly demonstrates a stronger correlation, which makes it easier to identify and distinguish temperature influences, resulting in a more reliable and accurate TRF. Statistically, the coefficient of variation (CV) is reduced from 14.73% to 9.26%, and the absolute value of the PCC is increased from 0.39 to 0.67, indicating the effectiveness of the decomposition analysis in improving the accuracy and reliability of derived TRFs.

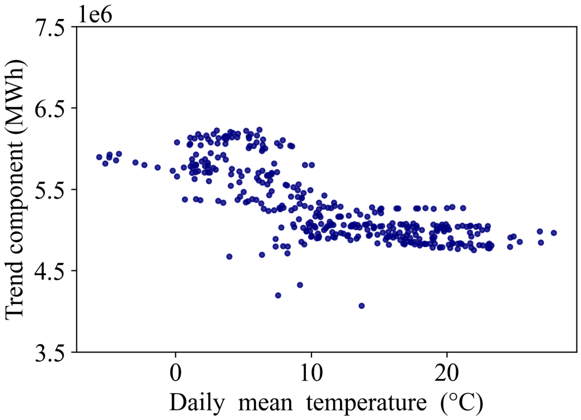

Figure 3.18.: Scatter plots of daily mean temperature and the trend component of electricity demand.

However, in time series analysis, significant outliers can distort decomposition results. These outliers can skew the trend component calculation, lead to incorrect identification of seasonal patterns, and therefore influence the residual component, which should ideally represent random noise. To mitigate the impact of rare or anomalous data points on the analysis, the Z-score technique is applied to remove significant outliers from the dataset. The Z-score is a statistical measure that quantifies how far a data point deviates from the mean, expressed in terms of standard deviations (Abdi, 2007). This method effectively identifies unusually high or low values within the context of the overall distribution. Data points with a Z-score far from 0 may indicate extreme observations. The Z-score is calculated for each data point in the time series, as shown in Equation 3.15. Outliers are identified as data points with an absolute Z-score exceeding a threshold, which is set to 3 in this analysis, corresponding to 99.7% of data within 3 standard deviations for a normal distribution.

$$Z = \frac{x - \mu}{\sigma} \tag{3.15}$$

where:

- Z is the Z-score for a data point, indicating how many standard deviations the data point is from the mean.
- x is the data point whose Z-score is being calculated.
- μ is the mean of the dataset, representing the average value of all data points.
- σ is the standard deviation of the dataset, a measure of the spread or variability of the data.

To better demonstrate the different components of electricity demand, Figure 3.19a presents the various components for Germany in the year 2022. The trend component, shown in Figure 3.19b, captures the long-term behavior of electricity demand, reflecting the overall direction and growth patterns, with electricity demand peaking during the winter, indicating a clear need for heating. The seasonal component, depicted in Figure 3.19c, identifies the repeating patterns associated with weekdays. A closer analysis of a single calendar week reveals a clear fluctuation in the seasonal component, which follows a typical weekday pattern: demand increases at the beginning of the week, peaking on Wednesday, and then declines after Friday, reaching its minimum on the weekend. This decrease is likely attributed to reduced business operations and commuting activities during the weekend. Holidays are well captured in the residual component, as shown in Figure 3.19d, where peak residuals align with major holiday seasons. Notably, all significant holiday periods in Germany, except for Labor Day [1], exhibit a strong overlapping with the peak residuals observed.

---

[1] The reason that Labor Day is not identified as a peak is that Labor Day in the year 2022 happens to be a Sunday, which is already reflected in the seasonal components.

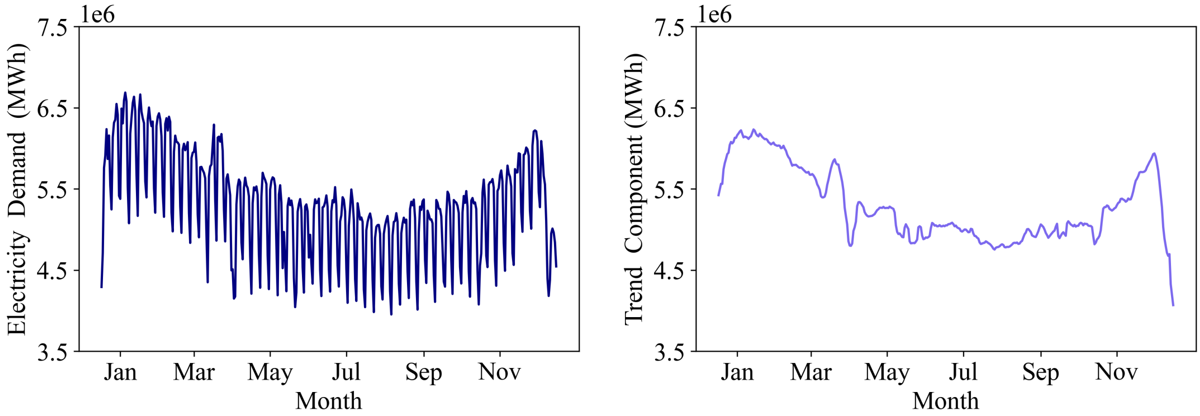

(a) Daily electricity demand

(b) Trend component

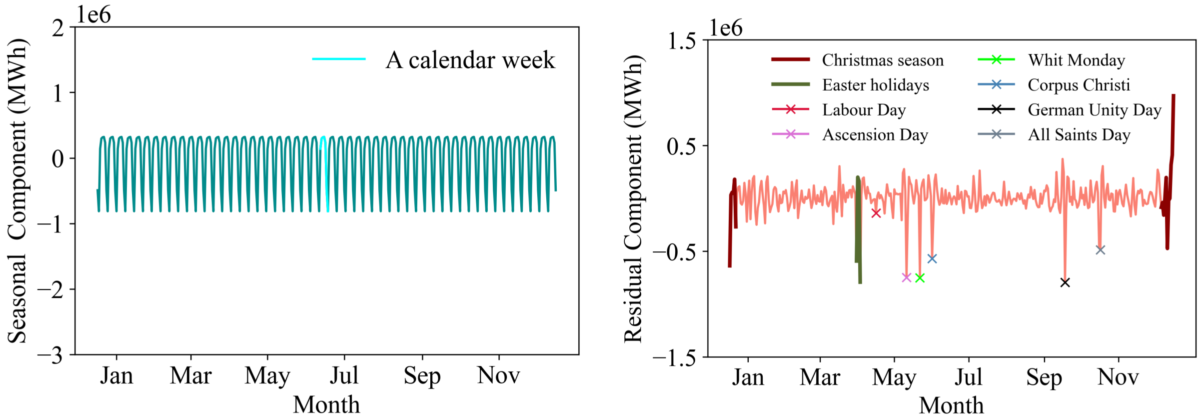

(c) Seasonal component

(d) Residual component

Figure 3.19.: Decomposition analysis for the daily electricity demand of Germany.

Construction of TRFs Using Piecewise Regression

To formulate TRFs, the "minimize" function from the Python package SciPy is used. This optimization tool is designed to find the minimum of a scalar function. To perform a piecewise regression, an objective function is defined to calculate the Sum of Squared Errors (SEE) between the historical and predicted demand as indicated in Equation 3.16. In this context, the minimize function in SciPy iteratively adjusts the parameters of the piecewise function, such as slopes and intercepts, to minimize the SEE, thereby finding the best-fitting values for the piecewise regression.

$$\min \sum_{i=1}^{n} \left(D_i - \hat{D}_i\right)^2 \tag{3.16}$$

Where:

- D_i is the observed historical electricity demand for the i-th data point.

- $\hat{D}_i$ is the predicted demand for the i-th data point.

- n is the total number of data points.

However, it is important to note that the TRFs exhibit different shapes across different regions. In general, it can be categorized into three distinct forms as depicted in Figure 3.20: a linear decreasing curve, a linear decreasing curve followed by a horizontal segment, and two discernible linear components separated by a horizontal line. To model these diverse TRF shapes, different function forms tailored to each case are employed. The linear decreasing curve, as represented in Figure 3.20a and Equation 3.17, is frequently observed in Northern European countries, reflecting the TRF's response to cold weather primarily associated with heating demand. The linear curve with a horizontal segment, as indicated in Figure 3.20b and Equation 3.18, is prevalent in countries with cold and intermediate climates. In these regions, the TRF captures the heating demand and the comfort zone following the heating BPT. Lastly, the V-shaped curve with a "comfort zone" in between, illustrated in Figure 3.20c and Equation 3.19, is prevalent in intermediate or warm countries, where the TRF reflects both heating and cooling demands.

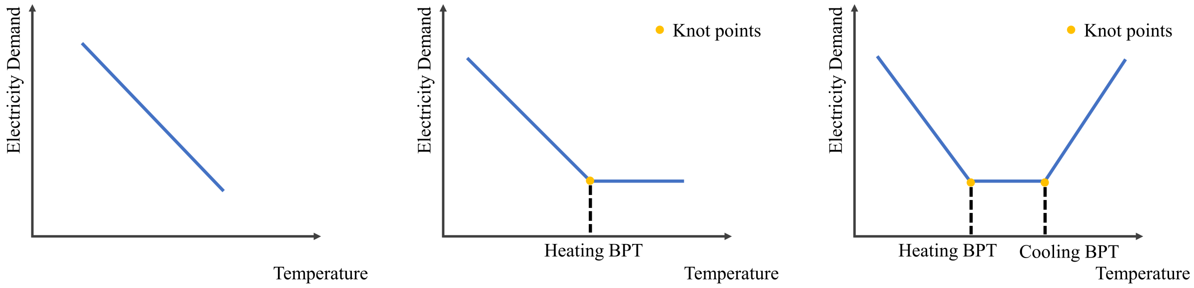

(a) Continuous linear decreasing curve, normally observed in cold climates regions.

(b) Linear decreasing curve with a horizontal segment, normally observed in cold and intermediate regions.

(c) Linear decreasing curve with a comfort zone, normally observed in intermediate and warm regions.

Figure 3.20.: Different shapes of TRFs across Europe.

$$D = m_{left} \times T + b_0 \tag{3.17}$$

$$D = \begin{cases} m_{left} \times T + b_1, & \text{if } T \leq BPT_H \\ D_0, & \text{if } T > BPT_H \end{cases} \tag{3.18}$$

$$D = \begin{cases} m_{left} \times T + b_2, & \text{if } T \leq BPT_\mathrm{H} \\ D_0, & \text{if } BPT_\mathrm{H} < T \leq BPT_\mathrm{C} \\ m_{right} \times T + b_3, & \text{if } T > BPT_\mathrm{C} \end{cases} \tag{3.19}$$

Where:

- D is the electricity demand.
- T is the temperature.
- m_{left} and m_{right} represent the left and right slope, indicating heating and cooling demand, respectively.
- BPT_H and BPT_C are the Heating and Cooling Balance Point Temperatures.
- b_0, b_1, b_2, b_3 are intercepts.
- D_0 is the Comfort zone demand (non-weather sensitive demand)

Prior to the model fitting, the trend components are first normalized from 0 to 1 to set the trend components of different countries on a common scale. During the model fitting process, Huber loss is applied to identify outliers and assign less weight to them, thereby mitigating their impact on the analysis. Huber loss is a robust loss function that combines the benefits of both Mean Squared Error (MSE) and Mean Absolute Error (MAE), as shown in Equation 3.20. For small residuals, when the prediction error is small, Huber loss behaves like MSE, penalizing errors quadratically to encourage the model to be accurate. For large residuals, when the prediction error is large, Huber loss behaves like MAE, penalizing errors linearly, which reduces the impact of large outliers (Huber, 1992). This combination allows the model to balance sensitivity to small errors while maintaining robustness to large outliers, making the model fitting process more robust to noisy or outliers (Huber, 1992; Meyer, 2021).

$$L_\delta(y, \hat{y}) = \begin{cases} \frac{1}{2}(y - \hat{y})^2, & \text{if } |y - \hat{y}| \leq \delta \\ \delta |y - \hat{y}| - \frac{1}{2}\delta^2, & \text{if } |y - \hat{y}| > \delta \end{cases} \tag{3.20}$$

Where:

- $L_\delta(y, \hat{y}$ is the Huber loss function.
- y is the true value (target value).
- $\hat{y}$ is the predicted value (model output).
- δ is a threshold that controls when the loss transitions from quadratic to linear.

In the regression process for Equation 3.19, it is important to assign appropriate boundary conditions for the two BPTs to ensure the reliability of the model results. Boundary conditions are important in this case because they ensure that the function behaves correctly at the points where the segments meet and thereby avoid unrealistic or inconsistent transitions between different segments.

The most widely adopted BPT value in literature is 18.3 °C or 18 °C, retrieved from the American Society of Heating, Refrigerating, and Air-Conditioning Engineers (ASHRAE) Handbooks (American Society of Heating et al., 2013). However, BPT values can vary by region (Bessec and Fouquau, 2008; Hiruta et al., 2022). To ascertain proper boundary conditions for BPT values, a literature review is conducted, as summarized in Table 3.2. From this table, it is evident that the range of heating BPT typically falls between 12 °C and 18 °C. Although studies on Switzerland and Germany (Christenson et al., 2006; Olonscheck et al., 2011) suggest heating BPT values as low as 8 °C or 10 °C, these values are not based on direct measurements but are instead applied within specific scenarios in these studies. As a result, they may not accurately reflect real-world conditions. To ensure a more conservative estimate, a lower bound of 12 °C is adopted for this analysis.

In comparison, the cooling BPT typically ranges between 18 °C and 25 °C. Similar to the heating BPT, while one study conducted by Alhuwayil et al. (2023) reports a maximum value of 27 °C of the cooling BPT. This study is based on data from Saudi Arabia, where extreme summer temperatures are common. Since this dissertation focuses on Europe, a more suitable upper bound of 25 °C is chosen. These selected lower bound and upper bound values for BPT are used as boundary conditions in the regression process in addition to the objective function. This method is implemented independently for each study region and year to derive the TRFs for the normalized trend components.

Table 3.2.: Overview of BPT (°C) across literatures

Literatures	Region	BPT [2]	Heating BPT	Cooling BPT
American Society of Heating et al. (2013)	US	18.3	-	-
Eurostat (2020)	Europe	-	15	24
Carbon Trust (2012)	UK and Germany	-	15.08 (UK), 15.58 (Germany)	-
Swiss Society of Engineers and Architects (SIA) (2016)	Switzerland	-	12	-
Jakubcionis and Carlsson (2017)	Europe	18	-	-
Hao et al. (2022)	China	-	7.08 - 12.71	-
Cömert and Yildiz (2019)	Turkey	15.42	-	-

Continued on next page

Table 3.2 – continued from previous page

Literatures	Region	BPT	Heating BPT	Cooling BPT
Ruth and Lin (2006)	Maryland, US	-	15.56	15.56
Dubin (2008)	US	11.11 - 13.89	-	-
Verbai et al. (2014)	Hungary	-	12	-
Huang and Gurney (2016)	US	11 - 21	-	-
Sailor and Muñoz (1997)	US	14 - 21	-	-
Lindelöf (2017)	Switzerland	17.4 ± 1.9	-	-
Christenson et al. (2006)	Switzerland	-	8, 10, 12	18.3, 20, 22
Giannakopoulos and Psiloglou (2006)	Athens, Greece	22	-	-
Olonscheck et al. (2011)	Germany	-	10, 12	22
Andrade et al. (2021)	Portugal	-	18	25
Psiloglou et al. (2009)	Greece and UK	16 (Athens), 20 (London)	-	-
Papakostas et al. (2010)	Greece	-	15	24
Tsikaloudaki et al. (2011)	South Europe	-	-	23
Alhuwayil et al. (2023)	Saudi Arabia	-	19	27

3.2.3. Scenario Assumptions

To thoroughly grasp the dynamics of TRFs and integrate the development of residential buildings into the analysis, this study examines the impact of varying levels of space cooling penetration, passive cooling, electrification, and thermal insulation within the scenario assumptions. In total, five scenarios are defined, representing distinct levels of policy intervention and residential building development until the year

---

[2] For literature that does not specify heating or cooling BPT. If the type of BPTs is specified, this column will be empty.

2100. The influences of the scenario settings on the BPTs, left and right slopes of the TRFs are quantified in Section 3.2.4.

- **Scenario 0 (S0)**, Static TRFs: This scenario serves as a baseline scenario, employing historical averaged TRFs to calculate future demand. The TRFs remain static over time, assuming no changes in space cooling penetration rate, passive cooling, electrification, or thermal insulation.
- **Scenario 1 (S1)**, Moderate Policy: In this scenario, the space cooling penetration rate remains constant, with renovations of existing buildings focusing primarily on limited thermal insulation improvements. Newly constructed buildings exhibit bigger improvements in thermal insulation. Electrification is introduced in the heating sector of these new buildings, accompanied by a set of limited passive cooling measurements. Both the renovation rate and new build rate are kept low, set at 1% [3] and 0.5% [4] respectively.
- **Scenario 2 (S2)**, Strict Policy: In this scenario, a stringent policy and regulatory framework aimed at enhancing building energy performance is enforced. Building renovation leads to improved thermal insulation, consideration of electrification in the heating sector, and the incorporation of limited passive cooling measures. Newly constructed buildings have significant enhancements in thermal insulation, along with the consideration of electrification in the heating sector and effective passive cooling measures. The renovation and new build rates are set optimistically at 3% [5] and 1% [6], respectively. The second stage of renovation begins once all existing building blocks have undergone renovation. This second phase aims to elevate the energy performance of renovated buildings to the same level as newly constructed ones.
- **Scenario 3 (S3)**, Moderate Policy with boosted space cooling penetration: In this scenario, the Moderate policy is maintained, but boosted space cooling demand is considered in the future. The level of thermal insulation, passive cooling, electrification rate, renovation rate, and new build rate for renovated and newly built buildings remain consistent with S1.
- **Scenario 4 (S4)**, Strict Policy with boosted space cooling penetration: This scenario assumes a combination of strict policy and boosted space cooling penetration in the future.

---

[3] This percentage is derived from the report by Buildings Performance Institute Europe (BIEP) (Economidou et al., 2011), which indicates that the current average renovation rate in Europe stands at approximately 1%.

[4] Regarding the new build rate, the BIEP report (Economidou et al., 2011) also indicates an annual growth rate of approximately 1% in the residential sector. However, it is noteworthy that the same report highlights a recent decrease in the new build rate across many countries. Consequently, for this scenario, a more conservative value of 0.5% is adopted.

[5] This value is retrieved from the Energy Efficiency plan by the European Commission (European Commision, 2011), where the renovation rate of at least 3% is recommended

[6] This value is obtained from the BIEP report (Economidou et al., 2011), where an observed new build rate of 1% is documented. It is assumed that the new build rate will persist at the current level, under the assumption that effective policy incentives will drive the construction of new buildings with a focus on energy savings.

For a better illustration, Figure 3.21 provides a visual representation of the defined scenarios, focusing on their differences in policy intervention levels and space cooling penetration rate.

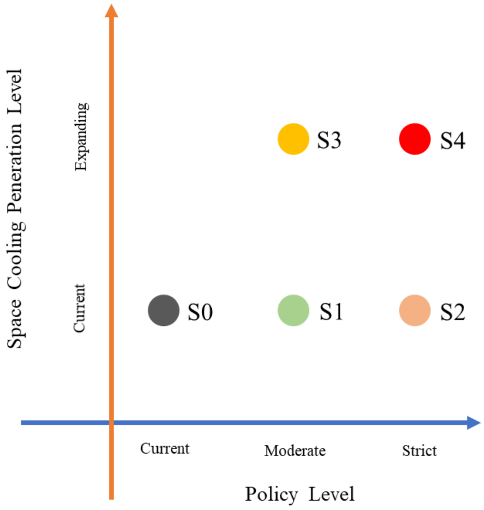

Figure 3.21.: Illustration of five scenarios defined in this section.

3.2.4. Projecting TRFs for Different Scenarios

TRFs consist of four crucial components: two-knot points that represent the heating and cooling BPTs, and two linear components that capture the incremental impact on demand due to additional exposure to heat or cold. Therefore, understanding the changes of these crucial components is necessary for projecting future TRFs. Among these components, the y coordinate of knot points represents the non-weather sensitive energy demand and is not influenced by temperature (Fazeli et al., 2016). Consequently, it is treated as a constant in this analysis. The detailed methodologies for projecting other TRF components are introduced in the subsequent sections.

Future BPT

It is important to note that the x-coordinates of the knot points correspond to BPTs, presumed to be predominantly influenced by the thermal performance of the buildings. However, the relationship between BPTs and the thermal performance of the buildings is complicated and rarely discussed in the literature, posing a significant challenge in establishing a statistical relationship between BPTs and other variables associated with residential buildings. To address this complexity, a comprehensive literature review is conducted to identify suitable BPT values for both new and renovated buildings, these values are then integrated into the defined scenarios.

The findings from the literature review are already presented in Table 3.2, which has been used to establish the boundary conditions for the piecewise regression discussed in Section 3.2.2. In general, a lower heating BPT indicates a better-insulated building, while a higher cooling BPT indicates a building with better ventilation. For each defined scenario, distinct values are assigned to renovated and newly constructed houses. The minimum heating BPT value extracted from literature is 7 °C. Consequently, this value is assigned to newly constructed houses in S2 and S4. For cooling BPTs, a maximum value of 27 °C is assigned to the newly constructed houses in S2 and S4. A summary of the BPT values used in different scenarios is presented in Table 3.3.

Table 3.3.: Future BPT (°C) value for renovated and new built buildings for different Scenarios

	Building categories	S0	S1	S2	S3	S4
Heating BPT (°C)	Renovated buildings	-	11	8	11	8
	New built buildings	-	10	7	10	7
Cooling BPT (°C)	Renovated buildings	-	24	26	24	26
	New built buildings	-	25	27	25	27

To obtain future BPT values, Equation 3.21 is applied. This equation incorporates the renovation and new build rates to calculate the percentage of current, renovated, and newly constructed buildings. The current BPT value is computed as the average BPT value [7] across the years. However, it is worth noting that the current cooling BPT values in Sweden, Norway, Ireland, and the Czech Republic are unavailable since the TRFs in these regions do not show cooling demand, as illustrated in Figure 3.20b and Equation 3.18. As a result, a cooling BPT value of 25 °C is assigned to these countries, representing the upper bound within the boundary conditions for cooling BPT.

$$BPT_f = \alpha_c \cdot BPT_c + \alpha_r \cdot BPT_r + \alpha_n \cdot BPT_n \tag{3.21}$$

Where:

- α_c, α_r, and α_n are the percentages of current, renovated, and new buildings, respectively.
- BPT_f, BPT_c, BPT_r, and BPT_n are the BPT values for future, current, renovated, and new buildings, respectively.

Future Left Slope

In the overall energy demand for buildings, the left slope corresponds to the heat loss coefficient of the building, commonly denoted as the K value, as indicated in studies by Lindelöf (2017) and Lindelöf et al. (2018). The K value, often referred to as the heat loss coefficient, represents the rate at which a building loses heat due to factors such as its insulation, windows, and building materials. However, when it comes

---

[7] The average value is used instead of the value in 2022 to provide a more representative estimate.

to electricity demand, the situation is more complex due to the additional influence of the electrification rate. To simplify this process, Sweden is used as a benchmark due to its high share of electricity use (Mantzos et al., 2018) and generally good thermal insulation in residential buildings (Economidou et al., 2011). This assumption extends to other factors, including the coefficient of performance (COP) value of heat pumps and the distribution between air and ground-source heat pumps, which are assumed to align with conditions in Sweden. Comprehensive analyses of heat pump use in Sweden can be found in existing studies, such as Johansson (2021), Sandvall and Karlsson (2023), and Ministry of Infrastructure (Sweden) (2021).

Currently, the electrification rate in Sweden is 44%, ranking among one of the highest electrification rates in European countries. Meanwhile, this percentage also corresponds with future electrification rate projections from a study by the European Commission, which assumes the residential sector electricity share in heating will grow to between 22% and 44% by 2050 (European Commision, 2018). Additionally, the thermal insulation of Swedish residential buildings ranks among one of the best in Europe (Economidou et al., 2011; Odyssee Energy, 2021). Therefore, the left slope value of Sweden (-0.49) is chosen as a benchmark for scenarios that involve both increased electrification rates and improved thermal insulation. The left slope is determined in Equation 3.22. Specifically, for renovated buildings in Scenarios S2 and S4, and new buildings in S1 and S3, the left slope value of -0.49 is assigned. For newly constructed houses in S2 and S4, where a more significant thermal insulation improvement is assumed, a slope value of -0.30 is assumed.

$$m_{left,f} = \alpha_c \cdot m_{left,c} + \alpha_r \cdot m_{left,r} + \alpha_n \cdot m_{left,n} \tag{3.22}$$

Where:

- α_c, α_r, and α_n are the percentages of current, renovated, and new buildings, respectively.
- $m_{left,f}$, $m_{left,c}$, $m_{left,r}$, and $m_{left,n}$ represent the left slope values for future, current, renovated, and new buildings, respectively.

For the renovated buildings in Scenarios S1 and S3, where no changes in the electrification rate are assumed, the focus is solely on improving thermal insulation. Consequently, the absolute value of the slope is likely to decrease due to improved thermal insulation. However, this reduction is expected to vary across countries based on their respective policies. Countries with more stringent regulations on residential buildings are anticipated to experience a more significant decrease in the absolute value of the left slope.

According to a study by Lindelöf (2017), where a case study in Switzerland was conducted, it was observed that the K value of post-retrofit buildings decreased by 30% compared to pre-retrofit buildings, indicating a 30% reduction in the slope value. To extrapolate this reduction value for other countries, 30% reduction in Switzerland is used as a benchmark. This value is then scaled proportionally according to the ODYSSEE Overall Energy Efficiency Score (Odyssee Energy, 2021). This score documents the policy intervention level for various European countries, considering factors like energy efficiency level, progress, and policies, as depicted in Figure 3.22. Additionally, Table 3.4 summarizes the left slope reduction in renovated and newly constructed buildings for different scenarios.

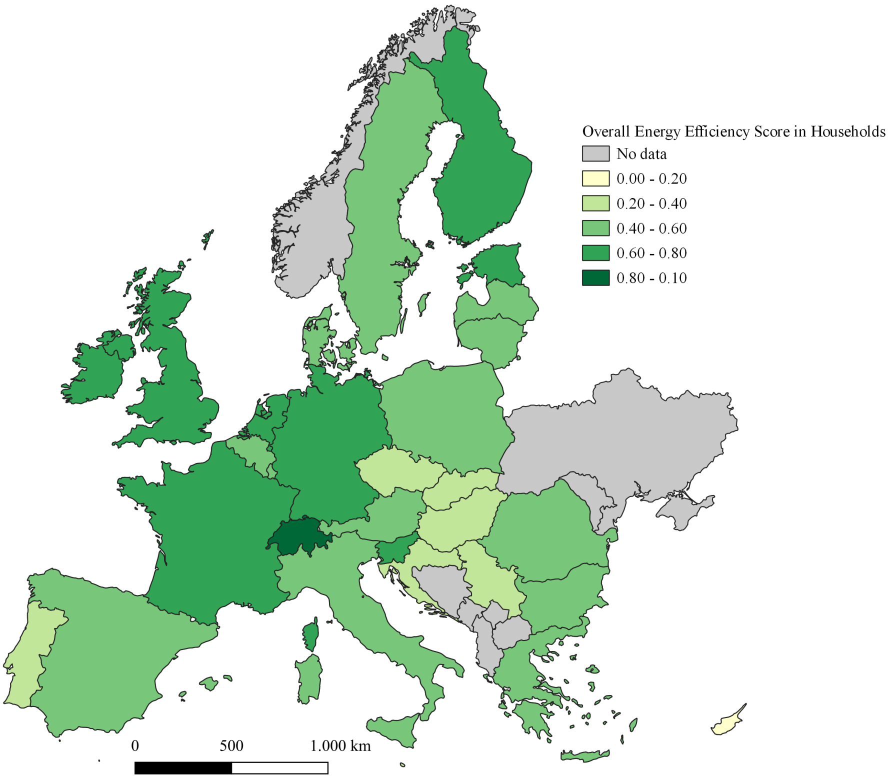

Figure 3.22.: ODYSSEE Energy Efficiency Score.

Table 3.4.: Future Left Slope value for renovated and new built buildings for different Scenarios

Building categories	S0	S1 and S3	S2 and S4
Renovated buildings	-	Reduction scaled according to ODYSSEE score	-0.049
New built buildings	-	-0.049	-0.030

Meanwhile, an alternative method, which considers the electrification rate and U value, is presented in the Appendix A.2. This method establishes a linear relationship between the electrification rate, U value, and the left slope, enabling the extrapolation of future left slope values. However, due to the data availability and the complexity of finding a representative U value for all building inventories in each study country, this method is not discussed in this section.

Future Right Slope

Concerning the right slope, the objective is to establish a statistical relationship between the right slope value and the space cooling penetration rate. This is achieved through a linear regression analysis, as illustrated in Figure 3.23, which presents a scatter plot and the results of the linear regression between the space cooling penetration rate and the right slope [8]. The results yield a p-value of 0.000002, and an R^2 score of 0.645, indicating a satisfactory fit given the limited sample size. The linear function is represented by Equation 3.23. This function is then used to obtain future right slope values once the future space cooling penetration rate is determined. In the defined scenarios with boosted space cooling usage, a linear increase in the space cooling penetration rate is assumed, reaching its full potential as defined in Section 3.2.1 and illustrated in Figure 3.16b until the year 2050. Subsequently, the rate remains constant.

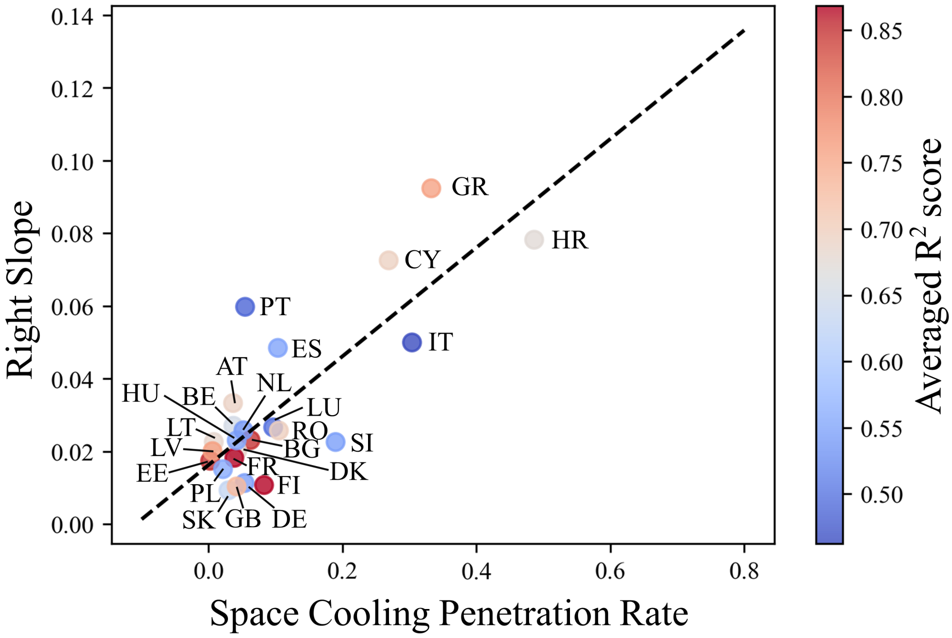

Figure 3.23.: Linear regression between space cooling penetration rate and right slope

$$m_{right} = 0.149 \cdot \beta + 0.016 \tag{3.23}$$

Where:

- m_{right} is the right slope value.
- β is the space cooling penetration rate.

---

[8] The correlation is showcased for countries within the available dataset due to data availability in space cooling penetration rates.

Meanwhile, it is also important to account for the impact of passive cooling. However, capturing its influence can be intricate. On one hand, research, such as that conducted by Alhuwayil et al. (2023), concludes that passive cooling is significantly more effective in warmer regions. On the other hand, while numerous studies focus on energy saving through passive cooling, there is a research gap in investigating how passive cooling influences the slope value in TRFs. To address these complexities, Italy is used as a benchmark due to its distinction of having the highest average summertime temperature across the years and regions across studied regions. This information is derived from temperature reanalysis data obtained from ERA5, as introduced in Section 2.2 and illustrated in Figure 3.24.

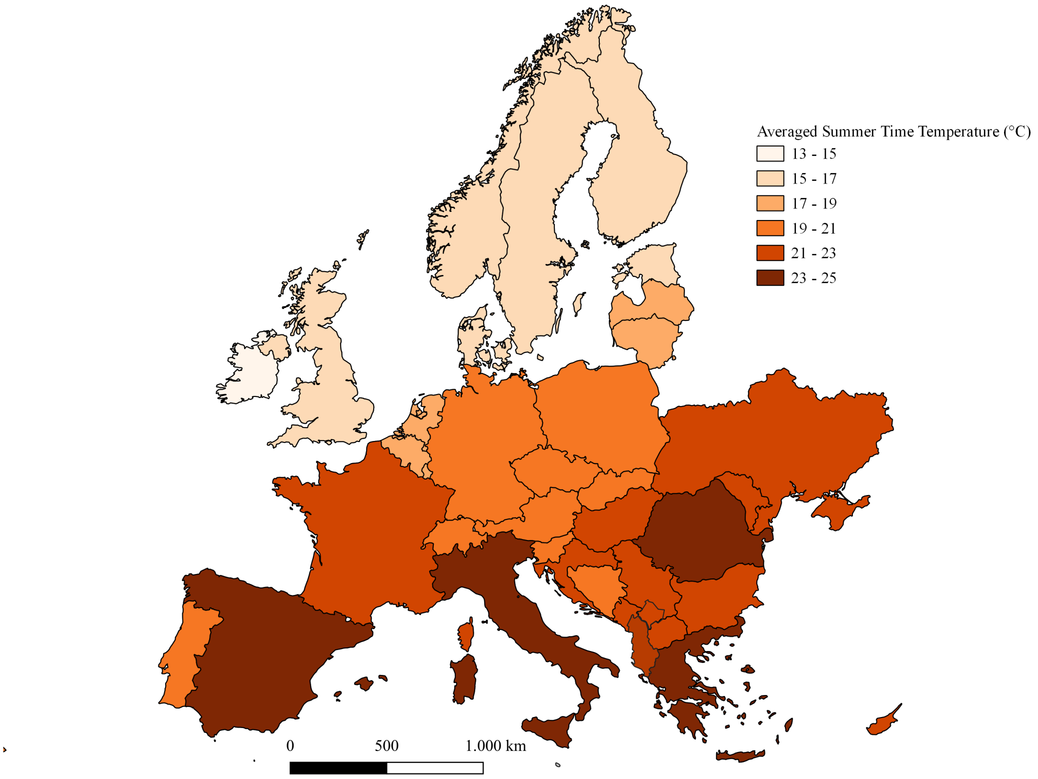

Figure 3.24.: Summertime temperature map.

In strict policy scenarios, it is assumed that passive cooling in new and renovated buildings in Italy can reduce the right slope value by 30% and 15%, respectively. The assumption of a 30% reduction in the right slope value is based on a review study by Song et al. (2021). Their comprehensive literature review assessed the energy-saving potential of various passive cooling measures. According to their findings, the reduction in energy consumption varies depending on the specific passive cooling method employed. For instance, energy consumption decreased by 8% to 70% with the use of external shading, by 37% with cool-colored paint roofs, by 25% with the creation of green spaces, by 7.88% with the construction of prismatic buildings, by 32% to 100% with vegetation-based walls, by 50% with Phase change material (PCM) based walls, by 33% with insulation incorporation into walls, by 10% to 20%

with buildings equipped with solar chimneys, and by 25% with radiative cooling systems. Given the significant variations among different passive cooling strategies, an average value of approximately 30% is used in this study for new buildings.

However, it is important to note that a 30% reduction in energy consumption does not equate to a 30% reduction in slope. Due to the lack of research on how passive cooling impacts slope values, this 30% reduction is assumed for this analysis. As for the renovated buildings, the assumption is that the level of energy savings achieved through passive cooling is lower compared to new buildings. Therefore, a 15% reduction of the right slope value for renovated buildings is assumed.

For moderate policy scenarios, a 15% reduction is assumed for new buildings, as it is posited that the effectiveness of passive cooling measures in these scenarios is lower than in strict policy scenarios. To account for regional variation in the effectiveness of passive cooling, the values assumed for Italy are scaled for other countries based on historically averaged summertime temperatures, as shown in Figure 3.24, which illustrates the average summertime temperatures across the research countries. In summary, the calculation of the right slope is presented in Table 3.5, using Italy as an example.

Table 3.5.: Future Right Slope reduction due to passive cooling for different Scenarios for Italy. Reductions for other countries are scaled based on the comparison of average summertime temperatures between these countries and Italy.

Building categories	S0	S1 and S3	S2 and S4
Renovated buildings	-	-	reduction of 15%
New built buildings	-	reduction of 15%	reduction of 30%

To summarize, Figure 3.25 depicts the approaches and input dataset employed in this section, aiming at constructing future TRFs and electricity demand time series.

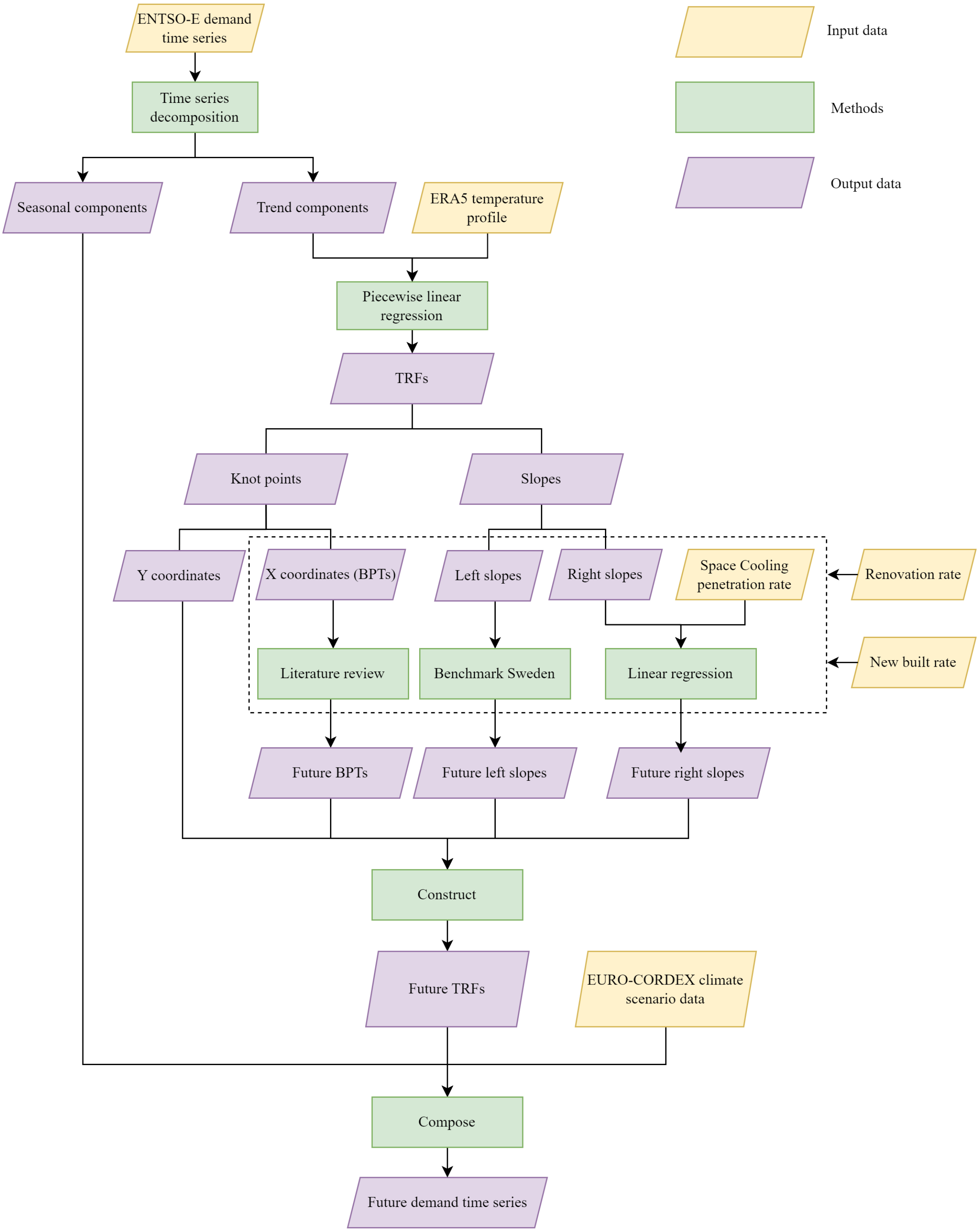

Figure 3.25.: Flow Chart illustrating the sequential steps for constructing future electricity demand time series

3.3. Generation of Synthetic Weather Years and Evaluation of System Robustness

3.3.1. Data and Model Description

To generate synthetic weather years and assess their impact on energy systems, this section outlines the time series data required for residual load calculation, including electricity demand and renewable energy generation time series. Additionally, it provides a description of the ESOM used in this dissertation.

Electricity Demand Time Series

To generate electricity demand time series data, the bottom-up approach described in the work by Slednev (2024) is employed. To ensure the demand time series reflects weather dependency, this method employs national energy balances derived from the "Distributed Energy" scenario from the Ten-Year Network Development Plan (TYNDP) 2022 (ENTSO-E, 2022), and focuses on fixed demands for electrical appliances, mobility services, and industrial processes. By using standard load profiles and time series data, this method can estimate electricity demand across various sectors while accounting for regional variations. The method has been calibrated with regional data and validated on an hourly basis against historical consumption patterns. The demand time series data are generated for a 30-year historical period spanning from 1991 to 2020.

Renewable Energy Generation Time Series

The renewable energy potential time series is generated using the global Energy Data Analysis Tool (EnDAT) (Scholz, 2012; Stetter, 2014). The time series also covers 30 historical years from 1991 to 2020. The process begins with an area analysis in EnDAT, where exclusion zones and area competition criteria are applied. Geographic constraints such as land cover, distance from settlements, elevation, protected areas, and others are considered alongside area suitability factors to assess the area potential for renewable energy generation. Wind speeds, solar irradiance, and temperatures are extracted for the identified areas from meteorological datasets. In the case of this dissertation, the database used is also the global ERA5 reanalysis data. Finally, power plant models of wind and PV plants are applied to calculate the capacities that can potentially be installed and the corresponding power generation time series. The data are initially calculated for each grid cell and then spatially aggregated to obtain renewable energy potentials at the national level.

To align the renewable generation and electricity demand time series with the system configuration used in this dissertation, both datasets are scaled based on renewable capacity values and demand levels derived from the FlexMex dataset. FlexMex is a model experiment dataset (Gils et al., 2022; Gardian et al., 2022). This publicly available dataset contains harmonized exogenous parameters, such as plant capacities, techno-economic factors, and heat demand, across 16 distinct test scenarios. These scenarios differ in terms of renewable energy capacity, the inclusion of endogenous capacity expansion options for flexibility, and the scope of technological components considered in the system (Gils et al., 2022).

Specifically, this study uses FlexMex scenario 4D, which incorporates endogenous flexibility capacities and assumes an IRE penetration level of 160% relative to annual electricity demand (Gils et al., 2022). The 160% IRE penetration is selected to account for losses and curtailment associated with renewable generation. This scaling approach produces hourly solar PV, onshore wind, offshore wind, and electricity demand profiles, as well as daily run-of-river generation data.

Residual Load Time Series

Residual load, defined as the difference between electricity demand and non-dispatchable power generation [9], is a key metric in this dissertation. Residual load can be calculated using the generated electricity demand time series and the renewable energy generation time series introduced in this section. A positive residual load indicates that demand exceeds power generation by non-dispatchable units, suggesting a potential electricity shortfall, while a negative residual load indicates surplus generation. Figure 3.26 presents the input demand, solar PV, onshore wind, offshore wind generation, and residual load time series for all study countries aggregated in the year 2020. To ensure consistency and comparability across all years, all time series in this section are standardized to 8760 hours per year, with February 29th removed from leap years in the analysis.

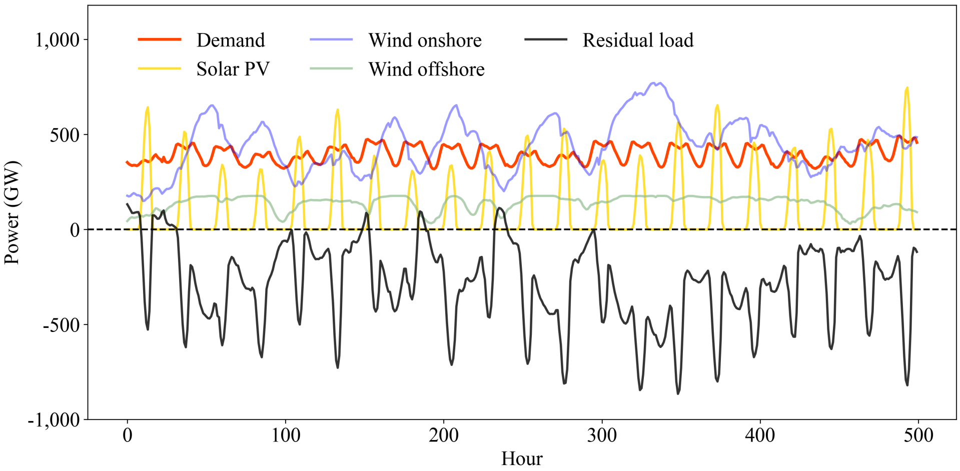

Figure 3.26.: The residual load, electricity demand, solar PV, wind onshore and offshore generation time series in the year 2020 for all study countries aggregated. For better visualization, only the first 500 hours are displayed.

---

[9] Run-of-river generation is excluded from the residual load calculation due to an assumed constant time series across all weather years and its relatively small contribution compared to other renewable technologies.

Energy System Optimization Model (ESOM)

To investigate the impact of different weather years on the energy system, the ESOM with the framework of REMix (Wetzel et al., 2024) is used. REMix is an open-source modeling framework designed to identify cost-optimal energy system configurations under a wide range of constraints. It supports the analysis of energy systems across nearly any temporal, spatial, and technological scale with a high level of detail. REMix can represent and connect a wide variety of processes, including extraction, storage, conversion, transmission, and demand, for multiple commodities, typically energy carriers such as electricity, gases, or heat. Each process within the model can be characterized by indicators such as cost, emissions, or efficiency. The mathematical core supports both integer and continuous decision variables, and the objective function can incorporate one or multiple performance indicators (Wetzel et al., 2024). In this dissertation, the model is configured to optimize system capacities and operations over a one-year period with hourly resolution, with the objective of minimizing overall system costs.

Besides the time series input data, other technological data used in this section are also derived from the FlexMex model experiment dataset. The time horizon of the model is set to 2050, and it considers 11 countries in Central Europe, corresponding to 11 model regions: Austria, Belgium, Denmark, Czech Republic, France, Germany, Italy, Luxembourg, the Netherlands, Poland, and Switzerland. The scope of the study includes a variety of technologies across different categories. For energy generation, the model includes PV, Onshore and Offshore Wind Turbines, Hydropower with Reservoir Storage and Run-of-River Hydropower. Gas-driven thermal power plants are split into two technology groups: Combined Heat and Power - Backpressure Combined Cycle Gas Turbines with Heat Extraction (CHP-ExCCGT) and Methane Gas Turbines (CH4-GT) for power production alone. Energy storage technologies considered in the model include Lithium-Ion Batteries, Hydrogen (H_2) Caverns, Hydrogen Tanks, Thermal Storage, along with Pumped Hydro storage. Heating technologies, such as District Heating with CHP-ExCCGT, Heat Pumps, Gas Boilers, and Electric Boilers are also included. Additionally, the model also accounts for Electric Vehicles (EVs) with uncontrolled charging and decentralized Hydrogen Electrolysis with flexible hydrogen production. Power transmission is modeled with an aggregated representation of the high-voltage electricity transmission network within the model scope. The model optimizes transmission capacities and power flows based on cost estimates from the Ten-Year Network Development Plan (TYNDP) (ENTSO-E, 2016).

3.3.2. Generation of Extreme Weather Years

This section describes the methodology applied to generate different synthetic extreme weather years and the model scopes for two different system setting scenarios and for evaluating the system robustness.

Intensity and duration score

The first method applied in the dissertation is identifying the most extreme weather years from the historical data. This process starts with establishing a ranking system to assess the extremity of each year, similar to the study conducted by Li et al. (2023b). The residual load time series are first aggregated across all 11 study countries before the analysis, enabling the examination of extreme conditions on a large scale. An extreme condition is defined as a residual load exceeding the 95th percentile of all hourly historical residual loads, which corresponds to approximately 153 GW. The "extreme periods" are any intervals where this threshold is exceeded. To quantify the extremity of each year, both the intensity and the duration of these extreme periods are assessed. While the duration is defined as the number of consecutive hours in which the residual load exceeds the 95th percentile threshold, the calculation of the intensity of extreme periods is described in Equation 3.24.

$$\mathrm{Int} = \sum_{i}^{\mathrm{Dur}} (\mathrm{R}_i - \mathrm{T}) \tag{3.24}$$

where,

- Int is the intensity of an extreme weather event
- Dur is the duration of an extreme event
- R_i is the residual load at the hour i
- T is the threshold for the extreme period, in this study, T is set to the 95th percentile of all historical residual load

Once the intensity and duration of extreme periods are calculated, each candidate year is ranked according to these two dimensions. To select the most extreme year, equal weight is assigned to both duration and intensity, similar to the study conducted by Li et al. (2023b), and these are combined to calculate a final score for each year. The year with the highest final score is chosen as the representative extreme historical year. Before calculating the final score, the duration and intensity values are normalized to a scale of 0 to 1 to ensure uniformity across all metrics.

Table 3.6 presents the intensity, duration, and final scores for each historical year. From this table, it is apparent that 1997 appears to be the most extreme year, both in terms of the intensity and duration of the events. Besides 1997, other relatively extreme historical years include 1991, 2006, 2002, and 2004.

Table 3.6.: Overview of the duration, intensity, and final scores for each historical year

Year	Duration Score	Intensity Score	Final Score	Year	Duration Score	Intensity Score	Final Score
1991	0.784	0.642	0.713	2006	0.728	0.686	0.707
1992	0.507	0.469	0.488	2007	0.440	0.308	0.374
1993	0.456	0.590	0.523	2008	0.000	0.000	0.000
1994	0.416	0.344	0.380	2009	0.355	0.341	0.348
1995	0.472	0.235	0.354	2010	0.533	0.335	0.434
1996	0.592	0.459	0.525	2011	0.499	0.381	0.440
1997	1.000	1.000	1.000	2012	0.480	0.502	0.491
1998	0.104	0.199	0.152	2013	0.435	0.378	0.406
1999	0.131	0.044	0.088	2014	0.523	0.427	0.475
2000	0.373	0.437	0.405	2015	0.184	0.388	0.286
2001	0.392	0.457	0.424	2016	0.573	0.447	0.510
2002	0.680	0.695	0.687	2017	0.336	0.560	0.448
2003	0.549	0.532	0.541	2018	0.312	0.183	0.247
2004	0.672	0.637	0.655	2019	0.035	0.008	0.021
2005	0.131	0.075	0.103	2020	0.269	0.214	0.242

Finkelstein-Schafer statistics method

The Finkelstein-Schafer (FS) statistic is a widely used method for measuring the distance between two cumulative distribution functions (CDFs) and is frequently used in the Sandia method (Hall et al., 1978a). The Sandia method evaluates nine critical climatic indices, including daily maximum, minimum, and mean dry bulb and dew point temperatures, daily maximum and mean wind speeds, and daily total horizontal solar radiation. This dissertation, however, focuses exclusively on the residual load time series.

The core concept of the developed method involves selecting 12 representative months, which are then aggregated to construct a representative year as illustrated in Figure 2.6. The selection of each representative month is based on the calculated distance between the CDF of that month in each historical year, referred to as the short-term CDF, and the CDF of all 30 historical years, referred to as the long-term CDF. This distance is measured using the FS statistic, as defined in Equation 3.25.

$$\mathrm{FS}(y,m) = \frac{1}{N}\sum_{i=1}^{N} |\mathrm{CDF}_m(x_i) - \mathrm{CDF}_{y,m}(x_i)| \tag{3.25}$$

where,

- FS represents Finkelstein-Schafer (FS) statistics
- x_i is an ordered sample value in a set of n observations sorted in ascending order
- y is the calendar year (for years 1991 to 2020 in this study)
- m is the calendar month
- N is the resampling rate of the CDF (in this analysis, it is set to 1000 per month).
- $\mathrm{CDF}_m(x_i)$ is the long-term CDF for the month m
- $\mathrm{CDF}_{y,m}(x_i)$ is the short-term (for the year y) CDF of the daily variable x for the month m

In the Sandia method, which aims at generating the TMY, the month with the smallest absolute FS value, indicating the closest match between the short-term and long-term CDFs, is selected as the representative month. However, this dissertation, which aims to identify a representative extreme year that captures the critical conditions for the energy system, adopts a different approach. In addition to selecting months with the smallest absolute FS values, months with the highest positive and negative FS values are also identified. These correspond to months with extremely high and low overall residual loads, respectively, as illustrated in Figure 3.27, which presents examples of both long-term and short-term CDFs for January.

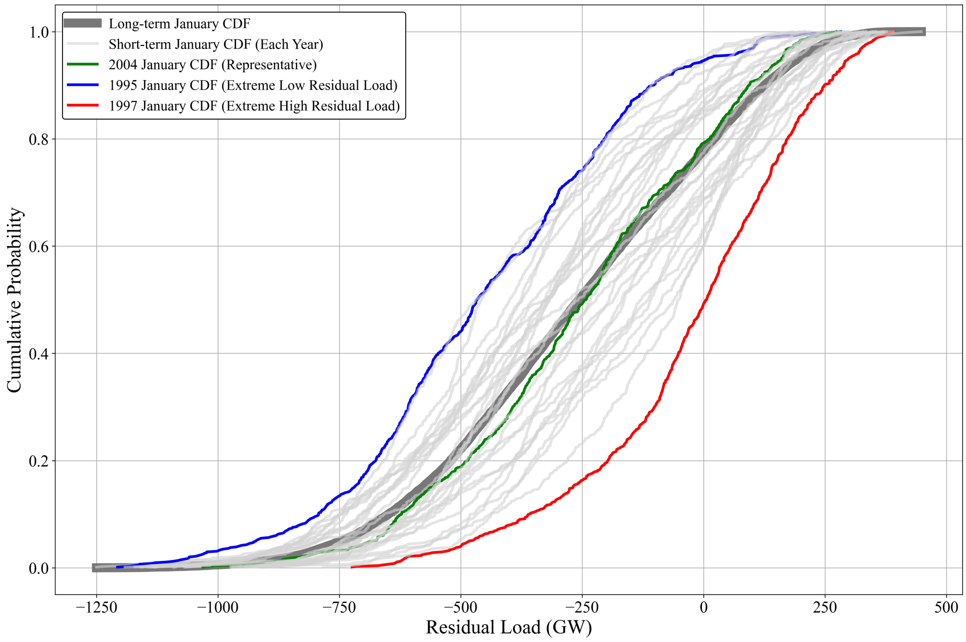

Figure 3.27.: Long-term and short-term CDFs for January. January 2004 is identified as the Typical Meteorological Month (TMM) due to its smallest absolute FS statistic. In comparison, January 1997 and 1995 represent an extreme high and low residual load month, respectively.

This approach enables the generation of three synthetic weather years:

- **TMY**: Typical Meteorological Year, representing historical average residual load conditions.
- **ELY**: Extreme Low Residual Load Year, representing overall low residual load.
- **EHY**: Extreme High Residual Load Year, representing overall high residual load.

After applying this procedure for each month, Table 3.7 presents the selected typical and extreme representative months for synthetic weather years TMY, ELY, and EHY. Once the representative months are identified, they are aggregated to construct the corresponding representative weather years. The generated TMY, ELY, and EHY are presented in Figure 3.28.

Table 3.7.: Selected typical and extreme representative months for synthetic weather years TMY, ELY, and EHY

	TMY	ELY	EHY
January	2004	1995	1997
February	2008	2002	1993
March	2002	1995	1996
April	2019	2003	1996
May	2014	2006	2008
June	2015	1991	2016
July	2005	2007	1994
August	2020	2008	1997
September	1999	2004	2014
October	1992	1998	2007
November	2001	2009	1993
December	1998	1993	1995

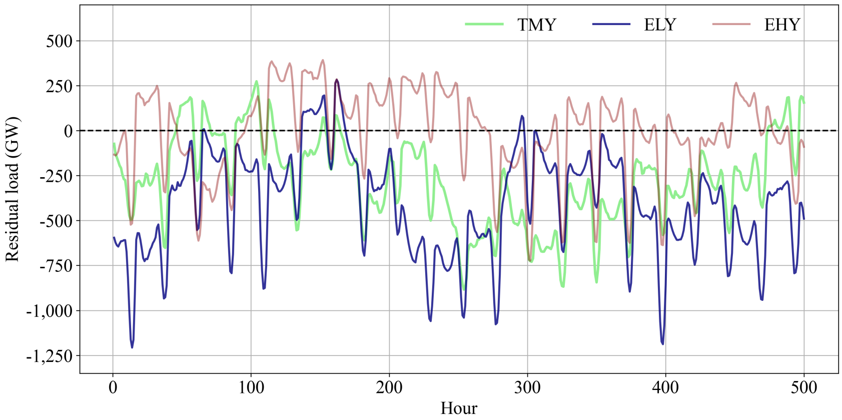

Figure 3.28.: TMY, ELY, EHY determined by the FS statistic method. For better visualization, only the first 500 hours are presented.

Extreme weather events method

In Section 3.3.2, the representative historical extreme weather year is identified based on the intensity and duration of extreme periods during which the residual load exceeds the 95th percentile. However, to better understand and assess extreme weather events and their impacts on energy systems, it is crucial to identify specific extreme weather events instead of simplifying them as periods exceeding the 95th percentile. The definition of such events, however, varies significantly across studies (Kittel and Schill, 2024) and often focuses on meteorological events like heatwaves or windstorms. For example, from an intensity perspective, Li et al. (2023b) defined extreme events as those surpassing the 95th percentile, while from a duration perspective, Mockert et al. (2023) characterized extreme events as lasting a minimum of two consecutive weeks.

This dissertation analyzes extreme weather events from the perspective of residual load, focusing on three duration phases: one day, one week, and two weeks. The aim is to identify the most extreme one-day, one-week, and two-week events across all historical years. To accomplish this, the most extreme events of each duration are first identified for every individual historical year, referred to as yearly extreme events. These events are defined as the periods within a year during which the maximum sum of consecutive residual load values occurs within a specified time window. For example, to determine the most extreme one-week event in 1997, a rolling window of one week (168 hours) is applied to calculate the consecutive residual load sums throughout the year. Figure 3.29 presents the resulting values for 1997 using this method. The maximum residual load sum for the one-week window is found to occur between hours 97 and 264, identifying this period as the most extreme one-week event for that year.

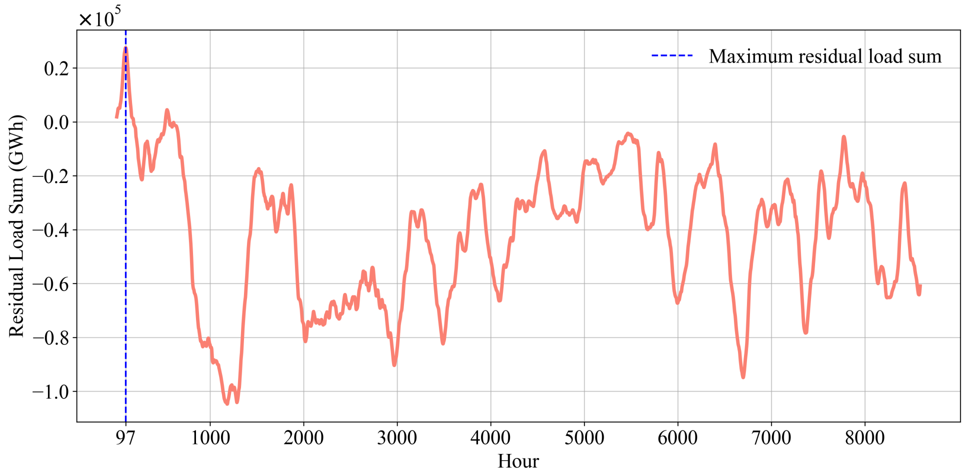

Figure 3.29.: Consecutive residual load sums for 1997, calculated using a one-week rolling window. The most extreme event begins at hour 97, marking the period with the highest cumulative residual load within this week.

After determining the yearly extreme events, a comparative analysis is conducted across all 30 historical years to determine the most extreme event overall, defined as the period with the highest residual load sum. Table 3.8 summarizes the most extreme one-day, one-week, and two-week events across all historical years. These identified extreme events are then used to replace the corresponding periods in the TMY and EHY years generated using the FS statistic method. This approach enables the generation of the following SWYs [10]:

- TMY_1D: TMY with the extreme one-day event

---

[10] No extreme one-week event is replaced in EHY because the most extreme one-week event occurs in January 1997, which is already represented in January of EHY.

- TMY_1W: TMY with the extreme one-week event
- TMY_2W: TMY with the extreme two-week event
- EHY_1D: EHY with the extreme one-day event
- EHY_2W: EHY with the extreme two-week event

Table 3.8.: The identified most extreme weather events among all historical years

Events type	Occured year	Starting hour	Ending hour
One-day Event	2017	8463	8486
One-week Event	1997	97	264
Two-week Event	2002	87	422

Meanwhile, Figure 3.30 showcases the differences by comparing TMY with TMY_1D, TMY_1W, and TMY_2W, as well as EHY with EHY_1D and EHY_2W.

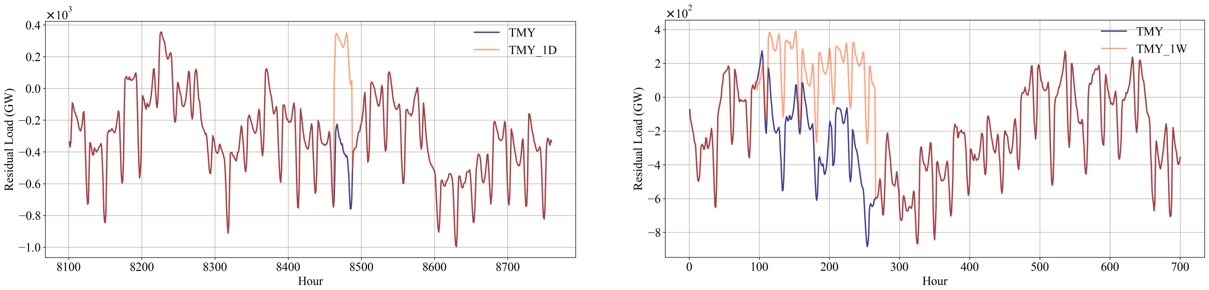

(a) Comparison between TMY and TMY_1D

(b) Comparison between TMY and TMY_1W

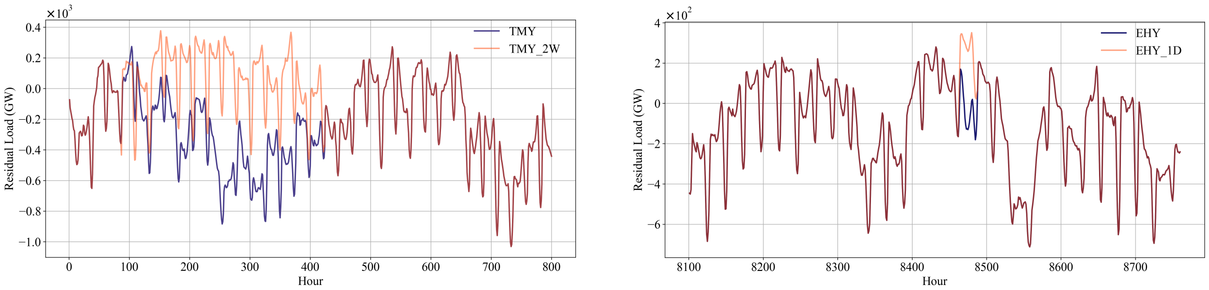

(c) Comparison between TMY and TMY_2W

(d) Comparison between EHY and EHY_1D

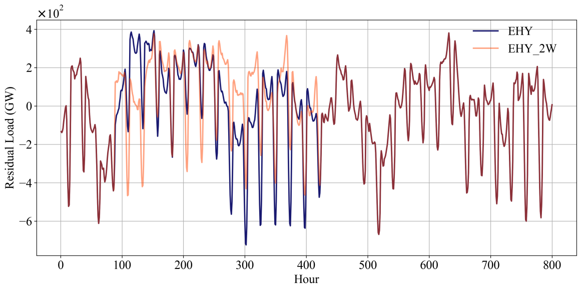

(e) Comparison between EHY and EHY_2W

Figure 3.30.: Comparison between the synthetic weather years generated from FS statistic method (TMY and EHY) and the synthetic weather years generated from extreme weather events method

3.3.3. System configuration scenarios

In this section, detailed overviews of the model scopes for two renewable capacity expansion scenarios are presented. Additionally, this section describes the methodology used to evaluate system robustness. The main difference between these two system configuration scenarios lies in whether the renewable technologies, namely solar PV, onshore wind, and offshore wind, are allowed to expand freely within the model. This distinction is important not only because it affects the cost-optimal system configuration, but also because it determines the residual load. In the scenario with flexible capacity expansion for renewables, the residual load can only be calculated after the optimization process is completed.

System Configuration Scenarios

In the Exogenous-RE scenario, the energy system model is analyzed by fixing the capacities for solar PV, onshore wind, and offshore wind according to the values specified in FlexMex Scenario 4D. By applying fixed renewable capacities, this scenario reflects predefined political objectives, such as National Development Plans. Table 3.9 presents the derived capacity values for solar PV, onshore wind, and offshore wind across the countries included in the dissertation. The model scope for the Exogenous-RE scenario is illustrated in Figure 3.31a.

Table 3.9.: The capacity values (GW) for renewable energy in the Exogenous-RE scenario, derived from the FlexMex Scenario 4D.

Country	Solar PV	Wind Onshore	Wind Offshore
Austria	48.8	43.6	0
Belgium	184.1	12.7	11.2
Switzerland	86.2	28.3	0
Czech Republic	38.3	54.0	0
Germany	419.8	233.8	143.9
Denmark	17.7	26.1	1.2
France	279.8	439.9	0
Italy	247.4	247.2	0
Luxembourg	12.4	1.4	0
Netherlands	98.2	21.3	51.2
Poland	77.2	107.0	0

In contrast, the Endogenous-RE scenario allows for the endogenous determination of solar PV, onshore wind, and offshore wind capacities. In this scenario, the system optimizes the capacities of renewable energy sources, storage, and flexibility options to minimize overall system costs. This scenario enables the model to explore the most cost-effective combination of renewable and conventional generation, storage, and flexibility solutions to meet system needs, as shown in Figure 3.31b. Meanwhile, the lower bound values are also assigned to renewable capacities derived from the International Renewable Energy Agency (IRENA) Renewable Capacity Statistics 2023 (IRENA, 2023) to ensure a minimum level of renewable energy generation is maintained.

A key challenge in the Endogenous-RE scenario, in contrast to the Exogenous-RE scenario, is that renewable capacities are not predetermined. Since renewable generation is dependent on the installed capacity, the renewable generation time series cannot be determined until the optimization process of the energy system model is finished. Consequently, the residual load can only be calculated after the optimization process is completed. However, it is important to note that the generation of synthetic weather years is still based on residual load values derived from exogenous capacity factors in the Exogenous-

RE scenario. As a result, the same synthetic weather years are used for both the Endogenous-RE and Exogenous-RE scenarios.

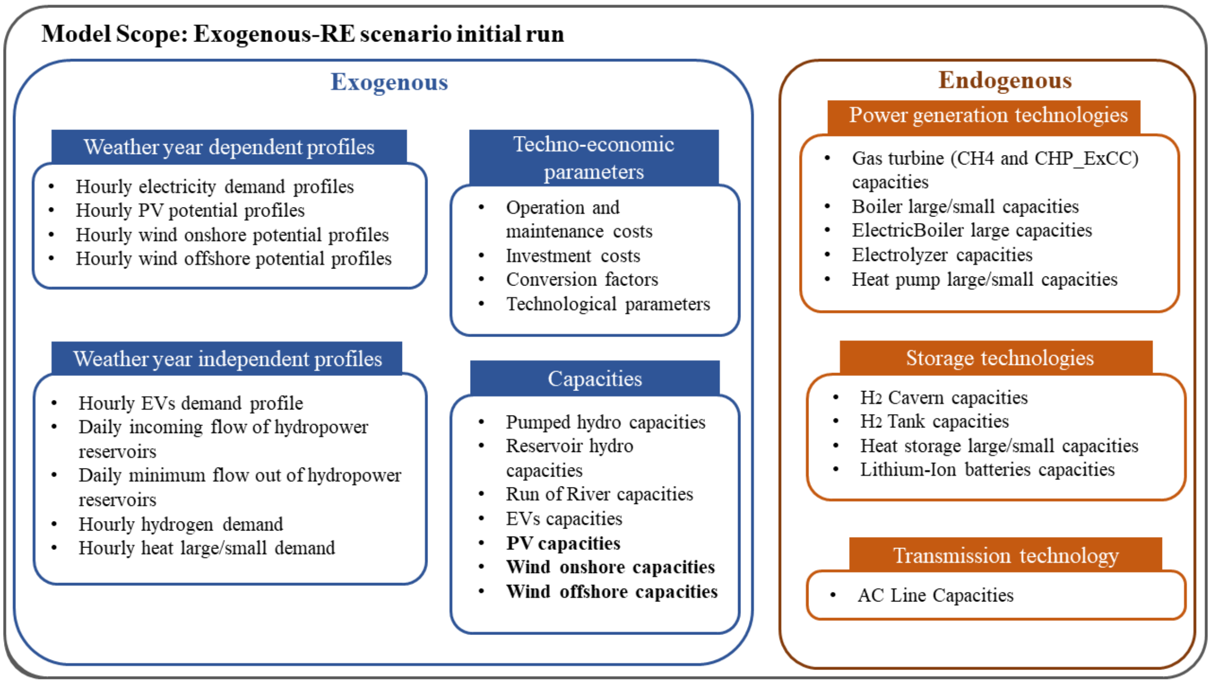

(a) Exogenous-RE scenarios

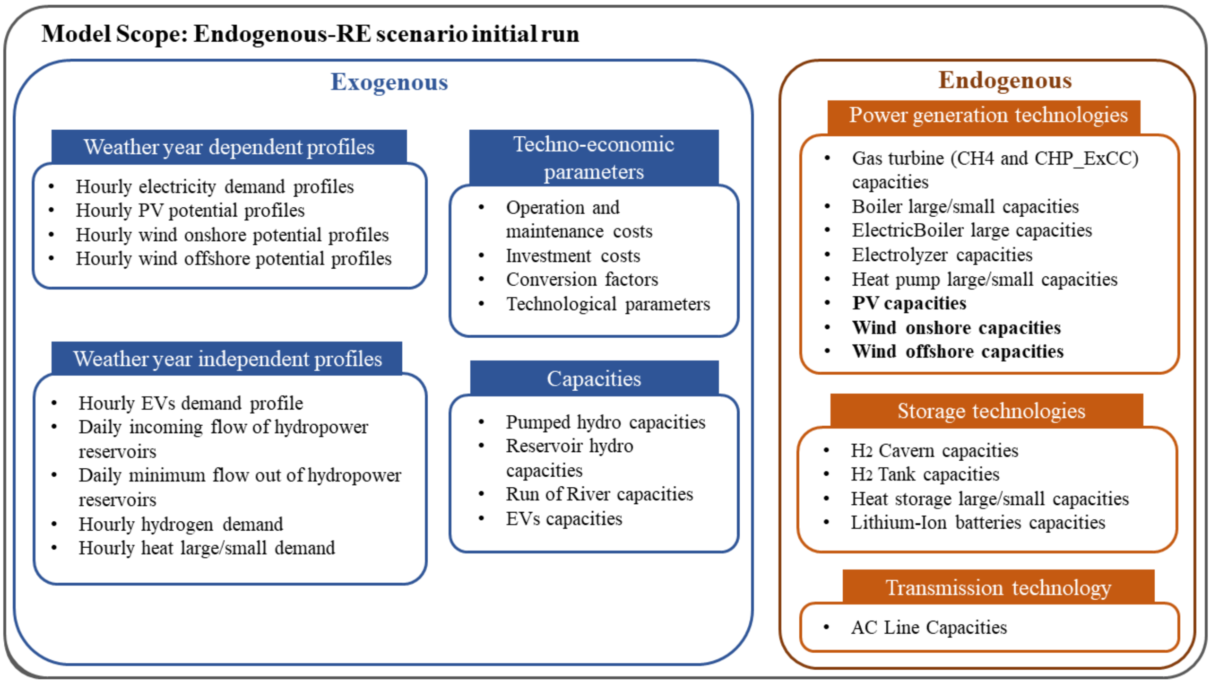

(b) Endogenous-RE scenarios

Figure 3.31.: The model scope of Exogenous-RE and Endogenous-RE expansion scenarios.

System Robustness Evaluation Framework

This section describes the process for assessing whether a system configuration can accommodate the conditions of a specific historical year. The process is carried out in two steps using the ESOM REMix.

For instance, to evaluate whether the system configuration of year A can accommodate the weather conditions of year B, the weather year-dependent time series of year A, including demand, solar PV, and wind onshore and offshore profiles, are first input into either the Exogenous-RE or Endogenous-RE scenario, as outlined in Section 3.3.3. This process allows for the determination of the required capacities for various energy generation, storage, and transmission technologies for year A.

In the second step, the capacities of all technologies, including generation, storage, and transmission lines, are fixed based on the values derived from year A. The weather year-dependent time series of year B are then input to assess whether the system can accommodate the energy demand under the conditions of year B. To avoid infeasibilities, slack variables are introduced into the model. The slack costs for commodities such as electricity, heat, and hydrogen are set considerably high, ensuring that the optimizer only uses slack when there is no other way to supply demand. If slack appears in the resulting optimal system operation, it indicates that the system configuration optimized for year A is insufficient for year B, and vice versa. This is also reflected in a significant increase in system costs due to high slack costs. The model scope for this framework is illustrated in Figure 3.32.

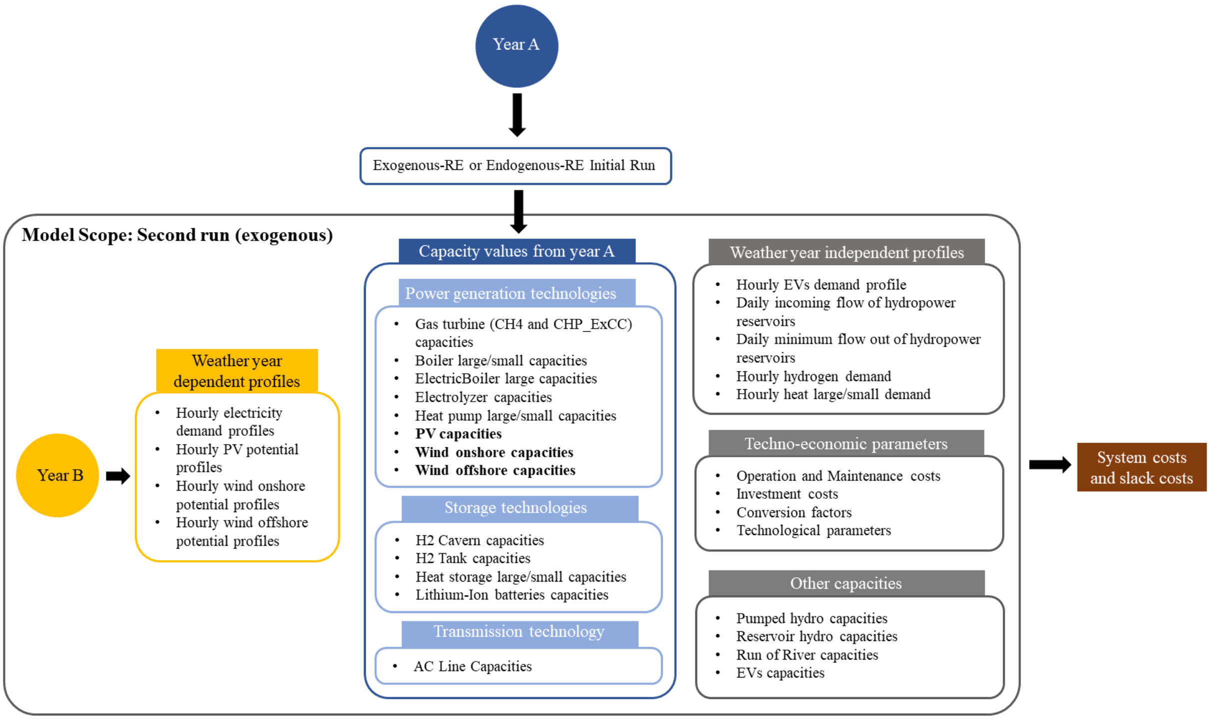

Figure 3.32.: The model scope for the framework to evaluate the system robustness. This framework is used to determine whether the system configuration of year A can accommodate the weather conditions of year B.

4. Results and Discussion

This chapter presents the results and discussion related to the three key uncertainties addressed in this dissertation: the spatial resolution of wind data, the dynamics of electricity demand under various climate and policy intervention scenarios, and the robustness of energy system designs under extreme weather conditions. The findings are based on the author's published and submitted papers.

4.1. Comparison and Validation of Downscaled Wind Speed Data

This chapter focuses on the results of the statistical downscaling of ERA5 wind speed data, as detailed in the author's publication 'Downscaling ERA5 wind speed data: A machine learning approach considering topographic influences' published in *Environmental Research Letters*.

4.1.1. Topographic Classification Results

In the preprocessing classification phase of the regression-based statistical downscaling approach, a Random Forest Classification process is first conducted to classify the terrain types based on the quality of ERA5 data. The results indicate that the Random Forest Classification Model yields a model accuracy of 0.76 for the entire testing data set, meaning that 76% of the samples are correctly classified by the model. However, when specifically considering Class 3 stations, the model accuracy increased to 0.90. Figure 4.1 compares the relative significance of each input feature. This plot showcases the relative importance of different features in predicting the station classes. The analysis reveals that 75 km Radius TPI has the most pronounced impact on the local-scale wind speed, with Elevation, 5 km Radius TPI, TDI, Slope, and Aspect following in that order. This suggests that among the various topographic metrics, 75 km Radius TPI has the strongest correlation with the predicted station classes, and therefore, plays the most significant role in determining the ERA5 quality. This also explains why TPI is widely used in wind-related studies (Weiss, 2001; Winstral et al., 2017; Solbakken et al., 2021; Molina et al., 2021).

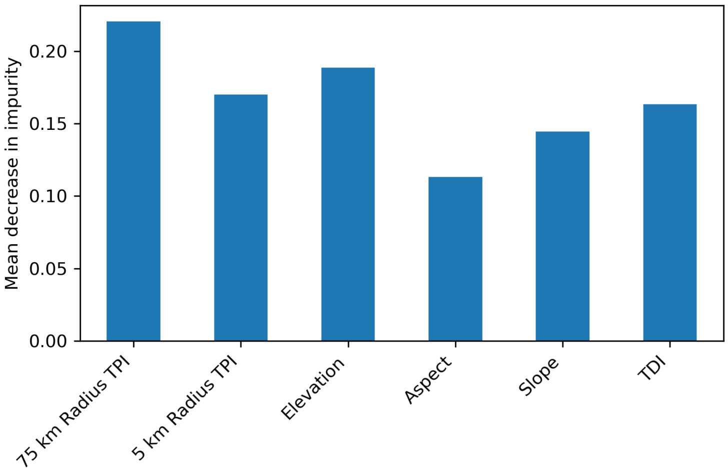

Figure 4.1.: Feature importance plot for the Random Forest Classification trained on all the available observation stations.

Furthermore, the Random Forest Classification Model can be applied to predict the ERA5 quality for regions where no observational data is available. Using topographic metrics derived from the DEM, a comprehensive map of ERA5 quality predictions for Europe can be generated. This process involves first extracting key topographic features, including elevation, slope, aspect, 75 km and 5 km radius TPI, and TDI, from the DEM for each grid cell. These topographic metrics serve as input features to the trained Random Forest Model, which classifies regions into three ERA5 quality classes (Class 1, Class 2, and Class 3) based on predicted biases. The model can then be applied to the entire region, generating a gridded map where each pixel is classified according to the predicted ERA5 quality.

The resulting map, presented in Figure 4.2, visually represents the distribution of ERA5 accuracy across Europe, with each pixel categorized by the level of bias predicted. Regions are classified into three categories: Class 1 (small biases in ERA5), Class 2 (moderate biases), and Class 3 (significant biases). Since the map is generated using the DEM, its spatial resolution corresponds to that of the DEM, approximately 1 km by 1 km. From this map, it is evident that much of Europe falls into the Class 1 category, indicating relatively flat and homogeneous terrain. However, areas such as the Alps, the Pyrenees, the Scandinavian Mountains in western Norway, and the Balkans are classified as Class 2 or Class 3. This classification is consistent with the diverse and mountainous topography of these regions, where more complex terrain results in greater biases in ERA5 data.

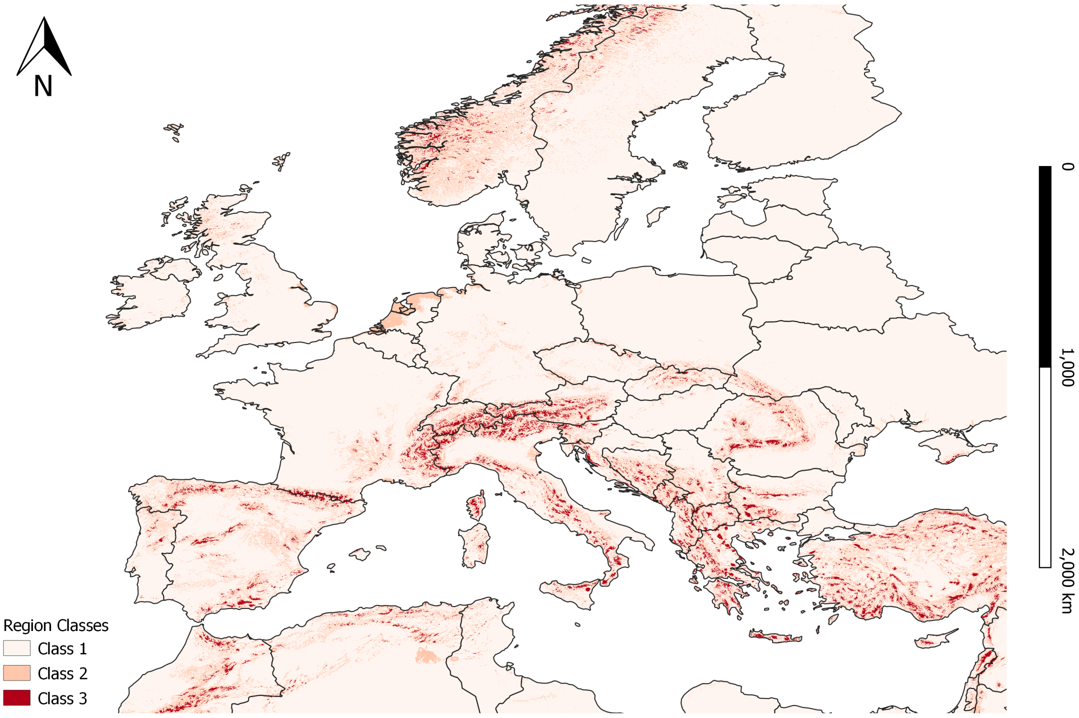

Figure 4.2.: Map displaying the prediction of region classes after implementing the Random Forest Classification method across Europe.

4.1.2. Model Generalization and Regression Performance

To assess whether a Machine Learning Model is prone to overfitting, it is important to compare its performance on both training and testing datasets. When the error rates for both datasets are similar, it indicates that the model has successfully generalized to unseen data, rather than overfitting to the training data. Therefore, in this dissertation, the statistical metrics for both training and testing datasets of the Machine Learning Model are compared, as summarized in Table 4.1. The results reveal that all four statistical metrics (RMSE, PCC, R^2, KSD) for the training and testing datasets are similar, which suggests that the model has generalized effectively and is not overfitting.

Table 4.1.: Comparison of statistical metrics (RMSE, PCC, R^2, KSD) for training and testing data for different classes in the Machine Learning Model.

Class	RMSE (m/s)		PCC		R^2		KSD	
	training	testing	training	testing	training	testing	training	testing
Class 1	0.85	0.85	0.76	0.76	0.58	0.58	0.23	0.23
Class 2	1.33	1.35	0.72	0.72	0.52	0.52	0.30	0.30
Class 3	2.08	2.12	0.82	0.81	0.67	0.66	0.19	0.19

Meanwhile, Table 4.2 presents the improvements achieved through the regression process. The table compares the statistical indicators between the observed wind speed, ERA5, COSMO-REA6, and the corrected wind speed time series obtained from the Machine Learning Model. The statistical metrics are averaged across all stations in each class. From this table, it is evident that for both Class 1 and Class 2 stations, the corrected wind speed time series show improvements over both ERA5 and COSMO-REA6, with better performance in terms of RMSE, PCC, and R^2. However, it is observed that the KSD worsens slightly. This is likely due to the fact that for Class 1 and Class 2 stations, the ERA5 data is already relatively accurate, meaning the introduction of the Machine Learning Model does not lead to substantial improvements in distribution alignment. As a result, the model's adjustments might inadvertently cause a shift in the predicted distribution, making it slightly diverge from the already good ERA5 data, which increases the KSD.

The most significant improvements are seen in Class 3 stations, where the model exhibits a substantial reduction in RMSE, from 4.22 $\mathrm{m/s}$ for ERA5 and 4.03 $\mathrm{m/s}$ for COSMO-REA6 to 2.05 $\mathrm{m/s}$. PCC increases from 0.47 (ERA5) and 0.51 (COSMO-REA6) to 0.73, R^2 rises from 0.22 (ERA5) and 0.26 (COSMO-REA6) to 0.53, and KSD decreases from 0.59 (ERA5) and 0.40 (COSMO-REA6) to 0.24. These results clearly indicate a great improvement in the regression model's ability to correct for the biases of ERA5 in Class 3 regions.

Table 4.2.: Comparison of statistical metrics (RMSE, PCC, R^2, KSD) across the stations for each class between observations and three datasets: the original ERA5, COSMO-REA6, and the corrected wind speed time series obtained from the Machine Learning Model.

Class	Statistic metrics	ERA5	COSMO-REA6	Corrected
Class 1	RMSE (m/s)	1.03	1.39	0.84
	PCC	0.54	0.59	0.67
	R^2	0.29	0.35	0.49
	KSD	0.20	0.18	0.35
Class 2	RMSE (m/s)	1.70	1.58	1.32
	PCC	0.52	0.62	0.65
	R^2	0.27	0.38	0.42
	KSD	0.25	0.09	0.36
Class 3	RMSE (m/s)	4.22	4.03	2.05
	PCC	0.47	0.51	0.73
	R^2	0.22	0.26	0.53
	KSD	0.59	0.40	0.24

To visually demonstrate these improvements, Figure 4.3 presents scatter plots and histograms for a randomly selected station in each class. For Class 1 and Class 2 stations, such as REH and HAI, the correction leads to only minor improvements in wind speed accuracy. In contrast, for Class 3 station DOL, the scatter plot of the corrected wind speed aligns much closer with the diagonal line, and the histogram distribution more closely resembles the observations compared to ERA5 and COSMO-REA6 data. Meanwhile, the scatter plots and histograms of the original ERA5 and COSMO-REA6 indicate an underestimation of the wind speed. These comparisons suggest a significant reduction in biases and a better agreement with the observations for the corrected wind speed, particularly for Class 3 station DOL.

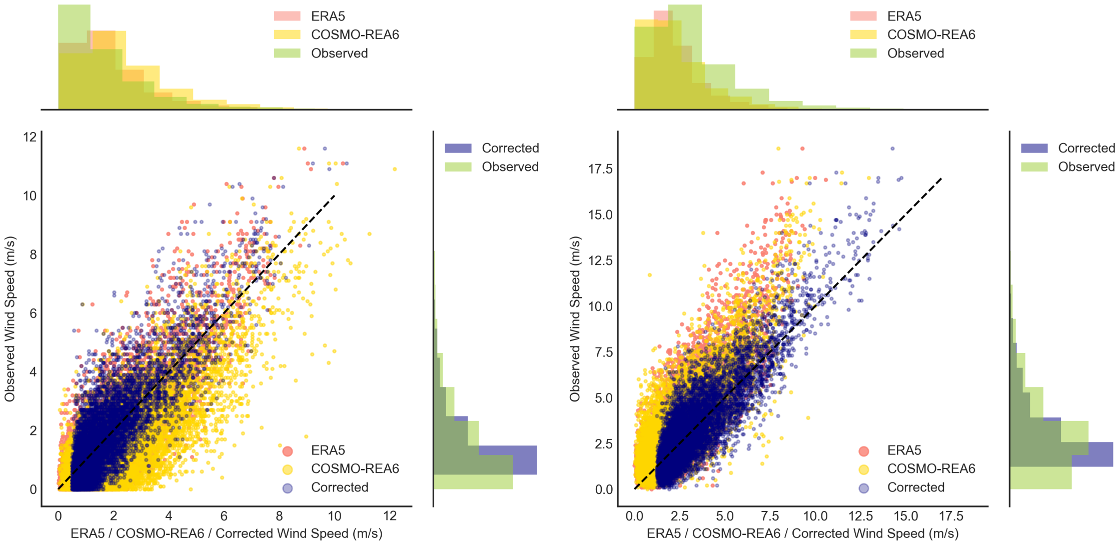

(a) Station REH in Zürich Affoltern (Class 1)

(b) Station HAI in Salen-Reutenen (Class 2)

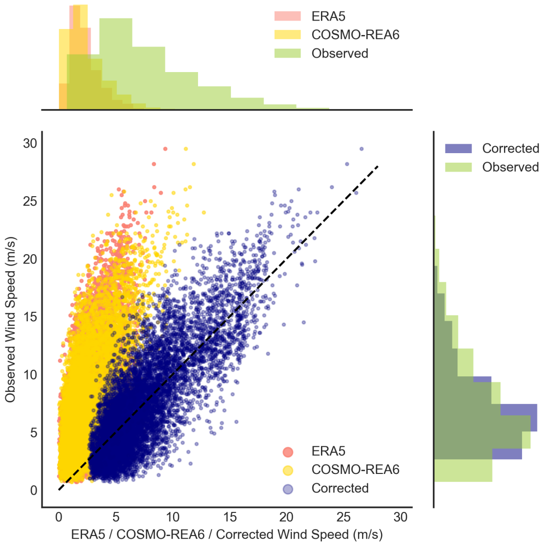

(c) Station DOL at the mountain peak La Dôle (Class 3)

Figure 4.3.: Scatter plots and histograms comparing observations with three datasets (original ERA5, COSMO-REA6, and corrected wind speed) are shown for three MeteoSwiss stations

Meanwhile, the extent to which various input features impact the target variables is demonstrated in Figure 4.4. The plot showcases the relative importance of different features in predicting the wind speed time series at the local scale. The result indicates that ERA5 wind speed is the most dominant feature among all classes, and its importance significantly surpasses all other features in Class 1 and Class 2 regions. However, this is not observed in Class 3 regions, where the influences of all features are more evenly distributed. For Class 3 regions, GWD is the second most crucial predictor, following ERA5 wind speed, and is followed by 75 km Radius TPI, 5 km Radius TPI, and wind direction.

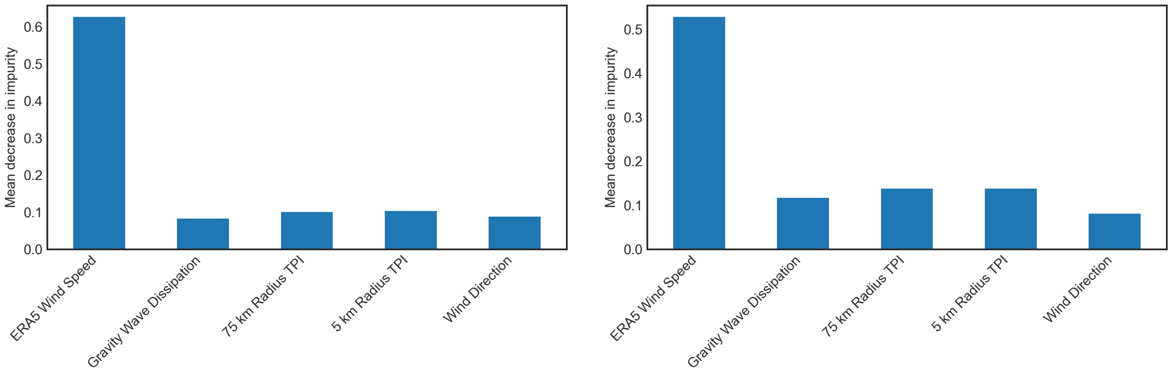

(a) Class 1

(b) Class 2

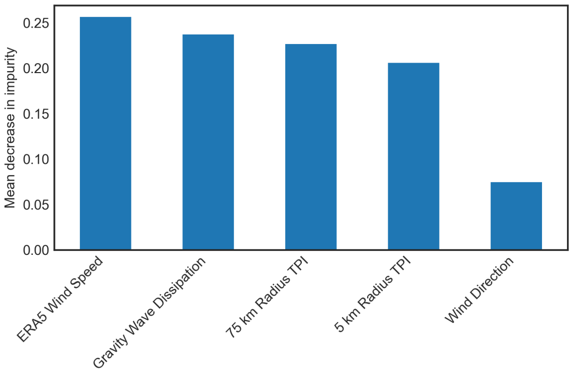

(c) Class 3

Figure 4.4.: Feature importance plot for the XGBoost regression process for each class.

4.1.3. Cross-dataset Validation

To assess the robustness of the regression model, a comprehensive cross-dataset validation is conducted using two distinct approaches. Cross-dataset validation is important because it helps assess the model's ability to perform well across different datasets, ensuring that the model is not overfitting to a specific dataset or time period. First, the model is applied to all MeteoSwiss weather stations, using data from different years to evaluate its generalizability over time. This approach examines if the downscaling approach can maintain its performance when applied to data from different time periods, accounting for potential temporal variations. Secondly, the approach is tested using data from the DWD observations to evaluate the model's ability to generalize across different geographic locations.

Cross-dataset Validation Across Different Years

The first cross-dataset validation validates the model across different years, testing its robustness and ability to generalize to unseen historical data.

To acquire the downscaled wind speed time series for MeteoSwiss observation stations across multiple years, the following procedure is implemented. First, the ERA5 wind speed time series for the test year is obtained, serving as the time-dependent input feature. In addition to this time-dependent feature, time-independent features, including topographic metrics that were already collected and calculated during the model training phase, are input together into the previously trained regression model. The model then generates the corrected wind speed for the given year. It is important to note that this process does not involve training the model on new data. Rather, it uses the existing model to make new predictions based on the updated input features.

The results of the cross-validation are summarized in Table 4.3, which presents the downscaling approach applied to the years 2017 and 2019. From the table, it is clear that the downscaling method improves the RMSE, PCC, and R^2 for Class 1 and Class 2 stations, though KSD does not show similar improvement. This is similar to the results observed when training the model with 2018 data. However, Class 3 stations show significant improvements in both 2017 and 2019. Specifically, in 2017, RMSE decreases from 5.03 m/s for ERA5 and 4.56 m/s for COSMO-REA6 to 2.48 m/s, PCC increases from 0.54 (ERA5) and 0.51 (COSMO-REA6) to 0.77, R^2 rises from 0.28 (ERA5) and 0.26 (COSMO-REA6) to 0.59, and KSD decreases from 0.62 (ERA5) and 0.48 (COSMO-REA6) to 0.18. Similar improvements are observed in 2019, where RMSE decreases from 5.18 m/s (ERA5) and 4.64 m/s (COSMO-REA6) to 2.45 m/s, PCC increases from 0.55 (ERA5) and 0.54 (COSMO-REA6) to 0.78, R^2 increases from 0.30 (ERA5) and 0.29 (COSMO-REA6) to 0.61, and KSD decreases from 0.62 (ERA5) and 0.48 (COSMO-REA6) to 0.15. These results demonstrate the model's robustness when applied to independent datasets.

Table 4.3.: Comparison of statistical metrics (RMSE, PCC, R^2, KSD) across the stations for each class in 2017 and 2019 between observations and three datasets: the original ERA5, COSMO-REA6, and the corrected wind speed time series.

Class	Statistic metrics	ERA5		COSMO-REA6		Corrected	
		2017	2019	2017	2019	2017	2019
Class 1	RMSE (m/s)	1.03	1.10	1.41	1.45	0.92	0.95
	PCC	0.51	0.61	0.57	0.57	0.61	0.72
	R^2	0.26	0.37	0.32	0.32	0.37	0.52
	KSD	0.21	0.11	0.22	0.18	0.37	0.23
Class 2	RMSE (m/s)	1.64	1.77	1.52	1.63	1.41	1.40
	PCC	0.50	0.57	0.61	0.60	0.60	0.70
	R^2	0.25	0.32	0.37	0.36	0.36	0.49
	KSD	0.24	0.20	0.07	0.08	0.41	0.29
Class 3	RMSE (m/s)	5.03	5.18	4.56	4.64	2.48	2.45
	PCC	0.53	0.55	0.51	0.54	0.77	0.78
	R^2	0.28	0.30	0.26	0.29	0.59	0.61
	KSD	0.62	0.62	0.48	0.48	0.18	0.15

A visual representation of these results is provided in Figure 4.5, which includes scatter plots and histograms for three representative stations, and Figure 4.6, which displays time series plots. Due to limited data availability in COSMO-REA6 after August 2019, the comparison for the year 2019 is focused on the first 8 months. Figure 4.5 illustrates that the Class 1 station REH exhibits the smallest improvement, while the Class 2 station HAI shows a moderate improvement. In comparison, the Class 3 station DOL demonstrates a substantial improvement in both 2017 and 2019, as the scatter plots of the corrected wind speed more closely align with the diagonal line, and the histogram distributions more accurately reflect the observed values compared to ERA5 and COSMO-REA6 data. This suggests a significant reduction in biases and a better agreement with the observations. Similarly, Figure 4.6 reveals a stronger overlap between the corrected wind speed and observational data for Station DOL in both years, further revealing the significant reduction in biases.

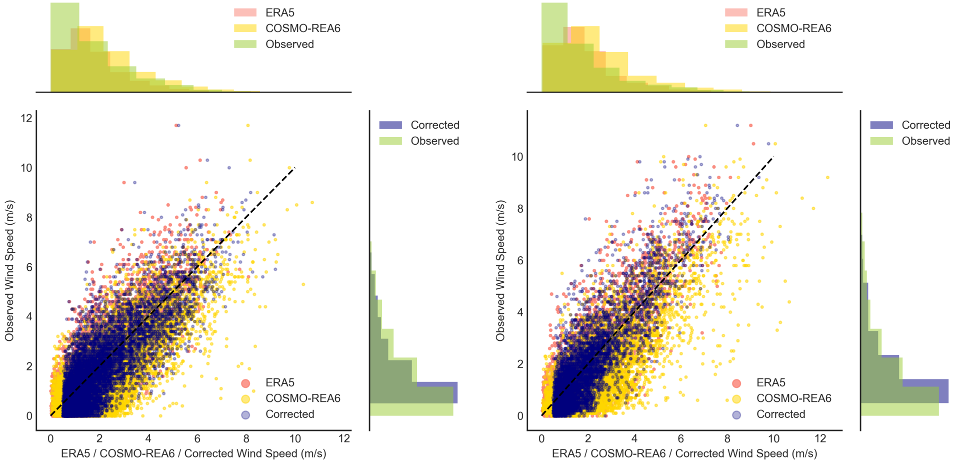

(a) Station REH (Class 1) in 2017
(b) Station REH (Class 1) in 2019

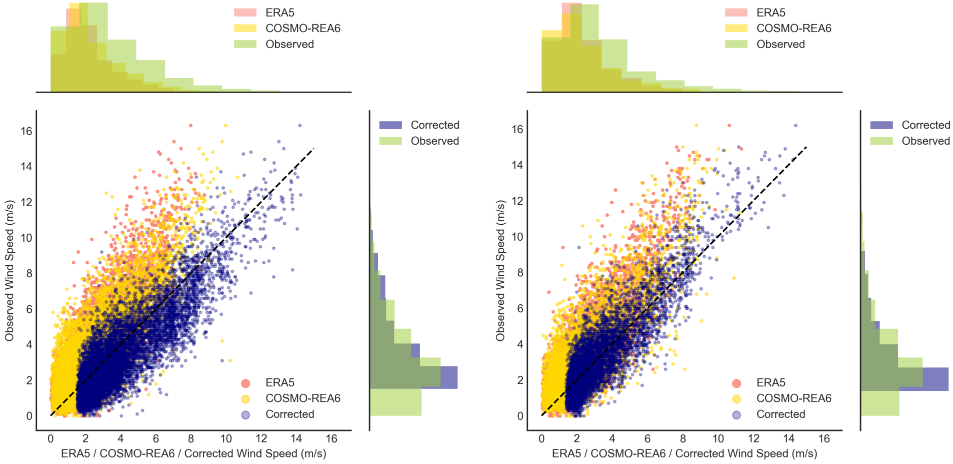

(c) Station HAI (Class 2) in 2017
(d) Station HAI (Class 2) in 2019

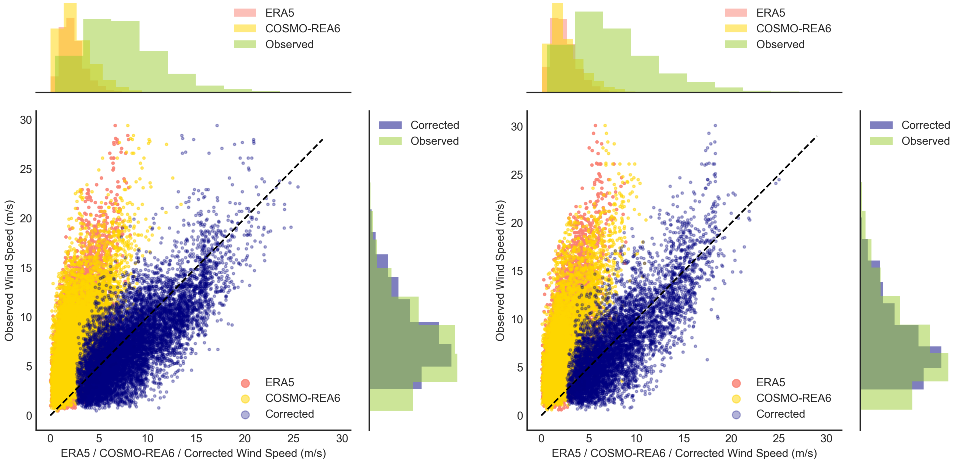

(e) Station DOL (Class 3) in 2017
(f) Station DOL (Class 3) in 2019

Figure 4.5.: The scatter plots and histograms compare observations with three datasets (original ERA5, COSMO-REA6, and corrected wind speed) in 2017 and 2019.

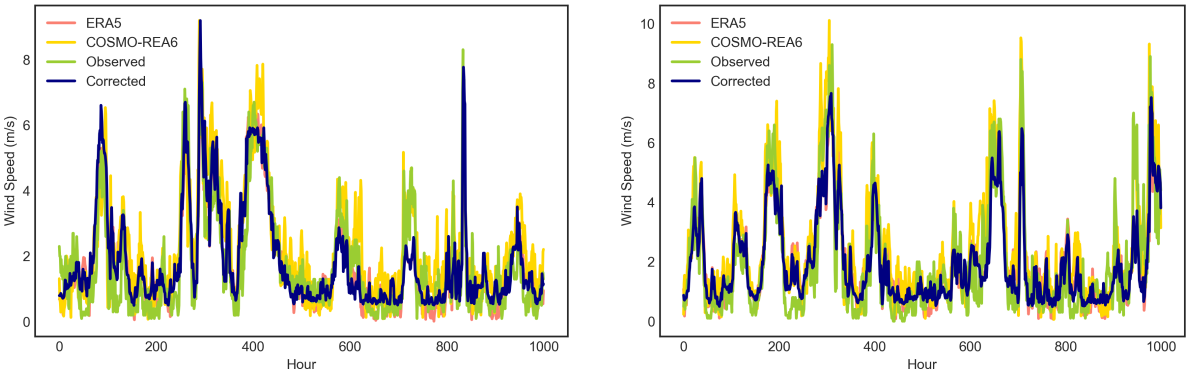

(a) Station REH (Class 1) in 2017

(b) Station REH (Class 1) in 2019

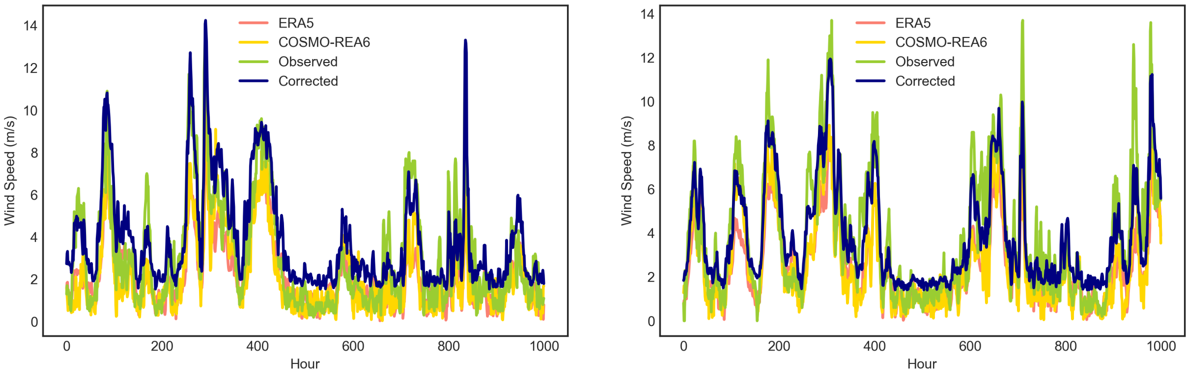

(c) Station HAI (Class 2) in 2017

(d) Station HAI (Class 2) in 2019

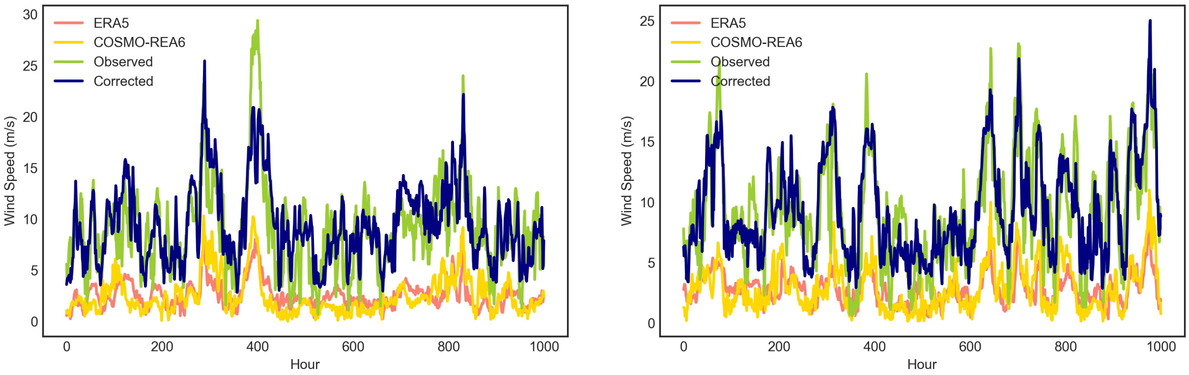

(e) Station DOL (Class 3) in 2017

(f) Station DOL (Class 3) in 2019

Figure 4.6.: Time series plots in 2017 and 2019 for the observations, original ERA5, COSMO-REA6, and the corrected wind speed. For clarity, only the first 1000 hours are displayed.

Cross-dataset Validation Across Different Locations

The second cross-dataset validation is conducted across different locations. For this, cross-validation with DWD observation stations is performed by first calculating the input features at the locations of the DWD stations. These features include the large-scale ERA5 time series and the corresponding topographic metrics of the DWD stations. The computed features are then fed into the previously trained regression model to generate the corrected wind speed time series for DWD stations. Similar to Section 4.1.3, this procedure does not involve retraining the model but rather applying it to new data for validation.

The results are presented in Table 4.4. This table shows significant improvement in Class 3 stations, with RMSE reducing from 5.07 m/s of ERA5 and 4.84 m/s of COSMO-REA6 to 2.77 m/s, PCC increasing from 0.69 (ERA5) and 0.71 (COSMO-REA6) to 0.76, R^2 increasing from 0.48 (ERA5) and 0.50 (COSMO-REA6) to 0.58, and KSD decreasing from 0.62 (ERA5) and 0.47 (COSMO-REA6) to 0.21. However, this improvement is not reflected in Class 2 and Class 1 stations, where a slight increase in RMSE and KSD and a corresponding decrease in PCC and R^2 have been observed. In summary, while the regression model significantly enhances accuracy for Class 3 stations across Germany, it fails to yield similar improvements for Class 1 and Class 2 stations.

Table 4.4.: Comparison of statistical metrics (RMSE, PCC, R^2, KSD) across the stations for each class between DWD observations and three datasets: the original ERA5, COSMO-REA6, and the corrected wind speed time series.

Class	Statistic metrics	ERA5	COSMO-REA6	Corrected
Class 1	RMSE (m/s)	1.40	1.24	1.90
	PCC	0.79	0.80	0.78
	R^2	0.62	0.64	0.61
	KSD	0.14	0.05	0.34
Class 2	RMSE (m/s)	1.96	1.71	2.08
	PCC	0.73	0.79	0.74
	R^2	0.53	0.62	0.55
	KSD	0.10	0.06	0.19
Class 3	RMSE (m/s)	5.07	4.84	2.77
	PCC	0.69	0.71	0.76
	R^2	0.48	0.50	0.58
	KSD	0.62	0.47	0.21

To further investigate the improvements observed in Class 3 stations, Table 4.5 provides a detailed comparison of statistical metrics across all 10 Class 3 DWD stations. The results indicate consistent improvement, with some stations experiencing particularly significant improvements. For instance, the weather station Brocken exhibits significantly improved statistical indicators: RMSE decreases from 8.23 m/s (ERA5) and 7.94 m/s (COSMO-REA6) to 2.96 m/s, PCC increases from 0.79 (ERA5) and

0.84 (COSMO-REA6) to 0.88, R^2 increases from 0.62 (ERA5) and 0.71 (COSMO-REA6) to 0.77, and KSD decreases from 0.70 (ERA5) and 0.68 (COSMO-REA6) to 0.17. Comparable improvements are also observed in stations such as Feldberg, Großer, and Weinbiet weather stations.

Table 4.5.: Comparison of statistical metrics (RMSE, PCC, R^2, KSD) for all Class 3 DWD stations between observations and three datasets: the original ERA5, COSMO-REA6, and the corrected wind speed time series.

Station	Statistic metrics	ERA5	COSMO-REA6	Corrected
Brocken	RMSE (m/s)	8.23	7.94	2.96
	PCC	0.79	0.84	0.88
	R^2	0.62	0.71	0.77
	KSD	0.70	0.68	0.17
Kahler	RMSE (m/s)	3.03	2.83	2.11
	PCC	0.86	0.84	0.86
	R^2	0.73	0.71	0.73
	KSD	0.49	0.46	0.32
Feldberg	RMSE (m/s)	6.72	6.14	3.49
	PCC	0.71	0.80	0.78
	R^2	0.50	0.64	0.61
	KSD	0.69	0.60	0.17
Fichtelberg	RMSE (m/s)	6.08	5.12	4.80
	PCC	0.77	0.81	0.84
	R^2	0.59	0.66	0.71
	KSD	0.64	0.49	0.51
Großer	RMSE (m/s)	4.89	4.06	2.29
	PCC	0.67	0.75	0.78
	R^2	0.45	0.56	0.61

Continued on next page

Table 4.5 – *Continued from previous page*

Station	Statistic metrics	ERA5	COSMO-REA6	Corrected
	KSD	0.63	0.45	0.11
Hornisgrinde	RMSE (m/s)	4.89	4.40	2.34
	PCC	0.76	0.76	0.81
	R^2	0.58	0.58	0.66
	KSD	0.59	0.49	0.10
Wasserkuppe	RMSE (m/s)	3.96	3.03	2.00
	PCC	0.71	0.80	0.77
	R^2	0.50	0.64	0.59
	KSD	0.53	0.34	0.08
Weinbiet	RMSE (m/s)	3.64	3.94	1.69
	PCC	0.81	0.73	0.86
	R^2	0.66	0.53	0.74
	KSD	0.49	0.52	0.11
Zugspitze	RMSE (m/s)	6.22	5.68	3.57
	PCC	0.35	0.51	0.61
	R^2	0.12	0.26	0.37
	KSD	0.82	0.72	0.31
Mittenwald	RMSE (m/s)	3.03	2.57	2.40
	PCC	0.48	0.58	0.36
	R^2	0.23	0.34	0.13
	KSD	0.60	0.41	0.26

Meanwhile, Figure 4.7 displays scatter plots and histograms plots for six selected Class 3 stations, all located in mountainous regions: Brocken, Hornisgrinde, Wasserkuppe, Weinbiet, Kahler, and Zugspitze [1]. This figure reveals that, for all stations, the scatter plots of the corrected wind speed align more closely with the diagonal line, indicating a stronger correlation with observed values. Additionally, the histograms show that the corrected wind speed distribution more closely resembles the observed distribution compared to ERA5 and COSMO-REA6, suggesting reduced biases and improved agreement with observations. While stations such as Weinbiet and Kahler still exhibit slight underestimation in the corrected wind speed, the downscaling process still outperforms ERA5 and COSMO-REA6. In comparison, other stations demonstrate significant improvements. These findings further confirm the robustness of the regression model when applied to independent datasets and different locations.

Additionally, the time series plots in Figure 4.7 provide a further comparison of the corrected wind speed time series and the reanalysis data ERA5 and COSMO-REA6. This figure reveals a stronger overlap between the corrected wind speed and observed data across all stations, also indicating a reduction in biases and improved alignment with observations. However, a consistent underestimation of extreme high wind speeds above 20 m/s is observed across all stations. This suggests that while the regression model effectively enhances overall accuracy, it remains limited in predicting extreme wind speed.

---

[1] Zugspitze is the highest mountain in Germany with the elevation around 2962 meters above sea level (Sigmund et al., 2019).

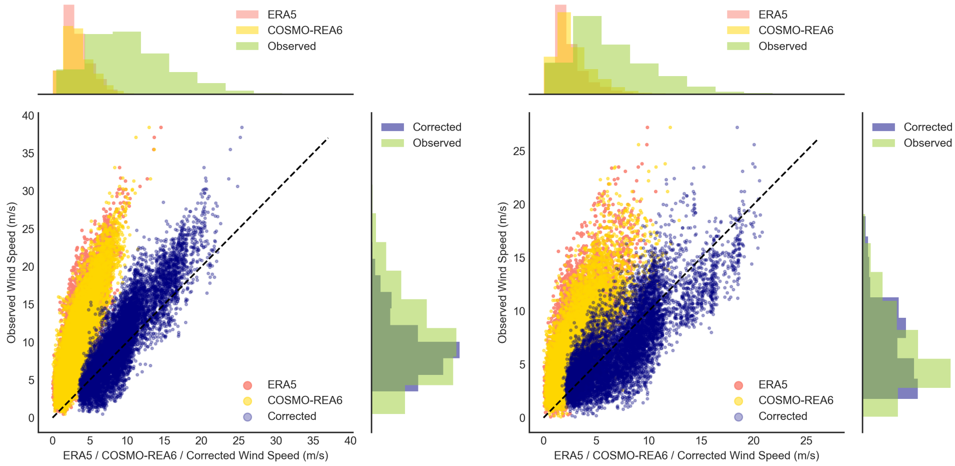

(a) Station Brocken (b) Station Hornisgrinde

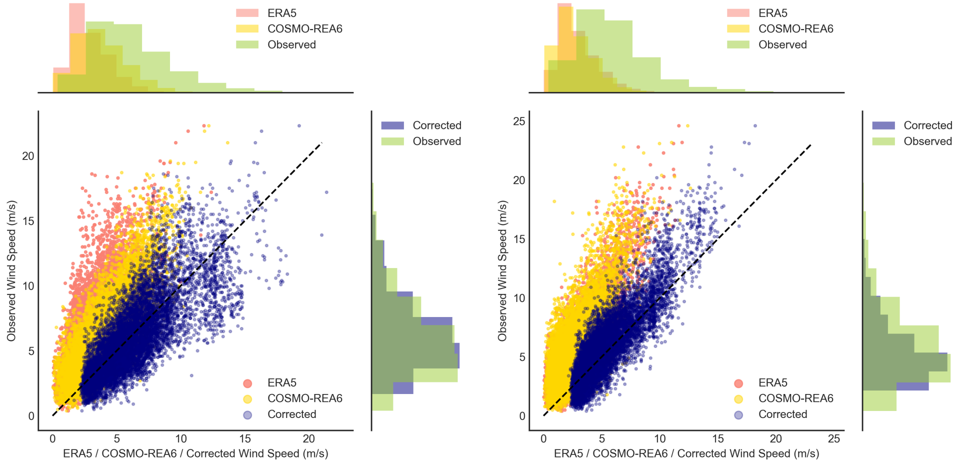

(c) Station Wasserkuppe (d) Station Weinbiet

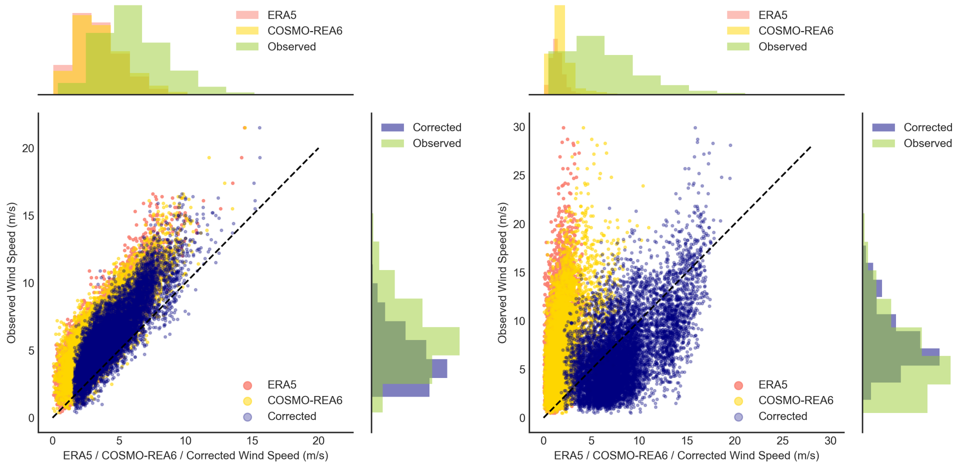

(e) Station Kahler (f) Station Zugspitze

Figure 4.7.: Scatter plots and histogram comparisons for 6 representative DWD stations between observations and three datasets: the original ERA5, COSMO-REA6, and the corrected wind speed time series.

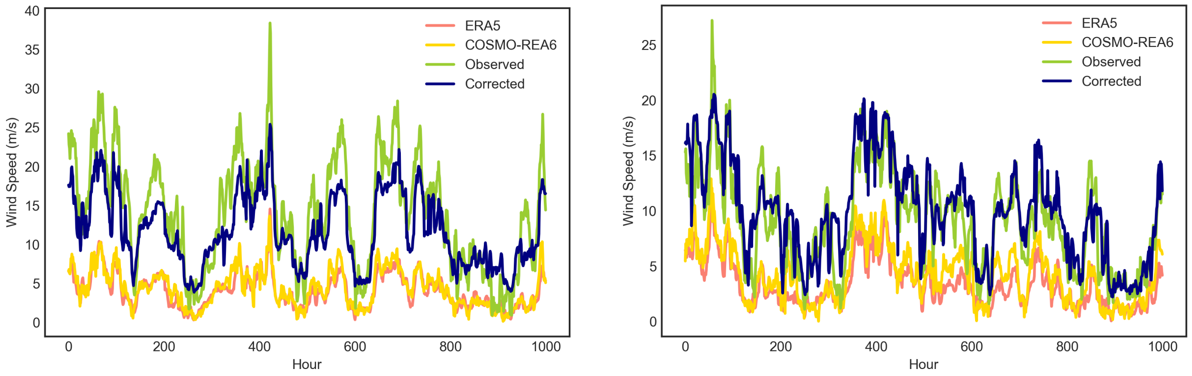

(a) Station Brocken (b) Station Hornisgrinde

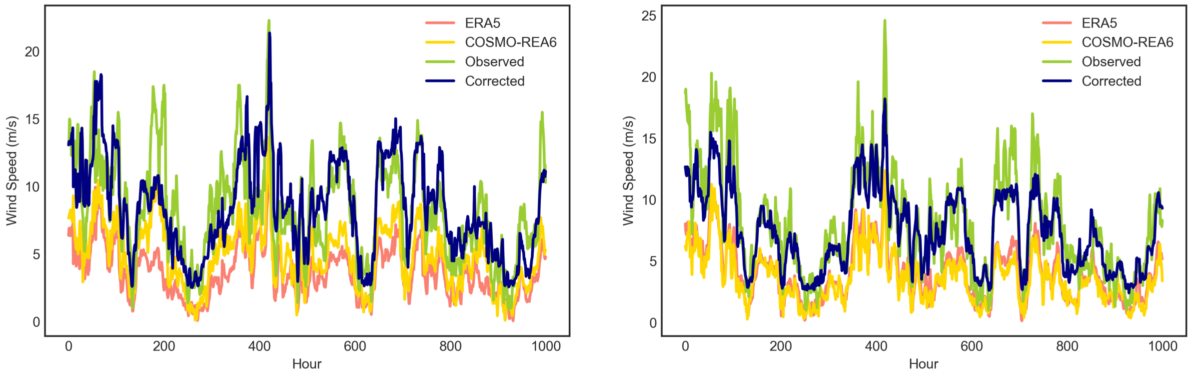

(c) Station Wasserkuppe (d) Station Weinbiet

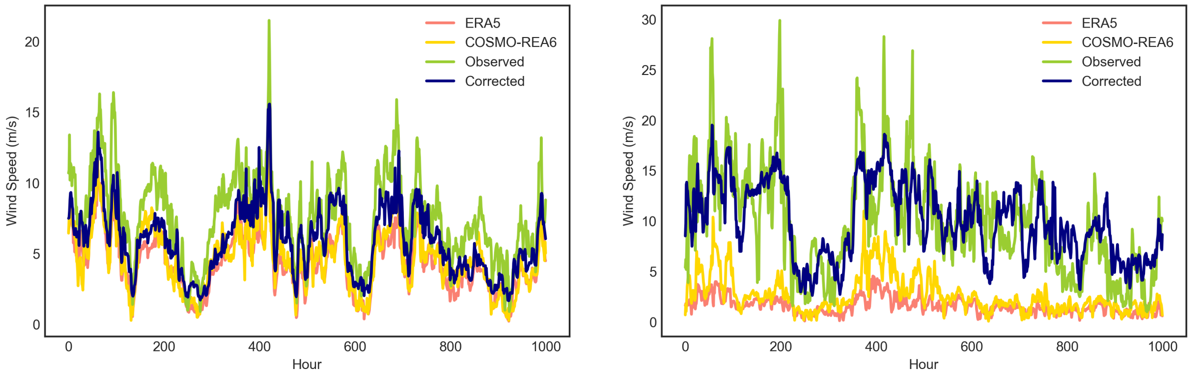

(e) Station Kahler (f) Station Zugspitze

Figure 4.8.: Time series plots for 6 representative DWD stations between observations and three datasets: original ERA5, COSMO-REA6, and the corrected wind speed. For clarity, only the first 1000 hours are displayed.

4.1.4. Summary and Discussion

In the preprocessing step, the impact of various topographic metrics, including elevation, slope, aspect, 75 km and 5 km radius TPI, and TDI, on the accuracy of ERA5 wind speed estimates is investigated.

This preprocessing step uses a Random Forest classification model to categorize the region into three classes based on these metrics:

- **Class 1**: High ERA5 quality region
- **Class 2**: Moderate ERA5 quality region
- **Class 3**: Poor ERA5 quality region

The results indicate that all considered topographic metrics play a crucial role in determining the performance of ERA5, indicating their strong influence on wind dynamics. The model accuracy of the Random Forest Classification indicates a strong performance overall, especially in Class 3 region, where topographic influences are most pronounced. Additionally, the region classification map of Europe reveals that most areas fall under Class 1 regions with relatively high-quality ERA5 data, while Class 3 regions are primarily located in mountainous areas. This finding suggests that downscaling techniques are unnecessary in regions where ERA5 already provides high-quality data. Instead, focusing on improving ERA5 accuracy in complex terrain areas can significantly reduce computational effort while enhancing overall model efficiency. This conclusion also indicates the importance of the preprocessing step before implementing downscaling techniques.

In the regression step, the results confirm that the model is well-fitted and does not have overfitting issue, as evidenced by the small differences in statistic metrics between training and testing datasets. The regression significantly improves ERA5 data quality, particularly in Class 3 regions. Furthermore, the improvement in KSD suggests that this downscaling process not only decreases statistical error but also maintains a high degree of wind speed variability. Feature importance analysis reveals distinct influences across different regions. In Class 1 and Class 2 regions, large-scale ERA5 data remains the dominant predictor. In comparison, in Class 3 regions, TPI and GWD play an equally significant role in estimating local wind speed, indicating the strong impact of topographic conditions. This also suggests that wind speeds in Class 3 regions are heavily influenced by local terrain, whereas Class 1 and Class 2 regions, which are predominantly composed of flat terrain, are less affected by topographic conditions.

The cross-dataset validation using MeteoSwiss observations across different years further demonstrates a significant improvement in wind speed estimates, particularly in Class 3 stations. This demonstration of generalizability suggests that the model can effectively apply to unseen datasets and is applicable across different years. However, when extending the model to Germany, the results reveal a marked improvement only for Class 3 stations. The corrected wind speeds in Class 1 and Class 2 stations show a larger bias compared to ERA5 and COSMO-REA6.

In summary, this section describes the important role of topographic conditions in determining the spatially disparate quality of ERA5 wind speed data. By establishing relationships between large-scale reanalysis dataset ERA5, topographic metrics, and local-scale wind speed observations using Machine Learning, the proposed regression-based statistical downscaling method can significantly improve the quality of ERA5 data, especially in Class 3 regions, characterized by complex terrain.

4.2. Projection of Future TRFs and Electricity Demand

This chapter presents the results of the projection of TRFs and electricity demand, based on the author's publication 'Future electricity demand for Europe: Unraveling the dynamics of the Temperature Response Function' published in *Applied Energy*.

4.2.1. Simulating TRFs Using Piecewise Regression

As introduced in Chapter 3.2.2, to establish a statistical representation of TRFs, a piecewise regression model is employed. The performance of this model is assessed using two statistical indicators: RMSE and R^2. Detailed RMSE and R^2 values for each region and year are provided in Appendix A.3.1. Data with R^2 values smaller than 0.4, as indicated in Appendix A.3.2, are excluded from the analysis. This exclusion is performed because, in such cases, the correlation between temperature and electricity demand is not predominant, and excluding these data can enhance the accuracy of the analysis. The aggregated results for these evaluation indicators are presented in this section. Table 4.6 lists the mean RMSE and R^2 scores across multiple years for each country. Similarly, Table 4.7 presents the mean RMSE and R^2 scores across all countries for each year.

Table 4.6.: Summary of the average RMSE and R^2 for each country

Region	RMSE	R^2	Region	RMSE	R^2	Region	RMSE	R^2
AT	0.143	0.690	FR	0.977	0.868	MK	0.113	0.824
BA	0.145	0.634	GB	0.147	0.728	NL	0.183	0.531
BE	0.138	0.652	GR	0.117	0.757	NO	0.087	0.918
BG	0.105	0.848	HR	0.139	0.672	PL	0.121	0.559
CH	0.120	0.775	HU	0.131	0.556	PT	0.157	0.487
CY	0.141	0.693	IE	0.153	0.613	RO	0.127	0.697
CZ	0.119	0.700	IT	0.113	0.462	RS	0.104	0.874
DE	0.141	0.545	LT	0.139	0.680	SE	0.094	0.885
DK	0.139	0.681	LU	0.130	0.496	SI	0.129	0.544
EE	0.100	0.849	LV	0.121	0.758	SK	0.133	0.631
ES	0.126	0.551	MD	0.146	0.577	UA	0.110	0.858
FI	0.092	0.868	ME	0.145	0.711	XK	0.102	0.883

Table 4.7.: Summary of the average RMSE and R^2 for each year

Year	RMSE	R^2
2015	0.133	0.700
2016	0.123	0.697
2017	0.120	0.714
2018	0.111	0.751
2019	0.123	0.704
2020	0.160	0.637
2021	0.122	0.722
2022	0.119	0.716

Meanwhile, Figure 4.9 displays the piecewise regression results for selected countries in the year 2022. These selected regions are distributed across various geographical locations in Europe. It is apparent that their TRFs exhibit different shapes. For example, in countries with cold or intermediate winters, such as Norway and Germany, heating is dominant. The electricity cooling, however, is not obvious in the plot. In countries with warmer summers, such as Bulgaria and Serbia, although the cooling demand is obvious, the heating effect is still more pronounced. In comparison, in countries with hot summers, such as Greece, the cooling effect is as dominant as heating, and in Italy, the cooling is even more dominant.

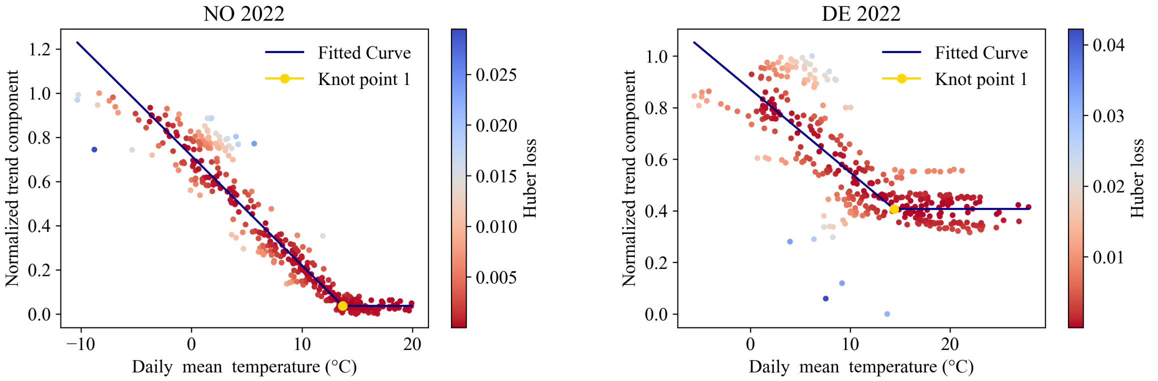

(a) Norway (b) Germany

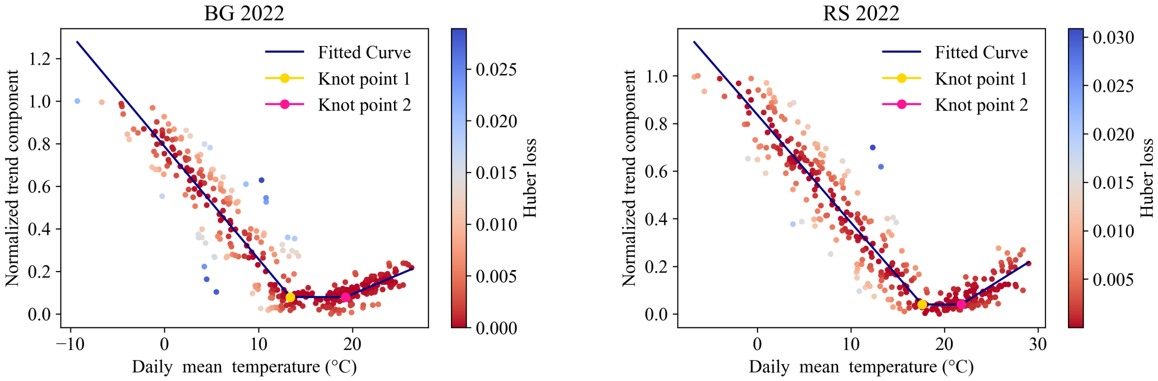

(c) Bulgaria (d) Serbia

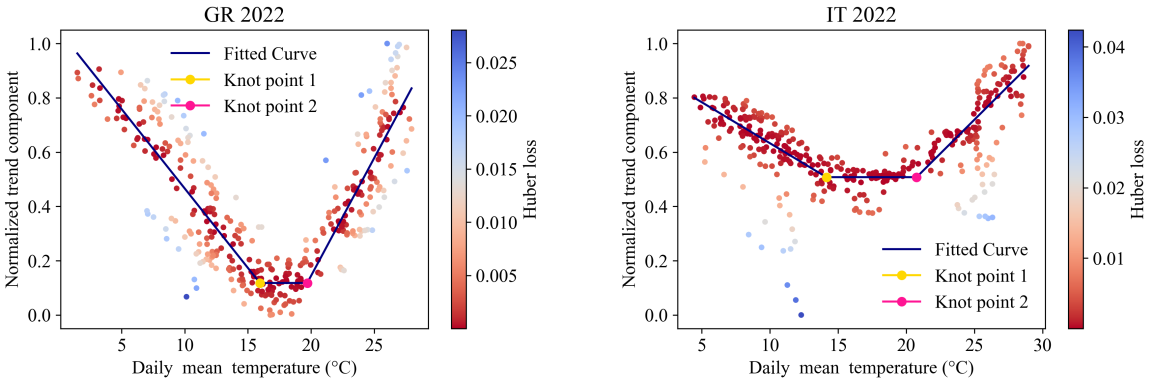

(e) Greece (f) Italy

Figure 4.9.: Piecewise regression results for selected countries.

4.2.2. Projecting Components of TRFs

This section presents a visualization of the dynamics of various TRF components over time. In this context, results for four representative countries are showcased: Finland (FI), Germany (DE), Bulgaria (BG), and Spain (ES). The following figures illustrate the evolving patterns and variations of heating BPTs, cooling BPTs, left slopes, and right slopes over time.

Heating BPT

The change of heating BPT over time is presented in Figure 4.10. From this figure, a consistent decline of heating BPT is observed for all scenarios compared to the baseline scenario (S0). The strict policy scenarios (S2 and S4) exhibit a notably greater decrease than the moderate policy scenarios (S1 and S3). Taking Germany as an example, the moderate policy scenario decreases the heating BPT from the current approximately 15 °C to around 12 °C by 2100. In contrast, the strict policy scenario demonstrates a more pronounced decrease, reaching around 8 °C before 2055 in the initial renovation stage. The reduction then stabilizes in the second renovation stage, reaching around 7 °C, resulting in substantial electricity savings.

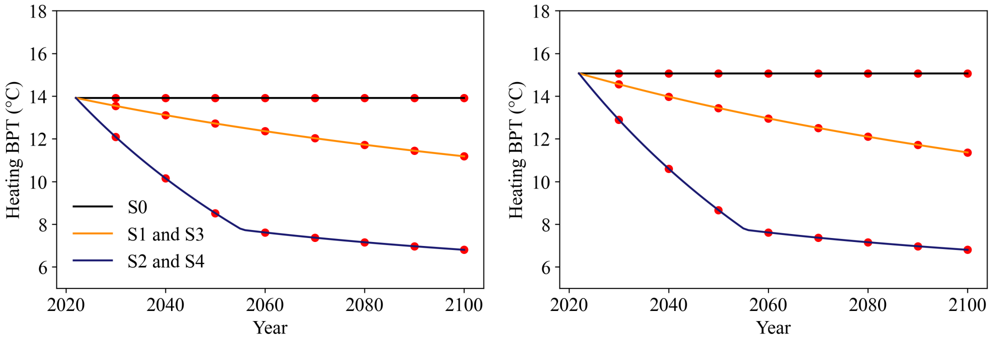

(a) Finland

(b) Germany

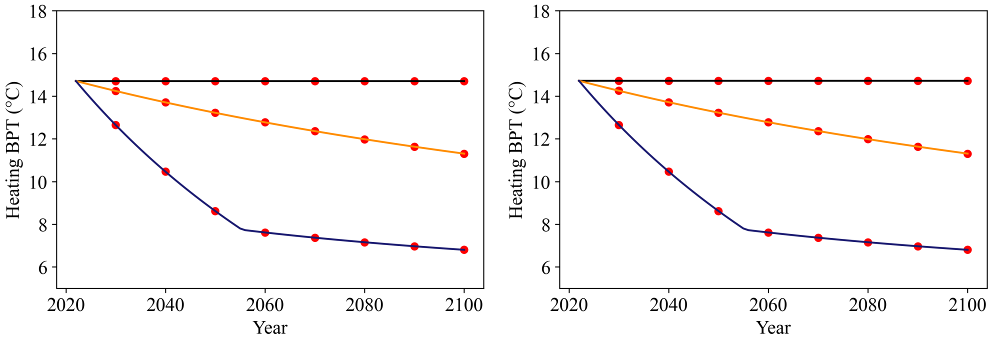

(c) Bulgaria

(d) Spain

Figure 4.10.: Change of heating BPT over time for representative countries.

Cooling BPT

For the cooling BPT, the opposite trend is observed, as indicated in Figure 4.11. For example, in Germany, the cooling BPT increases from 20 °C to around 23 °C in the moderate policy scenario and experiences a significant rise under the strict policy scenario. In the first renovation stage, it elevates to around 26 °C and can further reach 27 °C by 2100.

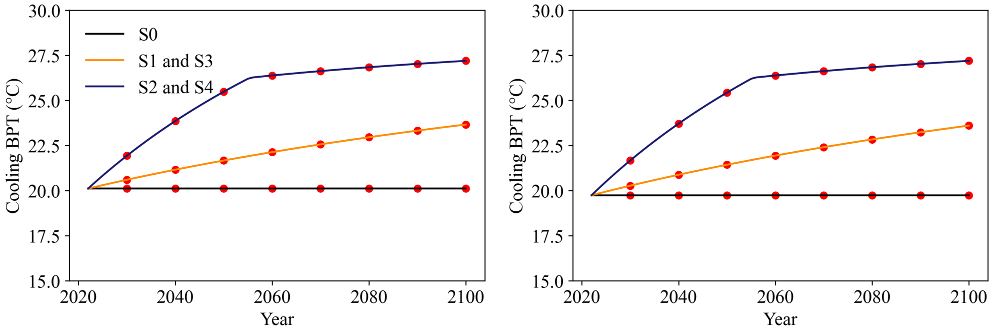

(a) Finland (b) Germany

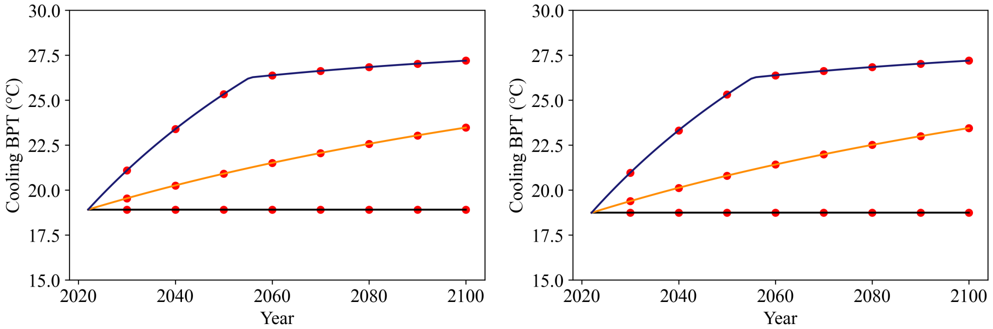

(c) Bulgaria (d) Spain

Figure 4.11.: Change of cooling BPT over time for representative countries.

Left Slope

Figure 4.12 demonstrates the changes of the left slope. From this figure, it is evident that the moderate policy scenario reveals a general decrease in the absolute value of slopes across all countries. This suggests that electricity demand becomes less sensitive to cold temperatures, primarily due to improvements in the thermal insulation of buildings.

However, a distinct trend can be observed in the strict policy scenario. In Finland and Germany, the slope initially decreases until 2055, followed by an upward trajectory. In Bulgaria and Spain, on the other hand, the slope experiences a slight increase until 2055, followed by a more pronounced rise until 2100. This pattern indicates the impact of electrification on different countries. In Germany and Finland, where the current absolute slope value is modest due to efficient thermal building performance, the implementation of strict policies, despite the improvement in thermal insulation, can result in higher winter electricity demand due to an increased electrification rate. Conversely, in countries like Spain and Bulgaria, where thermal insulation is less effective, the impact of thermal improvement on the left slope value is more pronounced. In the long run, the collective enhancement of thermal insulation results in a substantial increase in the absolute value of the left slope for all countries.

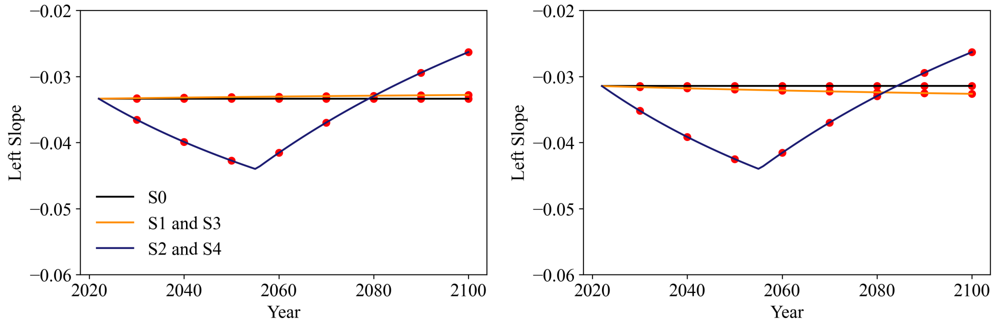

(a) Finland (b) Germany

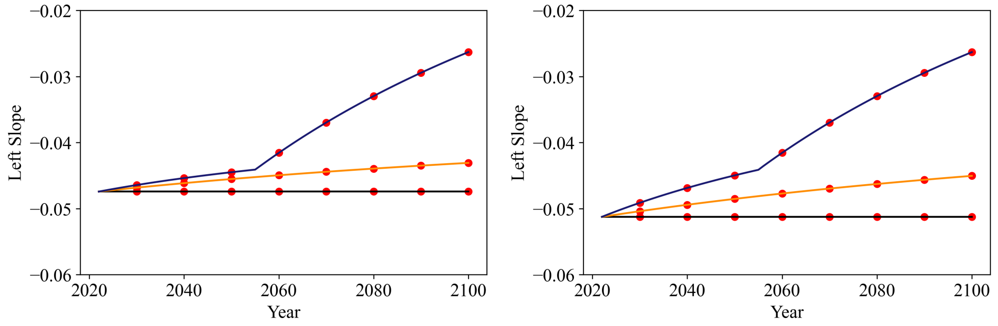

(c) Bulgaria (d) Spain

Figure 4.12.: Change of left slope over time for representative countries.

Right Slope

Figure 4.13 illustrates the changes of the right slope. Regarding the right slope, in scenarios where the space cooling penetration rate remains at the current level (S1 and S2), passive cooling demonstrates its ability to decrease the right slope value. This effect is particularly pronounced in the strict policy scenario (S2), where passive cooling is applied to both renovated and new buildings. This reduction is more pronounced in warmer countries like Bulgaria and Spain. This suggests that, in the long run, the right slope will exhibit less sensitivity to temperature, potentially reducing electricity demand during the summer.

However, when considering scenarios with boosted space cooling penetration rates (S3 and S4), there is a notable increase in the right slope value, especially in warmer countries. For Bulgaria and Spain, the increase is significant in both scenarios. Notably, in Scenario S4, where passive cooling is implemented alongside boosted space cooling, the right slope value begins to decrease after 2050. This is attributed to the space cooling penetration rate reaching its full potential in 2050, and the subsequent impact of passive cooling measures.

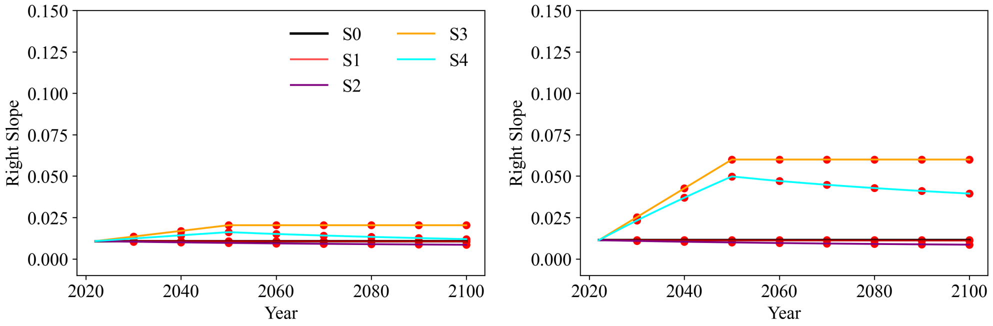

(a) Finland (b) Germany

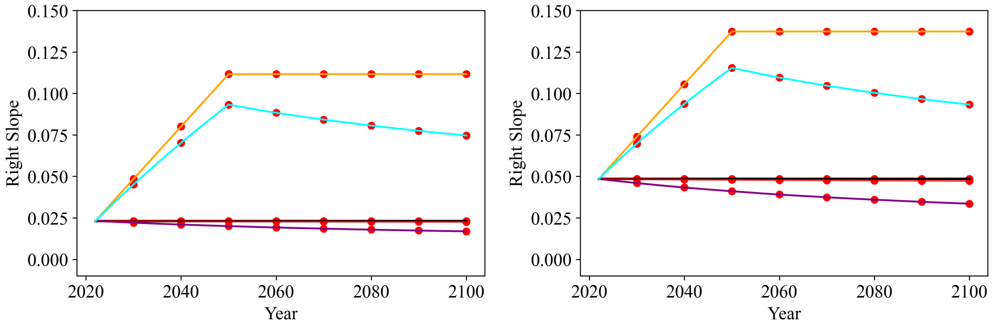

(c) Bulgaria (d) Spain

Figure 4.13.: Change of right slope over time for representative countries.

4.2.3. Projecting TRFs

With these essential components of the TRF established, the TRFs until the year 2100 can be constructed using these elements. For a better visualization, Figure 4.14 presents the future TRFs for these countries in the years 2025, 2050, and 2100.

By comparing current and future TRFs across various climate scenarios, substantial changes in the TRF shapes become apparent. The future TRFs and time series for all countries are provided in Supplementary Material 3 of Hu et al. (2024). The most pronounced changes are observed in Bulgaria and Spain, attributed to a substantial increase in space cooling usage. Meanwhile, the enhancement of building thermal insulation, addressed by both moderate and strict policies, leads to considerably larger comfort zones compared to the present TRF. This indicates the effectiveness of policy interventions, particularly building code regulations, in reducing the overall electricity demand.

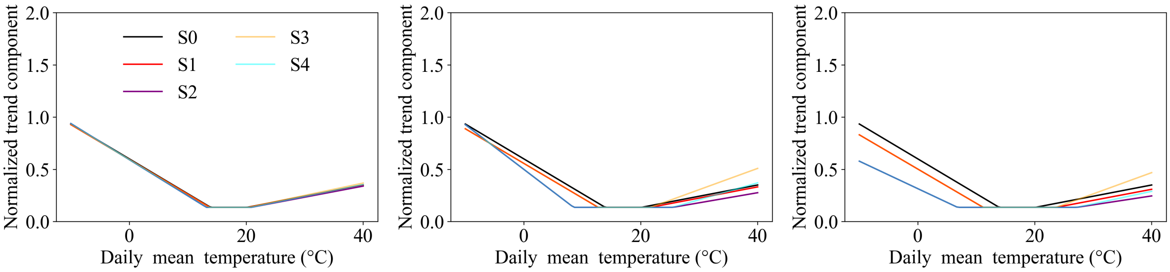

(a) FI in 2025 (b) FI in 2050 (c) FI in 2100

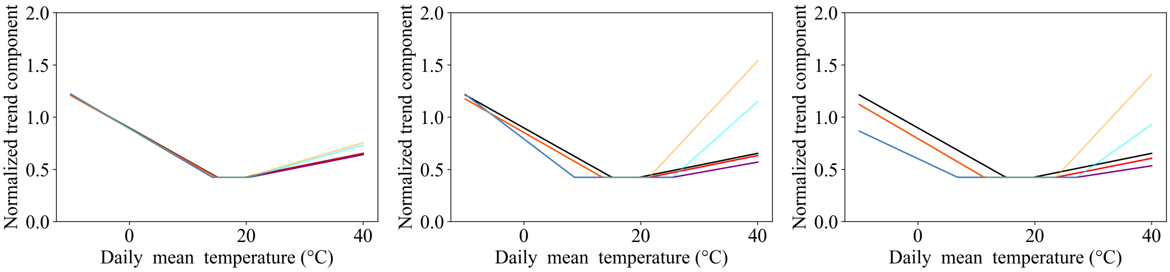

(d) DE in 2025 (e) DE in 2050 (f) DE in 2100

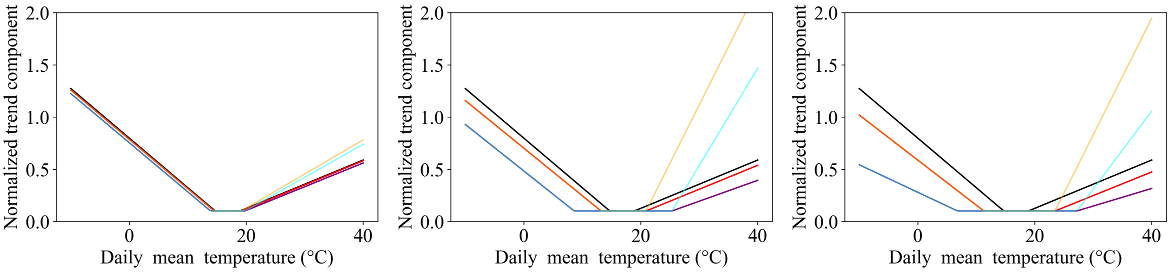

(g) BG in 2025 (h) BG in 2050 (i) BG in 2100

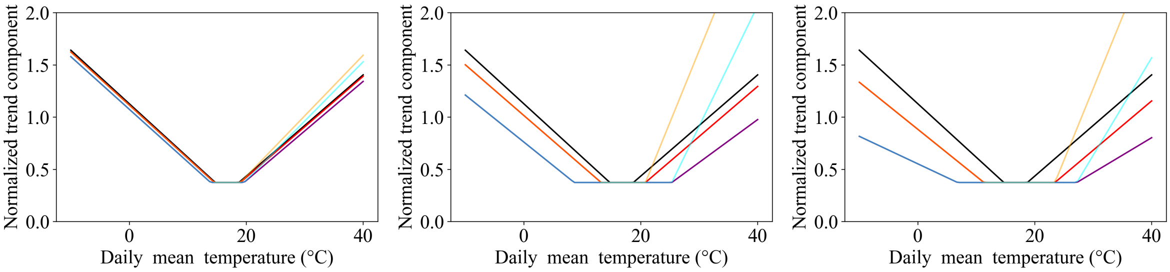

(j) ES in 2025 (k) ES in 2050 (l) ES in 2100

Figure 4.14.: TRFs in years 2025, 2050, and 2100 for representative countries.

4.2.4. Projecting Demand Time Series

After constructing the future TRFs, the relationship between temperature and electricity demand can be determined. TRFs can be used to derive time series of electricity demand for future years using the climate scenario data introduced in Section 3.2.1. However, to accurately reconstruct the electricity demand time series, two additional steps are necessary. Firstly, the normalized trend components need to be denormalized by rescaling the data back to the minimum and maximum values of the historically averaged trend components. Subsequently, the historical averaged seasonal components are added to these denormalized trend components. The residual component is not included in this analysis as it serves as an anomaly indicator and can include noise or irregularities that are not necessarily representative of the underlying structure.

The resulting daily electricity demand time series under various scenarios for the years 2050 and 2100 are illustrated in Figure 4.15 and Figure 4.16. For clarity, only the results from ensemble realization r1 of the climate scenario data are showcased. The electricity demand time series for ensemble realization r2 is available in Supplementary Material 4 of Hu et al. (2024).

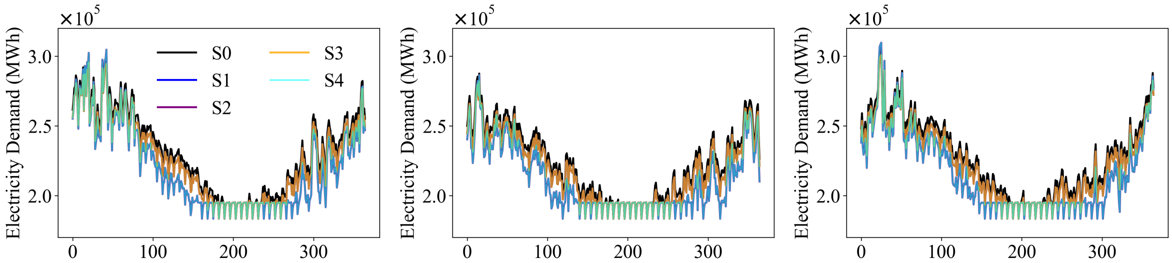

(a) FI RCP2.6 (b) FI RCP4.5 (c) FI RCP8.5

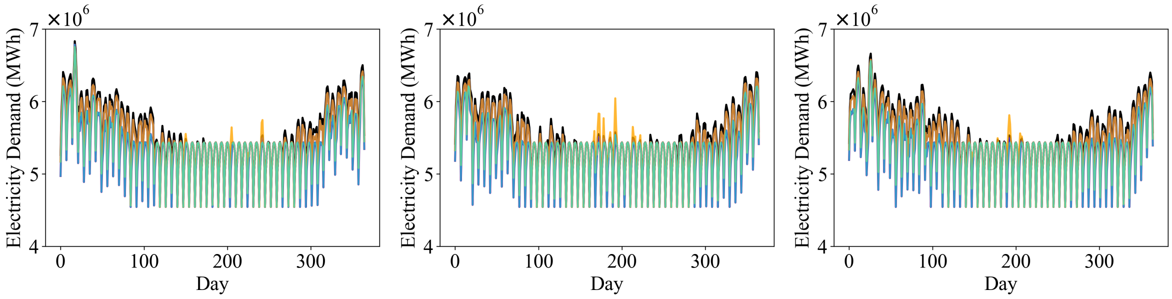

(d) DE RCP2.6 (e) DE RCP4.5 (f) DE RCP8.5

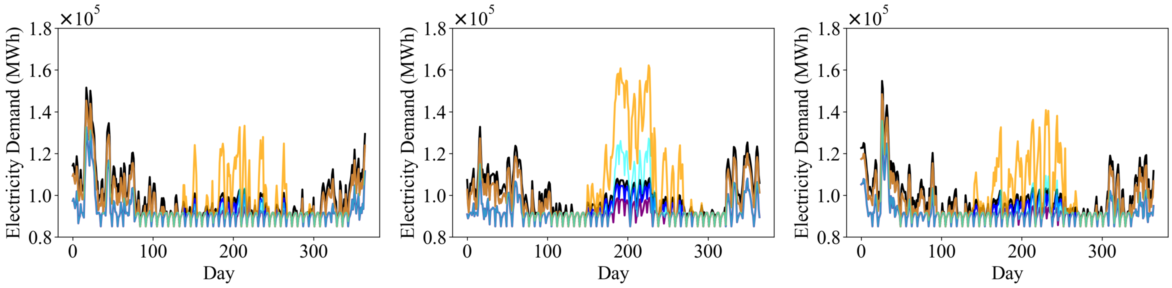

(g) BG RCP2.6 (h) BG RCP4.5 (i) BG RCP8.5

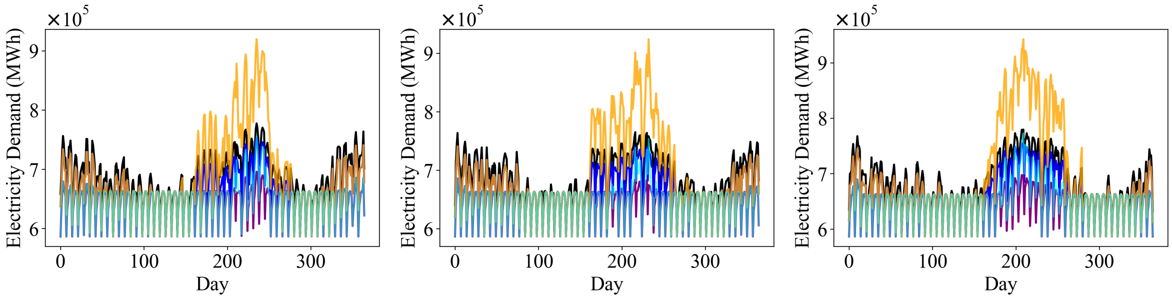

(j) ES RCP2.6 (k) ES RCP4.5 (l) ES RCP8.5

Figure 4.15.: Daily time series plot under different climate scenarios in the year 2050 for representative countries.

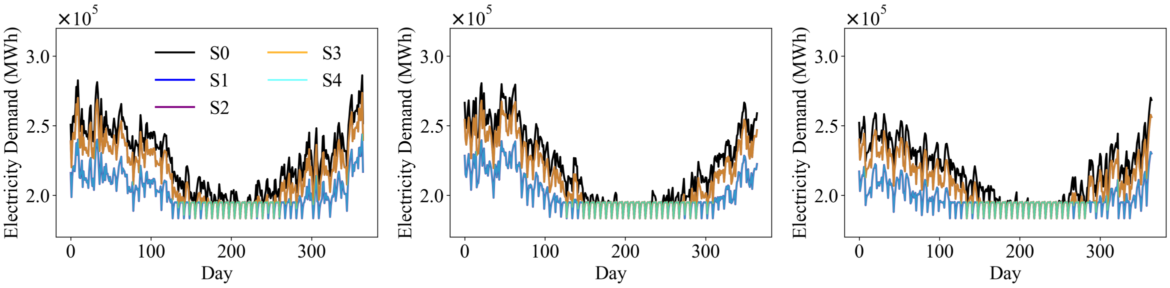

(a) FI RCP2.6 (b) FI RCP4.5 (c) FI RCP8.5

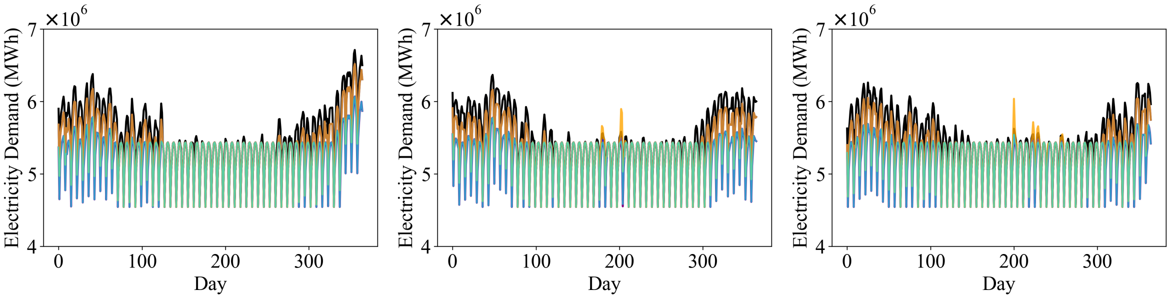

(d) DE RCP2.6 (e) DE RCP4.5 (f) DE RCP8.5

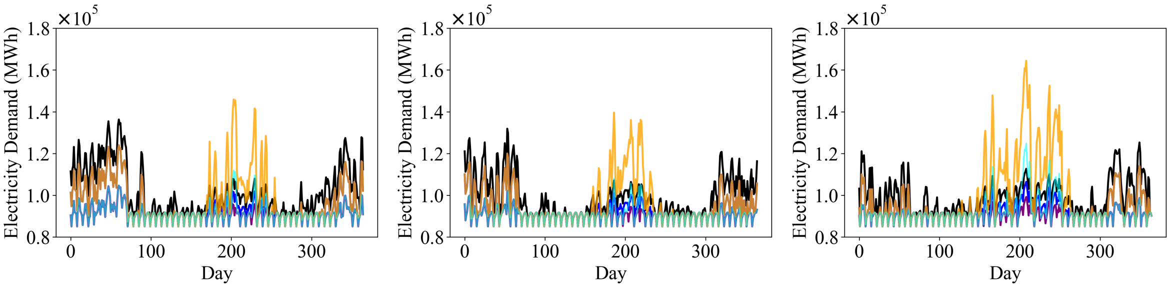

(g) BG RCP2.6 (h) BG RCP4.5 (i) BG RCP8.5

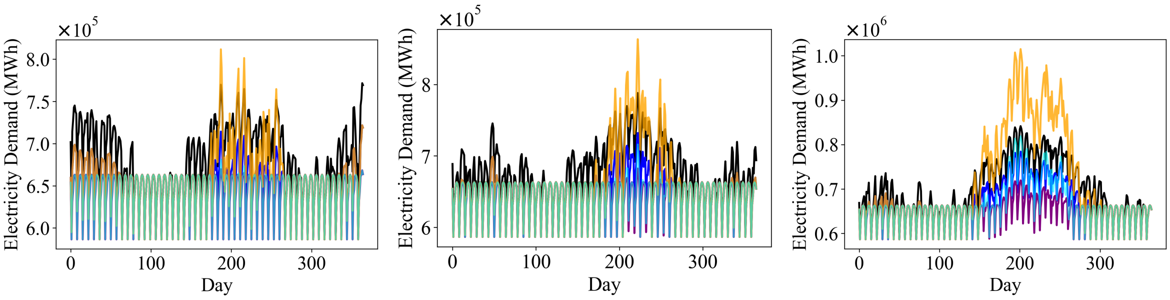

(j) ES RCP2.6 (k) ES RCP4.5 (l) ES RCP8.5

Figure 4.16.: Daily time series plot under different climate scenarios in the year 2100 for representative countries.

After constructing the time series, the impact of dynamic TRFs becomes evident, illustrating significant differences in the electricity demand patterns. In the case of Finland, the most significant variance appears in the winter months (January, February, and December). In 2050, the differences between scenarios are insignificant for both summer and winter months; however, by 2100, under RCP 8.5, a substantial 13.7% reduction is observed in the strict policy scenarios (S2 and S4). This phenomenon is attributed to the combined effects of electrification rates and improved thermal insulation. While the thermal insulation effects are in place in 2050, the impact on electricity demand reduction in scenarios S2 and S4 is less pronounced due to increased electrification rates. A similar trend in the winter months is also observed in Germany. However, in the summer months (June, July, and August), Germany exhibits a significant increase of the peak demand in 2050 under RCP 4.5 for S3, yet this significant increase is balanced in S4, where passive cooling is implemented.

In comparison to Finland and Germany, warmer countries experience more substantial changes in both the summer and winter months. For example, in winter, under RCP 2.6 in 2050, moderate and strict policy scenarios can reduce electricity demand in Bulgaria by 4.1% and 12.8%, respectively. However, for the summer months, a significant increase in total electricity demand and peak demand can be observed. Under RCP 4.5 in 2050, compared to S0, S3 and S4 increase total summer demand in Bulgaria by 24.8% and 2.2%. Specifically, in Bulgaria, under the RCP 8.5 scenario, when compared to S3, the projections indicate that the implementation of effective passive cooling measurements in S4 is expected to reduce the electricity demand during the summer months of 2100 by around 1.1 TWh. In Spain, this reduction is notably higher at 3.7 TWh. This implies the long-term effectiveness of passive cooling, particularly in warmer regions.

4.2.5. Summary and Discussion

In the piecewise regression analysis, variations in the shape of the TRFs are observed across different regions. From the mean RMSE and R^2 score across different regions, on average, the RMSE is 0.114 and the R^2 score is 0.671, suggesting that the piecewise model performs well in accurately estimating the TRFs. However, it is noteworthy that certain regions, such as Italy, Luxembourg, and Portugal, have lower R^2 scores, indicating that the temperature's influence on demand may not be strong in these areas.

Meanwhile, from the mean R^2 score across different years, it is also observed that the R^2 score is around 0.7, except for the year 2020, which has a lower R^2 score of 0.637. This suggests that the temperature's influence on electricity demand in 2020 was weaker compared to other years and may have been obscured by other influential factors. Notably, the COVID-19 pandemic occurred in 2020, and previous studies, such as (Covid, 19; Krarti and Aldubyan, 2021; Santiago et al., 2021), have documented significant changes in people's behavior and demand patterns during the pandemic. These changes likely contributed to the reduced influence of temperature on electricity demand observed in 2020.

When projecting future electricity demand, five scenarios are designed that not only take into account the enforcement of moderate and strict building regulations but also factor in the escalating use of space cooling. The results indicate the profound impacts of these variables on the shape of TRFs, and consequently on the time series. This finding demonstrates a significant difference in policy development across various countries.

In colder countries where heating predominates, stringent policies are likely to lead to increased electricity demand until around 2050, driven by the increase in the electrification rate. Nevertheless, this increase is expected to be offset by a subsequent reduction in electricity demand, attributable to enhanced thermal insulation in buildings and an optimistic renovation and new built rate. Meanwhile, in regions where cooling demand is pronounced, the effect of moderate policy is limited. Under the moderate policy framework, a substantial increase in electricity demand and peak loads during summer can still be observed due to the significant increase in space cooling use. Under a strict policy framework, however, the electricity demand is projected to witness a considerable reduction, potentially even returning to current levels despite a significant increase in space cooling penetration, thanks to the implementation of passive cooling measures. In summary, these results indicate the critical role of interventions, such as enhanced thermal insulation and the adoption of effective passive cooling methods, in reducing future residential electricity demand.

4.3. Influence of Dispatchable Generation and Extreme Weather Events on Energy System Design

This chapter reveals the factors influencing the robustness of cost-optimal energy system designs, as discussed in the manuscript ’Robustness of cost-optimal energy system designs: The role of short-term extreme weather events and dispatchable generation’ submitted to *Solar Energy*. After constructing the various SWYs as introduced in Chapter 3.3.2, these weather years are then used in the ESOM REMix model to evaluate their influence on the energy system. The comparison is based on several key indicators, including system costs, annual capacity values, electricity generation, and capacity factors (CF) across different technologies.

4.3.1. Exogenous-RE Expansion Scenario

In the initial run of the Exogenous-RE scenario, the renewable energy generation and demand time series from both historical and synthetic weather years are input into the ESOM REMix model. Figure 4.17 illustrates the system costs across various weather years. From the figure, it is evident that 1997 exhibits the highest system costs among the 30 historical years. In terms of SWYs, EHY, EHY_1D, and EHY_2W result in even higher system costs than 1997, with EHY_1D having the highest system costs. This finding aligns with the earlier residual load analysis presented in Section 3.3.2, which identified 1997 as the most extreme year. The higher system costs observed for EHY, EHY_1D, and EHY_2W further confirm that the extreme high SWYs, generated using the FS statistic method and the extreme weather events method, also present significant challenges for the energy system.

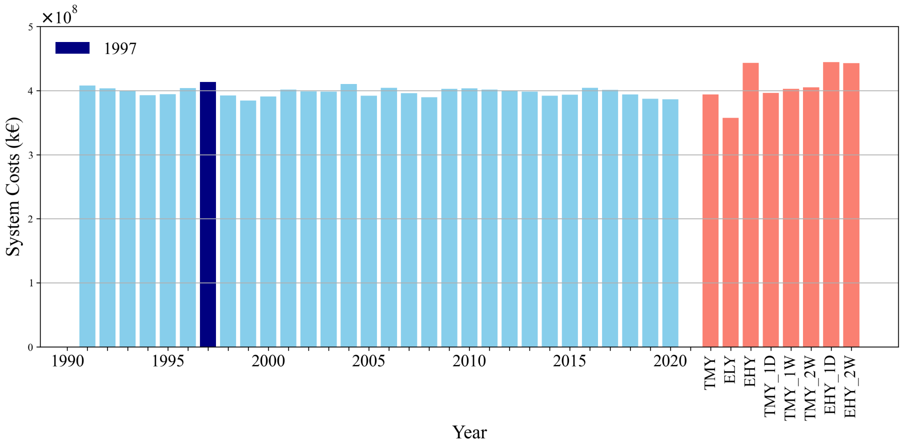

Figure 4.17.: System costs for various weather years in the Exogenous-RE scenario for Europe.

The capacity values for various power generation technologies are presented in Figure 4.18. From this figure, it can be observed that the capacities for both PV and wind onshore are the largest among all technologies. In this scenario, since the renewable capacities are fixed, only the gas turbine GH4-GT and CHP-ExCCGT capacities vary across the weather years. Among all historical and synthetic weather years, the highest CH4-GT capacity occurs in 2015, at 273.12 GW, which is nearly 60 GW higher than the second-highest capacity in 2011 (214.80 GW). The lowest CH4-GT capacity is observed in EHY_2W, with only 0.71 GW. However, EHY_2W has the highest CHP-ExCCGT capacity, at 196.82 GW. While other significantly high CHP-ExCCGT years occur in EHY_1D (189.76 GW) and EHY (184.19 GW), years such as ELY and 1999 are among the lowest for CHP-ExCCGT capacity, with values below 1 GW.

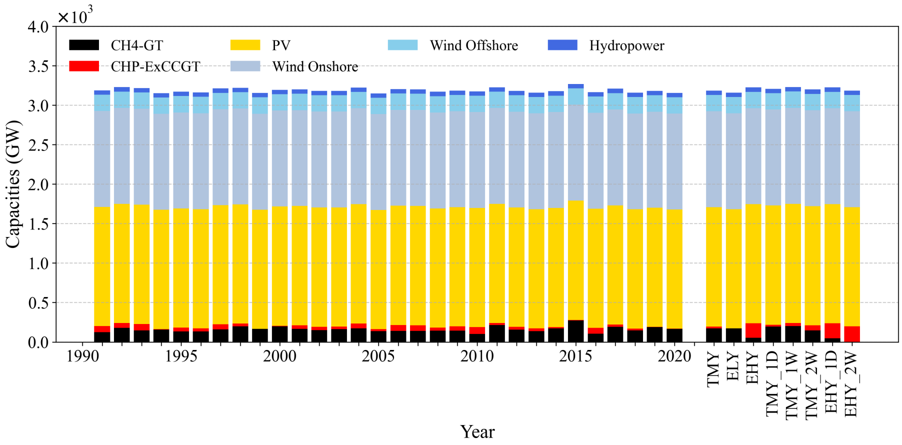

Figure 4.18.: Hypothetical capacity values for various technologies across different weather years in the Exogenous-RE scenario for Europe. For clarity, the capacities of reservoir hydropower and run-of-river hydropower are combined into a single hydropower capacity, as they are relatively low compared to other technologies.

The variation in CH4-GT and CHP-ExCCGT capacities suggests that, although both are dispatchable generation technologies, some years rely more heavily on one technology. To provide a clearer understanding of the overall dispatchable generation capacities and improve visualization, the CH4-GT and CHP-ExCCGT capacity values are aggregated, as shown in Figure 4.19. From this figure, it is evident that the highest aggregated gas turbine capacity occurs in 2015, at 280.37 GW, which is about 40 GW higher than the second-highest capacity in TMY_1W (240.44 GW) and the third-highest in 1992 (239.91 GW).

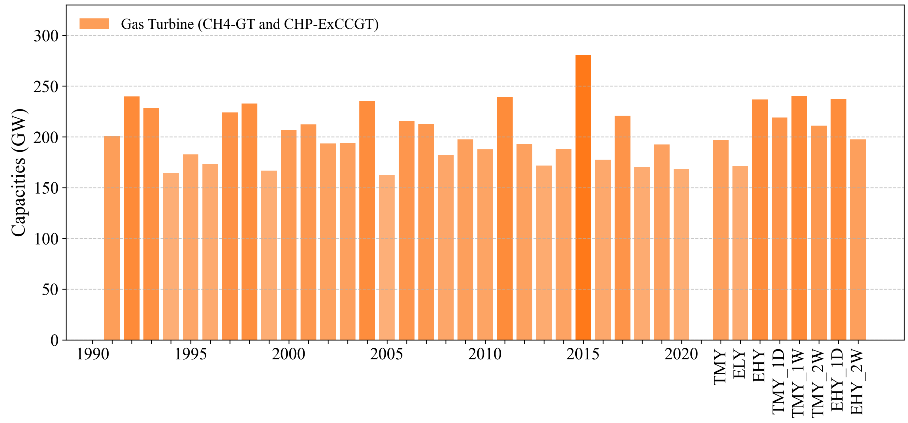

Figure 4.19.: Aggregated capacities of gas turbines CH4-GT and CHP-ExCCGT across different weather years in the Exogenous-RE scenario for Europe.

Meanwhile, Figure 4.20 illustrates the electricity generation for each weather year. The figure shows that the majority of electricity generation across all weather years comes from PV and onshore wind, with PV generation remaining relatively consistent throughout the years. In addition to these sources, offshore wind and hydropower also contribute a significant share. In contrast, gas turbines CH4-GT and CHP-ExCCGT play a relatively smaller role in the overall electricity generation.

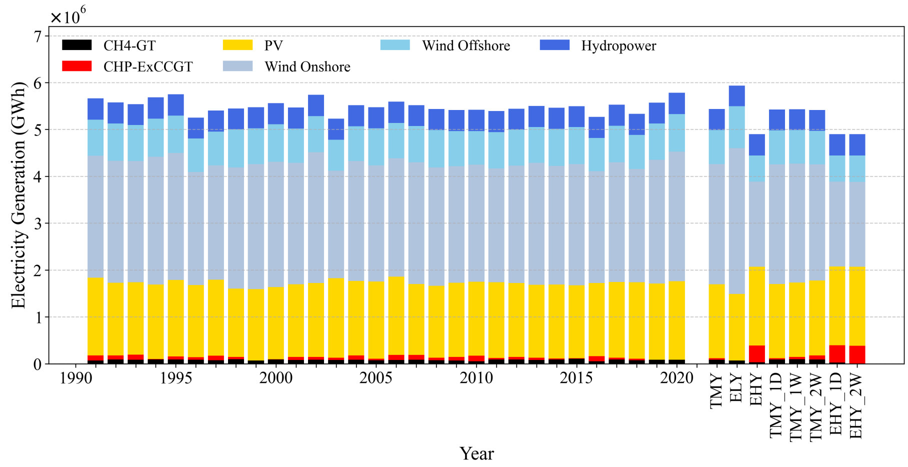

Figure 4.20.: Electricity generated for various technologies across different weather years in the Exogenous-RE scenario for Europe. For better visualization, the electricity generation of reservoir hydro and run-of-river hydro are combined into a single hydropower generation.

In addition, Figure 4.21 presents they corresponding Capacity Factor (CF) for different technologies. CF represents the actual energy output of an electricity-generating device divided by the energy output that would be produced if it operated at its rated power output for the entire year (Muratori et al., 2017). Among all technologies, CH4-GT exhibits a relatively low CF, particularly when compared to offshore wind and reservoir hydropower. The highest CF for CH4-GT occurs in the year EHY_2W at 0.078, which corresponds to approximately 483.7 GWh of electricity generation. A similar trend is observed for CHP-ExCCGT, where EHY_2W has the second-highest CF (0.222), slightly lower than the year EHY (0.222), generating approximately 382.3 TWh of electricity. However, in the year EHY_2W, both onshore and offshore wind exhibit some of the lowest CF values, with 0.170 for onshore wind and 0.309 for offshore wind, generating approximately 1812.1 TWh and 561.5 TWh of electricity, respectively. A similar pattern, with relatively high CF for gas turbines and lower CF for wind, is also observed in the years EHY and EHY_1D. This suggests that, under the weather conditions represented by these years, the system relies more heavily on gas turbines to meet demand due to the lower availability of wind energy.

In contrast, for ELY, the CF of gas turbine is the lowest among all years, with 0.044 for CH4-GT and 0.120 for CHP-ExCCGT, generating approximately 66.3 TWh and only 0.6 GWh of electricity, respectively. Meanwhile, the CF for onshore wind (0.292) and offshore wind (0.493) are the highest, generating approximately 3112.3 TWh and 895.1 TWh of electricity, respectively. This indicates that during the weather conditions represented by ELY, the system benefits from high wind generation, reducing the need for gas turbines, implying that ELY represents a year of favorable weather conditions for renewable generation. Meanwhile, it is worth noting that although the capacities of CH4-GT and overall gas turbines are observed to be the highest in 2015, the CF for CH4-GT in 2015 (0.045) is the second lowest among all years, only slightly higher than the lowest CF observed in ELY (0.044), generating approximately 108 TWh of electricity.

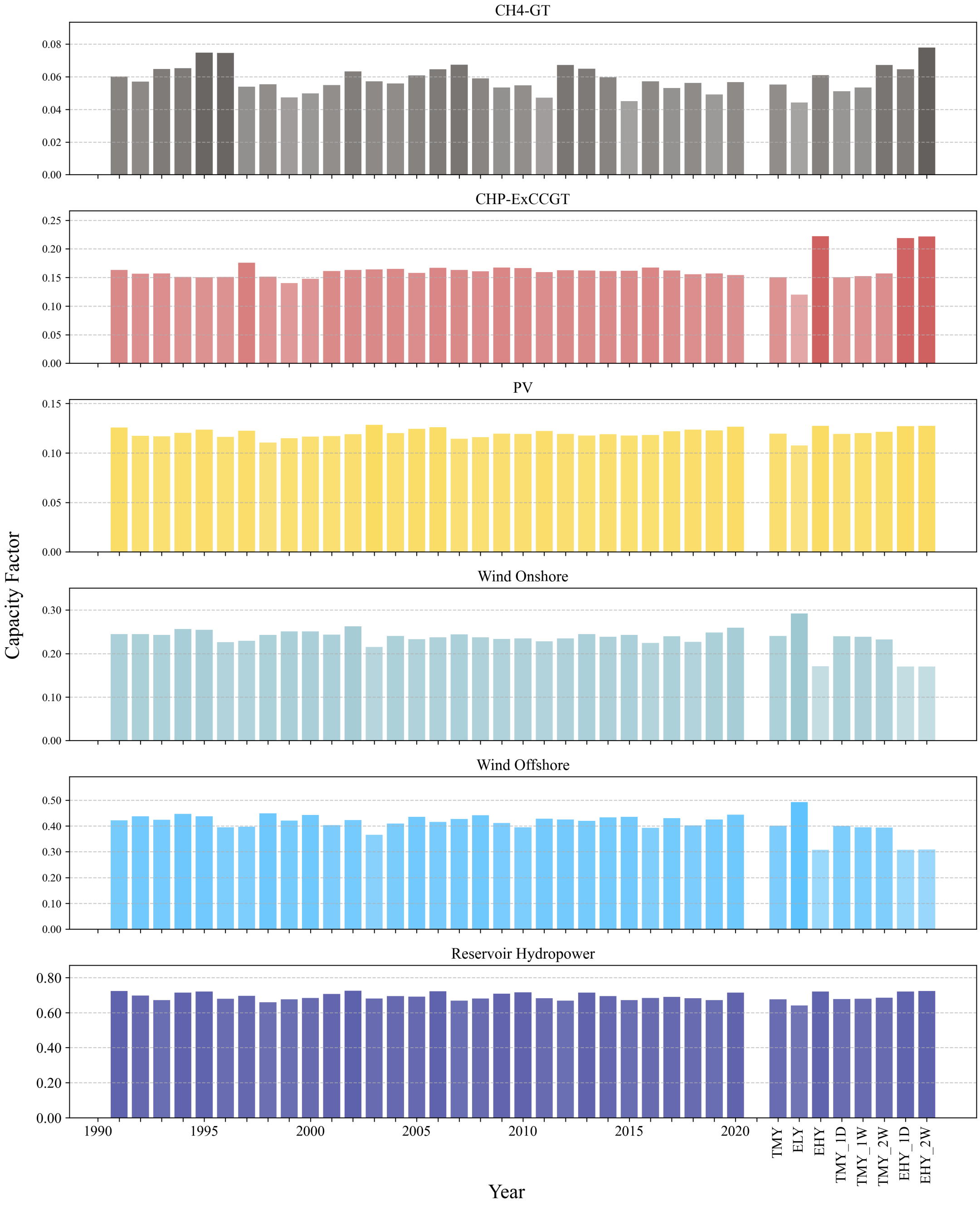

Figure 4.21.: Hypothetical capacity factors for various technologies across different weather years in the Exogenous-RE scenario for Europe. The capacity factor for Run-of-river hydro is constant at 1 across all weather years and is therefore not displayed in the figure.

To evaluate system robustness, the second model run is conducted as described in Section 3.3.3. The robustness of each weather year is presented in the heatmap in Figure 4.22. This figure reveals that 2015 is the most robust weather year, as its system configuration can accommodate not only all historical years but also all synthetic weather years. However, none of the other historical or synthetic weather years can accommodate 2015. 1997 ranks as the second most robust year, capable of accommodating 35 out of

38 years, including 27 historical years and all synthetic weather years. Following closely are TMY_1W, 2011, and EHY, accommodating 34, 34, and 33 years, respectively.

This outcome is somewhat unexpected, as the extreme years identified and synthesized in Section 3.3.2 (1997, ELY, EHY_1D, and EHY_2W) fail to accommodate certain historical years. For example, although EHY_2W exhibits the second-highest system costs and the highest CF for gas turbines, it can only accommodate 12 other years. A detailed discussion of this discrepancy is provided in Section 4.3.3. Additionally, ELY fails to accommodate any other year, while 2005 and 2008 can only accommodate ELY, making them the least robust years. This observation is consistent with the findings in the previous section.

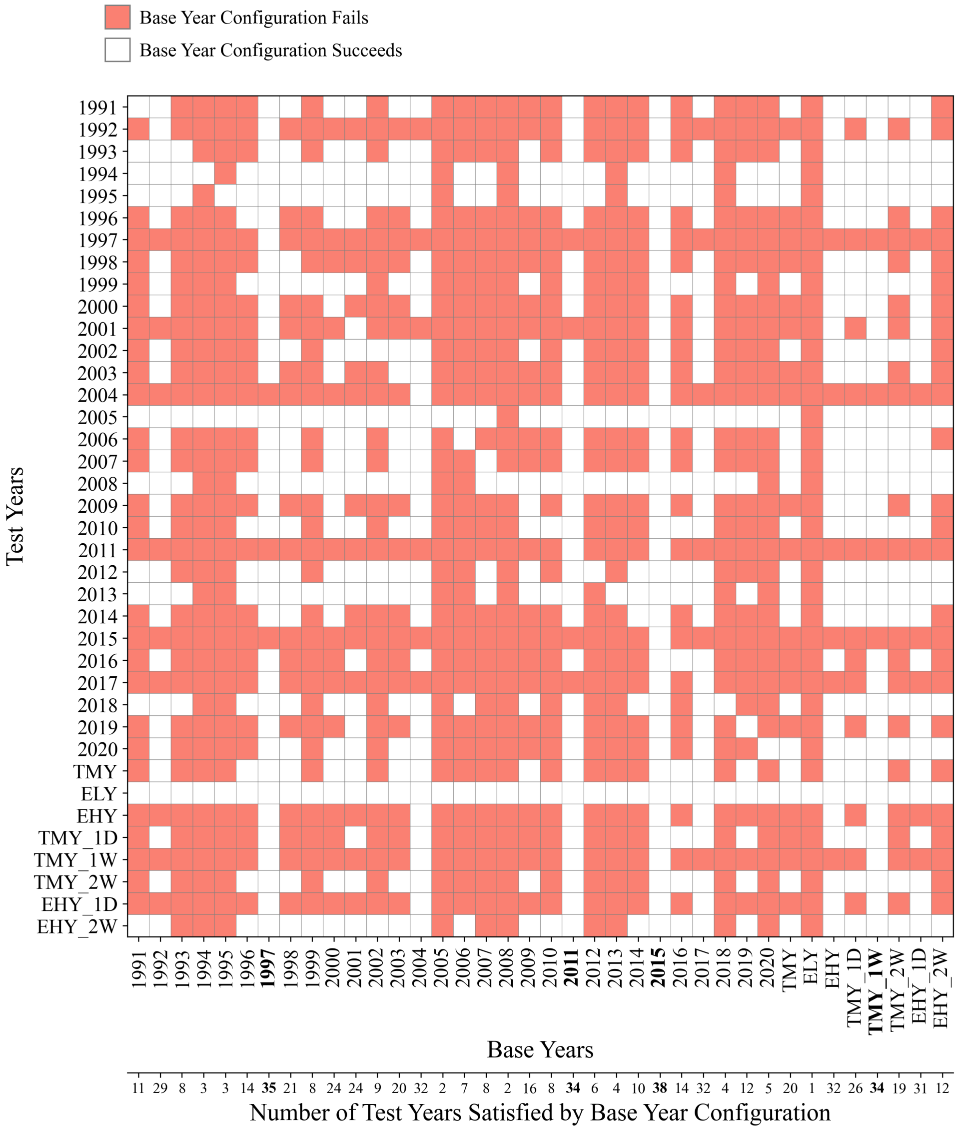

Figure 4.22.: Heatmap showing the ability of energy system configurations based on different base years in the Exogenous-RE scenario to accommodate various test years. The x-axis at the bottom quantifies the total number of test years satisfied by each base year configuration.

4.3.2. Endogenous-RE Expansion Scenario

In the Endogenous-RE scenario, the system costs for various weather years are presented in Figure 4.23. Compared to the Exogenous-RE scenario, the system costs of all weather years are lower in the Endogenous-RE scenario due to the ability to fully optimize the renewable energy capacities and, therefore, adapt to demand in a more cost-efficient way. However, the same conclusion can be drawn, as the figure reveals that 1997 continues to have the highest system costs among the 30 historical years. Similarly, synthetic weather years EHY, EHY_1D, and EHY_2W also have higher system costs compared to 1997, with EHY_1D being the year with the highest system costs.

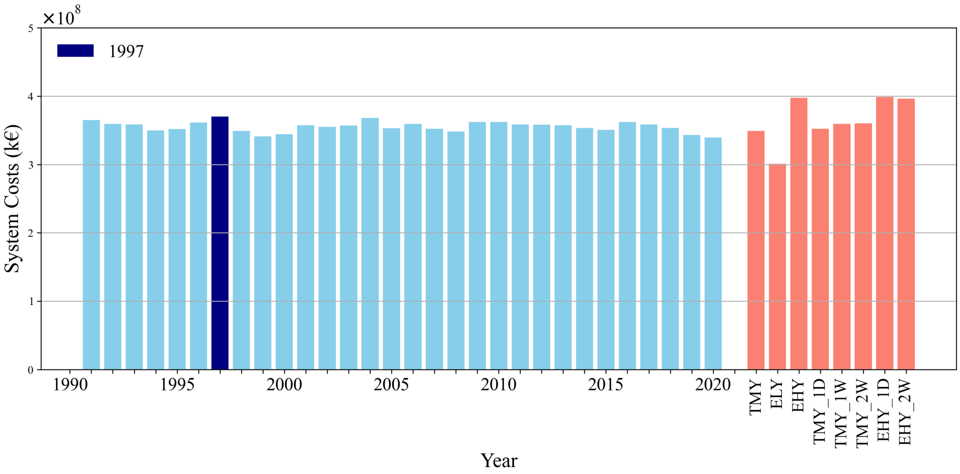

Figure 4.23.: System costs for various weather years in the Endogenous-RE scenario for Europe.

The capacity values for various technologies are presented in Figure 4.24. Similar to the Exogenous-RE scenario, in the Endogenous-RE scenario, PV and onshore wind continue to have the largest capacities compared to other technologies. However, it is worth noting that offshore wind capacity for all weather years is just 16.43 GW, which is the lower bound set for this scenario. This limited expansion is mainly due to the high costs of offshore wind turbines compared to other renewable energy technologies.

Meanwhile, onshore wind capacities remain relatively consistent across the weather years, in contrast to the more variable PV capacities. Compared to other years, PV capacities are significantly higher in the years EHY_2W (2122.5 GW), EHY_1D (2101.3 GW), and EHY (2085.2 GW). This is likely due to the limited wind availability in these years, and the system compensates for these extreme conditions by expanding PV as a cost-effective solution to mitigate the impact of persistent high residual load periods. Regarding gas turbines, the largest CH4-GT capacity is observed in 2000, with approximately 202.9 GW, followed by 2015 at 189.8 GW, and TMY_1W with 142.4 GW. For CHP-ExCCGT, the largest capacity is found in EHY_2W (157.7 GW), followed by EHY_1D (148.0 GW) and EHY (142.5 GW).

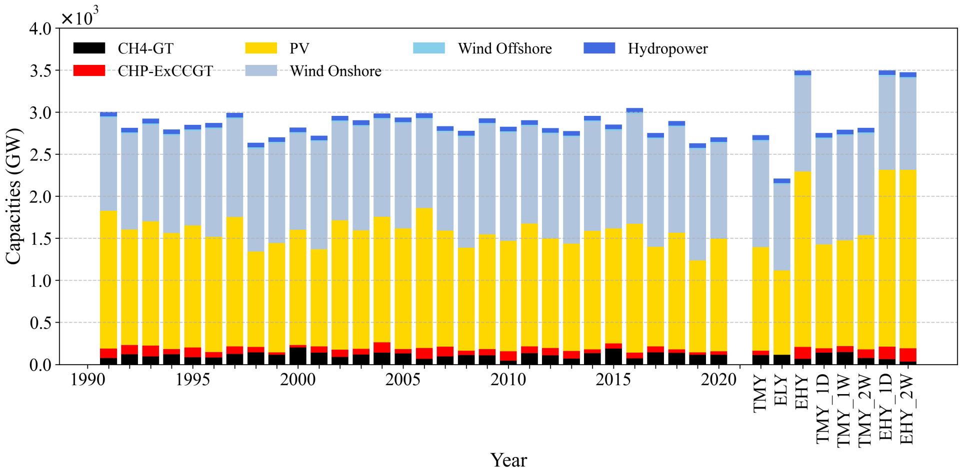

Figure 4.24.: Hypothetical capacity values for various technologies across different weather years in the Endogenous-RE scenario for Europe. For clarity, the capacities of reservoir hydro and run-of-river hydro are combined into a single hydropower capacity.

Similar to the Exogenous-RE scenario, the aggregated gas turbine capacities are shown in Figure 4.25. The lowest gas turbine capacity is observed in ELY, with only 113.79 GW, while the highest capacity occurs in 2004, at 263.6 GW, followed by 2015 (249.7 GW) and 1992 (229.6 GW). These values are lower than those in the Exogenous-RE scenario, where 2015 exhibits the highest gas turbine capacity at 280.37 GW.

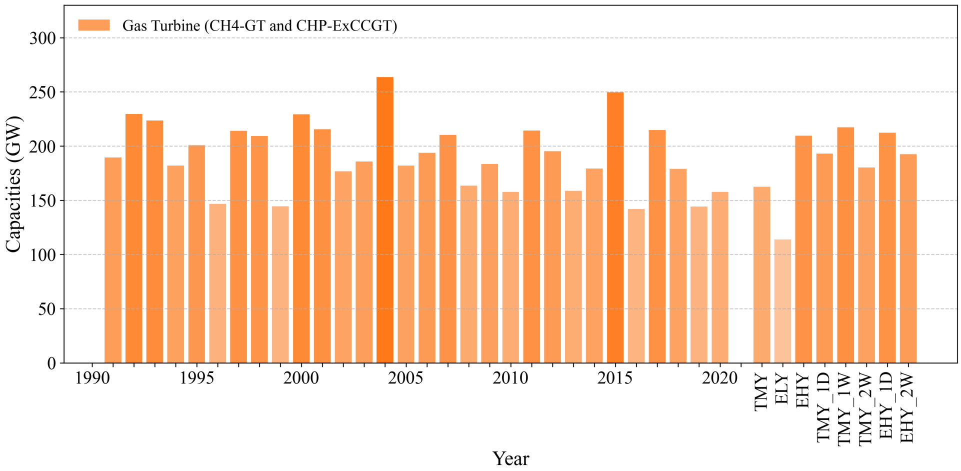

Figure 4.25.: Aggregated capacities of gas turbines CH4-GT and CHP-ExCCGT across different weather years in the Endogenous-RE scenario for Europe.

Meanwhile, Figure 4.26 illustrates the electricity generation across different weather years. From this figure, it is clear that the majority of electricity generation comes from PV and onshore wind. The increased electricity generation from PV in the years EHY, EHY_1D, and EHY_2W further indicates the system's reliance on PV expansion to compensate for high residual load conditions.

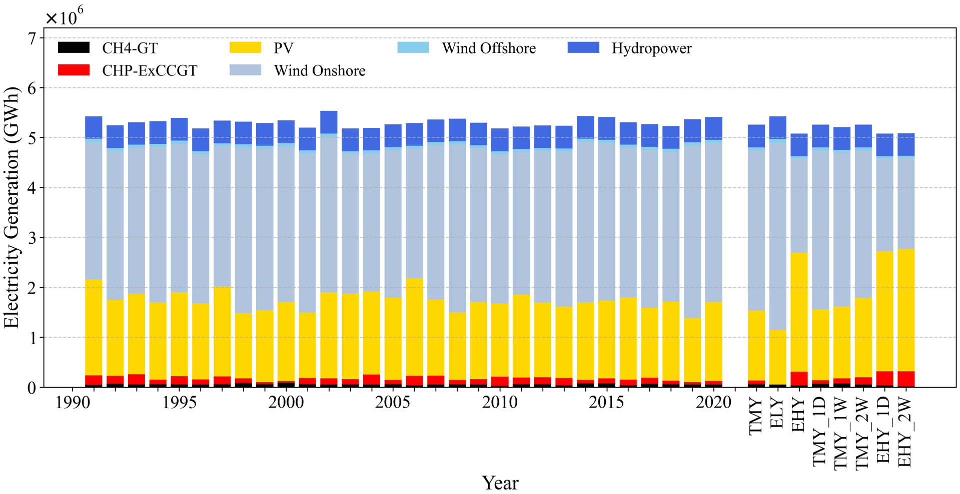

Figure 4.26.: Electricity generated for various technologies across different weather years in the Exogenous-RE scenario for Europe. For better visualization, the electricity generation of reservoir hydro and run-of-river hydro are combined into a single hydropower generation.

Figure 4.27 presents the CF for various technologies across different weather years. In this scenario, TMY_2W exhibits the highest CF for CH4-GT at 0.075, generating around 49.5 TWh of electricity. Other years with high CH4-GT CF include 2006 (0.074), 1995 (0.073), and 1996 (0.073), while the lowest CF is observed in 2004 at 0.043, generating 53.6 TWh of electricity. For CHP-ExCCGT, similar to the Exogenous-RE scenario, the significantly high CF is observed in the years EHY (0.218), EHY_1D (0.217), and EHY_2W (0.215), generating 272.5 TWh, 281.7 TWh, and 296.6 TWh of electricity, respectively. The lowest CF is observed in ELY (0.134), generating only 1.4 GWh of electricity.

As with the Exogenous-RE scenario, the CF for PV remains relatively consistent across all weather years. In contrast, onshore and offshore wind show low CF in the years EHY (0.191 and 0.315 for onshore and offshore wind, respectively), EHY_1D (0.191 and 0.315), and EHY_2W (0.191 and 0.317), generating 1887.7 TWh, 1857.1 TWh, and 1818.4 TWh from onshore wind, and 45.4 TWh, 45.3 TWh, and 45.6 TWh from offshore wind, respectively. In contrast, ELY exhibits the highest CF for wind energy, with 0.418 for onshore wind and 0.539 for offshore wind, generating 3745.0 TWh and 77.5 TWh of electricity, respectively, further indicating that ELY represents a year with favorable weather conditions for wind generation. Furthermore, similar to the case of 2015 in the Exogenous-RE scenario, while 2004 has the highest overall gas turbine capacity, its CH4-GT CF (0.043) is the lowest among all years, and the CHP-ExCCGT CF (0.183) ranks in the middle, generating 250.4 TWh of electricity in total.

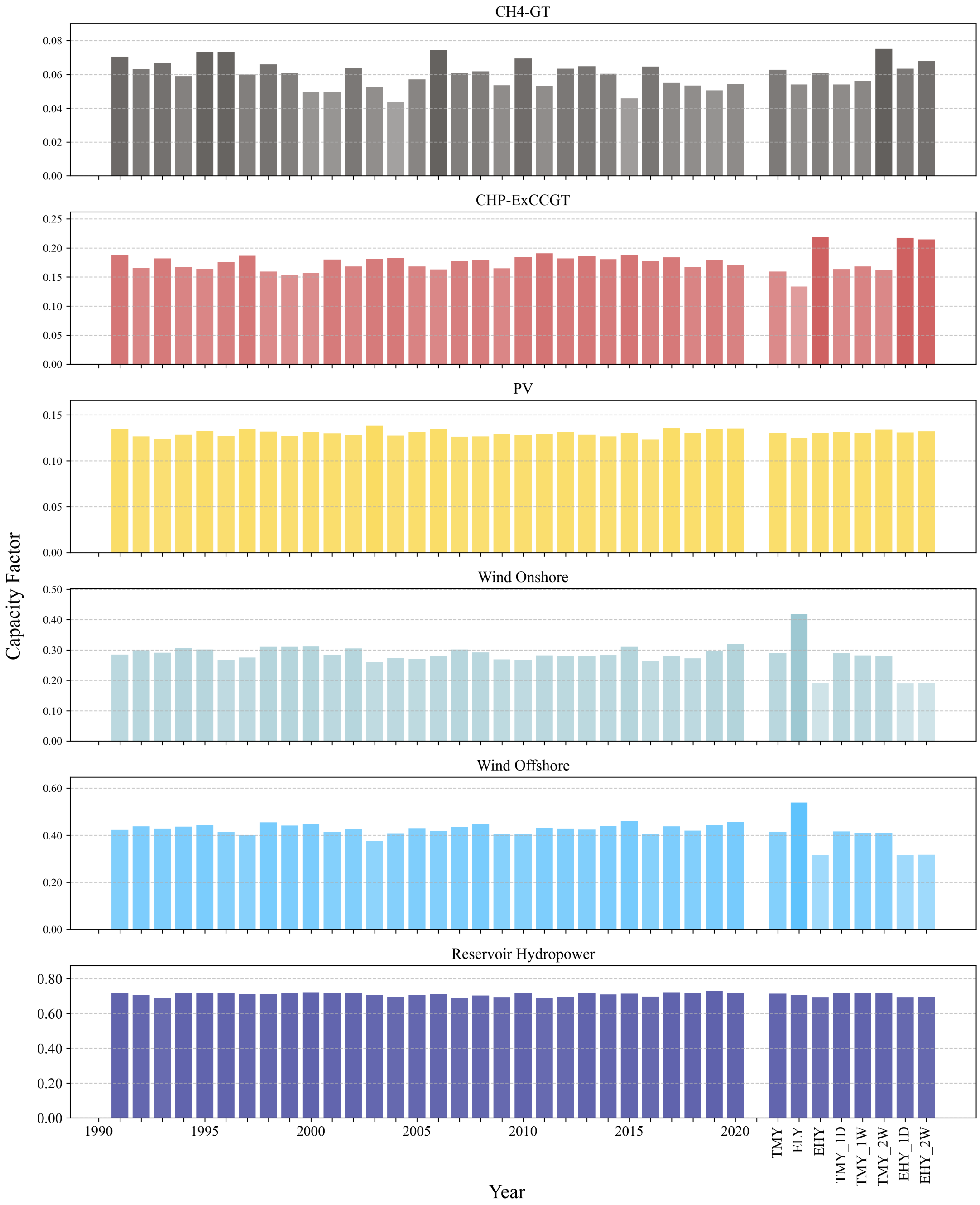

Figure 4.27.: Hypothetical capacity factors for various technologies across different weather years in the Endogenous-RE scenario for Europe. The capacity factor for Run-of-river hydro is constant at 1 across all weather years and is therefore not displayed in the figure.

For the second model run, the results are presented in the heatmap in Figure 4.28. This figure reveals that 2004 is the most robust year, capable of accommodating all historical and synthetic weather years. 1992 and 2015 emerge as the second most robust years, each accommodating 34 weather years. Close behind are 1997, 2001, and TMY_1W, each capable of accommodating 32 years. Additionally, similar to the Exogenous-RE scenario, ELY is the least robust year, as it fails to accommodate any other years.

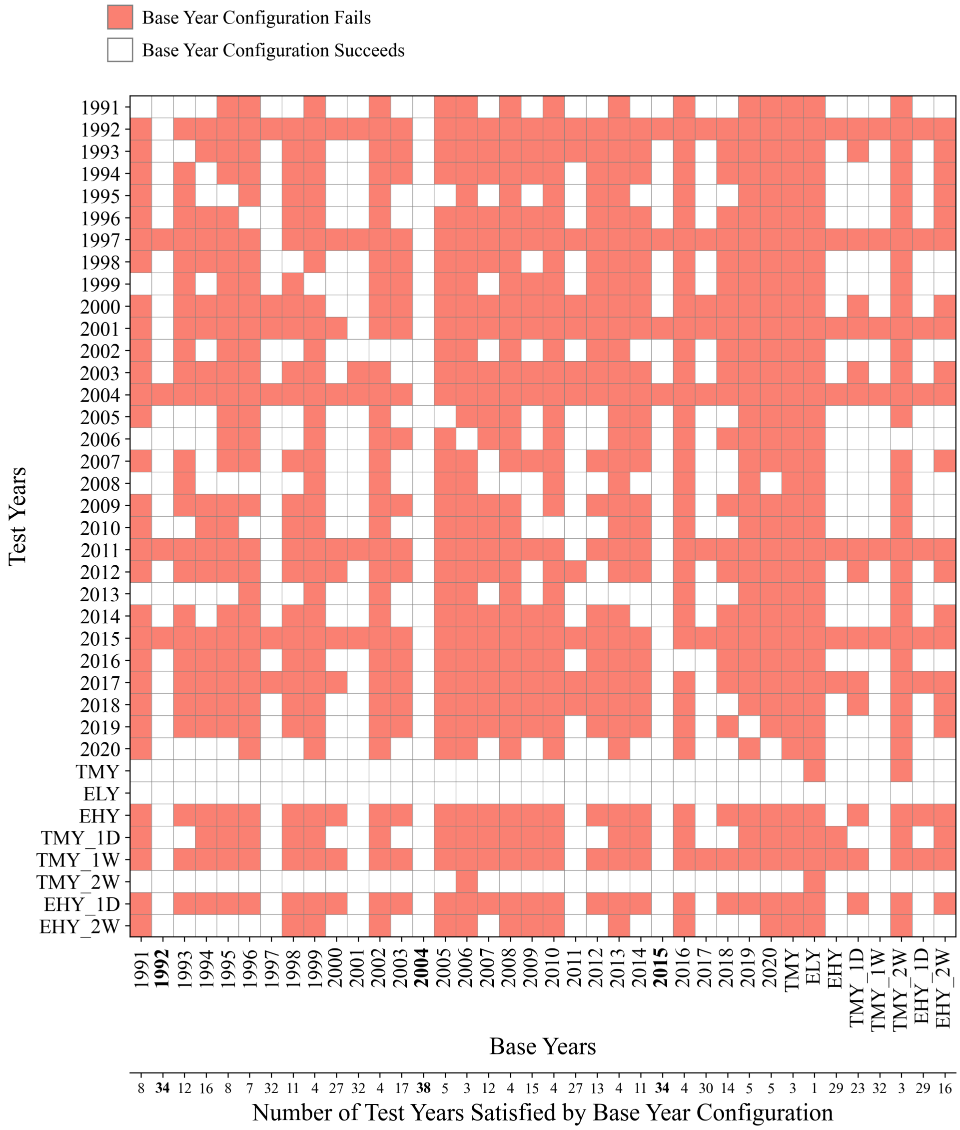

Figure 4.28.: Heatmap showing the ability of energy system configurations based on different base years in the Endogenous-RE scenario to accommodate various test years. The x-axis at the bottom quantifies the total number of test years satisfied by each base year configuration.

4.3.3. Summary and Discussion

Impact of Gas Turbine Usage on System Costs

Based on the previous analysis, years such as 1997, EHY, EHY_1D, and EHY_2W exhibit higher system costs compared to other years in both scenarios. This can be attributed to a strong correlation between system costs and the usage of gas turbines. As the usage of gas turbines increases, reflected by higher gas turbine CF, the system relies more on gas turbine operation, leading to higher fuel consumption and carbon costs. In contrast, years with low usage of gas turbines, characterized by lower gas turbine CF, such as ELY in both scenarios, tend to have greater contributions from abundant renewable energy generation, thus having the lowest system costs. The scatter plots in Figure 4.29 confirm this relationship, showing a high positive correlation between the overall gas turbine CF of both CH4-GT and CHP-ExCCGT and system costs, with Correlation Coefficients (CC) of 0.89 in the Exogenous-RE scenario and 0.83 in the Endogenous-RE scenario.

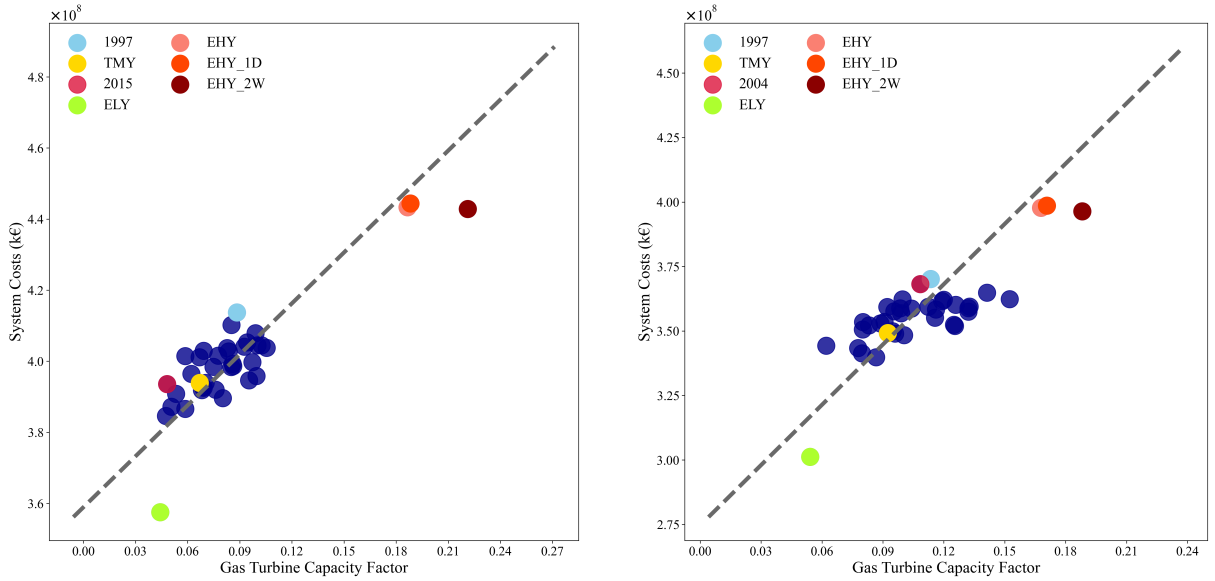

(a) Exogenous-RE scenario (CC = 0.89)

(b) Endogenous-RE scenario (CC = 0.83)

Figure 4.29.: Scatter plots showing the relationship between aggregated gas turbine CF and system costs. Years with low gas turbine CF, such as ELY, have low system costs, while years with high gas turbine CF, such as EHY, EHY_1D, and EHY_2W, have high system costs.

Impact of Gas Turbine Capacities on System Robustness

However, higher system costs do not necessarily indicate a more robust system. As shown in the previous sections, 2015 in the Exogenous-RE scenario and 2004 in the Endogenous-RE scenario are the most robust weather years. A common factor between these years is that their aggregated gas turbine capacities are the highest among all historical years. This relationship is further illustrated in the scatter plot in Figure 4.30, which depicts the correlation between the aggregated gas turbine capacity and the number of years satisfied. In the Exogenous-RE scenario, the CC is 0.83, while in the Endogenous-RE scenario, it is 0.82. These high correlation coefficients also indicate a strong positive correlation between gas turbine capacity and a year's ability to accommodate other years, suggesting that higher gas turbine capacities increase the likelihood of accommodating other years.

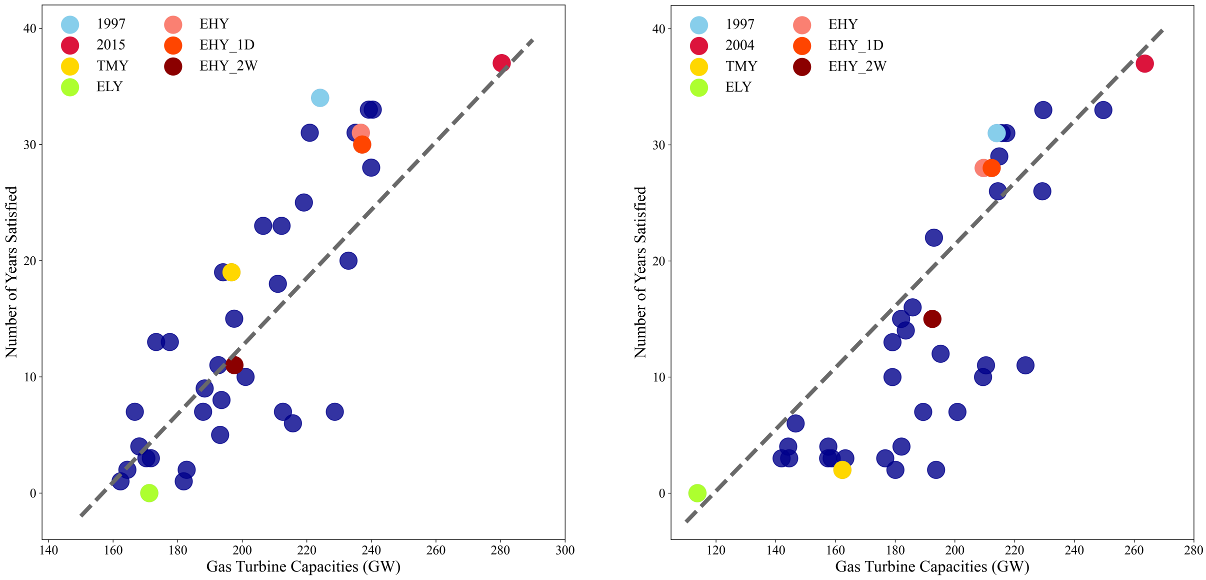

(a) Exogenous-RE scenario (CC = 0.83)

(b) Endogenous-RE scenario (CC = 0.82)

Figure 4.30.: Scatter plots showing the relationship between aggregated gas turbine capacities and the number of years satisfied. Years with low gas turbine capacity, such as ELY, fail to accommodate any other years, while years with high gas turbine capacity, such as 2015 in the Exogenous-RE scenario and 2004 in the Endogenous-RE scenario, can accommodate all other weather years.

In addition to having the highest gas turbine capacities, 2015 and 2004 share another characteristic: the CF for gas turbines, especially the CH4-GT is relatively low compared to other years. This indicates that, despite their substantial gas turbine capacities, these turbines are less frequently used throughout the year. However, this indicates that there may be severe extreme periods within the year that require such a high gas turbine capacity to satisfy the demand. In other words, their operation is likely required for specific short-term periods of high demand or low renewable generation, rather than sustained, prolonged usage.

Meanwhile, it is evident that more robust years such as 2015 and 2004 in their respective scenarios, tend to rely more on CH4-GT, whereas years with high system costs and prolonged periods of high residual load, such as EHY, EHY_1D, and EHY_2W, predominantly use CHP-ExCCGT. This is likely due to the characteristics of these gas turbines. In the model configuration of this dissertation, CHP-ExCCGT has higher investment costs compared to CH4-GT. For years with short-term periods of high residual load, CH4-GT is the more favorable option due to its lower costs. However, when a year experiences prolonged periods of high residual load, the system favors CHP-ExCCGT, as it can provide both electricity and heat, making it a more cost-effective choice in the long run.

Impact of Short-term Events on Gas Turbine Capacities

To investigate whether 2015 and 2004 exhibit short-term extreme events that are the most severe among historical years, an analysis is conducted on the periods during which the energy system configuration, optimized for years such as 1997, fails to accommodate 2015 and 2004 in their respective scenarios. Specifically, periods with high slack values in the optimization results are examined.

The results reveal that, in the Exogenous-RE scenario, the system configuration of 1997 is unable to accommodate 2015 during a critical 16-hour period (i.e., hours 1002 to 1017). To assess the extremity of this period, a 16-hour window is rolled across the residual load time series in 2015, identifying that the most extreme 16-hour period indeed occurs between hours 1002 and 1017, as shown in Figure 4.31a. This period not only represents the most critical window in 2015 but also the most extreme across all historical years, as illustrated in Figure 4.32a, which compares the cumulative residual load for the 16-hour window across all years. Similarly, in the Endogenous-RE scenario, the system configuration of 1997 fails to accommodate 2004 due to a 17-hour critical period (i.e., hours 8321 to 8337). This has been identified as the most extreme 17-hour event in 2004 and across all historical years, as shown in Figures 4.31b and 4.32b.

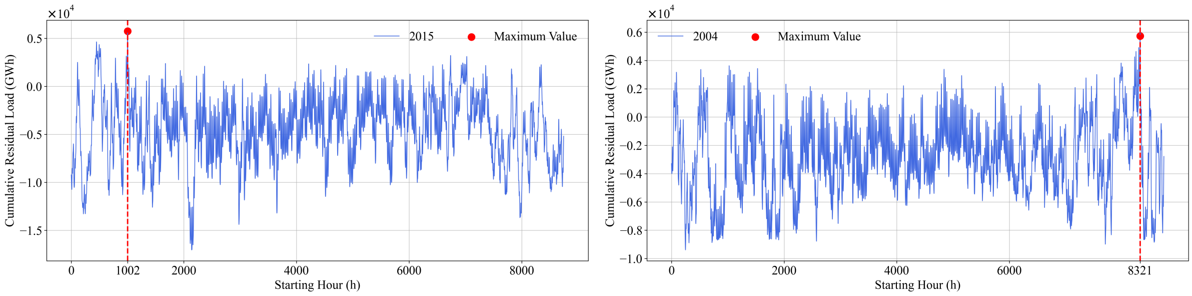

(a) Cumulative residual load in 2015 for a 16-hour window in the Exogenous-RE scenario. The most extreme 16-hour event occurs between hours 1002 and 1017.

(b) Cumulative residual load in 2004 for a 17-hour window in the Endogenous-RE scenario. The most extreme 17-hour event occurs between hours 8321 and 8337.

Figure 4.31.: Cumulative residual load in 2015 for the Exogenous-RE scenario and 2004 for the Endogenous-RE scenario.

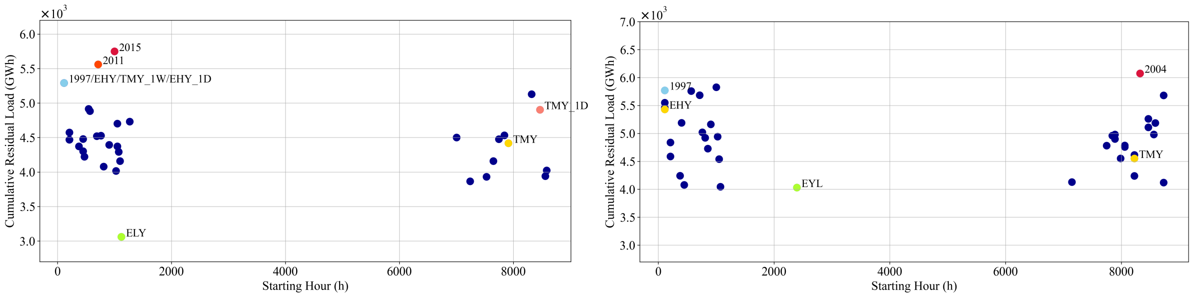

(a) Exogenous-RE scenario

(b) Endogenous-RE scenario

Figure 4.32.: The starting hour and cumulative residual load of the most extreme 16-hour and 17-hour events for each weather year in Exogenous-RE and Endogenous-RE scenarios, respectively. The intensity of these events, as indicated by the cumulative residual load, shows that the most severe 16-hour event across all historical years in the Exogenous-RE scenario occurs in 2015, starting at hour 1002, while the most severe 17-hour event in the Endogenous scenario occurs in 2004, starting at hour 8321

These findings indicate the importance of short-term extreme events. In fact, the intensity of these events is closely correlated with gas turbine capacities, as indicated in Figure 4.33. In the Exogenous-RE scenario, the CC is 0.82, and in the Endogenous-RE scenario, it is 0.90. These correlations suggest that the intensity of these short-term extreme events necessitates high gas turbine capacity, thereby contributing to the system's robustness in accommodating a broader range of years.

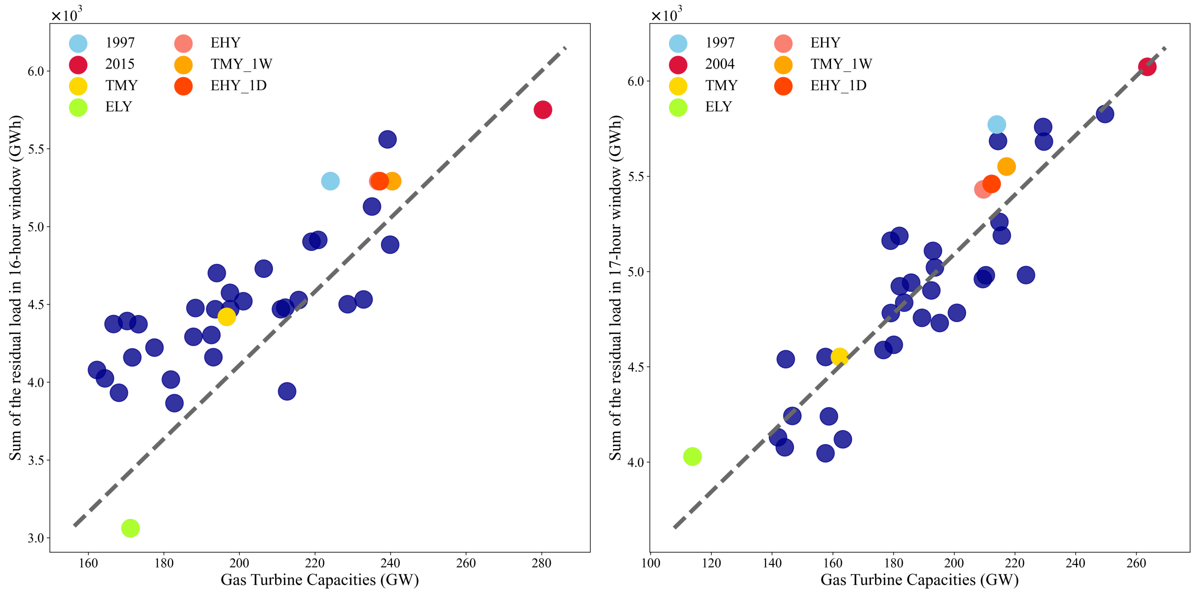

(a) Exogenous-RE scenario (CC=0.82)

(b) Endogenous-RE scenario (CC=0.90)

Figure 4.33.: Scatter plots showing the relationship between the severity of extreme weather events and gas turbine capacity, with a fixed window size. Years with low gas turbine capacity, such as ELY, exhibit low cumulative residual load, while years with high gas turbine capacity, such as 2015 and 2004 in their respective scenarios, show high cumulative residual load.

Window Size Selection for Short-term Events

In the previous analysis, 16-hour and 17-hour windows are identified as critical for the Exogenous-RE and Endogenous-RE scenarios, respectively. The intensity of extreme events within these windows strongly correlates with gas turbine capacity and, consequently, influences system robustness. However, to determine whether these are the only influential window sizes or if other durations better represent the extremity of extreme events, further analysis is conducted.

The analysis begins by examining the correlation between extreme event intensity and gas turbine capacity as a function of window size, as indicated in Figure 4.34. The results reveal that the window sizes yielding the highest correlation coefficients are 17 hours in the Exogenous-RE scenario and 18 hours in the Endogenous-RE scenario. This suggests that while the initially identified windows are close to optimal, slightly longer windows may better capture the impact of extreme events on system robustness

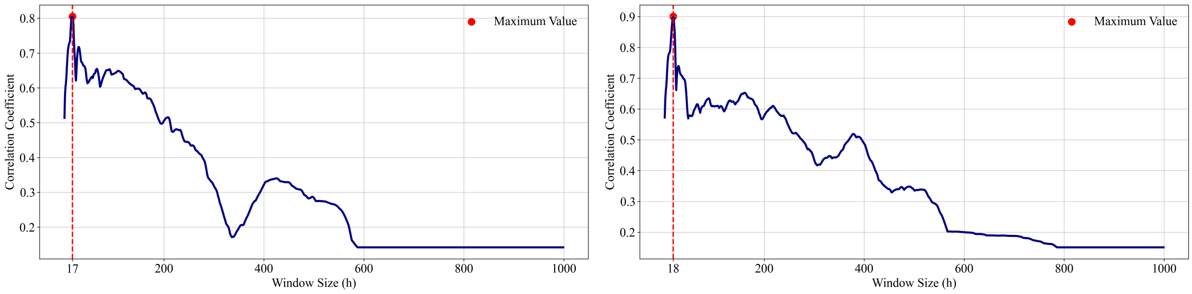

(a) Exogenous-RE scenario

(b) Endogenous-RE scenario

Figure 4.34.: CC between extreme event intensity and gas turbine capacity as a function of window size. The x-axis represents the window size, while the y-axis shows the CC. The highest CC is observed for a window size of 17 hours and 18 hours in Exogenous-RE and Endogenous-RE scenarios, respectively.

Additionally, Figure 4.35 ranks the weather years based on the severity of the extreme events across different window sizes. In the Exogenous-RE scenario, 2015 is the most extreme year in terms of short-term extreme events for window sizes between 14 and 18 hours, while 1997 stands out for its long-term extreme events, particularly for window sizes between 100 to 200 hours and 600 to 1000 hours. In the Endogenous-RE scenario, 2004 is the most extreme year for short-term events within the 16 to 20-hour window size.

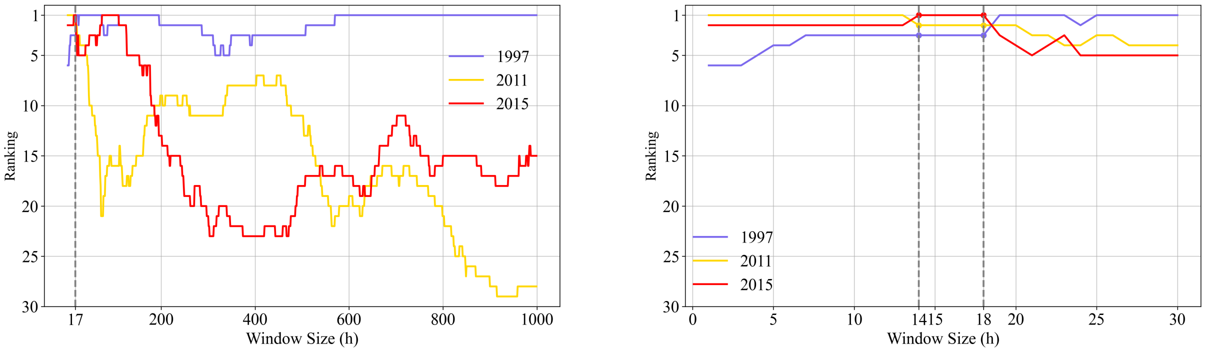

(a) Window size until 1000 for the years 1997, 2011, and 2015 in the Exogenous-RE scenario

(b) Zoom in view until window size to 30 in the Exogenous-RE scenario

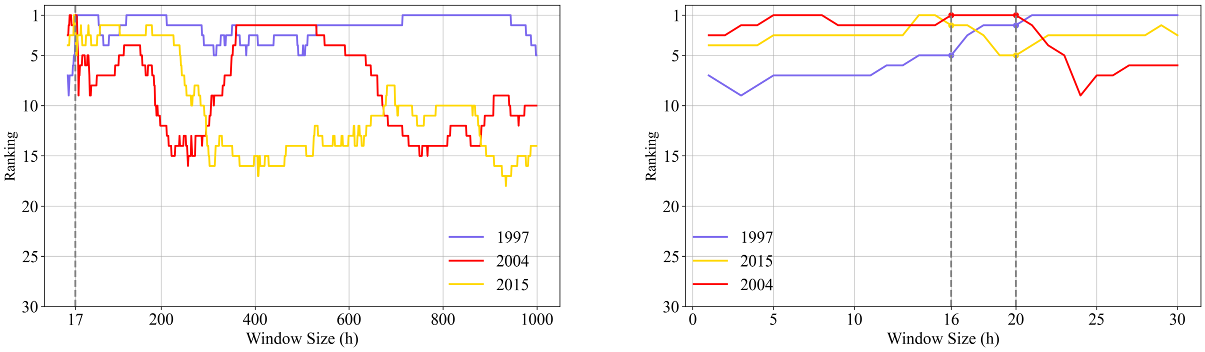

(c) Window size until 1000 for the years 1997, 2004, and 2015 in the Endogenous-RE scenario

(d) Zoom in view until window size to 30 in the Endogenous-RE scenario

Figure 4.35.: Ranking of the selected weather years based on the intensity of extreme events across various window sizes for Exogenous-RE and Endogenous-RE scenarios.

5. Limitations and Outlooks

This dissertation investigates two key uncertainties in the weather-dependent input data for ESMs: wind speed and electricity demand. By analyzing the residual load derived from these inputs, it further examines the impact of extreme weather conditions on energy systems. However, it is important to note that ESMs depend on a wide range of weather-driven inputs, many of which are not addressed in this work. In the context of renewable energy generation, this study focuses exclusively on wind speed data. Other important meteorological inputs, such as solar irradiation, including GHI and DNI, which influence solar PV potential, and hydrological data that determine hydro power inflows, are not addressed here. Moreover, weather data influences more than just renewable energy generation. As outlined in Section 2.3.3 and Table 2.3, extreme weather events can affect various components of the energy system, including transmission and distribution networks, grid performance, and battery storage efficiency, and so on. These broader impacts, however, fall outside the scope of this dissertation.

5.1. Regression-Based Statistical Downscaling Method

The proposed Machine Learning based statistical downscaling method demonstrates significant improvements in ERA5 data, primarily in Class 3 regions, characterized by complex terrain. However, no significant improvements are observed in Class 1 and Class 2 regions. One possible explanation is that the topographic influences in these regions are so minimal that considering topographic-related features in a machine-learning regression model would result in inaccurate predictions. However, to better correct wind speeds in Class 1 and Class 2 regions, one possible approach is to increase the amount of training data for the regression model. Given that the current regression model is solely trained for MeteoSwiss data, incorporating more observations from Class 1 and Class 2 stations in diverse regions could lead to improved outcomes. Another possibility is to incorporate topography-independent features into the model, such as weather regimes and air pressure. These features, as previously noted in studies such as (Brayshaw et al., 2011; Garrido-Perez et al., 2020), play a more significant role in affecting the quality of reanalysis data in Class 1 and Class 2 regions, and should be considered accordingly.

Another limitation of the proposed statistical downscaling approach is its focus on downscaling wind speeds at 10 meters height. In wind energy modeling, however, wind speeds at higher altitudes, typically corresponding to wind turbine hub heights (e.g., 80 to 150 meters), are more relevant. This limitation arises due to the limited availability of wind speed observations at these higher altitudes, as most weather stations only record wind speeds at 10 meters. Nevertheless, the same model can be applied to downscale wind speeds at higher altitudes once a sufficient amount of observational data becomes available. In the meantime, to estimate wind speeds at turbine-relevant heights, the logarithmic wind profile, or other vertical extrapolation methods such as the power law, can be used to interpolate from the downscaled 10-meter wind speeds, as demonstrated in various studies (Tennekes, 1973; Jung and Schindler, 2021; Xu et al., 2018; Lopez-Villalobos et al., 2022).

Additionally, the proposed statistical downscaling method shares several common limitations with other statistical downscaling approaches. It relies heavily on high-quality, long-term observational datasets; in this dissertation, for instance, the accuracy of the model depends significantly on the quality of MeteoSwiss and DWD data used for training. Furthermore, statistical downscaling methods offer limited physical representation. Unlike dynamical models, they do not explicitly simulate atmospheric processes, which may result in the omission of various interactions within the climate system. Lastly, one of the most fundamental limitations is the assumption that the statistical relationships developed under current climate conditions will remain valid in the future (Van Uytven et al., 2020; Ekström et al., 2015b). Given the ongoing changes in local climate patterns driven by climate change, such relationships may no longer hold, posing challenges for future applications.

It is also worth noting that the spatial resolution of the final wind speed predictions is determined by the topographic data used. Since the topographic metrics in this dissertation are derived from a DEM with approximately 1 km × 1 km resolution, the resulting local wind speed estimates have the same resolution. However, in practical applications, this method can be adapted to different resolutions depending on the DEM used.

Meanwhile, it is also worth mentioning that this dissertation focuses exclusively on the spatial downscaling of wind speed. In comparison, temporal resolution is also particularly important, especially for solar irradiation, as it affects solar PV modeling and thus influences grid stability and storage requirements. Various temporal downscaling techniques have been widely studied in this direction (Buster et al., 2021; Bailey et al., 2024; Castillejo-Cuberos et al., 2024; Zhang et al., 2018). For wind energy, capturing short-term variability is also essential for accurately modeling wind power fluctuations. However, temporal downscaling of wind speed is more challenging than solar irradiation due to the higher spatiotemporal complexity and variability of wind patterns (Omoyele et al., 2024). Methods such as dynamic downscaling, which considers sub-diurnal meteorological effects (Horvath et al., 2011), or statistical downscaling of wind speed distributions (Shin et al., 2018; Carapellucci and Giordano, 2013; Olauson et al., 2017), have been addressed in existing literature.

5.2. Modeling Future Electricity Demand Under Evolving TRF Conditions

The second source of uncertainty in the input data for ESMs addressed in this dissertation is electricity demand. By examining the dynamic characteristics of the TRFs, this dissertation enables the projection of electricity demand under various scenario assumptions. However, electricity demand is only one aspect of the overall energy demand modeled in ESMs. Heating and cooling demands are also crucial components, as they represent a significant share of total energy demand and are also highly sensitive to temperature variations. Although this dissertation does not directly model heating and cooling demands, the derived BPTs can be used to calculate HDD and CDD, which in turn can be used to estimate heating and cooling demand, as demonstrated in previous studies (Gils, 2015; Harvey, 2020).

When using the piecewise regression approach to construct TRFs across different countries, the model explained in Section 3.2.2 shows good overall performance. The mean RMSE and R^2 scores across these regions are 0.114 and 0.671, respectively, as shown in Table 4.6, suggesting that the piecewise model captures the TRFs of electricity demand reasonably well. However, certain regions, such as Italy, Luxembourg, and Portugal, show lower R^2 scores, indicating a weaker correlation between temperature and electricity demand. These findings indicate the need for more detailed, region-specific analyses to better understand the diverse drivers of electricity demand patterns in these regions.

Another significant limitation of the proposed method is the assumption of a constant y-value at the knot point, which introduces uncertainties into the analysis. Given the evolving economy and population dynamics, the y-value is unlikely to remain constant in the future. Since the y-value is influenced by various socio-economic factors and is rarely addressed in existing literature, future research could explore which socio-economic variables influence the y-value and how these factors impact its behavior. These investigations can better capture the dynamic characteristics of TRFs and enable more accurate and realistic electricity demand projections.

In addition, another notable limitation arises from the simplifications made in the scenario design, which considers only four residential building-related variables. In reality, electricity demand is shaped by a complex set of interrelated factors. Other socio-economic variables such as consumer behavior, evolving thermal comfort expectations, electricity prices, and national development trajectories also play a role in determining the form of TRFs. Additionally, technological, infrastructural, and policy-related elements, such as the implementation of Demand Side Management (DSM) strategies for both heating (e.g., heat pumps) and non-heating loads (e.g., electric vehicles), improvements in energy storage technologies, enhanced grid flexibility, and cross-border electricity exchange, can also significantly affect future residential electricity demand. Expanding scenario frameworks to include these variables would contribute to a more comprehensive understanding of potential TRF developments.

In the meantime, a substantial research gap remains in understanding how thermal insulation measures, the adoption of heat pumps, and the application of passive cooling techniques affect the slope of TRFs. Due to the limited availability of empirical studies, particularly on passive cooling, the assumptions made in this dissertation rely on estimated changes to slope values. As further research becomes available, more evidence-based assumptions can be incorporated to reduce uncertainty and improve the robustness of scenario outcomes.

Furthermore, the proposed method solely focuses on aggregated electricity demand, yet examining demand disaggregated by sector might yield further insights, as the influence of climate is different for different sectors (Zamanipour et al., 2023; MacMackin et al., 2019; Chang et al., 2016). Currently, comprehensive sector-specific electricity demand data for the study regions is unavailable. Once such data becomes accessible, sectoral disaggregation may enhance both the accuracy of piecewise linear regression models and the reliability of future electricity demand projections. Moreover, the analysis is limited to daily electricity demand. To achieve higher temporal resolution, incorporating intra-day variation based on typical demand patterns, as demonstrated in (Castillo et al., 2022), offers a promising approach.

5.3. Incorporating Synthetic Extreme Weather Years into the ESOM

This dissertation further investigates the influence of extreme weather events by proposing several methods for identifying and generating SWYs that capture extreme weather conditions across all historical years. The results demonstrate that traditional methods, such as TMY and other SWYs focusing on long-term extreme weather events (e.g., 1997 and EHY), fail to deliver energy system configurations that accommodate all historical weather years. This indicates the need for more representative weather years that can better capture the extreme conditions relevant to energy systems modeling. However, it is important to note that while years with long-term extreme events, such as 1997 and EHY, may not accommodate every historical year, they still successfully cover the majority of them. This is particularly important in Endogenous-RE scenarios, where residual load calculations prior to optimization are not possible.

One key limitation of the proposed SWYs generation method is the lack of spatial resolution in the analysis. Extreme events identified in the overall residual load do not necessarily reflect similar patterns across each country within the model. Different countries may experience varying weather conditions, which could affect residual load differently. Future work should incorporate spatial variation to provide a more detailed understanding of how extreme events affect different regions and improve the applicability of the findings.

Another limitation concerns the definition of extreme events, which varies widely across studies. In this dissertation, two types of extreme events are identified to generate synthetic weather years. The first, introduced in Section 3.3.2, defines extreme conditions as periods where residual load exceeds the 95th percentile of all historical residual loads. The second, described in Section 3.3.2, identifies one-day, one-week, and two-week extreme events based on the periods with the maximum consecutive residual load across all years. However, there is no widely recognized framework for defining and quantifying weather conditions in the context of energy systems (Kittel and Schill, 2024). Once such a standardized approach is developed, future research could align the criteria used in this study with widely accepted definitions, making the generated synthetic weather years more reliable and consistent with established standards.

Furthermore, while SWYs proposed in this dissertation are designed to represent extreme conditions, they may not fully capture the variability of extreme events in reality. These SWYs may be overly generalized or fail to capture other critical short-term extreme events not included in the analysis. Additionally, the deterministic approach used in this dissertation may not reflect long-term variability in climate patterns, potentially leading to less accurate representations of extreme conditions. Future research could explore stochastic methods to provide a more comprehensive investigation of synthetic weather years, better accounting for the uncertainty and variability in climate data.

The proposed approach also reveals that extreme weather events, particularly short-term events, are key factors in determining system robustness. However, it is important to note that demand-side management techniques, such as demand shedding and shifting, as well as the use of hydrogen in gas turbines, are not considered within the scope of the model. While short-term extreme weather events play a critical role in system robustness, demand-side management could mitigate the impacts of these extreme periods. Once short-term events are addressed using such techniques, long-term extreme weather events may become more critical for system robustness, as they may require sustained capacity adjustments over extended periods.

Meanwhile, sector-coupled ESOMs are highly sensitive to inputs and the model scope. The complex interactions between system components can either mitigate or amplify the impact of extreme weather events. For example, while 17-hour and 18-hour extreme events are critical in the findings, other factors, such as various storage technologies, might play an important role in mitigating the short-term extreme events. However, storage capacities do not significantly affect the handling of short-term extreme events, as shown in Figure A.7 and Figure A.8 in the Appendix A.4. This suggests that, within such short time frames and with events encompassing a wide geographical scope, gas turbines are more competitive than storage technologies. Future studies could explore scenarios where storage technologies become more competitive and investigate their role in enhancing the system's robustness. Similarly, incorporating a wider range of dispatchable generation technologies, including geothermal energy, biomass energy, and nuclear power, as applicable, in the assessment can enhance the understanding of system operation and improve flexibility during periods of low wind and solar resource availability.

Besides the storage technologies, renewable energy performance or broader geospatial scope, may also significantly influence the system's robustness. These additional factors could lead to different results and conclusions. Future research may also aim to identify a minimum viable model scope that can effectively capture the influence of extreme weather events. This would isolate the impact of short-term extreme events by eliminating the influence of other factors, providing a clearer understanding of their role in system robustness. As model complexity increases, more comprehensive analyses are needed to investigate the interaction between extreme weather events and system components. This simplified model could serve as a foundational tool for identifying critical weather patterns and their impacts without the complexity of full-scale sector coupling. Building on the findings of this study, future research can refine methodologies for designing robust energy systems that are resilient to a wide range of extreme weather conditions.

6. Conclusions

This dissertation addresses three critical sources of uncertainty in long-term energy systems modeling: the limitations of coarse spatial resolution in weather input data, the challenges in projecting electricity demand under varying climate and policy scenarios, and the influence of extreme weather events on system robustness. To mitigate these uncertainties, distinct methodologies are developed and applied to each source of uncertainty.

To improve the spatial resolution of input weather data, this dissertation focuses on wind speed and indicates the crucial role played by topographic conditions in determining the spatially disparate quality of ERA5 wind speed data. Complex terrain regions, as characterized as Class 3 regions through the preprocessing step, show the highest degree of inaccuracies in the ERA5 wind speed data. To address this, a Machine Learning based statistical downscaling approach is developed to downscale ERA5 data using local observations and topographic features. The robustness of the regression model is evaluated by comparing its output against measurement and other reanalysis data across different years and locations. The method proves effective in improving data quality, particularly in complex terrain regions, enabling downscaling from a 31 km × 31 km resolution to resolutions as fine as 1 km × 1 km, depending on the resolution of the DEM used. Unlike existing studies that focus solely on wind speed distribution downscaling, site-specific downscaling, or computationally intensive dynamic downscaling methods, this approach offers a scalable and computationally efficient solution for large-scale ERA5 wind speed downscaling. It emphasizes the critical role of topography in local wind speed estimation and requires only simple inputs, enabling accurate, high-resolution local wind resource assessment.

To project future electricity demand, a comprehensive method that incorporates dynamic changes in Temperature Response Functions (TRFs) is proposed. The results indicate that compared to using stationary TRFs, incorporating dynamic changes can lead to significant differences in future electricity demand patterns. The results reveal that the impact of policy intervention on electricity demand differs across regions. In northern and intermediate European countries, an increase in winter demand until around 2050 is anticipated due to the increase in electrification rates. However, improving the thermal insulation for buildings could potentially lead to decreased winter demand in the long run. Conversely, in Southern European countries, increased space cooling usage is projected to significantly increase summertime electricity demand. Addressing this increase may require investments in more flexible energy systems to manage peak demands. One proposed solution is the implementation of effective passive cooling measures in residential buildings, which could significantly reduce electricity demand during the summer months. Overall, this dissertation presents the first known study to model the dynamics of TRFs in the context of future policy and climate change. By capturing the dynamic nature of TRFs, shifts in demand patterns under varying climate and policy interventions can be identified, ultimately providing more realistic projections of future electricity demand.

To address the uncertainty posed by extreme weather events, this dissertation explores the critical role of short-term extreme weather events in influencing the capacities of dispatchable generation technologies, such as gas turbines, and therefore determining the robustness of energy system designs to different weather conditions. By generating and applying historical and Synthetic Weather Years (SWYs) in two energy system configuration scenarios, Exogenous-RE and Endogenous-RE scenarios, this dissertation demonstrates that traditional approaches like Typical Meteorological Year, as well as contemporary methods for creating SWYs, fail to fully capture the extreme conditions required for designing weather-robust systems. The results show that robust energy systems exhibit the highest gas turbine capacities and are designed using years with the most extreme short-term events among all historical years. Compared to existing literature, which primarily focuses on the generation of representative weather years, this dissertation not only integrates extreme weather events into the generation of SWYs but also focuses on residual load, which is rarely addressed in current studies. By analyzing two energy system scenarios, this dissertation reveals a strong correlation between the capacity of dispatchable generation, short-term extreme events, and overall system robustness.

In summary, this dissertation contributes to a deeper understanding of how to enhance the accuracy, adaptability, and robustness of energy system models. The proposed statistical downscaling method enables energy modelers to generate high-resolution wind speed data. The dynamic demand modeling framework provides a valuable foundation for demand projection by capturing the evolving relationships between temperature, residential buildings, and electricity demand. The analysis of extreme weather events offers practical guidance for selecting or SWYs for energy system optimization or simulations, especially when designing systems that are robust to extreme weather conditions. By addressing these key uncertainties, this dissertation offers a comprehensive framework to support more informed and robust energy planning for policymakers, stakeholders, and energy system modelers.

A. Appendix

A.1. Overview of Passive Cooling Technologies

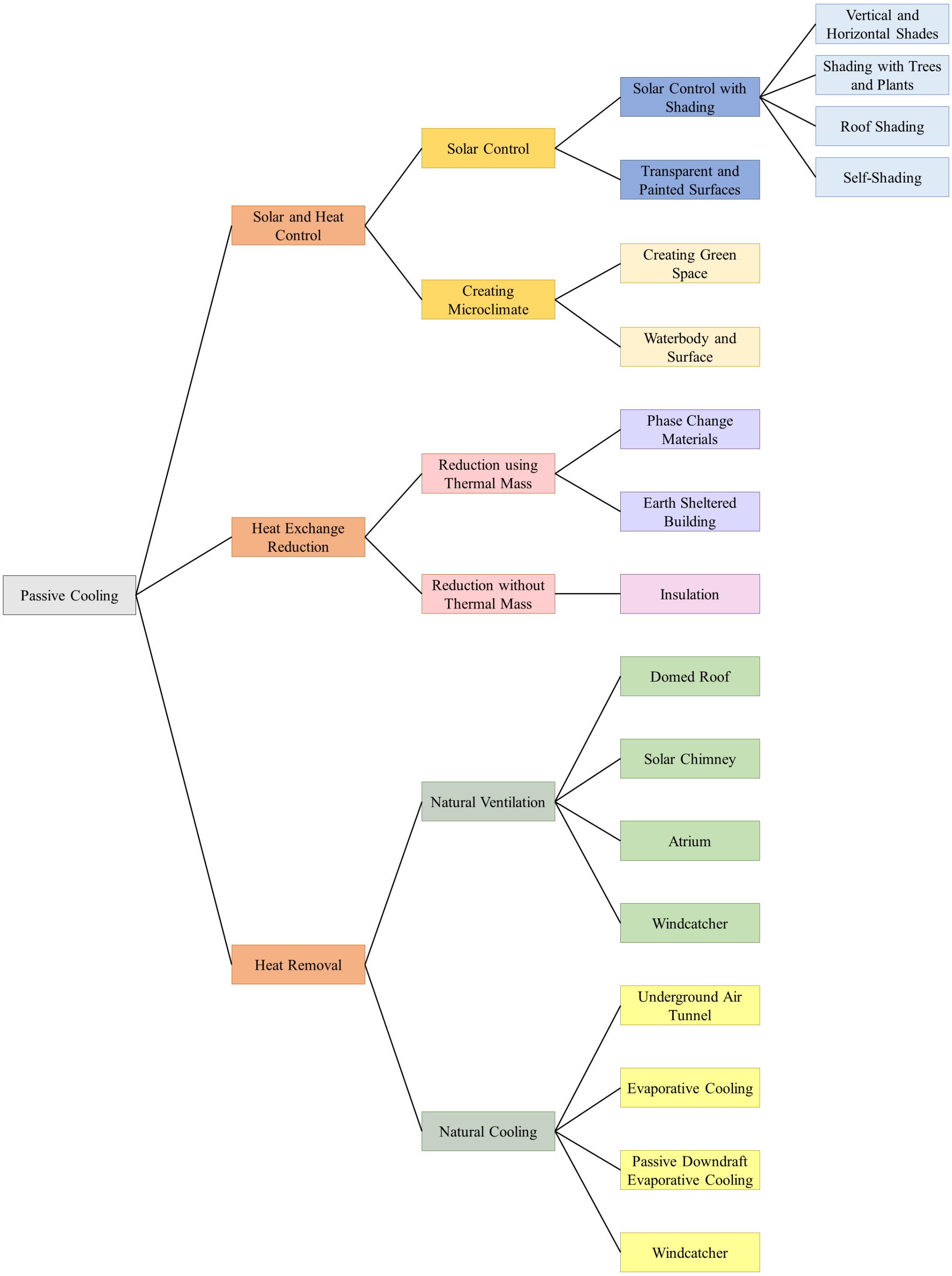

Figure A.1.: Overview of various passive cooling technologies, sourced from the study by Song et al. (Song et al., 2021).

A.2. Alternative method to project left slope

Section 3.2.4 describes a method for projecting the left slope, using Sweden's left slope value as a benchmark. This choice is based on Sweden's high electrification rate and effective thermal insulation in residential buildings. In this section, an alternative approach is presented that incorporates both the electrification rate and U-value for a more comprehensive analysis.

A.2.1. Electrification Rate

In Europe, the electrification rate differs by country. The residential heating electrification rate used in this section is extracted from the JRC database (European Commission, 2015). Figure A.2 presents the electrification rate for different countries across Europe.

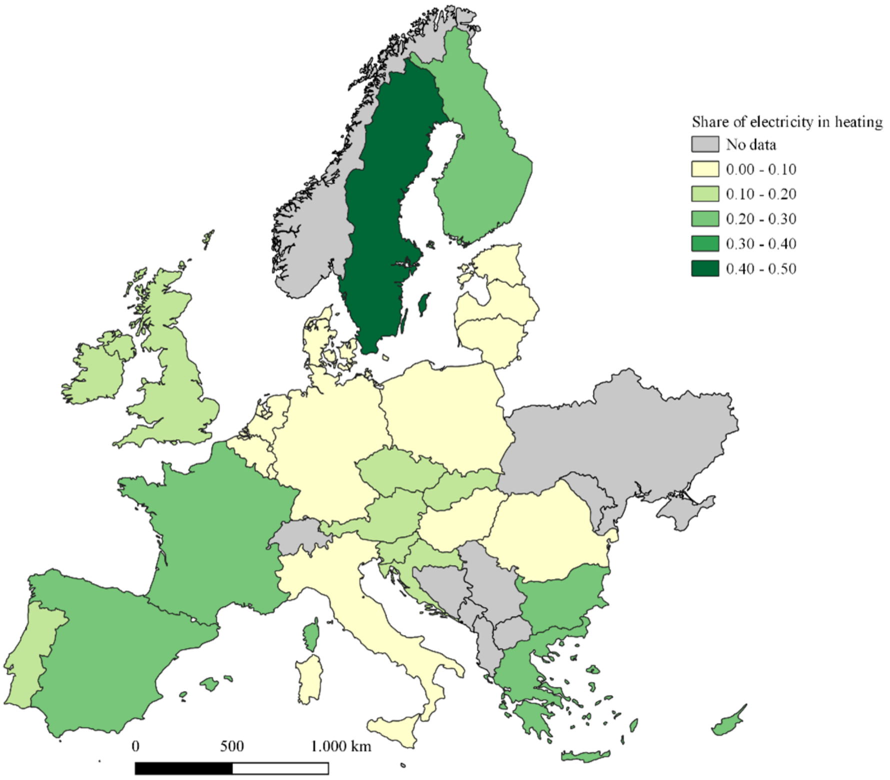

Figure A.2.: Electrification rate in European countries.

To depict the relationship between the electrification rate and the left slope value. Figure A.3a presents a linear correlation between these two variables. The linear regression model only yielded an R^2 score of 0.073, indicating a poor fit. However, the plot also reveals the presence of influential outliers, particularly observed in the data from Portugal and Cyprus. After excluding these outliers, the R^2 score experiences a substantial increase, reaching 0.166 as indicated in Figure A.3b. From this plot, a discernible trend can be observed: as the electrification rate increases, the left slope value decreases. This suggests a high sensitivity of electricity demand to temperature fluctuations, potentially leading to an increased demand.

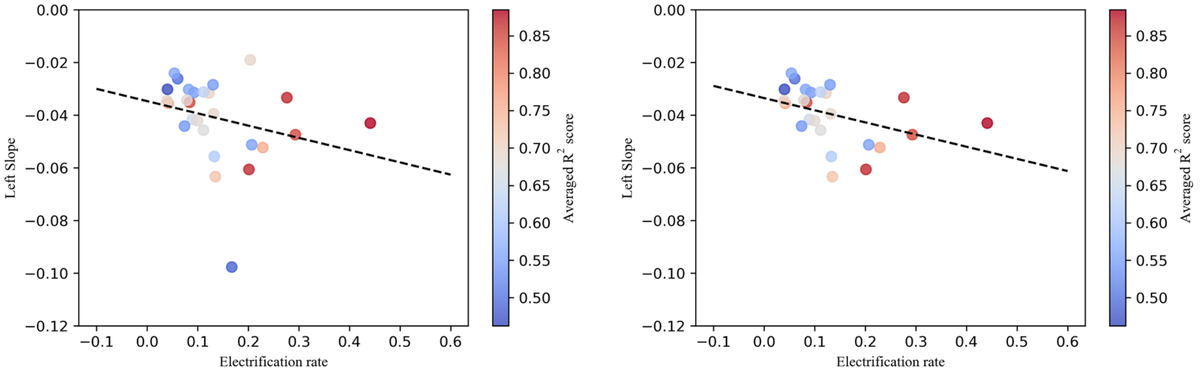

(a) All study countries

(b) After excluding Portugal and Cyprus

Figure A.3.: Scatter plots for electrification rate and left slope value

A.2.2. U-value

Another critical factor influencing electricity demand is the thermal insulation of buildings. Assessing the thermal insulation performance of building materials often involves using thermal transmittance, commonly known as the U-Value. The U-value represents the rate at which heat is transferred through a material or building element (such as walls, windows, roofs, or floors) due to a temperature difference between the inside and outside environments. The lower the U-value, the better the material is at insulating and retaining heat, which contributes to improved energy efficiency and reduced heating and cooling demands in buildings.

The U-value is calculated as the inverse of the total thermal resistance, R_{total}, of the material or building element, which accounts for all layers, including insulation, air gaps, and other structural components. The formula to calculate the U-value is illustrated in Equation A.1.

$$U = \frac{1}{R_{\text{total}}} \tag{A.1}$$

Where:

- R_{total} is the total thermal resistance of the material, and R for a single material layer is calculated by $R = d/k$.
- d is the thickness of the material (in meters).
- k is the thermal conductivity of the material (in watts per meter Kelvin, W/m·K).
- For multi-layer structures, the total thermal resistance is the sum of the individual resistances of each layer $R_{\text{total}} = R_{\text{layer 1}} + R_{\text{layer 2}} + \cdots + R_{\text{layer n}}$.

However, determining a country-wise U-Value for all buildings is challenging. This difficulty arises because the U-Value, measuring the insulation performance of materials, varies across different components of buildings, such as floors, walls, ceilings, and windows, each typically constructed with different materials and consequently possessing distinct U-Values. Furthermore, even if representative U-Values for different building components are known in each country, the challenge persists due to variations in building topology among different countries. The distribution of different building components varies, making it exceptionally challenging to derive a country-wise U-Value that accurately represents the diverse range of buildings.

To address this challenge, the U-values for floors, walls, ceilings, and windows are first extracted from Entranze (Entranze, 2008), a database documenting such values for 29 European countries. Given the diverse building topologies observed in both single and multi-family houses, the number of these houses per country is also extracted from the same data source. To delineate the specific topology for these two housing types, the TABULA WebTool (TABULA, 2015) database is used, which catalogues "average buildings" for single and multi-family houses across 16 European countries. These "average buildings" represent theoretical structures with geometrical and thermo-physical characteristics mirroring the average within each building stock subset (TABULA, nd). While acknowledging variations in topology within countries, for the sake of simplicity and to address missing data for some European countries, the averaged proportions of floors, walls, ceilings, and windows for both single and multi-family houses are calculated. These averaged values serve as representative indicators for all European countries. The percentage distribution of areas for each building component is summarized in Table A.1. Hence, applying this proportion data, the country-specific U-values can be calculated for building stocks, as illustrated in Figure A.4.

Table A.1.: Proportions for Floor, Wall, Windows, and Ceilings in Residential Buildings.

Building type	Floor	Wall	Window	Ceiling
Single-family house	26.9%	40.1%	7.9%	25.1%
Multi-family house	19.5%	48.9%	13.0%	18.5%

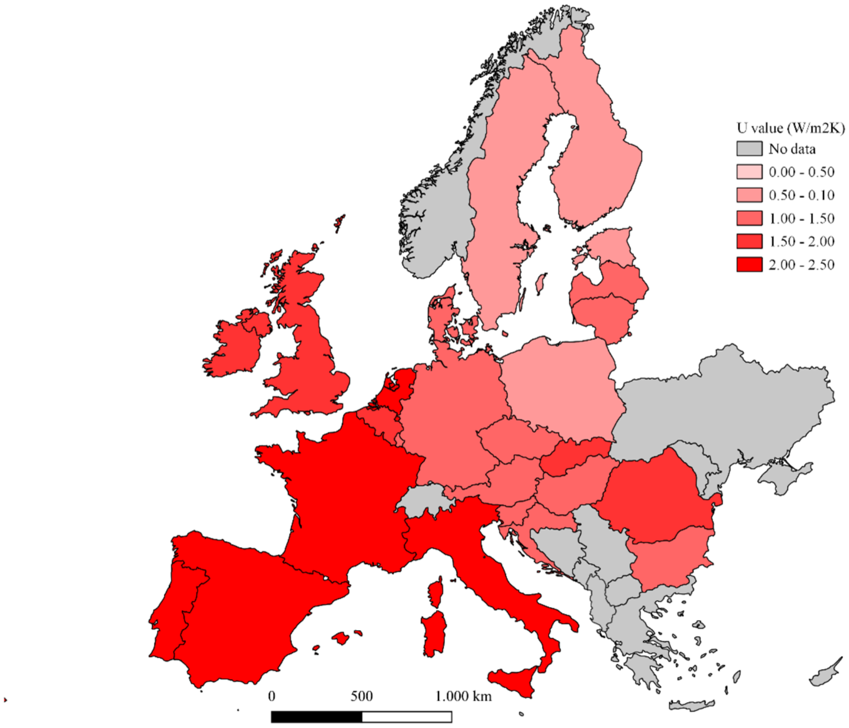

Figure A.4.: Representative U-values for the building stock.

Additionally, a linear regression between the U-value and the left slope value is conducted, as represented in Figure A.5. The R^2 score for the linear regression is 0.090. However, similar to the electrification rate analysis, the presence of two notable outliers, namely Portugal and Cyprus, is evident, as showcased in Figure A.5b. By excluding these outliers, the R^2 score improves to 0.176. Notably, the plot reveals a trend: with an increase in the U-value, the slope value decreases. This suggests that in poorly insulated houses, electricity demand is more sensitive to temperature fluctuations, consequently leading to an increase in electricity demand.

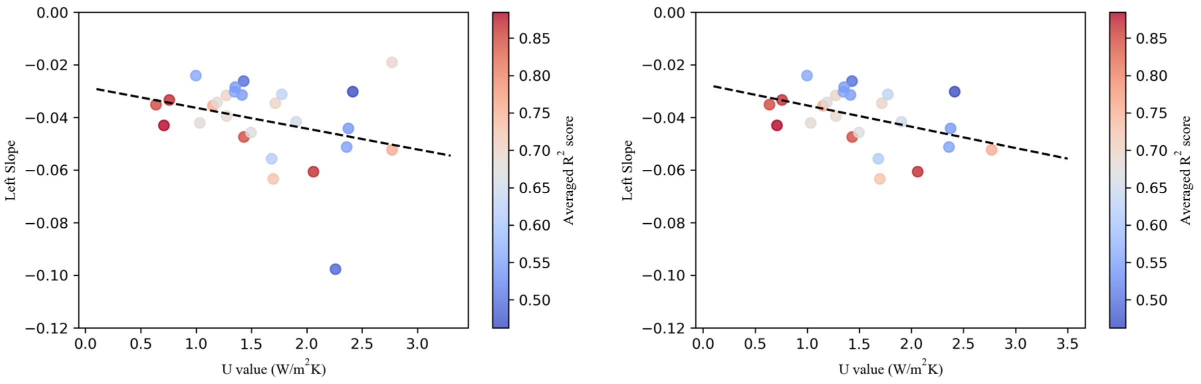

(a) All study countries

(b) After excluding Portugal and Cyprus

Figure A.5.: Scatter plots for U-value and left slope value

A.2.3. Multiple Linear Regression

Based on the analysis from the preceding section, linear correlations between the electrification rate, U-value, and left slope value can be observed. However, the R^2 scores for these individual linear correlations are suboptimal. To address this, a multiple linear regression technique is applied to establish a more robust statistical relationship involving the electrification rate, U-value, and left slope value. Multiple linear regression is a statistical method used to model the relationship between a dependent variable and multiple independent variables. Unlike simple linear regression, which considers only one predictor, multiple linear regression allows for a more comprehensive analysis by incorporating multiple factors.

The multiple linear regression is realized using Scipy python package. The result is presented in the Equation A.2. Meanwhile, the scatter plot between the left slope value and the prediction is presented in Figure A.6.

$$m_{left} = -0.0527 \cdot \gamma - 0.0092 \cdot U - 0.0186 \tag{A.2}$$

Where:

- m_{left} is the left slope value.
- γ is the Electrification Rate.
- U is the Country-specific representative U-value for all residential buildings.

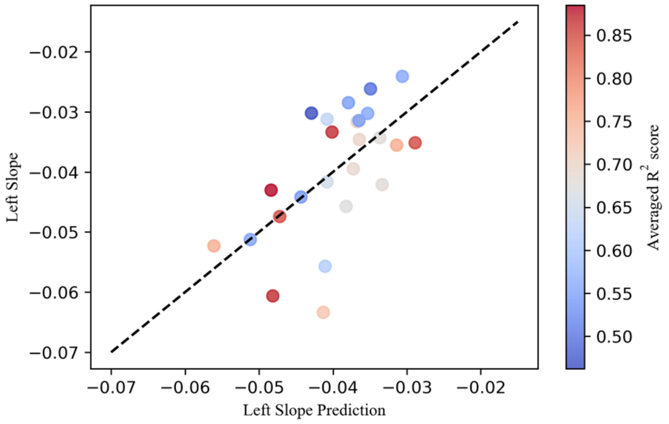

Figure A.6.: Scatter plots for left slope value and the predictions.

The results reveal a substantial increase in the R^2 score to 0.389, indicating the effectiveness of the multiple linear regression model. However, it is important to acknowledge the limitations imposed by the current sample size, inevitably introducing variability that may impact the reliability of the R^2 score as a statistical indicator for the regression results. However, once more comprehensive information, such as U-values and building topology data for additional countries and years are available, more robust and reliable regression results can potentially be achieved. Despite these limitations, the established equation remains valuable for left slope projections when applied to future scenarios that involve electrification rates and U-values.

A.3. Statistical Indicators

A.3.1. Statistical Indicators for All Countries and Years

The corresponding RMSE and R^2 scores for all studied countries and years (2015–2022) using piecewise regression are summarized in Table A.3.

Table A.3.: Summary of the statistic indicators for all studied countries and years

Region	Year	R^2	RMSE	Region	Year	R^2	RMSE
AT	2015	0.474	0.175	IT	2016	0.057	0.171
AT	2016	0.709	0.14	IT	2017	0.175	0.143
AT	2017	0.767	0.126	IT	2018	0.167	0.135
AT	2018	0.828	0.104	IT	2019	0.296	0.135
AT	2019	0.698	0.144	IT	2020	0.126	0.217
AT	2020	0.581	0.173	IT	2021	0.295	0.147
AT	2021	0.72	0.141	IT	2022	0.462	0.113
AT	2022	0.740	0.143	LT	2015	0.639	0.146
BA	2018	0.622	0.154	LT	2016	0.783	0.102
BA	2019	0.659	0.112	LT	2017	0.636	0.127
BA	2020	0.622	0.170	LT	2018	0.778	0.121
BA	2021	0.313	0.168	LT	2019	0.703	0.127
BE	2015	0.693	0.132	LT	2020	0.442	0.198
BE	2016	0.649	0.143	LT	2021	0.718	0.140

Continued on next page

Table A.3 – continued from previous page

Region	Year	R^2	RMSE	Region	Year	R^2	RMSE
BE	2017	0.725	0.122	LT	2022	0.740	0.151
BE	2018	0.725	0.134	LU	2015	0.192	0.131
BE	2019	0.685	0.132	LU	2016	0.186	0.137
BE	2020	0.438	0.180	LU	2017	0.347	0.119
BE	2021	0.663	0.132	LU	2018	-0.015	0.214
BE	2022	0.640	0.127	LU	2019	0.420	0.148
BG	2015	0.849	0.113	LU	2020	0.270	0.225
BG	2016	0.848	0.098	LU	2021	0.539	0.130
BG	2017	0.828	0.115	LU	2022	0.530	0.112
BG	2018	0.893	0.094	LV	2015	0.733	0.118
BG	2019	0.829	0.103	LV	2016	0.882	0.081
BG	2020	0.827	0.121	LV	2017	0.747	0.121
BG	2021	0.847	0.092	LV	2018	0.845	0.109
BG	2022	0.865	0.101	LV	2019	0.769	0.126
CH	2015	0.807	0.117	LV	2020	0.596	0.163
CH	2016	0.719	0.126	LV	2021	0.779	0.107
CH	2017	0.815	0.113	LV	2022	0.710	0.144
CH	2018	0.832	0.101	MD	2020	0.511	0.147
CH	2019	0.750	0.116	MD	2021	0.638	0.143
CH	2020	0.729	0.137	MD	2022	0.582	0.147
CH	2021	0.753	0.124	ME	2015	0.777	0.143
CH	2022	0.792	0.122	ME	2016	0.747	0.135

Continued on next page

Table A.3 – continued from previous page

Region	Year	R^2	RMSE	Region	Year	R^2	RMSE
CY	2017	0.684	0.153	ME	2017	0.718	0.143
CY	2018	0.740	0.133	ME	2018	0.642	0.154
CY	2021	0.656	0.137	ME	2019	0.722	0.143
CZ	2015	0.656	0.125	ME	2020	0.746	0.149
CZ	2016	0.690	0.117	ME	2021	0.666	0.146
CZ	2017	0.744	0.101	ME	2022	0.671	0.146
CZ	2018	0.756	0.093	MK	2018	0.851	0.100
CZ	2019	0.614	0.125	MK	2020	0.769	0.152
CZ	2020	0.596	0.181	MK	2021	0.842	0.103
CZ	2021	0.788	0.107	MK	2022	0.834	0.099
CZ	2022	0.759	0.104	NL	2015	0.495	0.172
DE	2015	0.398	0.133	NL	2016	0.485	0.192
DE	2016	0.489	0.128	NL	2017	0.578	0.170
DE	2017	0.576	0.120	NL	2018	0.628	0.160
DE	2018	0.563	0.107	NL	2019	0.633	0.164
DE	2019	0.399	0.136	NL	2020	0.405	0.228
DE	2020	0.415	0.218	NL	2021	0.471	0.204
DE	2021	0.609	0.145	NL	2022	0.637	0.173
DE	2022	0.619	0.128	NO	2015	0.889	0.100
DK	2015	0.659	0.148	NO	2016	0.933	0.071
DK	2016	0.749	0.115	NO	2017	0.918	0.09
DK	2017	0.630	0.148	NO	2018	0.934	0.081

Continued on next page

Table A.3 – continued from previous page

Region	Year	R^2	RMSE	Region	Year	R^2	RMSE
DK	2018	0.800	0.118	NO	2019	0.922	0.083
DK	2019	0.615	0.160	NO	2020	0.882	0.114
DK	2020	0.498	0.176	NO	2021	0.948	0.067
DK	2021	0.797	0.101	NO	2022	0.917	0.089
DK	2022	0.698	0.141	PL	2015	0.364	0.143
EE	2015	0.789	0.118	PL	2016	0.509	0.137
EE	2016	0.882	0.082	PL	2017	0.519	0.122
EE	2017	0.821	0.112	PL	2018	0.612	0.107
EE	2018	0.911	0.087	PL	2019	0.424	0.125
EE	2019	0.846	0.096	PL	2020	0.296	0.200
EE	2020	0.778	0.122	PL	2021	0.593	0.146
EE	2021	0.886	0.088	PL	2022	0.696	0.089
EE	2022	0.880	0.092	PT	2015	0.618	0.135
ES	2015	0.607	0.135	PT	2016	0.438	0.197
ES	2016	0.421	0.155	PT	2017	0.489	0.152
ES	2017	0.595	0.131	PT	2018	0.459	0.159
ES	2018	0.515	0.131	PT	2019	0.377	0.161
ES	2019	0.447	0.132	PT	2020	0.245	0.218
ES	2020	0.372	0.178	PT	2021	0.475	0.139
ES	2021	0.638	0.091	PT	2022	0.439	0.157
ES	2022	0.631	0.110	RO	2015	0.657	0.149
FI	2015	0.819	0.103	RO	2016	0.757	0.122

Continued on next page

Table A.3 – continued from previous page

Region	Year	R^2	RMSE	Region	Year	R^2	RMSE
FI	2016	0.895	0.071	RO	2017	0.775	0.110
FI	2017	0.851	0.094	RO	2018	0.790	0.109
FI	2018	0.912	0.080	RO	2019	0.662	0.123
FI	2019	0.862	0.089	RO	2020	0.612	0.153
FI	2020	0.818	0.115	RO	2021	0.670	0.130
FI	2021	0.909	0.088	RO	2022	0.651	0.116
FI	2022	0.881	0.097	RS	2016	0.886	0.101
FR	2015	0.890	0.086	RS	2017	0.898	0.088
FR	2016	0.876	0.096	RS	2018	0.886	0.102
FR	2017	0.893	0.083	RS	2019	0.876	0.102
FR	2018	0.883	0.092	RS	2020	0.834	0.125
FR	2019	0.865	0.098	RS	2021	0.839	0.119
FR	2020	0.789	0.134	RS	2022	0.897	0.093
FR	2021	0.877	0.095	SE	2015	0.843	0.109
FR	2022	0.875	0.097	SE	2016	0.918	0.072
GR	2015	0.749	0.123	SE	2017	0.882	0.096
GR	2016	0.797	0.112	SE	2018	0.922	0.080
GR	2017	0.771	0.110	SE	2019	0.884	0.093
GR	2018	0.752	0.113	SE	2020	0.834	0.120
GR	2019	0.773	0.111	SE	2021	0.917	0.080
GR	2020	0.703	0.134	SE	2022	0.878	0.106
GR	2021	0.747	0.112	SI	2015	0.388	0.161

Continued on next page

Table A.3 – continued from previous page

Region	Year	R^2	RMSE	Region	Year	R^2	RMSE
GR	2022	0.763	0.124	SI	2016	0.411	0.148
HR	2015	0.660	0.129	SI	2017	0.493	0.120
HR	2016	0.622	0.139	SI	2018	0.512	0.117
HR	2017	0.713	0.134	SI	2019	0.273	0.152
HR	2018	0.761	0.111	SI	2020	0.535	0.157
HR	2019	0.651	0.163	SI	2021	0.674	0.118
HR	2020	0.596	0.170	SI	2022	0.640	0.114
HR	2021	0.642	0.160	SK	2015	0.513	0.156
HR	2022	0.733	0.110	SK	2016	0.636	0.120
HU	2015	0.311	0.155	SK	2017	0.722	0.105
HU	2016	0.458	0.127	SK	2018	0.728	0.096
HU	2017	0.539	0.109	SK	2019	0.655	0.125
HU	2018	0.608	0.106	SK	2020	0.612	0.173
HU	2019	0.434	0.134	SK	2021	0.675	0.149
HU	2020	0.540	0.182	SK	2022	0.505	0.137
HU	2021	0.674	0.142	UA	2018	0.898	0.106
HU	2022	0.634	0.115	UA	2019	0.853	0.111
IE	2015	0.615	0.161	UA	2021	0.823	0.113
IE	2016	0.627	0.161	UK	2015	0.670	0.155
IE	2017	0.610	0.152	UK	2016	0.707	0.156
IE	2018	0.679	0.140	UK	2017	0.759	0.130
IE	2019	0.681	0.132	UK	2018	0.780	0.129

Continued on next page

Table A.3 – continued from previous page

Region	Year	R^2	RMSE	Region	Year	R^2	RMSE
IE	2020	0.464	0.203	UK	2019	0.791	0.125
IE	2021	0.617	0.119	UK	2020	0.660	0.187
IT	2015	0.356	0.125	XK	2022	0.883	0.102

A.3.2. Statistical Indicators for Excluded Dataset

After conducting piecewise regression to simulate the TRFs, data with R^2 values below 0.4 are excluded to improve the accuracy of the subsequent analysis. The excluded data and corresponding statistical indicators are provided in Table A.4.

Table A.4.: Overview of the excluded dataset and corresponding RMSE and R^2

Region	Year	R^2	RMSE	Region	year	R^2	RMSE
BA	2021	0.313	0.168	SI	2015	0.388	0.161
HU	2015	0.311	0.155	SI	2019	0.273	0.152
LU	2015	0.192	0.131	ES	2020	0.372	0.178
LU	2016	0.186	0.137	IT	2016	0.057	0.171
LU	2017	0.347	0.119	IT	2017	0.175	0.143
LU	2018	0.148	0.214	IT	2018	0.167	0.135
LU	2020	0.27	0.225	IT	2019	0.296	0.135
PL	2015	0.364	0.143	IT	2020	0.126	0.217
PL	2020	0.296	0.2	IT	2021	0.295	0.147
PT	2019	0.377	0.161	DE	2015	0.398	0.133
PT	2020	0.245	0.218	DE	2019	0.399	0.136

A.4. Storage Capacities in Exogenous-RE and Endogenous-RE Scenarios

The following figures, Figure A.7 and Figure A.8, illustrate the capacities of various storage technologies, including H_2 Cavern, H_2 Tank, Heat Storage, and Lithium-Ion Batteries, in both the Exogenous-RE and Endogenous-RE scenarios. It is interesting to see that years such as 1997 and 2011, which exhibit long-duration periods of extremely high residual load, lead to considerably higher capacities of H_2 cavern storage. This indicates that when renewable shortfalls persist over extended periods, the model favors long-duration storage technologies capable of shifting energy over the long term. In contrast, years like 2015 and 2004 are characterized by short-term but high residual load spikes, which the system predominantly addresses through significantly higher gas turbine capacities. These technologies provide cost-effective, fast-ramping flexibility that is better suited for managing short-term extreme events.

However, it is worth mentioning that this duration-driven sensitivity is observed only for H_2 caverns. For other storage technologies, such as H_2 tanks, lithium-ion batteries, and heat storage, the model does not reveal a clear or consistent variation in installed capacity across years. This suggests that, compared to long-term storage solutions such as H_2 caverns, these short-term storage technologies are deployed more uniformly, likely reflecting their role in smoothing daily or intra-day fluctuations rather than reacting to long-term stress events.

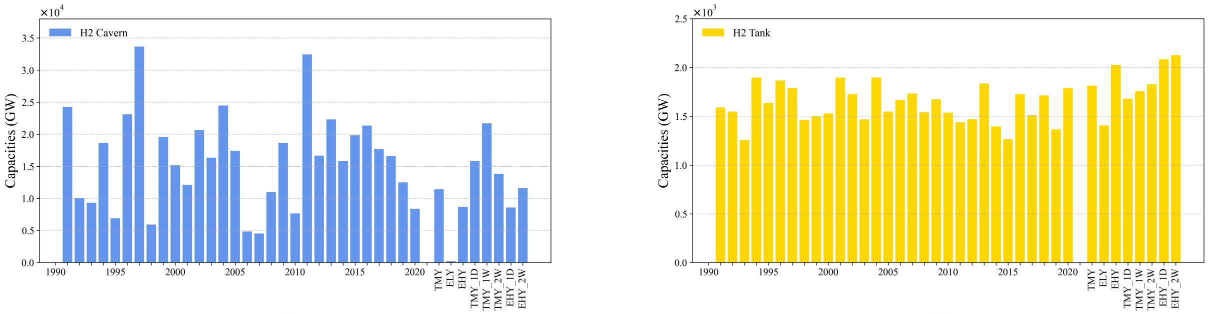

(a) H_2 cavern capacities

(b) H_2 tank capacities

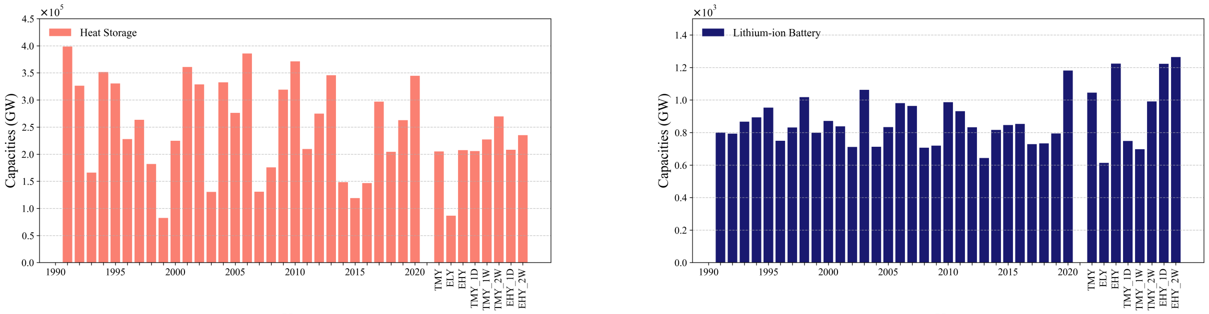

(c) Heat storage capacities

(d) Lithium-Ion battery capacities

Figure A.7.: Storage capacities of various technologies in the Exogenous-RE scenario. Pumped hydro and reservoir hydro are not presented here as their capacities remain constant across all weather years.

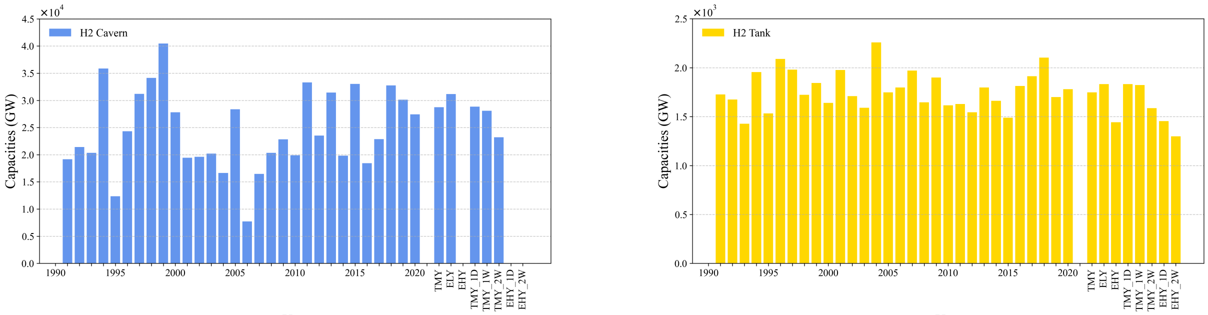

(a) H_2 cavern capacities

(b) H_2 tank capacities

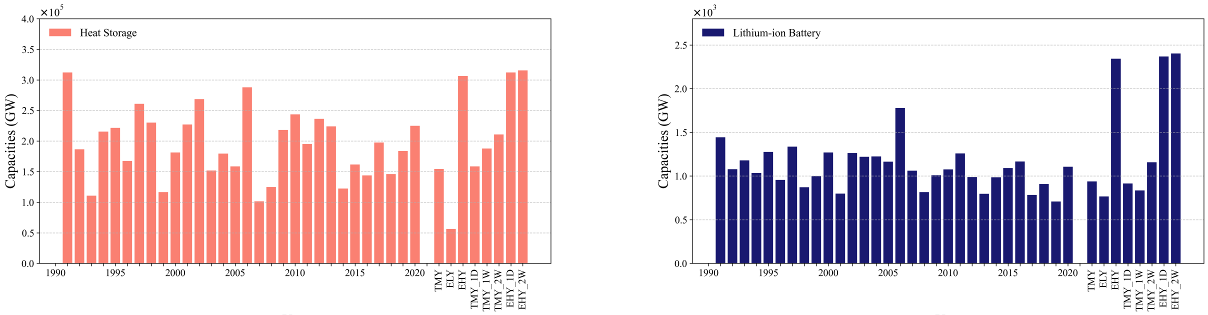

(c) Heat storage capacities

(d) Lithium-Ion battery capacities

Figure A.8.: Storage capacities of various technologies in the Endogenous-RE scenario. Pumped hydro and reservoir hydro are not presented here as their capacities remain fixed across all weather years.

B. Bibliography

Abdi, H. (2007). Z-scores. *Encyclopedia of measurement and statistics*, 3:1055–1058.

Adachi, S. and Tomita, H. (2020). Methodology of the constraint condition in dynamical downscaling for regional climate evaluation: A review. *Journal of Geophysical Research: Atmospheres*, 125(11):e2019JD032166.

Aigrain, S. and Foreman-Mackey, D. (2023). Gaussian process regression for astronomical time series. *Annual Review of Astronomy and Astrophysics*, 61(1):329–371.

Al-Duais, F. S. and Al-Sharpi, R. S. (2023). A unique markov chain monte carlo method for forecasting wind power utilizing time series model. *Alexandria Engineering Journal*, 74:51–63.

Alberini, A., Prettico, G., Shen, C., and Torriti, J. (2019). Hot weather and residential hourly electricity demand in italy. *Energy*, 177:44–56.

Alhuwayil, W. K., Almaziad, F. A., and Mujeebu, M. A. (2023). Energy performance of passive shading and thermal insulation in multistory hotel building under different outdoor climates and geographic locations. *Case Studies in Thermal Engineering*, 45:102940.

Alizadeh, M. J., Kavianpour, M. R., Kamranzad, B., and Etemad-Shahidi, A. (2019). A weibull distribution based technique for downscaling of climatic wind field. *Asia-Pacific Journal of Atmospheric Sciences*, 55:685–700.

Alodah, A. and Seidou, O. (2019). The adequacy of stochastically generated climate time series for water resources systems risk and performance assessment. *Stochastic environmental research and risk assessment*, 33(1):253–269.

Amato, A. D., Ruth, M., Kirshen, P., and Horwitz, J. (2005). Regional energy demand responses to climate change: methodology and application to the commonwealth of massachusetts. *Climatic Change*, 71(1-2):175–201.

Amato, U., Andretta, A., Bartoli, B., Coluzzi, B., Cuomo, V., Fontana, F., and Serio, C. (1986). Markov processes and fourier analysis as a tool to describe and simulate daily solar irradiance. *Solar energy*, 37(3):179–194.

American Society of Heating, R., Engineers, A.-C., Ashrae, Bagheri, H., and Owen, M. (2013). *2013 ASHRAE Handbook-Fundamentals*. ASHRAE HANDBOOK: FUNDAMENTALS. ASHRAE.

An, P., Wang, Z., and Zhang, C. (2022). Ensemble unsupervised autoencoders and gaussian mixture model for cyberattack detection. *Information Processing & Management*, 59(2):102844.

Andrade, C., Mourato, S., and Ramos, J. (2021). Heating and cooling degree-days climate change projections for portugal. *Atmosphere*, 12(6):715.

Añel, J. A., Fernández-González, M., Labandeira, X., López-Otero, X., and De la Torre, L. (2017). Impact of cold waves and heat waves on the energy production sector. *Atmosphere*, 8(11):209.

Apadula, F., Bassini, A., Elli, A., and Scapin, S. (2012). Relationships between meteorological variables and monthly electricity demand. *Applied Energy*, 98:346–356.

Asdrubali, F., D'Alessandro, F., and Schiavoni, S. (2015). A review of unconventional sustainable building insulation materials. *Sustainable Materials and Technologies*, 4:1–17.

Auffhammer, M. and Aroonruengsawat, A. (2011). Simulating the impacts of climate change, prices and population on california's residential electricity consumption. *Climatic change*, 109:191–210.

Badger, J., Sempreviva, A., Söderberg, S., Costa, P., Simoes, T., Estanqueiro, A., Gottschall, J., Dörenkämper, M., Callies, D., Montesinos, J. N., et al. (2019). Report on link to global wind atlas and national wind atlases (deliverable d4. 7). *Tech Rep*.

Bailey, M., Nychka, D., Sengupta, M., Yang, J., and Bandyopadhyay, S. (2024). Temporal and spatial downscaling for solar radiation. *arXiv preprint arXiv:2405.11046*.

Barrett, R., Keeble, E., Levermore, G., Muneer, T., Page, J., Sanders, C., and Wright, A. (2002). Cibse guide j: Weather, solar and illuminance data.

Bermúdez, M., Cea, L., Van Uytven, E., Willems, P., Farfán, J., and Puertas, J. (2020). A robust method to update local river inundation maps using global climate model output and weather typing based statistical downscaling. *Water Resources Management*, 34:4345–4362.

Bessec, M. and Fouquau, J. (2008). The non-linear link between electricity consumption and temperature in europe: A threshold panel approach. *Energy Economics*, 30(5):2705–2721.

Bevacqua, E., Rakovec, O., Schumacher, D. L., Kumar, R., Thober, S., Samaniego, L., Seneviratne, S. I., and Zscheischler, J. (2024). Direct and lagged climate change effects intensified the 2022 european drought. *Nature Geoscience*, pages 1–8.

Bhuvandas, N., Timbadiya, P. V., Patel, P. L., and Porey, P. D. (2014). Review of downscaling methods in climate change and their role in hydrological studies. *Int. J. Environ. Ecol. Geol. Mar. Eng*, 8:713–718.

Black, E., Blackburn, M., Harrison, G., Hoskins, B., Methven, J., et al. (2004). Factors contributing to the summer 2003 european heatwave. *Weather*, 59(8):217–223.

Bollmeyer, C., Keller, J. D., Ohlwein, C., Wahl, S., Crewell, S., Friederichs, P., Hense, A., Keune, J., Kneifel, S., Pscheidt, I., et al. (2015). Towards a high-resolution regional reanalysis for the european cordex domain. *Quarterly Journal of the Royal Meteorological Society*, 141(686):1–15.

Bouckaert, S., Pales, A. F., McGlade, C., Remme, U., Wanner, B., Varro, L., D'Ambrosio, D., and Spencer, T. (2021). Net zero by 2050: A roadmap for the global energy sector.

Brayshaw, D. J., Troccoli, A., Fordham, R., and Methven, J. (2011). The impact of large scale atmospheric circulation patterns on wind power generation and its potential predictability: A case study over the uk. *Renewable Energy*, 36(8):2087–2096.

Breiman, L. (2001). Random forests. *Machine learning*, 45:5–32.

Brouwer, A. S., Kuramochi, T., van den Broek, M., and Faaij, A. (2013). Fulfilling the electricity demand of electric vehicles in the long term future: An evaluation of centralized and decentralized power supply systems. *Applied energy*, 107:33–51.

Brown, J. S. and Domanski, P. A. (2014). Review of alternative cooling technologies. *Applied Thermal Engineering*, 64(1-2):252–262.

Brown, M. A., Cox, M., Staver, B., and Baer, P. (2016). Modeling climate-driven changes in us buildings energy demand. *Climatic Change*, 134:29–44.

Brown, T., Hörsch, J., and Schlachtberger, D. (2017). Pypsa: Python for power system analysis. *arXiv preprint arXiv:1707.09913*.

Buster, G., Rossol, M., Maclaurin, G., Xie, Y., and Sengupta, M. (2021). A physical downscaling algorithm for the generation of high-resolution spatiotemporal solar irradiance data. *Solar Energy*, 216:508–517.

Caldwell, P., Chin, H.-N. S., Bader, D. C., and Bala, G. (2009). Evaluation of a wrf dynamical downscaling simulation over california. *Climatic change*, 95:499–521.

Carapellucci, R. and Giordano, L. (2013). A methodology for the synthetic generation of hourly wind speed time series based on some known aggregate input data. *Applied Energy*, 101:541–550.

Carbon Trust (2012). Degree days for energy management. `https://www.sustainabilityexchange.ac.uk/files/degree_days_for_energy_management_carbon_trust.pdf`. Accessed: 10.10.2023.

Castillejo-Cuberos, A., Cardemil, J., and Escobar, R. (2024). Temporal upscaling of solar radiation components using an analytical model for variability modeling. *Renewable Energy*, 229:120783.

Castillo, V. Z., De Boer, H.-S., Muñoz, R. M., Gernaat, D. E., Benders, R., and van Vuuren, D. (2022). Future global electricity demand load curves. *Energy*, 258:124741.

Castro, C. L., Pielke Sr, R. A., and Leoncini, G. (2005). Dynamical downscaling: Assessment of value retained and added using the regional atmospheric modeling system (rams). *Journal of Geophysical Research: Atmospheres*, 110(D5).

Castrogiovanni, L., Sternai, P., Agostinetti, N. P., and Pasquero, C. (2025). A reversible-jump markov chain monte carlo algorithm to estimate paleo surface co2 fluxes linking temperature to atmospheric co2 concentration time series. *Computers & Geosciences*, 196:105838.

Chan, A. L., Chow, T.-T., Fong, S. K., and Lin, J. Z. (2006). Generation of a typical meteorological year for hong kong. *Energy Conversion and management*, 47(1):87–96.

Chang, Y., Kim, C. S., Miller, J. I., Park, J. Y., and Park, S. (2016). A new approach to modeling the effects of temperature fluctuations on monthly electricity demand. *Energy Economics*, 60:206–216.

Chen, H., Guo, J., Xiong, W., Guo, S., and Xu, C.-Y. (2010). Downscaling gcms using the smooth support vector machine method to predict daily precipitation in the hanjiang basin. *Advances in Atmospheric Sciences*, 27:274–284.

Chen, J., Brissette, F., Leconte, R., and Caron, A. (2012). A versatile weather generator for daily precipitation and temperature. *Transactions of the ASABE*, 55(3):895–906.

Chen, J., Brissette, F. P., and Zhang, X. J. (2014). A multi-site stochastic weather generator for daily precipitation and temperature. *Transactions of the ASABE*, 57(5):1375–1391.

Chen, T. and Guestrin, C. (2016). Xgboost: A scalable tree boosting system. In *Proceedings of the 22nd acm sigkdd international conference on knowledge discovery and data mining*, pages 785–794.

Christenson, M., Manz, H., and Gyalistras, D. (2006). Climate warming impact on degree-days and building energy demand in switzerland. *Energy conversion and management*, 47(6):671–686.

CIBSE, T. (2014). Design summer years for london, the chartered institution of building services engineers london.

Clarke, J. (2007). *Energy simulation in building design*. Routledge.

Colette, A., Vautard, R., and Vrac, M. (2012). Regional climate downscaling with prior statistical correction of the global climate forcing. *Geophysical Research Letters*, 39(13).

Cömert, M. and Yildiz, A. (2019). Climate change impacts on electricity demand in turkey. In *2019 International Artificial Intelligence and Data Processing Symposium (IDAP)*, pages 1–5. IEEE.

Connolly, D. (2017). Heat roadmap europe: Quantitative comparison between the electricity, heating, and cooling sectors for different european countries. *Energy*, 139:580–593.

Covid, I. (19). impact of electricity–statistical report may 2020. international energy agency; 2020.

Crawley, D. B., Lawrie, L. K., et al. (2015). Rethinking the tmy: is the 'typical'meteorological year best for building performance simulation. In *Conference: Building Simulation*, pages 2655–2662.

Crone, S. F. and Kourentzes, N. (2010). Feature selection for time series prediction–a combined filter and wrapper approach for neural networks. *Neurocomputing*, 73(10-12):1923–1936.

Crozier, C., Morstyn, T., and McCulloch, M. (2020). The opportunity for smart charging to mitigate the impact of electric vehicles on transmission and distribution systems. *Applied Energy*, 268:114973.

Curry, C. L., van der Kamp, D., and Monahan, A. H. (2012). Statistical downscaling of historical monthly mean winds over a coastal region of complex terrain. i. predicting wind speed. *Climate dynamics*, 38(7):1281–1299.

Dai, Y. and Zhao, P. (2020). A hybrid load forecasting model based on support vector machine with intelligent methods for feature selection and parameter optimization. *Applied energy*, 279:115332.

Davis, N. N., Badger, J., Hahmann, A. N., Hansen, B. O., Mortensen, N. G., Kelly, M., Larsén, X. G., Olsen, B. T., Floors, R., Lizcano, G., et al. (2023). The global wind atlas: A high-resolution dataset of climatologies and associated web-based application. *Bulletin of the American Meteorological Society*, 104(8):E1507–E1525.

Davy, R. J., Woods, M. J., Russell, C. J., and Coppin, P. A. (2010). Statistical downscaling of wind variability from meteorological fields. *Boundary-layer meteorology*, 135:161–175.

Desai, A., Freeman, C., Wang, Z., and Beaver, I. (2021). Timevae: A variational auto-encoder for multivariate time series generation. *arXiv preprint arXiv:2111.08095*.

Dickinson, R. E., Errico, R. M., Giorgi, F., and Bates, G. T. (1989). A regional climate model for the western united states. *Climatic change*, 15:383–422.

Diday, E. and Vrac, M. (2005). Mixture decomposition of distributions by copulas in the symbolic data analysis framework. *Discrete Applied Mathematics*, 147(1):27–41.

Doddy Clarke, E., Griffin, S., McDermott, F., Monteiro Correia, J., and Sweeney, C. (2021). Which reanalysis dataset should we use for renewable energy analysis in ireland? *Atmosphere*, 12(5):624.

Dörenkämper, M., Olsen, B. T., Witha, B., Hahmann, A. N., Davis, N. N., Barcons, J., Ezber, Y., García-Bustamante, E., González-Rouco, J. F., Navarro, J., et al. (2020). The making of the new european wind atlas–part 2: Production and evaluation. *Geoscientific model development*, 13(10):5079–5102.

Dubin, J. A. (2008). An integrated engineering–econometric analysis of residential balance point temperatures. *Energy economics*, 30(5):2537–2551.

Dujardin, J. and Lehning, M. (2022). Wind-topo: Downscaling near-surface wind fields to high-resolution topography in highly complex terrain with deep learning. *Quarterly Journal of the Royal Meteorological Society*, 148(744):1368–1388.

DWD Climate Data Center (2013). Historical hourly station observations of wind speed and wind direction for germany. `https://opendata.dwd.de/climate_environment/CDC/observations_germany/climate/hourly/wind/`. Accessed: 2022-04-14.

Eames, M. E. (2016). An update of the uk's design summer years: Probabilistic design summer years for enhanced overheating risk analysis in building design. *Building services engineering research and technology*, 37(5):503–522.

Economidou, M., Atanasiu, B., Despret, C., Maio, J., Nolte, I., Rapf, O., Laustsen, J., Ruyssevelt, P., Staniaszek, D., Strong, D., et al. (2011). Europe's buildings under the microscope. a country-by-country review of the energy performance of buildings.

Eirola, E. and Lendasse, A. (2013). Gaussian mixture models for time series modelling, forecasting, and interpolation. In *Advances in intelligent data analysis XII: 12th international symposium, IDA 2013, London, UK, october 17-19, 2013. Proceedings 12*, pages 162–173. Springer.

Ekström, J., Koivisto, M., Mellin, I., Millar, J., Saarijärvi, E., and Haarla, L. (2015a). Assessment of large scale wind power generation with new generation locations without measurement data. *Renewable Energy*, 83:362–374.

Ekström, M., Grose, M. R., and Whetton, P. H. (2015b). An appraisal of downscaling methods used in climate change research. *Wiley Interdisciplinary Reviews: Climate Change*, 6(3):301–319.

Enerdata (n.d.). Floor u-values (weighted average based on stock). `https://entranze.enerdata.net/floor-u-values.html`. Accessed: 10.10.2023.

Entranze (2008). Residential buildings u values for floor, wall, ceiling, and window. `https://entranze.enerdata.net/floor-u-values.html`. Retrieved 10 10, 2023.

ENTSO-E (2016). Ten-year network development plan 2016. Accessed: 2024-12-10.

ENTSO-E (2022). Ten-year network development plan 2022. Accessed: 2024-12-10.

Escandón, R., Suárez, R., and Sendra, J. J. (2019). Field assessment of thermal comfort conditions and energy performance of social housing: The case of hot summers in the mediterranean climate. *Energy policy*, 128:377–392.

ESRI (Environmental Systems Research Institute) (Last accessed: 27.06.2023a). Aspect. ESRI ArcGIS Resource Center.

ESRI (Environmental Systems Research Institute) (Last accessed: 27.06.2023b). Slope. ESRI ArcGIS Resource Center.

EURO-CORDEX (Accessed: 10.10.2023). Euro-cordex - coordinated downscaling experiment - european domain. Accessed: 10.10.2023.

European Commision (Published in 2011). Energy efficiency plan 2011, com(2011) 109 final. `https://eur-lex.europa.eu/LexUriServ/LexUriServ.do?uri=COM:2011:0109:FIN:EN:PDF`. Accessed: 10.10.2023.

European Commision (Published in 2018). In-depth analysis in support of the commisssion comminication com(2018) 773. `https://climate.ec.europa.eu/system/files/2018-11/com_2018_733_analysis_in_support_en.pdf`. Accessed: 10.10.2023.

European Commission (2015). Joint research centre data catalogue. Retrieved October 10, 2023.

European Environment Agency (2021). Adaptation challenges and opportunities for the european energy system. `https://www.eea.europa.eu/publications/adaptation-in-energy-system`. Accessed: 10.10.2023.

European Environment Agency (2022). Cooling buildings sustainably in europe: exploring the links between climate change mitigation and adaptation, and their social impacts. `https://www.eea.europa.eu/publications/cooling-buildings-sustainably-in-europe`. Accessed: 10.10.2023.

Eurostat (2019/2020). Energy statistics - cooling and heating degree days. `https://ec.europa.eu/eurostat/cache/metadata/en/nrg_chdd_esms.htm`. Accessed: 10.10.2023.

Fan, J.-L., Hu, J.-W., and Zhang, X. (2019). Impacts of climate change on electricity demand in china: An empirical estimation based on panel data. *Energy*, 170:880–888.

Farah, S., Saman, W., and Boland, J. (2018). Development of robust meteorological year weather data. *Renewable Energy*, 118:343–350.

Fazeli, R., Ruth, M., and Davidsdottir, B. (2016). Temperature response functions for residential energy demand–a review of models. *Urban Climate*, 15:45–59.

Ferrari, D. and Lee, T. (2008). Beyond tmy: Climate data for specific applications. In *Proceedings 3rd International Solar Energy Society conference–Asia Pacific region (ISES-AP-08)*.

Festa, R. and Ratto, C. F. (1993). Proposal of a numerical procedure to select reference years. *Solar Energy*, 50(1):9–17.

Fotis, P., Karkalakos, S., and Asteriou, D. (2017). The relationship between energy demand and real gdp growth rate: The role of price asymmetries and spatial externalities within 34 countries across the globe. *Energy Economics*, 66:69–84.

Fouillet, A., Rey, G., Wagner, V., Laaidi, K., Empereur-Bissonnet, P., Le Tertre, A., Frayssinet, P., Bessemoulin, P., Laurent, F., De Crouy-Chanel, P., et al. (2008). Has the impact of heat waves on mortality changed in france since the european heat wave of summer 2003? a study of the 2006 heat wave. *International journal of epidemiology*, 37(2):309–317.

Frame, D. J., Wehner, M. F., Noy, I., and Rosier, S. M. (2020). The economic costs of hurricane harvey attributable to climate change. *Climatic Change*, 160(2):271–281.

Füssel, H.-M., Jol, A., et al. (2012). Climate change, impacts and vulnerability in europe 2012 an indicator-based report.

Gao, R., Du, L., Duru, O., and Yuen, K. F. (2021). Time series forecasting based on echo state network and empirical wavelet transformation. *Applied Soft Computing*, 102:107111.

Gardian, H., Gils, H. C., Kittel, M., Murmann, A., Launer, J., Gaumnitz, F., Fehler, A., van Ouwerkerk, J., Mikurda, J., Torralba-Díaz, L., Krüger, C., Janßen, T., and Zerrahn, A. (2022). Model input and output data of the flexmex model comparison. `https://zenodo.org/records/5802178`. Accessed: 2024-08-02.

Garrido-Perez, J. M., Ordóñez, C., Barriopedro, D., García-Herrera, R., and Paredes, D. (2020). Impact of weather regimes on wind power variability in western europe. *Applied Energy*, 264:114731.

Gatta, F., Giampaolo, F., Prezioso, E., Mei, G., Cuomo, S., and Piccialli, F. (2022). Neural networks generative models for time series. *Journal of King Saud University-Computer and Information Sciences*, 34(10):7920–7939.

Gazela, M. and Mathioulakis, E. (2001). A new method for typical weather data selection to evaluate long-term performance of solar energy systems. *Solar Energy*, 70(4):339–348.

Ge, Y., Nan, Y., and Bai, L. (2019). A hybrid prediction model for solar radiation based on long short-term memory, empirical mode decomposition, and solar profiles for energy harvesting wireless sensor networks. *Energies*, 12(24):4762.

Geonames (Accessed: 10.10.2023). Geonames. Accessed: 10.10.2023.

Ghasemi, P., Karbasi, M., Nouri, A. Z., Tabrizi, M. S., and Azamathulla, H. M. (2021). Application of gaussian process regression to forecast multi-step ahead spei drought index. *Alexandria Engineering Journal*, 60(6):5375–5392.

Giannakopoulos, C. and Psiloglou, B. E. (2006). Trends in energy load demand for athens, greece: weather and non-weather related factors. *Climate research*, 31(1):97–108.

Gielen, D., Boshell, F., Saygin, D., Bazilian, M. D., Wagner, N., and Gorini, R. (2019). The role of renewable energy in the global energy transformation. *Energy Strategy Reviews*, 24:38–50.

Gilletly, S. D., Jackson, N. D., and Staid, A. (2023). Evaluating the impact of wildfire smoke on solar photovoltaic production. *Applied Energy*, 348:121303.

Gils, H. C. (2015). Balancing of intermittent renewable power generation by demand response and thermal energy storage.

Gils, H. C., Gardian, H., Kittel, M., Schill, W.-P., Murmann, A., Launer, J., Gaumnitz, F., van Ouwerkerk, J., Mikurda, J., and Torralba-Díaz, L. (2022). Model-related outcome differences in power system models with sector coupling—quantification and drivers. *Renewable and Sustainable Energy Reviews*, 159:112177.

Giorgetta, M., Jungclaus, J., Reick, C., Legutke, S., Brovkin, V., Crueger, T., Esch, M., Fieg, K., Glushak, K., Gayler, V., et al. (2012). Climate change from 1850 to 2100 in mpi-esm simulations for the coupled model intercomparison project 5. *J. Adv. Model. Earth Syst.*

Giorgi, F. and Bates, G. T. (1989). The climatological skill of a regional model over complex terrain. *Monthly Weather Review*, 117(11):2325–2347.

Giorgi, F. and Gutowski Jr, W. J. (2015). Regional dynamical downscaling and the cordex initiative. *Annual review of environment and resources*, 40:467–490.

Giorgi, F. and Mearns, L. O. (1991). Approaches to the simulation of regional climate change: a review. *Reviews of geophysics*, 29(2):191–216.

GLOBE Task Team, others (Hastings, David A., P. K. D. G. M. E. M. B. H. M. H. M. H. M. P. H. J. P. N. A. B. T. L. L. J.-P. M. G. S., and MacDonald), J. S. (1999). The global land one-kilometer base elevation (globe) digital elevation model, version 1.0. *National Oceanic and Atmospheric Administration, National Geophysical Data Center*. Digital data base on the World Wide Web.

Goffart, J., Mara, T., and Wurtz, E. (2017). Generation of stochastic weather data for uncertainty and sensitivity analysis of a low-energy building. *Journal of Building Physics*, 41(1):41–57.

Gonçalves, A. C., Costoya, X., Nieto, R., and Liberato, M. L. (2024). Extreme weather events on energy systems: a comprehensive review on impacts, mitigation, and adaptation measures. *Sustainable Energy Research*, 11(1):4.

Gonzalez-Aparicio, I., Monforti, F., Volker, P., Zucker, A., Careri, F., Huld, T., and Badger, J. (2017). Simulating european wind power generation applying statistical downscaling to reanalysis data. *Applied Energy*, 199:155–168.

Goubanova, K., Echevin, V., Dewitte, B., Codron, F., Takahashi, K., Terray, P., and Vrac, M. (2011). Statistical downscaling of sea-surface wind over the peru–chile upwelling region: diagnosing the impact of climate change from the ipsl-cm4 model. *Climate Dynamics*, 36:1365–1378.

Grantham, A., Pudney, P., and Boland, J. (2018). Generating synthetic sequences of global horizontal irradiation. *Solar Energy*, 162:500–509.

Gruber, K., Klöckl, C., Regner, P., Baumgartner, J., and Schmidt, J. (2019). Assessing the global wind atlas and local measurements for bias correction of wind power generation simulated from merra-2 in brazil. *Energy*, 189:116212.

Gruber, K. and Schmidt, J. (2019). Bias-correcting simulated wind power in austria and in brazil from the era-5 reanalysis data set with the dtu wind atlas. In *11. Internationale Energiewirtschaftstagung an der TU Wien*.

Günay, M. E. (2016). Forecasting annual gross electricity demand by artificial neural networks using predicted values of socio-economic indicators and climatic conditions: Case of turkey. *Energy Policy*, 90:92–101.

Guo, S., Yan, D., Hong, T., Xiao, C., and Cui, Y. (2019). A novel approach for selecting typical hot-year (thy) weather data. *Applied energy*, 242:1634–1648.

Hall, I., Prairie, R., Anderson, H., and Boes, E. (1978a). Generation of a typical meteorological year. Technical report, Sandia Labs., Albuquerque, NM (USA).

Hall, I. J., Prairie, R. R., Anderson, H. E., and Boes, E. C. (1978b). Generation of a typical meteorological year.

Hao, Z., Zhang, X., Xie, J., Yin, K., and Liu, J. (2022). Balance point temperature and heating degree-days in different climate conditions for building energy efficiency applications. *Building and Environment*, 216:109013.

Hart, M. and De Dear, R. (2004). Weather sensitivity in household appliance energy end-use. *Energy and Buildings*, 36(2):161–174.

Harvey, L. D. (2020). Using modified multiple heating-degree-day (hdd) and cooling-degree-day (cdd) indices to estimate building heating and cooling loads. *Energy and Buildings*, 229:110475.

Hashimoto, Y., Ohashi, Y., Nabeshima, M., Shigeta, Y., Kikegawa, Y., and Ihara, T. (2019). Sensitivity of electricity consumption to air temperature, air humidity and solar radiation at the city-block scale in osaka, japan. *Sustainable cities and society*, 45:38–47.

Hassan, M. A., Khalil, A., and Abubakr, M. (2021). Selection methodology of representative meteorological days for assessment of renewable energy systems. *Renewable Energy*, 177:34–51.

Hawker, G., Bell, K., MacIver, C., and Bialek, J. (2024). Management of extreme weather impacts on electricity grids: an international review. *Progress in Energy*.

Hawkins, E. and Sutton, R. (2009). The potential to narrow uncertainty in regional climate predictions. *Bulletin of the American Meteorological Society*, 90(8):1095–1108.

Hawkins, E. and Sutton, R. (2011). The potential to narrow uncertainty in projections of regional precipitation change. *Climate dynamics*, 37:407–418.

Hedegaard, K., Mathiesen, B. V., Lund, H., and Heiselberg, P. (2012). Wind power integration using individual heat pumps–analysis of different heat storage options. *Energy*, 47(1):284–293.

Hekkenberg, M., Benders, R., Moll, H., and Uiterkamp, A. S. (2009a). Indications for a changing electricity demand pattern: The temperature dependence of electricity demand in the netherlands. *Energy Policy*, 37(4):1542–1551.

Hekkenberg, M., Moll, H., and Uiterkamp, A. S. (2009b). Dynamic temperature dependence patterns in future energy demand models in the context of climate change. *Energy*, 34(11):1797–1806.

Henley, A. and Peirson, J. (1997). Non-linearities in electricity demand and temperature: parametric versus non-parametric methods. *Oxford bulletin of economics and statistics*, 59(1):149–162.

Herrera, M., Ramallo-González, A. P., Eames, M., Ferreira, A. A., and Coley, D. A. (2018). Creating extreme weather time series through a quantile regression ensemble. *Environmental Modelling & Software*, 110:28–37.

Hersbach, H., Bell, B., Berrisford, P., Hirahara, S., Horányi, A., Muñoz-Sabater, J., Nicolas, J., Peubey, C., Radu, R., Schepers, D., et al. (2020). The era5 global reanalysis. *Quarterly Journal of the Royal Meteorological Society*, 146(730):1999–2049.

Hill, D. C., McMillan, D., Bell, K. R., and Infield, D. (2011). Application of auto-regressive models to uk wind speed data for power system impact studies. *IEEE Transactions on Sustainable Energy*, 3(1):134–141.

Hirsh, R. F. and Koomey, J. G. (2015). Electricity consumption and economic growth: a new relationship with significant consequences? *The Electricity Journal*, 28(9):72–84.

Hiruta, Y., Gao, L., and Ashina, S. (2022). A novel method for acquiring rigorous temperature response functions for electricity demand at a regional scale. *Science of The Total Environment*, 819:152893.

Höhlein, K., Kern, M., Hewson, T., and Westermann, R. (2020). A comparative study of convolutional neural network models for wind field downscaling. *Meteorological Applications*, 27(6):e1961.

Holland, G., Done, J., Bruyere, C., Cooper, C. K., and Suzuki, A. (2010). Model investigations of the effects of climate variability and change on future gulf of mexico tropical cyclone activity. In *Offshore Technology Conference*, pages OTC–20690. OTC.

Höltinger, S., Mikovits, C., Schmidt, J., Baumgartner, J., Arheimer, B., Lindström, G., and Wetterlund, E. (2019). The impact of climatic extreme events on the feasibility of fully renewable power systems: A case study for sweden. *Energy*, 178:695–713.

Hor, C.-L., Watson, S. J., and Majithia, S. (2005). Analyzing the impact of weather variables on monthly electricity demand. *IEEE transactions on power systems*, 20(4):2078–2085.

Horvath, K., Bajić, A., and Ivatek-Šahdan, S. (2011). Dynamical downscaling of wind speed in complex terrain prone to bora-type flows. *Journal of applied meteorology and climatology*, 50(8):1676–1691.

Hosseini Baghanam, A., Norouzi, E., and Nourani, V. (2022). Wavelet-based predictor screening for statistical downscaling of precipitation and temperature using the artificial neural network method. *Hydrology Research*, 53(3):385–406.

Hosseini Baghanam, A., Nourani, V., Bejani, M., and Ke, C.-Q. (2024). Improving the statistical downscaling performance of climatic parameters with convolutional neural networks. *Journal of Water and Climate Change*, 15(4):1772–1796.

Hou, R., Li, S., Wu, M., Ren, G., Gao, W., Khayatnezhad, M., et al. (2021). Assessing of impact climate parameters on the gap between hydropower supply and electricity demand by rcps scenarios and optimized ann by the improved pathfinder (ipf) algorithm. *Energy*, 237:121621.

Hu, W., Scholz, Y., Yeligeti, M., Deng, Y., and Jochem, P. (2024). Future electricity demand for europe: Unraveling the dynamics of the temperature response function. *Applied Energy*, 368:123387.

Huang, A. and Chang, F.-J. (2021). Using a self-organizing map to explore local weather features for smart urban agriculture in northern taiwan. *Water*, 13(23):3457.

Huang, J. and Gurney, K. R. (2016). Impact of climate change on us building energy demand: sensitivity to spatiotemporal scales, balance point temperature, and population distribution. *Climatic change*, 137:171–185.

Huang, K. T. and Ou, W. S. (2011). Using modified sandia method in developing typical solar radiation year for photovoltaic electricity generation projection. *Applied Mechanics and Materials*, 71:4374–4381.

Huber, P. J. (1992). Robust estimation of a location parameter. In *Breakthroughs in statistics: Methodology and distribution*, pages 492–518. Springer.

Hussein, K., Alhosani, N., Al-Areeq, A. M., Al Aghbari, A. A., Elkamali, M., Alsumaiti, T., Sharif, H. O., Almurshidi, A. M., and Abdalati, W. (2025). Unprecedented rainfall in the united arab emirates: hydrologic and flood impact analysis of the april 2024 event. *Natural Hazards*, pages 1–23.

Ihara, T., Genchi, Y., Sato, T., Yamaguchi, K., and Endo, Y. (2008). City-block-scale sensitivity of electricity consumption to air temperature and air humidity in business districts of tokyo, japan. *Energy*, 33(11):1634–1645.

International Energy Agency (2018). The future of cooling. `https://www.iea.org/reports/the-future-of-cooling`. Accessed: 10.10.2023.

International Energy Agency (2022). The future of heat pumps. `https://iea.blob.core.windows.net/assets/4713780d-c0ae-4686-8c9b-29e782452695/TheFutureofHeatPumps.pdf`. Accessed: 10.10.2023.

International Energy Agency (n.d.a). Building envelopes. `https://www.iea.org/energy-system/buildings/building-envelopes`. Accessed: 10.10.2023.

International Energy Agency (n.d.b). Electrification. `https://www.iea.org/energy-system/electricity/electrification`. Accessed: 10.10.2023.

IRENA (2023). Renewable capacity statistics 2023. Accessed: 2024-12-10.

Jakubcionis, M. and Carlsson, J. (2017). Estimation of european union residential sector space cooling potential. *Energy Policy*, 101:225–235.

Jamil, F. and Ahmad, E. (2011). Income and price elasticities of electricity demand: Aggregate and sector-wise analyses. *Energy policy*, 39(9):5519–5527.

Janjai, S. and Deeyai, P. (2009). Comparison of methods for generating typical meteorological year using meteorological data from a tropical environment. *Applied Energy*, 86(4):528–537.

Jentsch, M. F., Eames, M. E., and Levermore, G. J. (2015). Generating near-extreme summer reference years for building performance simulation. *Building Services Engineering Research and Technology*, 36(6):701–727.

Jeon, J., Kim, J., Song, H., Cho, S., and Park, N. (2022). Gt-gan: General purpose time series synthesis with generative adversarial networks. *Advances in Neural Information Processing Systems*, 35:36999–37010.

Jiang, Q., Cioffi, F., Conticello, F. R., Giannini, M., Telesca, V., and Wang, J. (2023). A stacked ensemble learning and non-homogeneous hidden markov model for daily precipitation downscaling and projection. *Hydrological Processes*, 37(9):e14992.

Jiang, Y. (2010). Generation of typical meteorological year for different climates of china. *Energy*, 35(5):1946–1953.

Jin, B. and Xu, X. (2024). Forecasting wholesale prices of yellow corn through the gaussian process regression. *Neural Computing and Applications*, 36(15):8693–8710.

Jin, X.-B., Gong, W.-T., Kong, J.-L., Bai, Y.-T., and Su, T.-L. (2022). Pfvae: a planar flow-based variational auto-encoder prediction model for time series data. *Mathematics*, 10(4):610.

Jochem, P., Whitehead, J., and Dütschke, E. (2021). The impact of electric vehicles on energy systems. int. encycl. transp., 1, 560–565, doi: 10.1016. Technical report, B978-0-08-102671-7.10515-9.

Johansson, P. (2021). Heat pumps in sweden–a historical review. *Energy*, 229:120683.

Jones, P., Kilsby, C., Harpham, C., Glenis, V., and Burton, A. (2010). Uk climate projections science report: Projections of future daily climate for the uk from the weather generator. *UK Climate Projections science report*.

Jourdier, B. (2020). Evaluation of era5, merra-2, cosmo-rea6, newa and arome to simulate wind power production over france. *Advances in Science and Research*, 17:63–77.

Jung, C., Demant, L., Meyer, P., and Schindler, D. (2022). Highly resolved modeling of extreme wind speed in north america and europe. *Atmospheric Science Letters*, 23(5):e1082.

Jung, C. and Schindler, D. (2021). The role of the power law exponent in wind energy assessment: A global analysis. *International Journal of Energy Research*, 45(6):8484–8496.

Kemsley, S. W., Osborn, T. J., Dorling, S. R., and Wallace, C. (2024). Pattern scaling the parameters of a markov-chain gamma-distribution daily precipitation generator. *International Journal of Climatology*, 44(1):144–159.

Kennedy, S. and Rogers, P. (2003). A probabilistic model for simulating long-term wind-power output. *Wind Engineering*, 27(3):167–181.

Kimura, F. and Kitoh, A. (2007). Downscaling by pseudo global warming method. *The Final Report of ICCAP*, 4346:463–478.

Kirchmeier, M. C., Lorenz, D. J., and Vimont, D. J. (2014). Statistical downscaling of daily wind speed variations. *Journal of applied meteorology and climatology*, 53(3):660–675.

Kittel, M. and Schill, W.-P. (2024). Measuring the dunkelflaute: How (not) to analyze variable renewable energy shortage. *Environmental Research: Energy*, 1(3):035007.

Klöckl, B. and Papaefthymiou, G. (2010). Multivariate time series models for studies on stochastic generators in power systems. *Electric Power Systems Research*, 80(3):265–276.

Knight, K., Klein, S., and Duffie, J. (1991). A methodology for the synthesis of hourly weather data. *Solar Energy*, 46(2):109–120.

Krarti, M. and Aldubyan, M. (2021). Review analysis of covid-19 impact on electricity demand for residential buildings. *Renewable and Sustainable Energy Reviews*, 143:110888.

Krese, G., Lampret, Ž., Butala, V., and Prek, M. (2018). Determination of a building's balance point temperature as an energy characteristic. *Energy*, 165:1034–1049.

Kuchar, L. (2004). Using wgenk to generate synthetic daily weather data for modelling of agricultural processes. *Mathematics and Computers in Simulation*, 65(1-2):69–75.

Laddimath, R. S. and Patil, N. S. (2019). Artificial neural network technique for statistical downscaling of global climate model. *Mapan*, 34(1):121–127.

Lamb, H. (1950). Types and spells of weather around the year in the british isles: annual trends, seasonal structure of the year, singularities. *Quarterly Journal of the Royal Meteorological Society*, 76(330):393–429.

Lau, K. K.-L., Ng, E. Y.-Y., Chan, P.-W., and Ho, J. C.-K. (2017). Near-extreme summer meteorological data set for sub-tropical climates. *Building Services Engineering Research and Technology*, 38(2):197–208.

Le, D. D., Gross, G., and Berizzi, A. (2015). Probabilistic modeling of multisite wind farm production for scenario-based applications. *IEEE Transactions on Sustainable Energy*, 6(3):748–758.

Lechtenböhmer, S. and Schüring, A. (2011). The potential for large-scale savings from insulating residential buildings in the eu. *Energy efficiency*, 4:257–270.

Legasa, M., Manzanas, R., Calviño, A., and Gutiérrez, J. M. (2022). A posteriori random forests for stochastic downscaling of precipitation by predicting probability distributions. *Water Resources Research*, 58(4):e2021WR030272.

Levermore, G. J. and Parkinson, J. (2006). Analyses and algorithms for new test reference years and design summer years for the uk. *Building services engineering research and technology*, 27(4):311–325.

Li, B., Basu, S., Watson, S. J., and Russchenberg, H. W. (2021a). A brief climatology of dunkelflaute events over and surrounding the north and baltic sea areas. *Energies*, 14(20):6508.

Li, B., Basu, S., Watson, S. J., and Russchenberg, H. W. (2021b). Mesoscale modeling of a "dunkelflaute" event. *Wind Energy*, 24(1):5–23.

Li, H., Yu, S., and Principe, J. (2023a). Causal recurrent variational autoencoder for medical time series generation. In *Proceedings of the AAAI conference on artificial intelligence*, volume 37, pages 8562–8570.

Li, H., Zhang, T., Wang, A., Wang, M., Huang, J., and Hu, Y. (2023b). A new method of generating extreme building energy year and its application. *Energy*, 278:128020.

Li, X., Metsis, V., Wang, H., and Ngu, A. H. H. (2022). Tts-gan: A transformer-based time-series generative adversarial network. In *International conference on artificial intelligence in medicine*, pages 133–143. Springer.

Li, X. and Sailor, D. (1995). Electricity use sensitivity to climate and climate change. *World Resource Review*, 7(3).

Li, Y., Pizer, W. A., and Wu, L. (2019). Climate change and residential electricity consumption in the yangtze river delta, china. *Proceedings of the National Academy of Sciences*, 116(2):472–477.

Liao, S., Yao, W., Han, X., Wen, J., and Cheng, S. (2017). Chronological operation simulation framework for regional power system under high penetration of renewable energy using meteorological data. *Applied Energy*, 203:816–828.

Lin, Y., Chen, K., Zhang, X., Tan, B., and Lu, Q. (2022). Forecasting crude oil futures prices using bilstm-attention-cnn model with wavelet transform. *Applied Soft Computing*, 130:109723.

Lindelöf, D. (2017). Bayesian estimation of a building's base temperature for the calculation of heating degree-days. *Energy and buildings*, 134:154–161.

Lindelöf, D., Alisafaee, M., Borsò, P., Grigis, C., and Viaene, J. (2018). Bayesian verification of an energy conservation measure. *Energy and Buildings*, 171:1–10.

Lopez-Villalobos, C. A., Martinez-Alvarado, O., Rodriguez-Hernandez, O., and Romero-Centeno, R. (2022). Analysis of the influence of the wind speed profile on wind power production. *Energy Reports*, 8:8079–8092.

Lund, H. (1991). The design reference year.

MacMackin, N., Miller, L., and Carriveau, R. (2019). Modeling and disaggregating hourly effects of weather on sectoral electricity demand. *Energy*, 188:115956.

Magnano, L., Boland, J. W., and Hyndman, R. J. (2008). Generation of synthetic sequences of half-hourly temperature. *Environmetrics: The official journal of the International Environmetrics Society*, 19(8):818–835.

Mantzos, L., MATEI, N.-A., MULHOLLAND, E., RÓZSAI, M., TAMBA, M., WIESENTHAL, T., et al. (2018). The jrc integrated database of the european energy system.

Marengo, J. A., Cunha, A. P., Cuartas, L. A., Deusdará Leal, K. R., Broedel, E., Seluchi, M. E., Michelin, C. M., De Praga Baião, C. F., Chuchón Angulo, E., Almeida, E. K., et al. (2021). Extreme drought in the brazilian pantanal in 2019–2020: Characterization, causes, and impacts. *Frontiers in Water*, 3:639204.

Mathews, D., Gallachoir, B. O., and Deane, P. (2023). Systematic bias in reanalysis-derived solar power profiles & the potential for error propagation in long duration energy storage studies. *Applied Energy*, 336:120819.

Mattsson, N., Verendel, V., Hedenus, F., and Reichenberg, L. (2021). An autopilot for energy models–automatic generation of renewable supply curves, hourly capacity factors and hourly synthetic electricity demand for arbitrary world regions. *Energy Strategy Reviews*, 33:100606.

MeteoSwiss (2013). The data portal of meteoswiss for research and teaching.

Meyer, G. P. (2021). An alternative probabilistic interpretation of the huber loss. In *Proceedings of the ieee/cvf conference on computer vision and pattern recognition*, pages 5261–5269.

Miller, N. L., Hayhoe, K., Jin, J., and Auffhammer, M. (2008). Climate, extreme heat, and electricity demand in california. *Journal of Applied Meteorology and Climatology*, 47(6):1834–1844.

Ministry of Infrastructure (Sweden) (2021). Sweden's report under article 14(1) of directive 2012/27/eu on energy efficiency – promotion of efficiency in heating and cooling. `https://energy.ec.europa.eu/system/files/2021-10/se_ca_2020_en.pdf`. Accessed: 12.02.2024.

Misra, V. and Kanamitsu, M. (2004). Anomaly nesting: A methodology to downscale seasonal climate simulations from agcms. *Journal of Climate*, 17(17):3249–3262.

Mockert, F., Grams, C. M., Brown, T., and Neumann, F. (2023). Meteorological conditions during periods of low wind speed and insolation in germany: The role of weather regimes. *Meteorological Applications*, 30(4):e2141.

Mohammadi, H. A., Ghofrani, S., and Nikseresht, A. (2023). Using empirical wavelet transform and high-order fuzzy cognitive maps for time series forecasting. *Applied Soft Computing*, 135:109990.

Molina, M. O., Gutiérrez, C., and Sánchez, E. (2021). Comparison of era5 surface wind speed climatologies over europe with observations from the hadisd dataset. *International Journal of Climatology*, 41(10):4864–4878.

Monahan, A. H. (2012). Can we see the wind? statistical downscaling of historical sea surface winds in the subarctic northeast pacific. *Journal of climate*, 25(5):1511–1528.

Moral-Carcedo, J. and Pérez-García, J. (2015). Temperature effects on firms' electricity demand: An analysis of sectorial differences in spain. *Applied energy*, 142:407–425.

Moral-Carcedo, J. and Vicéns-Otero, J. (2005). Modelling the non-linear response of spanish electricity demand to temperature variations. *Energy economics*, 27(3):477–494.

Morales, J. M., Minguez, R., and Conejo, A. J. (2010). A methodology to generate statistically dependent wind speed scenarios. *Applied Energy*, 87(3):843–855.

Moss, R. H., Edmonds, J. A., Hibbard, K. A., Manning, M. R., Rose, S. K., Van Vuuren, D. P., Carter, T. R., Emori, S., Kainuma, M., Kram, T., et al. (2010). The next generation of scenarios for climate change research and assessment. *Nature*, 463(7282):747–756.

Mukherjee, S. and Nateghi, R. (2017). Climate sensitivity of end-use electricity consumption in the built environment: an application to the state of florida, united states. *Energy*, 128:688–700.

Muratori, M., Ledna, C., McJeon, H., Kyle, P., Patel, P., Kim, S. H., Wise, M., Kheshgi, H. S., Clarke, L. E., and Edmonds, J. (2017). Cost of power or power of cost: A us modeling perspective. *Renewable and Sustainable Energy Reviews*, 77:861–874.

Murcia, J. P., Koivisto, M. J., Luzia, G., Olsen, B. T., Hahmann, A. N., Sørensen, P. E., and Als, M. (2022). Validation of european-scale simulated wind speed and wind generation time series. *Applied Energy*, 305:117794.

National Geographic (n.d.). Wildfires. Accessed: 2025-04-05.

National Weather Service (n.d.). Flood and flash flood. Accessed: 2025-04-05.

New, M., Lopez, A., Dessai, S., and Wilby, R. (2007). Challenges in using probabilistic climate change information for impact assessments: an example from the water sector. *Philosophical Transactions of the Royal Society A: Mathematical, Physical and Engineering Sciences*, 365(1857):2117–2131.

Nfaoui, H., Essiarab, H., and Sayigh, A. (2004). A stochastic markov chain model for simulating wind speed time series at tangiers, morocco. *Renewable Energy*, 29(8):1407–1418.

Nik, V. M. (2017). Application of typical and extreme weather data sets in the hygrothermal simulation of building components for future climate–a case study for a wooden frame wall. *Energy and Buildings*, 154:30–45.

Nishimwe, A. M. R. and Reiter, S. (2021). Estimation, analysis and mapping of electricity consumption of a regional building stock in a temperate climate in europe. *Energy and Buildings*, 253:111535.

Nitsch, F., Scholz, Y., Hu, W., von Krbek, K., Stegen, R., El Ghazi, A. A., Frey, U., Nienhaus, K., Finck, R., Slednev, V., et al. (2023). Versorgungsicherheit in deutschland und mitteleuropa während extremwetter-ereignissen (vermeer)-der beitrag des transnationalen stromhandels bei hohen anteilen erneuerbarer energien.

Nodelman, U., Shelton, C. R., and Koller, D. (2012). Continuous time bayesian networks. *arXiv preprint arXiv:1301.0591*.

Odyssee Energy (2021). 2021 eu energy efficiency scoreboard. Accessed: 10.10.2023.

Oh, M., Lee, J., Kim, J.-Y., and Kim, H.-G. (2022). Machine learning-based statistical downscaling of wind resource maps using multi-resolution topographical data. *Wind Energy*, 25(6):1121–1141.

Ohba, M., Kanno, Y., and Bando, S. (2023). Effects of meteorological and climatological factors on extremely high residual load and possible future changes. *Renewable and Sustainable Energy Reviews*, 175:113188.

Olauson, J. (2018). Era5: The new champion of wind power modelling? *Renewable energy*, 126:322–331.

Olauson, J., Bergkvist, M., and Rydén, J. (2017). Simulating intra-hourly wind power fluctuations on a power system level. *Wind Energy*, 20(6):973–985.

Olonscheck, M., Holsten, A., and Kropp, J. P. (2011). Heating and cooling energy demand and related emissions of the german residential building stock under climate change. *Energy Policy*, 39(9):4795–4806.

Omoyele, O., Hoffmann, M., Koivisto, M., Larraneta, M., Weinand, J. M., Linßen, J., and Stolten, D. (2024). Increasing the resolution of solar and wind time series for energy system modeling: A review. *Renewable and Sustainable Energy Reviews*, 189:113792.

Palacios-Garcia, E., Moreno-Munoz, A., Santiago, I., Flores-Arias, J., Bellido-Outeirino, F., and Moreno-Garcia, I. (2018). A stochastic modelling and simulation approach to heating and cooling electricity consumption in the residential sector. *Energy*, 144:1080–1091.

Palma, R. M., Ramos, J. S., Delgado, M. G., Amores, T. R. P., D'Angelo, G., and Domínguez, S. Á. (2023). Extending the concept of high-performance buildings to existing dwellings. *Energy and Buildings*, 296:113431.

Papaefthymiou, G. and Klockl, B. (2008). Mcmc for wind power simulation. *IEEE transactions on energy conversion*, 23(1):234–240.

Papakostas, K., Mavromatis, T., and Kyriakis, N. (2010). Impact of the ambient temperature rise on the energy consumption for heating and cooling in residential buildings of greece. *Renewable Energy*, 35(7):1376–1379.

Parliament, T. E. and the Council of the European Union (2010). Directive 2010/31/eu of the european parliament and of the council of 19 may 2010 on the energy performance of buildings (recast). *Official Journal of the European Union*.

Parliament, T. E. and the Council of the European Union (2012). Directive 2012/27/eu of the european parliament and of the council of 25 october 2012 on energy efficiency, amending directives 2009/125/ec and 2010/30/eu and repealing directives 2004/8/ec and 2006/32/ec text with eea relevance. *Official Journal of the European Union*.

Pedregosa, F., Varoquaux, G., Gramfort, A., Michel, V., Thirion, B., Grisel, O., Blondel, M., Prettenhofer, P., Weiss, R., Dubourg, V., et al. (2011). Scikit-learn: Machine learning in python. *Journal of machine learning research*, 12(Oct):2825–2830.

Pernigotto, G., Prada, A., and Gasparella, A. (2020). Extreme reference years for building energy performance simulation. *Journal of Building Performance Simulation*, 13(2):152–166.

Pesch, T., Schröders, S., Allelein, H.-J., and Hake, J.-F. (2015). A new markov-chain-related statistical approach for modelling synthetic wind power time series. *New journal of physics*, 17(5):055001.

Petrakis, M., Lykoudis, S., and Kassomenos, P. (1996). A software tool for the creation of a typical meteorological year. *Environmental Software*, 11(4):221–227.

Pezzutto, S., Fazeli, R., De Felice, M., and Sparber, W. (2016). Future development of the air-conditioning market in europe: an outlook until 2020. *Wiley Interdisciplinary Reviews: Energy and Environment*, 5(6):649–669.

Pielke Sr, R. A. and Wilby, R. L. (2012). Regional climate downscaling: What's the point? *Eos, Transactions American Geophysical Union*, 93(5):52–53.

Planchon, O., Quénol, H., Irimia, L., and Patriche, C. (2015). European cold wave during february 2012 and impacts in wine growing regions of moldavia (romania). *Theoretical and Applied Climatology*, 120:469–478.

Pour, S. H., Shahid, S., Chung, E.-S., and Wang, X.-J. (2018). Model output statistics downscaling using support vector machine for the projection of spatial and temporal changes in rainfall of bangladesh. *Atmospheric research*, 213:149–162.

Psiloglou, B., Giannakopoulos, C., Majithia, S., and Petrakis, M. (2009). Factors affecting electricity demand in athens, greece and london, uk: A comparative assessment. *Energy*, 34(11):1855–1863.

Qian, B., De Jong, R., Yang, J., Wang, H., and Gameda, S. (2011). Comparing simulated crop yields with observed and synthetic weather data. *Agricultural and forest meteorology*, 151(12):1781–1791.

Qian, C., Ye, Y., Jiang, J., Zhong, Y., Zhang, Y., Pinto, I., Huang, C., Li, S., and Wei, K. (2024). Rapid attribution of the record-breaking heatwave event in north china in june 2023 and future risks. *Environmental Research Letters*, 19(1):014028.

Qin, P., Xu, H., Liu, M., Xiao, C., Forrest, K. E., Samuelsen, S., and Tarroja, B. (2020). Assessing concurrent effects of climate change on hydropower supply, electricity demand, and greenhouse gas emissions in the upper yangtze river basin of china. *Applied Energy*, 279:115694.

Rahman, I. A. and Dewsbury, J. (2007). Selection of typical weather data (test reference years) for subang, malaysia. *Building and Environment*, 42(10):3636–3641.

Rajeevan, M., Rohini, P., Nair, S. A., Tirkey, S., Goswami, T., and Kumar, N. (2023). Heat and cold waves in india: Processes and predictability. Accessed: 2025-04-05.

Rastogi, P. (2016). On the sensitivity of buildings to climate: the interaction of weather and building envelopes in determining future building energy consumption. Technical report, EPFL.

Rastogi, P. and Andersen, M. (2015). Embedding stochasticity in building simulation through synthetic weather files. *Proceedings of BS 2015*, pages 963–970.

Reed, D. A., Powell, M. D., and Westerman, J. M. (2010). Energy supply system performance for hurricane katrina. *Journal of Energy Engineering*, 136(4):95–102.

Ritter, M., Shen, Z., Cabrera, B. L., Odening, M., and Deckert, L. (2015). A new approach to assess wind energy potential. *Energy Procedia*, 75:671–676.

Rocheta, E., Evans, J. P., and Sharma, A. (2017). Can bias correction of regional climate model lateral boundary conditions improve low-frequency rainfall variability? *Journal of Climate*, 30(24):9785–9806.

Rojas, M. and Seth, A. (2003). Simulation and sensitivity in a nested modeling system for south america. part ii: Gcm boundary forcing. *Journal of climate*, 16(15):2454–2471.

Ruggles, T. H. and Caldeira, K. (2022). Wind and solar generation may reduce the inter-annual variability of peak residual load in certain electricity systems. *Applied Energy*, 305:117773.

Ruth, M. and Lin, A.-C. (2006). Regional energy demand and adaptations to climate change: methodology and application to the state of maryland, usa. *Energy policy*, 34(17):2820–2833.

Sailor, D. J. and Muñoz, J. R. (1997). Sensitivity of electricity and natural gas consumption to climate in the usa—methodology and results for eight states. *Energy*, 22(10):987–998.

Samuel, D. L., Nagendra, S. S., and Maiya, M. (2013). Passive alternatives to mechanical air conditioning of building: A review. *Building and Environment*, 66:54–64.

Sandvall, A. and Karlsson, K. B. (2023). Energy system and cost impacts of heat supply to low-energy buildings in sweden. *Energy*, 268:126743.

Santiago, I., Moreno-Munoz, A., Quintero-Jiménez, P., Garcia-Torres, F., and Gonzalez-Redondo, M. (2021). Electricity demand during pandemic times: The case of the covid-19 in spain. *Energy policy*, 148:111964.

Saraiva, S. V., de Oliveira Carvalho, F., Santos, C. A. G., Barreto, L. C., and Freire, P. K. d. M. M. (2021). Daily streamflow forecasting in sobradinho reservoir using machine learning models coupled with wavelet transform and bootstrapping. *Applied Soft Computing*, 102:107081.

Sato, T., Kimura, F., and Kitoh, A. (2007). Projection of global warming onto regional precipitation over mongolia using a regional climate model. *Journal of Hydrology*, 333(1):144–154.

Schär, C., Frei, C., Lüthi, D., and Davies, H. C. (1996). Surrogate climate-change scenarios for regional climate models. *Geophysical Research Letters*, 23(6):669–672.

Schill, W.-P. (2014). Residual load, renewable surplus generation and storage requirements in germany. *Energy Policy*, 73:65–79.

Schnur, R. and Lettenmaier, D. P. (1998). A case study of statistical downscaling in australia using weather classification by recursive partitioning. *Journal of Hydrology*, 212:362–379.

Scholz, Y. (2012). Renewable energy based electricity supply at low costs: development of the remix model and application for europe.

Scholz, Y., von Bremen, L., Lohmann, G., Hu, W., and Schroedter-Homscheidt, M. (2023). Dunkelflaute and long-term electric energy shortage events in europe.

Schoof, J. T. and Pryor, S. (2001). Downscaling temperature and precipitation: A comparison of regression-based methods and artificial neural networks. *International Journal of Climatology: A Journal of the Royal Meteorological Society*, 21(7):773–790.

Semenov, M. A. (2008). Simulation of extreme weather events by a stochastic weather generator. *Climate Research*, 35(3):203–212.

Senf, F., Heinold, B., Kubin, A., Müller, J., Schrödner, R., and Tegen, I. (2023). How the extreme 2019–2020 australian wildfires affected global circulation and adjustments. *Atmospheric Chemistry and Physics*, 23(15):8939–8958.

Seydi, S. T. (2025). Assessment of the january 2025 los angeles county wildfires: A multi-modal analysis of impact, response, and population exposure. *arXiv preprint arXiv:2501.17880*.

Shin, J.-Y., Jeong, C., and Heo, J.-H. (2018). A novel statistical method to temporally downscale wind speed weibull distribution using scaling property. *Energies*, 11(3):633.

Sigmund, A., Freier, K., Rehm, T., Ries, L., Schunk, C., Menzel, A., and Thomas, C. K. (2019). Multivariate statistical air mass classification for the high-alpine observatory at the zugspitze mountain, germany. *Atmospheric Chemistry and Physics*, 19(19):12477–12494.

Sinha, S. and Chandel, S. (2015). Review of recent trends in optimization techniques for solar photovoltaic–wind based hybrid energy systems. *Renewable and sustainable energy reviews*, 50:755–769.

Slednev, V. (2024). *Development of a techno-economic energy system model considering the highly resolved conversion and multimodal transmission of energy carriers on a global scale*. PhD thesis, Karlsruhe Institute of Technology, Karlsruhe, Germany.

Solbakken, K., Birkelund, Y., and Samuelsen, E. M. (2021). Evaluation of surface wind using wrf in complex terrain: Atmospheric input data and grid spacing. *Environmental Modelling & Software*, 145:105182.

Song, F., Zhu, Q., Wu, R., Jiang, Y., Xiong, A., Wang, B., Zhu, Y., and Li, Q. (2007). Meteorological data set for building thermal environment analysis of china.

Song, Y.-l., Darani, K. S., Khdair, A. I., Abu-Rumman, G., and Kalbasi, R. (2021). A review on conventional passive cooling methods applicable to arid and warm climates considering economic cost and efficiency analysis in resource-based cities. *Energy Reports*, 7:2784–2820.

Staffell, I. and Pfenninger, S. (2016). Using bias-corrected reanalysis to simulate current and future wind power output. *Energy*, 114:1224–1239.

Stetter, D. (2014). *Enhancement of the REMix energy system model: Global renewable energy potentials, optimized power plant siting and scenario validation*. PhD thesis, Universtität Stuttgart.

Sulaiman, N. A. F., Shaharudin, S. M., Ismail, S., Zainuddin, N. H., Tan, M. L., and Abd Jalil, Y. (2022). Predictive modelling of statistical downscaling based on hybrid machine learning model for daily rainfall in east-coast peninsular malaysia. *Symmetry*, 14(5):927.

Swiss Society of Engineers and Architects (SIA) (2016). SIA 380/1:2016 – Thermische Energie im Hochbau. `https://www.sia.ch/publikationen/normen/`. Swiss Standard for calculating thermal energy in buildings.

Szustak, G., Dąbrowski, P., Gradoń, W., and Szewczyk, Ł. (2022). The relationship between energy production and gdp: Evidence from selected european economies. *Energies*, 15(1):50.

TABULA (2015). Exemplary building stocks. `https://webtool.building-typology.eu/?c=ba#bm`. Retrieved 10 10, 2023.

TABULA (n.d.). Concept of "average buildings". `https://episcope.eu/monitoring/average-buildings/`. Retrieved 10 10, 2023.

Tang, B. H. and Bassill, N. P. (2018). Point downscaling of surface wind speed for forecast applications. *Journal of Applied Meteorology and Climatology*, 57(3):659–674.

Tang, K., Zhu, H., and Ni, P. (2021). Spatial downscaling of land surface temperature over heterogeneous regions using random forest regression considering spatial features. *Remote Sensing*, 13(18):3645.

Taylor, K. E., Stouffer, R. J., and Meehl, G. A. (2012). An overview of cmip5 and the experiment design. *Bulletin of the American meteorological Society*, 93(4):485–498.

Technical University of Denmark (2023). Global wind atlas. Online.

Tennekes, H. (1973). The logarithmic wind profile. *Journal of Atmospheric sciences*, 30(2):234–238.

Thellufsen, J. Z. and Lund, H. (2016). Roles of local and national energy systems in the integration of renewable energy. *Applied Energy*, 183:419–429.

Toktarova, A., Gruber, L., Hlusiak, M., Bogdanov, D., and Breyer, C. (2019). Long term load projection in high resolution for all countries globally. *International Journal of Electrical Power & Energy Systems*, 111:160–181.

Tradowsky, J. S., Philip, S. Y., Kreienkamp, F., Kew, S. F., Lorenz, P., Arrighi, J., Bettmann, T., Caluwaerts, S., Chan, S. C., De Cruz, L., et al. (2023). Attribution of the heavy rainfall events leading to severe flooding in western europe during july 2021. *Climatic Change*, 176(7):90.

Trieb, F. and Thess, A. (2020). Storage plants–a solution to the residual load challenge of the power sector? *Journal of Energy Storage*, 31:101626.

Trull, O., García-Díaz, J. C., and Troncoso, A. (2021). One-day-ahead electricity demand forecasting in holidays using discrete-interval moving seasonalities. *Energy*, 231:120966.

Tsikaloudaki, K., Laskos, K., and Bikas, D. (2011). On the establishment of climatic zones in europe with regard to the energy performance of buildings. *Energies*, 5(1):32–44.

UNEP DTU Partnership (2021). Climate technologies in an urban context. `https://tech-action.unepccc.org/wp-content/uploads/sites/2/2021/10/2021-06-tna-cities-guidebook-web.pdf`. Accessed: 10.10.2023.

Van der Heijden, M., Velikova, M., and Lucas, P. J. (2014). Learning bayesian networks for clinical time series analysis. *Journal of biomedical informatics*, 48:94–105.

van der Kamp, D., Curry, C. L., and Monahan, A. H. (2012). Statistical downscaling of historical monthly mean winds over a coastal region of complex terrain. ii. predicting wind components. *Climate dynamics*, 38:1301–1311.

van der Most, L., van der Wiel, K., Benders, R., Gerbens-Leenes, P., Kerkmans, P., and Bintanja, R. (2022). Extreme events in the european renewable power system: validation of a modeling framework to estimate renewable electricity production and demand from meteorological data. *Renewable and Sustainable Energy Reviews*, 170:112987.

Van Uytven, E., De Niel, J., and Willems, P. (2020). Uncovering the shortcomings of a weather typing method. *Hydrology and Earth System Sciences*, 24(5):2671–2686.

Vanella, D., Longo-Minnolo, G., Belfiore, O. R., Ramírez-Cuesta, J. M., Pappalardo, S., Consoli, S., D'Urso, G., Chirico, G. B., Coppola, A., Comegna, A., et al. (2022). Comparing the use of era5 reanalysis dataset and ground-based agrometeorological data under different climates and topography in italy. *Journal of Hydrology: Regional Studies*, 42:101182.

Verbai, Z., Lakatos, Á., and Kalmár, F. (2014). Prediction of energy demand for heating of residential buildings using variable degree day. *Energy*, 76:780–787.

Vidal, J.-P. and Wade, S. (2008). A framework for developing high-resolution multi-model climate projections: 21st century scenarios for the uk. *International Journal of Climatology*, 28(7):843–858.

Vrac, M., Stein, M., and Hayhoe, K. (2007). Statistical downscaling of precipitation through nonhomogeneous stochastic weather typing. *Climate Research*, 34(3):169–184.

Wais, P. (2017). A review of weibull functions in wind sector. *Renewable and Sustainable Energy Reviews*, 70:1099–1107.

Waite, M. and Modi, V. (2014). Potential for increased wind-generated electricity utilization using heat pumps in urban areas. *Applied Energy*, 135:634–642.

Wang, Y. and Bielicki, J. M. (2018). Acclimation and the response of hourly electricity loads to meteorological variables. *Energy*, 142:473–485.

Wang, Y. and Sun, X. (2022). Simulation and evaluation of statistical downscaling of regional daily precipitation over north china based on self-organizing maps. *Atmosphere*, 13(1):86.

Weiss, A. (2001). Topographic position and landforms analysis. In *Poster presentation, ESRI user conference, San Diego, CA*, volume 200.

Wetzel, M., Ruiz, E. S. A., Witte, F., Schmugge, J., Sasanpour, S., Yeligeti, M., Miorelli, F., Buschmann, J., Cao, K.-K., Wulff, N., et al. (2024). Remix: A gams-based framework for optimizing energy system models. *Journal of Open Source Software*, 9(99):6330.

Wilks, D. (2002). Realizations of daily weather in forecast seasonal climate. *Journal of Hydrometeorology*, 3(2):195–207.

Wilks, D. S. (2010). Use of stochastic weathergenerators for precipitation downscaling. *Wiley Interdisciplinary Reviews: Climate Change*, 1(6):898–907.

Wilks, D. S. and Wilby, R. L. (1999). The weather generation game: a review of stochastic weather models. *Progress in physical geography*, 23(3):329–357.

Winstral, A., Jonas, T., and Helbig, N. (2017). Statistical downscaling of gridded wind speed data using local topography. *Journal of Hydrometeorology*, 18(2):335–348.

Woods, J. and Fuller, C. (2014). Estimating base temperatures in econometric models that include degree days. *Energy Economics*, 45:166–171.

World Meteorological Organization (n.d.). Drought. Accessed: 2025-04-05.

Wu, W., Lynch, A. H., and Rivers, A. (2005). Estimating the uncertainty in a regional climate model related to initial and lateral boundary conditions. *Journal of climate*, 18(7):917–933.

Wu, Y., An, J., Gui, C., Xiao, C., and Yan, D. (2023). A global typical meteorological year (tmy) database on era5 dataset. In *Building Simulation*, volume 16, pages 1013–1026. Springer.

Wu, Y., Ni, J., Cheng, W., Zong, B., Song, D., Chen, Z., Liu, Y., Zhang, X., Chen, H., and Davidson, S. B. (2021). Dynamic gaussian mixture based deep generative model for robust forecasting on sparse multivariate time series. In *Proceedings of the AAAI Conference on Artificial Intelligence*, volume 35, pages 651–659.

Xiao, Q., Chaoqin, C., and Li, Z. (2017). Time series prediction using dynamic bayesian network. *Optik*, 135:98–103.

Xie, H., Yao, Z., Zhang, Y., Xu, Y., Xu, X., Liu, T., Lin, H., Lao, X., Rutherford, S., Chu, C., et al. (2013). Short-term effects of the 2008 cold spell on mortality in three subtropical cities in guangdong province, china. *Environmental health perspectives*, 121(2):210–216.

Xu, C., Hao, C., Li, L., Han, X., Xue, F., Sun, M., and Shen, W. (2018). Evaluation of the power-law wind-speed extrapolation method with atmospheric stability classification methods for flows over different terrain types. *Applied Sciences*, 8(9):1429.

Xu, Z. and Yang, Z.-L. (2012). An improved dynamical downscaling method with gcm bias corrections and its validation with 30 years of climate simulations. *Journal of Climate*, 25(18):6271–6286.

Yang, H., Yan, J., Liu, Y., and Song, Z. (2022). Statistical downscaling of numerical weather prediction based on convolutional neural networks. *Global Energy Interconnection*, 5(2):217–225.

Yao, Y., Zhuo, W., Gong, Z., Luo, B., Luo, D., Zheng, F., Zhong, L., Huang, F., Ma, S., Zhu, C., et al. (2023). Extreme cold events in north america and eurasia in november-december 2022: a potential vorticity gradient perspective.

Yildiz, B., Bilbao, J. I., and Sproul, A. B. (2017). A review and analysis of regression and machine learning models on commercial building electricity load forecasting. *Renewable and Sustainable Energy Reviews*, 73:1104–1122.

Yilmaz, H. Ü., Fouché, E., Dengiz, T., Krauß, L., Keles, D., and Fichtner, W. (2019). Reducing energy time series for energy system models via self-organizing maps. *IT-Information Technology*, 61(2-3):125–133.

Zainal, B. S., Ker, P. J., Mohamed, H., Ong, H. C., Fattah, I., Rahman, S. A., Nghiem, L. D., and Mahlia, T. I. (2024). Recent advancement and assessment of green hydrogen production technologies. *Renewable and Sustainable Energy Reviews*, 189:113941.

Zamanipour, B., Ghadaksaz, H., Keppo, I., and Saboohi, Y. (2023). Electricity supply and demand dynamics in iran considering climate change-induced stresses. *Energy*, 263:126118.

Zhang, W., Kleiber, W., Florita, A. R., Hodge, B.-M., and Mather, B. (2018). A stochastic downscaling approach for generating high-frequency solar irradiance scenarios. *Solar Energy*, 176:370–379.

Zhao, G., Li, D., Camus, P., Zhang, X., Qi, J., and Yin, B. (2024a). Weather-type statistical downscaling for ocean wave climate in the chinese marginal seas. *Ocean Modelling*, 187:102297.

Zhao, G., Li, D., Yang, S., Qi, J., and Yin, B. (2024b). The development of a weather-type statistical downscaling model for wave climate based on wave clustering. *Ocean Engineering*, 304:117863.

Zhong, S., Li, J., Whiteman, C. D., Bian, X., and Yao, W. (2008). Climatology of high wind events in the owens valley, california. *Monthly Weather Review*, 136(9):3536–3552.

Zhong, Z., Kassem, H., Haigh, I. D., Sifnioti, D. E., Gouldby, B., Liu, Y., and Camus, P. (2025). Advanced weather typing for downscaling of wave climate and storm surge at a uk nuclear power station. *Ocean Dynamics*, 75(4):1–19.

Zorita, E., Hughes, J. P., Lettemaier, D. P., and von Storch, H. (1995). Stochastic characterization of regional circulation patterns for climate model diagnosis and estimation of local precipitation. *Journal of Climate*, 8(5):1023–1042.

Zuo, J., Pullen, S., Palmer, J., Bennetts, H., Chileshe, N., and Ma, T. (2015). Impacts of heat waves and corresponding measures: a review. *Journal of Cleaner Production*, 92:1–12.

C. List of Figures

D. List of Tables